A Tale of Two Arcs: Petrogenesis of Ultramafic Xenoliths Sampling the Upper Mantle Wedge Beneath the West Bismarck Island Arc

TOLLAN, PETER,MICHAEL,EDWARD

A Tale of Two Arcs: Petrogenesis of Ultramafic Xenoliths Sampling the Upper Mantle Wedge Beneath the West Bismarck Island Arc

Peter Michael Edward Tollan

A thesis submitted in partial fulfilment of the requirements for the degree of Doctor of Philosophy at Durham University

Department of Earth Sciences

Durham University

June 2014

“If you just talk, I find that your mouth comes out with stuff”

-Karl Pilkington

Abstract

A Tale of Two Arcs: Petrogenesis of Ultramafic Xenoliths Sampling the Upper Mantle Wedge Beneath the West Bismarck Island Arc

Peter Michael Edward Tollan

Peridotite xenoliths transported to the surface in basaltic magma from the upper mantle wedge beneath the West Bismarck island arc, Papua New Guinea, present a rare opportunity to assess the nature of the mantle wedge in an active intra-oceanic island arc. This thesis reports comprehensive new geochemical and isotopic data for harzburgites, pyroxenites and dunites, from the island of Ritter, in order to understand how partial melting and hydrous metasomatism generate chemically, isotopically and physically distinct mantle.

The highly depleted major and moderately incompatible trace element composition of residual phases and the radiogenic strontium isotope composition of texturally well-equilibrated harzburgites are best explained by hydrous partial melting and metasomatism associated with a previous period of subduction. Harzburgites that record textural evidence for melt-rock reaction, meanwhile, have elevated equilibration temperatures, oxidised spinel compositions, elevated olivine water contents and strontium isotope compositions identical to regionally erupted basalts. These features reflect interaction between ambient mantle and primary hydrous, oxidised basaltic melts in the upper mantle wedge. Modelling of trace element diffusion profiles in olivine constrains this event to approximately one year before exhumation.

The low water contents of both coarse-grained olivine and orthopyroxene are consistent with equilibrium in chemically depleted upper mantle. The absence of hydrated silicon vacancies in olivine despite overall increases in water content during melt-rock reaction indicates that the mantle wedge may not change significantly in mechanical strength during hydrous melting and metasomatism. Chemical and radiogenic signatures of subduction are thus more likely to survive convective homogenisation.

The whole-rock budget of highly siderophile elements (HSE) is contained within heterogeneously distributed trace sulphides and inferred alloy phases, and is controlled by both partial melting and metasomatism. An absence of any correlation of Sr isotopes with either HSE or Os isotopes indicates these elements may be immobile in slab-derived fluids. Elevated concentrations of Pt and Pd in pyroxenite are mirrored by depletions in dunite, demonstrating that melt-rock reaction is instead responsible for enrichments in these elements in arc mantle. A correlation between whole-rock $^{187}Os/^{188}Os$ and phosphorous in olivine offers clues to ancient processes unrelated to active subduction, not recorded by any other chemical or isotopic system.

Thesis contents

Abstract **1**

Table of contents **2**

List of figures and tables **5**

Declaration **8**

Acknowledgements **9**

Chapter 1 ..... **11**

1.1 Rationale, background and objectives 12

1.2 Geological setting 15

1.3 Summary of chapters 17

1.4 Author contributions 18

1.5 References 20

Chapter 2 ..... **22**

2.1 Introduction 23

2.2 Petrography 28

2.3 Methods 30

2.4 Results 37

2.4.1 Mineral major elements 37

2.4.2 Major element thermometry and oxybarometry 38

2.4.3 Whole-rock trace elements 45

2.4.4 Orthopyroxene trace elements 51

2.4.5 Clinopyroxene trace elements 54

2.4.6 Olivine trace elements 58

2.5 Discussion 59

2.5.1 Conditions and environment of melting 59

2.5.2 Sub-solidus cooling 71

2.5.3 Silicate and carbonatite metasomatism 74

2.5.4 Melt-rock reaction 76

2.5.5 Summary of the petrological evolution of Ritter peridotites 82

2.5.6 Implications for the formation of cratonic mantle 83

2.6 References 86

Chapter 3 ..... **97**
3.1 Introduction 98
3.2 Methods 99
3.2.1 Sample preparation and FTIR analysis 99
3.2.2 Experimental methodology 103
3.3 Results 107
3.3.1 Olivine 107
3.3.2 Orthopyroxene 113
3.3.2 Hydroxylation experiments 115
3.4 Discussion 117
3.4.1 Equilibrium mantle water contents 117
3.4.2 Comparison to global dataset 121
3.4.3 Diffusive water-loss and magma ascent time 123
3.4.4 Water incorporation mechanisms and hydroxylation experiments 125
3.4.5 Role of redox on water in orthopyroxene 129
3.4.6 Effects of partial melting and sub-solidus cooling on water content 131
3.4.7 Effect of melt-rock reaction 136
3.4.8 Implications for mantle wedge dynamics and recycling of water in subduction zones 136
3.5 References 138

Chapter 4 ..... **145**
4.1 Introduction 146
4.2 Methods 148
4.3 Results 152
4.3.1 Sr, O and Os isotope compositions 152
4.3.2 Highly siderophile elements 155
4.4 Discussion 160
4.4.1 Effect of partial melting on HSE concentrations 160
4.4.2 Response of Sr and O isotopes to open-system processes 167
4.4.3 Response of highly siderophile elements to open-system processes 172
4.4.4 Mineral-scale control on highly siderophile element systematics 174
4.4.5 Mobility and control of Os in subduction zones 176
4.5 References 180

Chapter 5 ..... **188**
5.1 Introduction 189
5.2 Analytical methods 191
5.3 Results 195
5.4 Discussion 200
5.4.1 Evidence for involvement of a melt 200
5.4.2 T-fO_2-H_2O of xenolith and host magma 202
5.4.3 Diffusion modelling 205
5.4.4 Relative rates of element diffusion in olivine 209
5.4.5 Implications for interpretation of porphyroclastic texture and magmatic systems 211
5.5 References 212
Chapter 6 ..... **220**
6.1 Conclusions 221
6.1.1 Petrogenesis of the upper mantle beneath Ritter Island 221
6.1.2 The water content of the upper mantle wedge and the longevity of arc mantle 222
6.1.3 Mobility of Os and other highly siderophile elements in subduction zones 223
6.1.4 Origin of porphyroclastic texture and chemical diffusion in olivine 224
6.2 Recommendations for future work 225
6.3 References 227
Appendix **228**

List of figures and tables

Chapter 1 ..... **11**

Fig. 1.1 Photograph of peridotite xenolith hand sample 14

Fig. 1.2 Map of Bismarck Archipelago 16

Chapter 2 ..... **22**

Fig. 2.1 Photomicrographs of Ritter thin sections 25

Fig. 2.2 Scans of Ritter thick sections 26

Fig. 2.3 Plots of mineral major element compositions 36

Fig. 2.4 Plots of temperature, spinel Cr# and spinel Fe_2O_3/FeO 41

Fig. 2.5 The difference between differen oxybarometer calculations and spinel Cr# 42

Fig. 2.6 Comparison between whole-rock trace element compositions and global peridotites 44

Fig. 2.7 Th vs. La and Nb vs. La for whole-rock peridotites 46

Fig. 2.8 Primitive mantle-normalised whole-rock trace elements 47

Fig. 2.9 Primitive mantle-normalised orthopyroxene trace elements 50

Fig. 2.10 Primitive mantle-normalised clinopyroxene trace elements 53

Fig. 2.11 Olivine trace element systematics 56

Fig. 2.12 Ca profiles of 'residual' olivines 57

Fig. 2.13 'OSMA' diagram 60

Fig. 2.14 Hydrous and anhydrous melting models 64

Fig. 2.15 Modelling of REE concentrations in orthopyroxene 65

Fig. 2.16 Orthopyroxene/olivine trace element partitioning as a function of temperature 67

Fig. 2.17 Clinopyroxene/olivine trace element partitioning as a function of temperature 68

Fig. 2.18 Clinopyroxene/orthopyroxene trace element partitioning as a function of temperature 69

Fig. 2.19 Sub-solidus cooling models 70

Fig. 2.20 Correlations between whole-rock Sr, temperature, Mg# and spinel Fe_2O_3/FeO 77

Fig. 2.21 Comparison between erupted lava trace elements and peridotite trace elements 80

Fig. 2.22 Cartoon of petrological evolution of Ritter samples 85

Table. 2.1 Petrographic observations 27
Table. 2.2 Mineral major elements 32
Table. 2.3 Temperature, olivine Mg#, spinel Cr# and Spinel Fe_2O_3/FeO 39
Table. 2.4 Whole-rock trace elements 43
Table. 2.5 Orthopyroxene trace elements 48
Table. 2.6 Clinopyroxene trace elements 52
Table. 2.5 Olivine trace elements 55

Chapter 3 ..... **97**

Fig. 3.1 Experimental capsule design 104
Fig. 3.2 Thickness calibration from silicate overtones 106
Fig. 3.3 FTIR spectra of olivine 108
Fig. 3.4 Uncertainties on individual crystal measurements 111
Fig. 3.5 Rim to rim FTIR profiles of olivine 112
Fig. 3.6 FTIR spectra of orthopyroxene 113
Fig. 3.7 Rim to rim FTIR profiles of orthopyroxene 114
Fig. 3.8 Results of hydroxylation experiments 115
Fig. 3.9 Correlation between olivine crystal size and water content plus diffusion models 117
Fig. 3.10 Control of orthopyroxene Al_2O_3 and pressure on water partitioning 120
Fig. 3.11 Comparison of water contents of olivine with global mantle olivine dataset 122
Fig. 3.12 Correlations between water and FeO in orthopyroxene and spinel Fe_2O_3/FeO 130
Fig. 3.13 No control from temperature on water partitioning 133
Fig. 3.14 Regression of Cr partitioning thermometer and application to sub-solidus cooling 134
Fig. 3.15 Correlation between Cr in olivine and water 135
Table 3.1 FTIR results for olivine 109
Table 3.2 FTIR results for orthopyroxene 109
Table 3.3 Experimental results 116

Chapter 4 ..... **145**

Fig. 4.1 Correlations between HSE 156
Fig. 4.2 Primitive mantle-normalised whole-rock HSE 157
Fig. 4.3 Primitive mantle-normalised olivine HSE 159
Fig. 4.4 HSE partial melting model 161

Fig. 4.5 Whole-rock Pd_N/Ir_N vs. Yb in orthopyroxene 164
Fig. 4.6 Whole-rock incompatible trace elements vs. whole-rock $^{87}Sr/^{86}Sr$ 166
Fig. 4.7 Spinel Fe_2O_3/FeO vs. whole-rock $^{87}Sr/^{86}Sr$ 168
Fig. 4.8 Oxygen isotope compositions of olivine and orthopyroxene 169
Fig. 4.9 Whole-rock Pd_N/Ir_N vs. spinel Fe_2O_3/FeO and temperature 171
Fig. 4.10 $^{187}Os/^{188}Os$ vs. Re/Os, Yb in orthopyroxene, P in olivine and $^{87}Sr/^{86}Sr$ 179
Table 4.1 Os and Sr isotope compositions and HSE concentrations 153
Table 4.2 Oxygen isotope compositions of olivine and orthopyroxene 154
Table 4.3 Parameters used in partial melting model 163

Chapter 5 ..... **188**
Fig. 5 Whole thin section photomicrograph of sample 67-02A(3) 189
Fig. 5.2 Trace element composition of different olivine populations 196
Fig. 5.3 Concentration profiles for various trace elements in olivine and data regressions 197
Fig. 5.4 FTIR spectra and water profile 198
Fig. 5.5 Olivine/melt trace element partitioning 201
Fig. 5.6 Thermal diffusion model 204
Fig. 5.7 Diffusion modelling of Ca concentration profiles 207
Fig. 5.8 Relative diffusion rates of trace elements in olivine 210
Table 5.1 Major and trace element compositions of olivine populations and groundmass 194
Table 5.2 Clinopyroxene and orthopyroxene trace element compositions 195
Table 5.3 Diffusion model results 208

Appendix **228**
Fig. A1 LA-ICP-MS measurements of NIST 612 228
Fig. A2 Primitive mantle-normalised trace elements of individual orthopyroxenes 229
Fig. A3 Primitive mantle-normalised trace elements of individual clinopyroxenes 230
Fig. A4 Trace element profile of olivine from 'residual' sample 232
Fig. A5 Most enriched/most depleted harzburgite 233

Declaration

I declare that the work presented in this thesis, submitted for the degree of Doctor of Philosophy at Durham University, is entirely my own except where clearly stated. To the best of my knowledge, this thesis is distinct from any previously submitted or published work at this University or any other.

Peter Michael Edward Tollan

Durham University

2014

Acknowledgements

It has been quite a tumultuous and challenging four years, even by PhD standards. Problems aside, my time at Durham and various other locations around the world have forged many happy memories and friendships, for which I'm enormously grateful.

I'll start by thanking the staff here at Durham who helped me reach this stage. My supervisors, Jon Davidson, Colin Macpherson and Chris Dale have supported and encouraged me throughout. Particular thanks to Chris, who has shown remarkable patience and resilience in the face of my constant questioning and buffoonery in the lab, reading my chapters and my all-to-regular appearances at his office door. In the labs, Geoff Nowell and Chris Ottley have been excellent and without their support my thesis would be in much worse shape. Thanks to Ian Chaplin and Dave Sales for their help with sample prep. I would also like to thank staff not attached to my project but who helped through many a fruitful discussion; Helen Williams, Kevin Burton, Simon Matthias, Iain Neill and Pierre Bouilhol. Last but certainly not least, thank you to the admin staff, Karen Atkinson, Paula Elliott, Janice Oaks and April Furnal for their support and patience. Also thanks to Kevin and Ian for reading my thesis and all the great advice during the viva.

I am hugely grateful to staff at the Australian National University which I visited three times. Firstly, thanks to my supervisor Richard Arculus for providing the samples and boundless enthusiasm. Enormous thanks to Hugh O'Neill and Jörg Hermann for donating so much of their time to discuss science, help in the lab and read through my work (and for giving me a job!). Thanks also to Bob Rapp and Jung-Woo Park for their tireless assistance with the probe and laser.

I would like to thank staff at other universities. Ilya Bindeman and Jim Palandri at the University of Oregon for the help, chat and delicious barbecued salmon (Ilya) and Richard Brooker at the University of Bristol for advice on crystal polishing. A big thank you to Alex Nichols at JAMSTEC. Despite not having a chance to work much further with the data I measured there, Alex was a great friend throughout my three months in Japan and I'll always remember our daily ice cream breaks and late night karaoke sessions.

There are too many friends to thank properly here. At Durham I want to thank a few people in particular. Firstly, the golden oldies who long-since left but who are certainly not forgotten; Claire McLeod, Izzy Yeo, Dave Ashby, Kathy Mather, Dean Wilson, Dave Damby, Sarah Porter, Iona McIntosh, Sarah Hilton, Amy Clarke and Scott Dempsey. You guys were awesome and I miss you all. Apologies for, well, you know. Then there's Alex B-J, Clayton Grove and Tim Watton. What can I say guys, what a time. B-J, I'll never forget that 14 minute bar crawl down the Bailey. What an effort! Onto those still present. I have to start with Claire Nattrass, my fantastic housemate of nearly three years. How she's still even remotely sane I don't know. Alice Du Vivier, for all the support and friendship and hugs, thank you. Alex Baker. The tonnes, the KP, the tennis, the inane chatter…. I could go on. Rachey-B, my housemate of two years, sorry I didn't help more with the cleaning! Rachel, Leo, Harriet, Bottril, Suzie, Helen and Clarky, it's been a pleasure. My deskmate, Jing. Keep strong and you'll get there! Dave Selby, you know what I'd be saying if you were here in person. And then all my friends not attached to the department. Really, I can't list you all here but my various pool teammates and of course my awesome car-mates from the USA trip (Lloyd, Sophie, Sarah and Ed) deserve special mentions.

My friends at ANU: Mike Jollands, for having a surname similar to mine, for loving olivine and for always showing me a good time in Canberra. See you in a bit. Eleanor Mare, for the tea breaks, the chat, the science, and for driving me around when you really didn't have to. Thanks and see you soon. Paolo, Brendan, Nick, Alex, Kate, Lizzie, Laure, Tazz, Tanja, Jo, Christian and Philipp…thanks for making me feel welcome. Sarlae McAlpine, for helping with the samples and for giving me a room in your house for a week. Kelsie and Alice (and Bug) for the rooms in your houses too during my visits and generally making me feel at home. Charly Stamper, my old chum. So many great memories from our visit.

Lastly, and most importantly, I want to thank my family; Mike, Denise, Becky and Alice. The love, support and encouragement has meant so much to me, even if I haven't always shown it. Thank you.

Chapter 1

Introduction

1.1 Rationale, background and objectives

Subduction zones have existed on Earth for much of its history and are responsible for the recycling and generation of a significant portion of the habitable crust. Understanding the mechanisms operating in subduction zones and how they influence plate tectonics on a global scale, both in the present day and throughout Earth history, is therefore vital for constructing models of planetary evolution

A primary control on the behaviour of subduction zones is the nature of the mantle wedge ('arc mantle'), defined as the portion of the mantle between the underlying subducted oceanic lithospheric slab and overlying arc crust. The mantle wedge is the filter through which recycled crustal material is transported and is the source that melts to form primary basaltic arc magmas and their evolved lineage. These processes of recycling and melting may be instrumental in the formation of chemically depleted, mechanically stiff and buoyant cratonic mantle which is the stabilising force behind long-lived continental landmasses (Pearson and Wittig 2008). Yet amongst global mantle domains arc mantle is particularly enigmatic in nature, in spite of its central role in global plate tectonics. Unlike the mantle beneath mid-ocean ridge settings for example, arc mantle is fluxed by copious volatile-rich fluids* which, in addition to transporting a poorly constrained chemical cocktail, also change the phase relations of peridotite and differentiating magmas (Elliott et al. 1997, Schmidt and Poli 1998, Gaetani and Grove 1998). The cumulative effect of this is that resolving key properties of the arc mantle source, such as the thermal and redox state and volatile content, through studies of even the most primitive arc lavas, is often severely hampered.

As an alternative to studies of lavas, xenoliths of mantle peridotite, transported to the surface in arc volcanics and rapidly quenched from upper mantle conditions, may provide more detailed insights into the nature of arc mantle. Significantly, such samples retain the phase relations and chemical compositions of the upper mantle wedge and can inform with great detail on processes instrumental to the chemical and physical evolution of the mantle, such as partial melting and reaction with volatile-rich fluids. Arc peridotite xenoliths, however, are rarely recovered at the surface and thus represent only a fraction of arc systems sampled by lavas.

In July 2007, voyage SS06-2007 of Australia's Marine National Facility set out to sample submerged portions of the Bismarck arc. The principle aim of this voyage was to retrieve glassy volcanic rock and bulk lava samples which could be used to elucidate the nature of the mantle source beneath this tectonically complex region of the South West Pacific Ocean. An unexpected discovery on the final two sampling days of the voyage was of numerous xenoliths of peridotite (harzburgite, dunite and pyroxenite) encased in host basalt, retrieved from dredge operations of submerged volcanic cones off the coast of Ritter Island, West Bismarck Island Arc. This was the first occurrence of mantle xenoliths recovered from fore-arc volcanic centres in a submarine oceanic arc system, creating a unique opportunity to assess the petrogenetic processes operating in such a poorly sampled mantle domain. The work in this thesis focuses entirely on xenoliths recovered from Cone 4 located at 5°28"N, 148°02"E and dredged from a water depth of ~1050 m.

The overarching aim of this project was to evaluate the role of different subduction processes in generating compositionally distinct mantle, and whether such compositions could be preserved over long periods of geological time.

I identified four key areas I wanted to address throughout my thesis, which I felt complemented this aim:

1) ***Melting history.*** What is the origin of the mantle beneath island arcs? Most studies of both arc basalts and peridotites conclude that the mantle wedge is composed of highly depleted peridotite compared to the residues of mid-ocean ridge basalts, formed due to a previous melting event. Where did this melting event take place, under what conditions and at what time relative to the modern day tectonic setting? This has important implications not only for our broad understanding of the mantle sources of arc magmas but also specifically for understanding the tectonic evolution of the Bismarck Archipelago
2) ***Metasomatism and melt-rock reaction.*** The flux of fluid from the slab carries a unique geochemical and isotopic signature which can be used to constrain the origin and mass of material transferred into the mantle wedge and to determine the timescales of mass transfer back to the surface. Metasomatism is a broad term describing the transfer of such fluids from their source into the overlying

mantle, either cryptically or through mineralogical changes. Melt-rock reaction is a specific type of metasomatism involving interactions between melt (either silicate or carbonatite) and peridotite, typically producing distinct lithological and chemical changes such as veins of dunite or pyroxenite. I wanted to determine the physical and geochemical evidence for such interactions, investigate how such processes may change the local chemical composition and thermal and redox state of the mantle wedge, and try to link the chemistry of peridotite with that of regionally produced lavas and subducted material.

3) ***Water***. Water plays a pivotal role in all stages of petrogenesis in arc systems. However, it also may play an important role in controlling the fate of the mantle post-subduction, since water dissolved in nominally anhydrous minerals such as olivine can change the rheological properties of the mantle. I wanted to establish how much water is stored in the upper mantle and whether it is water saturated, how the water content of the mantle changes during interaction with hydrous fluids and also establish the physical and chemical controls on the water content of arc mantle peridotite.
4) ***Time***. What are the durations of the processes described above? For example, do metasomatically altered peridotites represent fluxing with fluids during long residence times in the mantle, or are these geochemical and textural changes induced rapidly, coincidental with modern day magmatism?

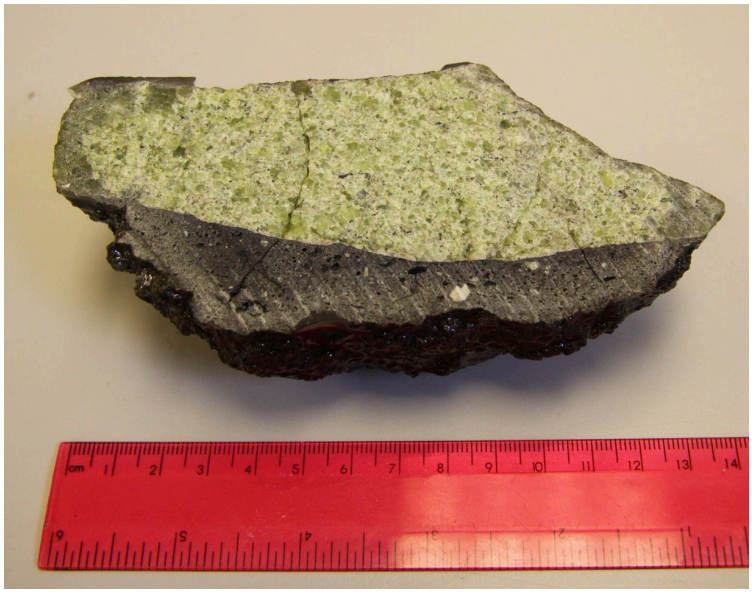

Fig. 1.1 One of the peridotite xenolith samples (67-02B(1)) recovered from Cone 4 off Ritter Island.

1.2 Geological setting

The Bismarck Archipelago is situated north east of Papua New Guinea (Fig. 1.1). It represents a highly complex tectonic setting broadly described by the oblique convergence of the Australian and Pacific plates, but which in detail comprises multiple small plates juxtaposed to form several zones of active and extinct subduction (Woodhead et al. 2010). To the east, the oceanic Solomon Sea plate is subducting northwards beneath the South Bismarck plate, resulting in magmatism which has produced the New Britain island arc (or alternatively, East Bismarck island arc). To the west of New Britain, oblique collision between the South Bismarck and Australian plates initiated around 3 to 3.7 Ma (Abbott et al. 1994) has led to subduction-related magmatism of the West Bismarck island arc. Collision and magmatism began in the far west of the West Bismarck arc and gradually spread eastwards, such that collision at ~148° longitude, close to Ritter Island, began within the last million years (Gill et al. 1983). The composition of lavas erupted from the New Britain island arc are compositionally distinct from those of West Bismarck, thought to reflect mantle sources that have experienced different degrees of prior melting but both fluxed by the same 'base' subduction component, perhaps related to the now extinct Vitiaz West-Melanesian trench (Woodhead et al. 1998, Woodhead et al. 2010, Cunningham et al. 2012). West Bismarck arc lavas have subsequently incorporated a greater proportion of subducted sediment during their genesis, most likely as a crustal contaminant (Cunningham et al. 2012). The West Bismarck lavas span a broad range of compositions, from high-MgO basalts through to rhyolites. Distinct geochemical trends are observed along-arc such that volcanics erupted to the east have the most primitive compositions. This is thought to reflect steadily decreasing degrees of partial melting westwards in response to arc-continent collision disrupting the typical subduction regime (Woodhead et al. 2010). Ritter Island itself is a small, crescent-shaped volcanic island located towards the most easterly extent of the West Bismarck Arc, approximately 23 km west of New Britain, with its current shape and volume forming following the collapse of approximately 5 km^3 of the western submarine flank on 13th March 1888 (Ward and Day 2003). Volcanic cones numerate the seafloor surrounding Ritter. They are composed of high-MgO (~15 wt. %)

olivine-clinopyroxene-plagioclase-phyric tholeiitic basalt, and were the magmatic hosts for the xenoliths described in this thesis (McAlpine and Arculus 2011).

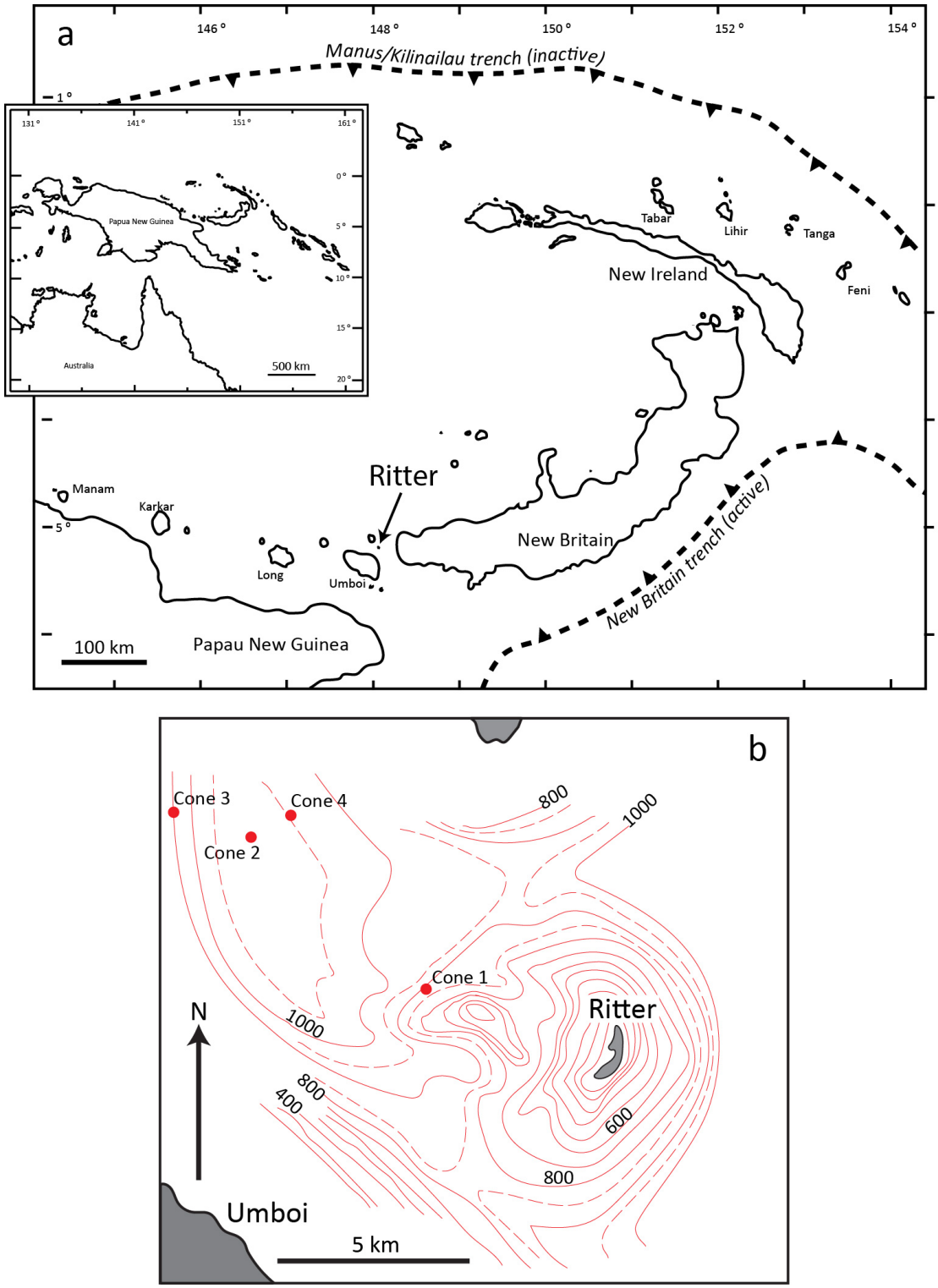

Fig. 1.2 a) Map showing the Bismarck archipelago and the location of key islands, including Ritter. The West Bismarck island arc extends westwards from the western-most point of New Britain b) Detailed map of Ritter Island, the surrounding ocean bathymetry and the locations of dredged cones. Only samples from Cone 4 are studied here. Map adapted from Ward and Day (2003)

1.3 Summary of chapters

This thesis consists of four research chapters which satisfy both the overall aim of this project and each of the key areas detailed in the previous section. The chapters are summarised as follows:

Chapter 2

This chapter presents a detailed whole-rock and *in-situ* major and trace element study of Ritter harzburgites, dunites and pyroxenites, combined with an assessment of the peridotite textures. I show through modelling of orthopyroxene trace element compositions that the suite formed originally as part of an 'ancient' subduction system, where hydrous melting resulted in highly depleted peridotite residues distinct from those formed under anhydrous conditions. I use the partitioning of trace elements between each major peridotite phase to determine the cooling history of the samples and the implications this has for interpreting *in-situ* geochemical data. Finally, I use the trace element chemistry of olivine and clinopyroxene to trace the involvement of distinct metasomatic agents, both in the present day mantle wedge and the previous subduction system.

Chapter 3

This chapter discusses measurements of water in olivine and orthopyroxene. I show a simple method of establishing the equilibrium water content of these phases, and use the ascent-induced dehydration of olivine to calculate a xenolith exhumation timescale. By performing a series of 'hydroxylation' experiments, I demonstrate that olivine in these xenoliths was approximately water saturated, and that the depleted chemical composition of both olivine and orthopyroxene in addition to redox state is the dominant control on the water content of the upper mantle wedge. I further discuss the implications this has for the preservation of subduction zone signatures in the mantle.

Chapter 4

This chapter deals with the concentrations of highly siderophile elements (HSE) and osmium, strontium and oxygen isotopic compositions of the Ritter peridotites. I show that

Sr isotopes clearly track the involvement of subducted sediments as part of the 'ancient' subduction system, and that melt-rock reaction involved fluids compositionally identical to regionally erupted lavas, supporting the conclusions of chapter 2. Both HSE and Os isotopes are largely decoupled from lithophile element systematics, indicating a dominant control by trace sulphides and alloy phases. Based on an absence of correlations between Sr isotopes and both HSE concentrations and Os isotopes, I show that these elements behave conservatively during dehydration processes in the subducted slab, but may be highly fractionated during both partial melting and melt-rock reaction.

Chapter 5

In this final research chapter I address the conditions and timescale under which the porphyroclastic texture formed in one of the Ritter harzburgites. Using the trace element composition and water content of peridotitic olivine porphyroclasts and neoblasts together with olivine phenocrysts from the host magma, I show that the texture is related to interaction between hydrous, oxidised basaltic melt and peridotite within the mantle wedge. Olivine porphyroclasts display significant zoning of trace elements, consistent with diffusion in response to this process. By modelling these diffusion profiles, I calculate a timescale of approximately one year, which represents the time between the infiltration of melt and the exhumation of the xenolith. Comparative modelling of trace and major elements in olivine indicates that they diffuse similarly quickly, irrespective of ionic radius or charge.

Chapter 6

This chapter summarises the petrological evolution of the Ritter suite and discusses broader implications for sub-arc mantle.

1.4 Author contributions

Throughout this thesis, the term 'we' is used to represent co-authorship on papers being prepared in tandem. The work presented is entirely my own. With the exceptions detailed below, all sample preparation and data acquisition and processing were performed by myself. The complete body of text was written by me, following corrections suggested by co-authors detailed below.

Professor Richard Arculus (Research School of Earth Sciences, Australian National University) led the cruise that collected and documented the samples studied as part of this thesis. He assisted in data interpretation and provided feedback on a draft manuscript equivalent to chapter 5.

Professor Ilya Bindeman (Department of Geological Sciences, University of Oregon) assisted with the preparation of samples for oxygen isotope measurement and aided interpretation of the data.

Mr Ian Chaplin and Mr Dave Sales (Department of Earth Sciences, Durham University) produced thin and thick sections for petrographic and geochemical work described in chapters 2, 3 and 5.

Dr Chris Dale (Department of Earth Sciences, Durham University) assisted with HSE and Os isotope chemistry and measurements, data interpretation and provided feedback on chapters 2 and 4.

Professor Jon Davidson (Department of Earth Sciences, Durham University) assisted with data interpretation and provided feedback on all chapters.

Professor Jörg Hermann (Research School of Earth Sciences, Australian National University) assisted with acquisition and interpretation of FTIR data. He provided feedback on chapters 4 and 5.

Mr Mike Jollands (Research School of Earth Sciences, Australian National University) assisted with the second hydroxylation experiment.

Dr Colin Macpherson (Department of Earth Sciences, Durham University) assisted with data interpretation and provided feedback on chapters 3 and 5.

Miss Eleanor Mare (Research School of Earth Sciences, Australian National University) modelled the timescale of heat diffusion detailed in chapter 5. She provided feedback on chapter 5.

Miss Sarlae McAlpine (Research School of Earth Sciences, Australian National University) processed the samples. She produced and provided mineral separates and whole rock powders which I utilised in geochemical measurements detailed in all chapters.

Dr Wolfgang Müller (Department of Earth Sciences, Royal Holloway) set up the laser ablation system at Royal Holloway and assisted with data acquisition and processing.

Dr Geoff Nowell (Department of Earth Sciences, Durham University) assisted with Sr isotope chemistry and measurements.

Professor Hugh O'Neill (Research School of Earth Sciences, Australian National University) performed a small number of laser ablation measurements of olivine and orthopyroxene which were used in chapter 5. He assisted with data interpretation and provided feedback on chapter 5.

Dr Chris Ottley (Department of Earth Sciences, Durham University) assisted with whole-rock trace element chemistry and measurements.

Dr Jose-Alberto Padrón-Navarta (then Research School of Earth Sciences, Australian National University) assisted with the first hydroxylation experiment. He also assisted with acquisition and interpretation of FTIR data.

Dr Jung-Woo Park (Research School of Earth Sciences, Australian National University) set up the laser ablation system at the Australian National University and assisted with data acquisition and processing.

1.5 References

Abbott, L.D., Silver, E.A., Thompson, P.R., Filewicz, M.V., Schneider, C., Abdoerrias, C., 1994. Stratigraphic constraints on the development and timing of arc-continent collision in northern Papua New Guinea. J. Sediment. Res. 648, 169-183

Cunningham, H., Gill, J., Turner, S., Caulfield, J., Edwards, L., Day, S., 2012. Rapid magmatic processes accompany arc-continent collision: the Western Bismarck arc, Papua New Guinea. Contrib. Mineral. Petrol. 164, 789-804

Elliott, T., Plank, T., Zindler, A., White, W., Bourdon, B., 1997. Element transport from slab to volcanic front at the Mariana arc. J. Geophys. Res. 102, 14991-15019

Gaetani, G., Grove, T., 1998. The influence of water on melting of mantle peridotite. Contrib. Mineral. Petrol. 131, 323-346

Gill, J.B., Morris, J.D., Johnson, R.W., 1993. Timescale for producing the geochemical signature of island arc magmas: U-Th-Po and Be-B systematics in recent Papua New Guinea lavas. Geochim. Cosmochim. Acta 57, 4269-4283

McAlpine, S.R.B., Arculus, R.J., 2011. Pristine mantle xenoliths from the active Bismarck Arc. Min. Mag. 75, 1261-1373

Pearson D.G., Wittig, N., 2008. Formation of Archaean continental lithosphere and its diamonds: the root of the problem. J. Geol. Soc. 165, 895-914

Schmidt, M.W., Poli, S., 1998. Experimentally based water budgets for dehydrating slabs and consequences for arc magma generation. Earth Planet. Sci. Lett. 163, 361-379

Ward, S.N., Day, S., 2003. Ritter Island Volcano - lateral collapse and the tsunami of 1888. Geophys. J. Int. 154, 891-902

Woodhead, J.D., Eggins, S.M., Johnson, R.W., 1998. Magma Genesis in the New Britain Island Arc: Further Insights into Melting and Mass Transfer Processes. J. Petrol. 39, 1641-1668

Woodhead, J., Hergt, J., Sandiford, M., Johnson, W., 2010. The big crunch: Physical and chemical expressions of arc/continent collision in the Western Bismarck arc. J. Volc. Geotherm. Res. 190, 11-24

**Throughout this thesis the term 'fluid' is used in the general sense, rather than in any special petrological sense. Particular types of fluid will be specified as such (e.g., aqueous fluid, silicate melt etc.)*

Chapter 2

Ancient and modern subduction processes revealed through an in-situ trace and major element study of peridotite xenoliths from the upper mantle wedge beneath Ritter Island, West Bismarck Island Arc

2.1 Introduction

Studies of magmas erupted at island arcs have led to a greater understanding of the role that subduction plays in the chemical and physical evolution of the mantle through hydrous melting and metasomatism, and the resultant generation of new crustal material. The widely accepted view is that arc magmas represent an amalgamation of; 1) fluids released during metamorphic reactions in the subducting oceanic lithosphere (Poli and Schmidt 1995, Elliott et al. 1997, Hermann and Spandler 2008, Skora and Blundy 2010); 2) fluids produced during hydrous melting of the overlying mantle wedge peridotite (Stolper and Newmann 1994, Gaetani and Grove 1998, Grove et al. 2012); and 3) crustal material incorporated during magmatic ascent and differentiation (Thirlwall et al. 1996, Dungan and Davidson 2004, Handley et al. 2011). This complex, multi-source nature of arc magmas means that, through careful geochemical inspection, they are capable of offering insights into a multitude of processes and chemical reservoirs operating on Earth both presently and throughout geological history. Unfortunately, many of these chemical signatures are either indistinct from each other or easily overprinted, limiting the detail that such studies can reveal on some of the most important stages of arc magmagenesis. The composition and petrogenetic history of the mantle wedge itself is particularly susceptible, since the incompatible trace element concentrations of slab-derived fluids and assimilated crustal material are typically much greater than partial mantle melts (Elliott et al. 1997). The mantle wedge may also be host to a variety of distinct fluids from various recycled sources which become integrated during transport through the mantle before entering the crust or in deep crustal magma storage regions (Annen et al. 2006).

Peridotite xenoliths included in a multitude of volcanic materials offer an opportunity to 'bypass' many of these problems associated with studies of magmas. Whilst they suffer through lack of *in-situ* lithospheric context compared to ophiolites, they have the benefit of rapid exhumation and quenching from mantle depths, thus preserving textures and chemical signatures pertaining to high temperature petrogenesis (Pearson et al. 2003). However, arc peridotite xenoliths are scarce compared to xenoliths recovered from other mantle domains limiting our current level of knowledge. The few previous studies of arc peridotites have nevertheless revealed important insights into

subduction zone processes. In particular, they have revealed greater detail on; 1) the composition and distribution of metasomatic fluids (Maury et al. 1992, Kepezhinskas et al. 1995, Franz et al. 2002, Widom et al. 2003, Ishimaru et al. 2007, Vannuci et al. 2007, Kamenov et al. 2008, Bénard and Ionov 2013); 2) mechanisms and timescales by which mantle-derived melts are transported through and interact with the surrounding ambient mantle (Arai et al. 2004, Bryant et al. 2007, Turner et al. 2012); 3) the thermal and redox state of the mantle wedge (Brandon and Draper 1996, Parkinson and Pearce 1998, Parkinson et al. 2003, Parkinson and Arculus 1999, Ionov 2010); 4) and ancient melting events (Parkinson et al. 1998). An important aspect of arc peridotites is that their low temperature and pressure equilibration conditions mean they rarely record partial melting as part of their respective active subduction zones. Instead, the melting histories recorded in mineral and whole-rock chemistry typically pertain to previous melting episodes which may or may not be subduction-related. The insights that any particular suite of arc peridotites can offer into the hydrous mantle melting processes in subduction zones is thus entirely sample specific.

Here we document the results of a detailed *in-situ* and whole-rock geochemical study of a representative subset of a diverse suite of peridotite xenoliths recovered from the island of Ritter in the West Bismarck island arc (Fig. 1.1; Fig 1.2). Our study reveals new insights into both the broad processes operating in subduction zone mantle and also the petrogenetic history of mantle specific to the tectonically complex Bismarck Archipelago. In particular, we utilise the trace element chemistry of orthopyroxene, clinopyroxene and olivine to inform on distinct events in the history of this sample suite. We show that the samples experienced two stages of subduction: an ancient period of melting and metasomatism in an extinct arc system, before cooling and more recent melt-rock reaction beneath the present day active arc. Our study further confirms that the mantle underlying subduction zones is exposed to melting and metasomatic processes similar to those that operated to form cratonic mantle, providing a plausible link between subduction zones and the genesis of long-lived continental landmasses (Pearson and Wittig 2008).

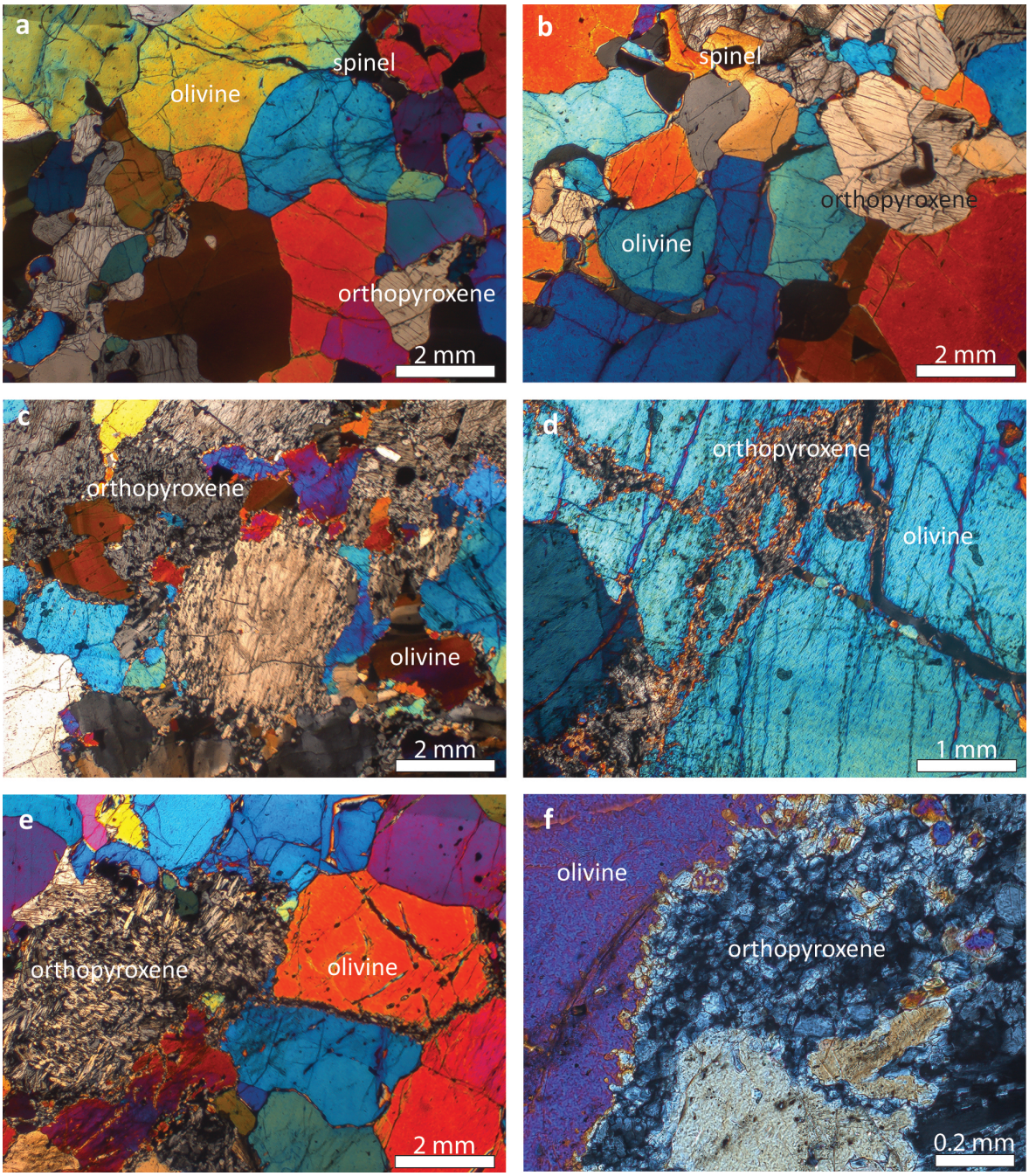

Fig. 2.1 Thin section photomicrographs (polarised light) of Ritter peridotites. 'a' and 'b' display typical coarse, well-equilibrated textures of 'residual' peridotites. 'c' to 'f' show formation of secondary orthopyroxene through reaction between olivine and silicate melt

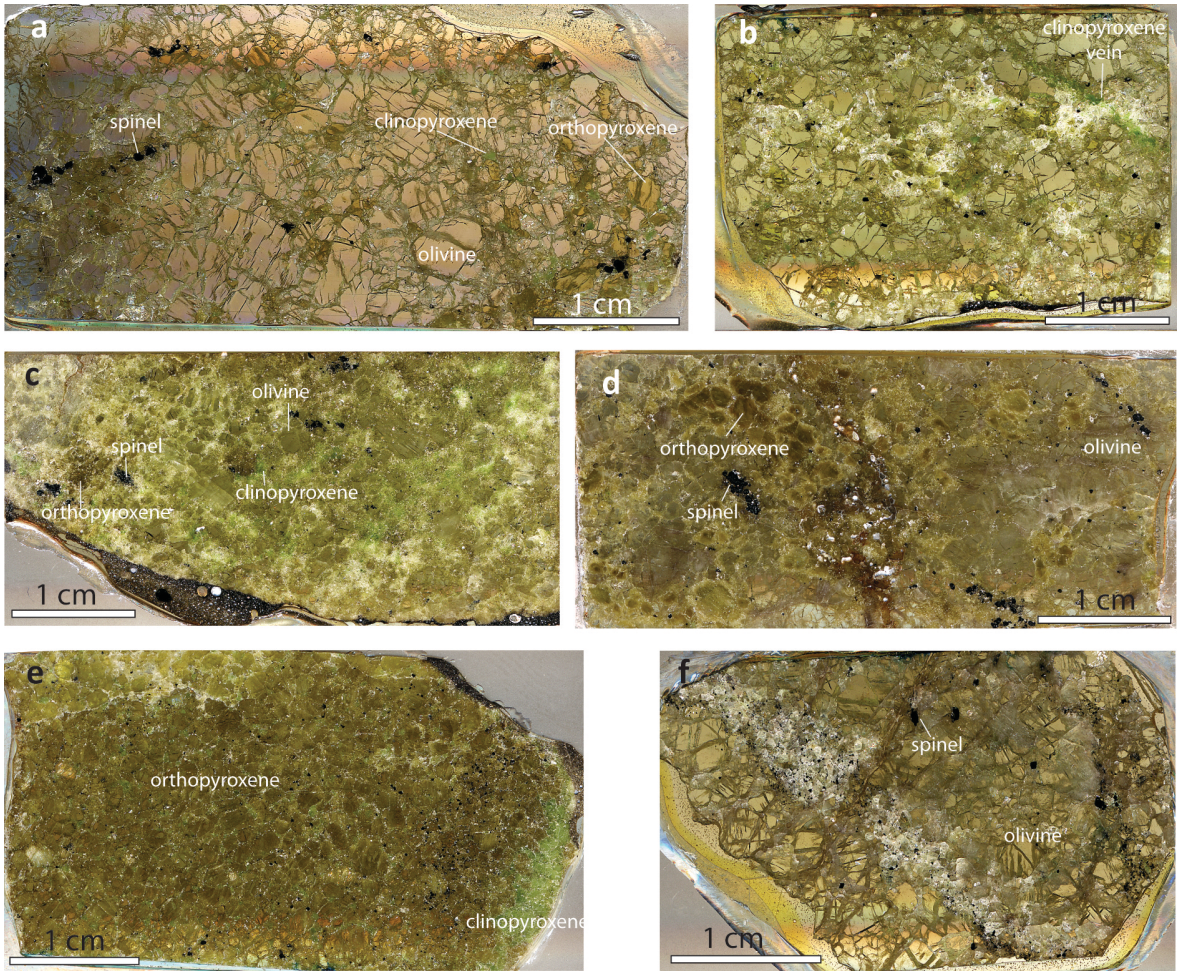

Fig. 2.2 Thick (300-600 µm) sections of Ritter samples. 'a' (67-02A(2)) and 'b' (67-02E(1)) are representative of 'residual' harzburgites. Note secondary vein of clinopyroxene (type I, see discussion) in 'b'. 'c'(67-02A(3)) is a 'reacted' peridotite displaying porphyroclastic texture. 'd' (67-02A(5)) is representative of the majority of 'reacted' harzburgites. 'e' (67-02B(6)) is a pyroxenite consisting of orthopyroxene- and clinopyroxene-rich layers. 'f' (67-02D(1)) is a 'fossil' dunite, composed of a primary coarse dunite cross-cut by a secondary finer-grained dunite vein.

Sample	Classification	Description
67-02A(1)	Pyroxenite	Dominated by opx, with subordinate cpx and sp. 1-2 sets of exsolution lamellae in opx
67-02A(2)	Residual	Coarser crystals than other harzburgites. Undulose extinction in ol and exsolution lamellae in opx, typical of 'residual' samples. Sp has dark red core and very thin black rim. Coarse ol are heavily fractured
67-02A(3)	Reacted	Porphyroclastic texture. Ol porphyroclasts have been partially recrystallised to neoblasts. Sp (black) and opx both show reaction textures. Precipitation of secondary fine grained cpx
67-02A(5)	Reacted	Many fibrous opx veins, some patches of fibrous and equant opx. Opx veins often cutting ol. Numerous inclusions in opx
67-02B(1)	Residual	Undulose extinction in ol and opx, but no evidence for reaction with melt other than thin black rim around red core of sp
67-02B(2)	Dunite	Very coarse ol crystals with large clusters of similarly coarse sp. Traces of melt often surround grain boundaries and fractures
67-02B(3)	Reacted	Many fibrous opx veins, often with relic ol within. Thin rims on olivine where close to opx veins
67-02B(5)	Reacted	Numerous coarse ol and opx with reacted crystal edges, but lacks abundant opx veins
67-02B(6)	Pyroxenite	Two layers. One dominantly opx but with cpx occuring regularly at grain boundaries. 2nd layer is clinopyroxenite. Sp common throughout and contains numerous melt inclusions
67-02D(1)	Residual	Similar textures to other 'residual' peridotites
67-02D(3)	Dunite	Coarse dunite cross-cut by vein of finer grained ol with intermixed, fine sp. Well equilibrated grain boundaries between primary and secondary dunites
67-02D(4)	Residual	Thick section typical of 'residual' peridotites. Thin section shows occasional patches of fibrous secondary opx. Coarse relic opx shows evidence for recrystallisation at rims. Reaction rims on ol close to opx veins
67-02D(7)	Reacted	No secondary opx present or other evidence for melt intrusion, but grain boundaries to all grains are distorted and not in equilibrium
67-02E(1)	Residual	Similar to 67-02B(1). No evidence for reaction with a melt from thin section, however thick section shows a thin vein of cpx
67-02E(3)	Residual	Numerous veins and patches of fibrous secondary opx

Table 2.1 Summary of petrographic observations of Ritter samples. ol = olivine, opx = orthopyroxene, cpx = clinopyroxene, sp = spinel

2.2 Petrography

The Ritter sample suite consists of harzburgites, with subordinate dunites and pyroxenites. A subset of this total sample suite was chosen for this study to represent the range of mineralogies and textures present (Fig. 2.1 and Fig. 2.2, Table 2.1). All samples collected are free of secondary alteration such as serpentinisation or weathering and hence fully retain both their mantle textures and the contact between the peridotite and host magma. The harzburgite suite chosen for this study can be broadly split into two groups based on their textures: 'residual' harzburgites and 'reacted' harzburgites. 'Residual' harzburgites display dominantly coarse (protogranular) textures with well-defined crystal boundaries and a general absence of dynamic recrystallization, secondary veining or any other feature attributable to late-stage melt-rock reaction or localised deformation such as shearing (Fig. 2.1a and b, Fig. 2.2a and b). Olivine crystals often contain undulose extinction and sub-grain domains, whilst orthopyroxene shows distinct fine exsolution lamellae. There is no obvious preferred crystal orientation or strain-induced elongation. Spinel usually occurs as individual coarse grains, or clusters of grains. Rarely spinel clusters are re-arranged into linear trails. In thin section, spinel in most 'residual' samples has a brick-red core with a thin black rim. No other crystal phases show any petrographic evidence for zoning. Clinopyroxene is rare and when present lacks exsolution lamellae and occurs as very small grains often at triple point junctures. Grain boundaries tend to be a little more disrupted than olivine, orthopyroxene and spinel indicating a possible secondary origin. This is supported by 'residual' sample 67-02E(1) and 'reacted' sample 67-02(7) which both contain cross-cutting veins of relatively coarse clinopyroxene (Fig. 2.2b). The grain boundaries between clinopyroxene in these veins and the surrounding material however are still relatively well-defined compared to orthopyroxene veins in 'reacted' harzburgites, which suggests that the origin of the veins were probably related to a much earlier event than that responsible for other veining observed in the rest of the sample suite. The samples contain no evidence for garnet or garnet breakdown such as pyroxene-spinel symplectites.

'Reacted' harzburgites all contain distinct textural evidence for melt-rock reaction and localisation of deformation, overprinting the primary 'residual' textures. The majority of 'reacted' samples retain coarse textures but with abundant patches and/or veins of

fibrous secondary orthopyroxene which appears to form at the expense of olivine (Fig. 2.1c to f). This reaction is most obvious in cases of orthopyroxene veins occurring along fractures within olivine grains themselves (Fig. 2.1d). Often orthopyroxene veins will retain small pockets of olivine, a remnant of incomplete reaction (Fig. 2.1f). Grain boundaries in 'reacted' harzburgites are highly sutured irrespective of whether they are adjacent to secondary minerals. Spinel grains have similar distribution and size to those of 'residual' harzburgites, but tend to lack the brick-red cores instead being entirely black. Often the spinel contains abundant inclusions of melt. Primary 'relic' orthopyroxenes in thick section lack transparent sections which are common in 'residual' harzburgites, instead forming pockets of coarse, cloudy grains with reaction rims, possibly indicating secondary growth (Fig. 2.2d). Clinopyroxene usually occurs at triple point junctures as with 'residual' harzburgites but tends to have even more poorly defined grain boundaries, similar to primary orthopyroxene and olivine. Occasionally traces of quenched melt containing small clinopyroxene crystals are observed associated with the reaction textures. One sample, 67-02A(3) has a distinct porphyroclastic texture, consisting of relic porphyroclasts of olivine and orthopyroxene with sutured grain boundaries surrounded by a fine-grained, recrystallized matrix of olivine and clinopyroxene neoblasts (Fig. 2.2c, Fig. 5.1). This sample, despite having a reacted texture lacks the secondary orthopyroxene veins and patches of other 'reacted' harzburgites. For a detailed discussion of this texture and its origins, the reader is referred to chapter 5. Finally it should be noted that one sample, 67-02D(4), whilst showing 'residual' textures in one section prepared from the hand specimen shows an abundance of reaction textures on another section made from a different part of the hand specimen. Likewise, bulk crushed material from sample 67-02A(3) contains crystals clearly originating from texturally 'residual' samples. These observations indicate that the reaction textures can be very localised even on hand sample (10-20 cm) scale.

The two dunites studied here are distinctly different in texture. 67-02B(2) is distinguished by large pockets of very coarse, texturally homogenous spinel grains. Occasional fine fractures which form a network around the olivine grains are surrounded by wisps of quenched melt. The other dunite, 67-02D(3), consists of a 'primary' dunite with coarse, transparent olivine grains and occasional spinel grains which is cross-cut by a

'secondary' dunite vein composed of well-mixed, finer-grained olivine and spinel (Fig. 2.2f). There is no obvious reaction zone between the 'primary' dunite and dunite vein and grain boundaries are lobate and well-defined. The two pyroxenites are dominated by orthopyroxene. 67-02A(1) approaches the orthopyroxenite end-member, with only the occasional clinopyroxene grain present. 67-02B(6) on the other hand contains more abundant clinopyroxene which forms at the grain boundaries of orthopyroxene (Fig. 2.2e). Spinel in this sample is much more abundant, fine-grained and contains abundant melt inclusions, similar to spinel grains from 'reacted' harzburgites. Finally, this sample contains a separate layer of almost pure clinopyroxene, in which the grains have highly irregular grain boundaries and internal fractures. The boundary between the clinopyroxenite and orthopyroxenite layers is not well-defined, with evidence for mixing of populations of orthopyroxene and clinopyroxene.

The contact between the host magma and xenolith is clearly defined in all samples, irrespective of texture and whilst there is evidence for populations of mantle xenocrysts in the host magma, there is no evidence for intrusion of the host magma into the xenolith or reaction at the boundary (e.g. Fig. 2.2c).

2.3 Methods

Whole rock trace elements were measured by inductively-coupled plasma mass spectrometry (Thermo Scientific X-SERIES 2) at the Department of Earth Sciences, Durham University. Approximately 100 mg of sample powder was dissolved in 29 M HF and 16 M HNO_3, dried down and then brought up in dilute HNO_3. Whilst all residual fluorides were brought into solution, we were unable to attain complete dissolution of residual spinels, although the minor modal proportions of spinel and typically very low trace element concentrations in this phase mean that this will have made little difference to the results (with the exceptions of Cr and V, which are hence not reported). Standards measured throughout the analytical session returned values typically within 10 % of accepted values. Total procedural blanks constituted ~10 % or less of the total abundance in each analysis.

The major element composition of olivine, orthopyroxene, clinopyroxene and spinel was determined on a Cameca SX100 electron probe micro-analyser at the Research

School of Earth Sciences, Australian National University. An operating voltage of 15 kV and current of 20 nA were used throughout. *In-situ* trace element compositions were measured by laser ablation inductively coupled plasma mass spectrometry (LA-ICP-MS) at the Australian National University. The laser ablation system utilises a 193 nm ArF excimer laser with a custom-built 'HelEx' two-volume ablation cell which feeds into an Agilent 7700 quadrupole mass spectrometer. Ablation was conducted under an atmosphere of He and Ar. The laser was run at a frequency of 5 Hz, and operating voltages varied between 26-30 kV in order to maintain energies of 30-50 mJ. Olivine compositions (^{23}Na, ^{27}Al, ^{29}Si, ^{31}P, ^{43}Ca, ^{45}Sc, ^{47}Ti, ^{51}V, ^{53}Cr, ^{55}Mn, ^{59}Co, ^{60}Ni and ^{89}Y) were determined with a large 137 µm spot size except for crystal traverses which utilised an 81 µm spot size. Orthopyroxene compositions were determined with three adjacent spots. A single spot (81 µm) measured the same elements as in olivine, whilst the other two spots (137 µm) measured concentrations of ^{29}Si, ^{43}Ca, ^{47}Ti, ^{89}Y, ^{90}Zr, ^{93}Nb, ^{139}La, ^{140}Ce, ^{141}Pr, ^{143}Nd, ^{147}Sm, ^{153}Eu, ^{157}Gd, ^{159}Tb, ^{163}Dy, ^{165}Ho, ^{166}Er, ^{169}Tm, ^{192}Yb, ^{175}Lu and ^{178}Hf. The two neighbouring spots were checked for consistency and combined to give an average value. All data was corrected against repeat measurements of SRM NIST 610 and 612 glasses, with ^{29}Si used as an internal standard. For clinopyroxene ^{88}Sr was added to the routine and the spot size reduced to 62 µm, due to the fine grain sizes. Additional analyses of olivine and orthopyroxene were conducted at the Department of Earth Sciences, Royal Holloway, University of London. The laser ablation system is of similar design to the system at the Australian National University and consisted of a 193 nm excimer laser, Laurin two-volume ablation cell and Agilent 7500 quadrupole mass spectrometer. For consistency data was acquired using identical acquisition parameters as used previously. Comparison of repeat analyses of NIST 612 from both Royal Holloway and the Australian National University are in excellent agreement (Fig. A1).

Olivine

	67-02B(2) Dunite	67-02D(3) Dunite	67-02A(2) Harzburgite Residual	67-02B(1) Harzburgite Residual	67-02D(1) Harzburgite Residual	67-02D(4) Harzburgite Residual	67-02E(1) Harzburgite Residual	67-02A(3) porphyroclast core Harzburgite Reacted	67-02A(3) neoblast Harzburgite Reacted	67-02A(5) Harzburgite Reacted	67-02B(3) Harzburgite Reacted	67-02B(5) Harzburgite Reacted	67-02D(7) Harzburgite Reacted	67-02E(3) Harzburgite Reacted
SiO_2	41.58	39.84	40.90	40.72	40.62	40.62	41.06	40.91	40.85	40.16	40.79	41.08	40.53	40.15
TiO_2	<0.05	<0.05	<0.05	<0.05	<0.05	<0.05	<0.05	<0.05	<0.05	<0.05	<0.05	<0.05	<0.05	<0.05
Al_2O_3	<0.04	<0.04	<0.04	<0.04	<0.04	<0.04	<0.04	<0.04	<0.04	<0.04	<0.04	<0.04	<0.04	<0.04
Cr_2O_3	<0.06	<0.06	<0.06	<0.06	<0.06	<0.06	<0.06	<0.06	<0.06	<0.06	<0.06	<0.06	<0.06	<0.06
FeO	6.00	7.72	8.15	8.05	8.21	8.96	9.04	8.02	8.63	8.25	8.27	8.21	7.74	9.36
MnO	0.12	0.08	0.11	0.13	0.11	0.13	0.13	0.13	0.13	0.13	0.14	0.15	0.12	0.17
MgO	53.05	50.82	50.67	50.53	50.81	50.48	49.56	50.54	50.55	50.41	51.34	51.02	51.00	49.82
CaO	<0.04	<0.04	<0.04	<0.04	<0.04	<0.04	<0.04	<0.04	0.17	<0.04	<0.04	<0.04	0.06	<0.04
Na_2O	<0.04	<0.04	<0.04	<0.04	<0.04	<0.04	<0.04	<0.04	<0.04	<0.04	<0.04	<0.04	<0.04	<0.04
NiO	0.47	0.41	0.46	0.44	0.42	0.40	0.39	0.46	0.39	0.44	0.44	0.43	0.45	0.45
Total	101.21	98.86	100.28	99.87	100.17	100.59	100.25	100.05	100.79	99.39	100.97	100.90	99.89	99.95
Mg#	0.940	0.921	0.917	0.918	0.917	0.909	0.907	0.918	0.913	0.916	0.917	0.917	0.922	0.905

Spinel

	67-02A(1) Pyroxenite	67-02B(6) Pyroxenite	67-02B(2) Dunite	67-02D(3) Dunite	67-02A(2) Harzburgite Residual	67-02B(1) Harzburgite Residual	67-02D(1) Harzburgite Residual	67-02D(4) Harzburgite Residual	67-02E(1) Harzburgite Residual	67-02A(3) Harzburgite Reacted	67-02A(5) Harzburgite Reacted	67-02B(3) Harzburgite Reacted	67-02B(5) Harzburgite Reacted	67-02D(7) Harzburgite Reacted	67-02E(3) Harzburgite Reacted
SiO_2	<0.1	<0.1	<0.1	<0.1	<0.1	<0.1	<0.1	<0.1	<0.1	<0.1	<0.1	<0.1	<0.1	<0.1	<0.1
TiO_2	0.20	0.34	0.10	0.15	<0.05	<0.05	<0.05	<0.05	0.08	0.15	0.34	<0.05	0.37	0.08	<0.05
Al_2O_3	15.46	12.23	5.52	10.14	23.12	24.04	20.88	20.26	27.75	10.13	15.94	25.24	15.82	16.61	23.69
Cr_2O_3	49.44	53.80	63.19	51.74	44.76	43.27	43.82	48.08	40.53	54.31	51.19	45.73	50.17	50.91	43.92
Fe_2O_3	4.76	6.87	5.41	8.02	3.04	2.23	6.29	2.46	0.48	7.99	5.86	1.32	6.88	4.63	3.13
FeO	21.65	14.24	13.52	20.76	15.10	15.93	16.51	18.43	17.79	12.00	13.14	13.87	13.35	14.05	16.60
MnO	<0.12	<0.12	<0.12	<0.12	<0.12	<0.12	<0.12	<0.12	<0.12	<0.12	<0.12	<0.12	<0.12	<0.12	<0.12
MgO	8.07	12.75	12.46	7.76	13.09	12.46	11.78	10.87	12.24	13.42	13.91	14.54	13.72	13.12	12.21
CaO	<0.04	<0.04	<0.04	<0.04	<0.04	<0.04	<0.04	<0.04	<0.04	<0.04	<0.04	<0.04	<0.04	<0.04	<0.04
Na_2O	<0.04	<0.04	<0.04	<0.04	<0.04	<0.04	<0.04	<0.04	<0.04	<0.04	<0.04	<0.04	<0.04	<0.04	<0.04
NiO	0.10	0.11	0.09	0.06	0.09	0.07	0.13	0.06	0.09	0.16	0.16	0.07	0.16	0.16	0.10
Total	99.92	100.36	100.28	98.63	99.34	98.16	99.42	100.18	99.05	98.36	100.55	100.78	100.48	99.75	99.68
Mg#	0.40	0.61	0.62	0.40	0.61	0.58	0.56	0.51	0.55	0.67	0.65	0.65	0.65	0.62	0.57
Cr#	0.68	0.75	0.88	0.77	0.56	0.55	0.58	0.61	0.49	0.78	0.68	0.55	0.68	0.67	0.55
Fe2O3/FeO	0.22	0.48	0.40	0.39	0.20	0.14	0.38	0.13	0.03	0.67	0.45	0.10	0.52	0.33	0.19

Orthopyroxene

	67-02A(1) Pyroxenite	67-02B(6) Pyroxenite	67-02A(2) Harzburgite Residual	67-02B(1) Harzburgite Residual	67-02D(1) Harzburgite Residual	67-02D(4) Harzburgite Residual	67-02E(1) Harzburgite Residual	67-02A(3) Harzburgite Reacted	67-02A(5) Harzburgite Reacted	67-02B(3) Harzburgite Reacted	67-02B(5) Harzburgite Reacted	67-02D(7) Harzburgite Reacted	67-02E(3) Harzburgite Reacted
SiO_2	55.97	57.48	56.98	55.60	56.53	57.20	57.26	57.29	56.00	56.53	56.91	56.48	55.82
TiO_2	<0.05	<0.05	<0.05	<0.05	<0.05	<0.05	<0.05	<0.05	<0.05	<0.05	<0.05	<0.05	<0.05
Al_2O_3	1.15	1.15	1.60	1.54	1.55	1.25	1.69	0.89	1.68	1.76	1.78	1.24	1.56
Cr_2O_3	0.48	0.46	0.53	0.47	0.59	0.45	0.46	0.40	0.57	0.61	0.49	0.49	0.44
FeO	7.17	5.75	5.26	5.44	5.45	5.99	5.70	5.35	5.53	5.60	5.62	5.13	6.17
MnO	0.16	0.15	0.14	0.13	0.13	0.14	0.13	0.15	0.14	0.15	0.10	0.13	0.16
MgO	34.86	35.10	34.99	35.58	34.96	35.21	34.90	35.04	35.17	35.52	35.41	35.43	34.83
CaO	0.59	0.81	0.89	0.51	1.12	0.60	0.53	1.23	0.48	0.40	0.56	0.60	0.67
Na_2O	<0.03	0.04	<0.03	<0.03	<0.03	<0.03	<0.03	<0.03	<0.03	<0.03	<0.03	<0.03	<0.03
NiO	0.09	0.08	0.07	0.10	0.09	0.08	0.09	0.12	0.10	0.09	0.10	0.08	0.07
Total	100.38	100.97	100.39	99.29	100.35	100.88	100.76	100.36	99.56	100.60	100.90	99.53	99.67
Mg#	0.897	0.916	0.922	0.921	0.920	0.913	0.916	0.921	0.919	0.919	0.918	0.925	0.910

Clinopyroxene

	67-02A(1) Pyroxenite	67-02B(6) Pyroxenite	67-02D(3) Dunite	67-02A(2) Harzburgite Residual	67-02B(1) Harzburgite Residual	67-02D(1) Harzburgite Residual	67-02D(4) Harzburgite Residual	67-02E(1) Harzburgite Residual	67-02A(3) Harzburgite Reacted	67-02A(5) Harzburgite Reacted	67-02B(3) Harzburgite Reacted	67-02B(5) Harzburgite Reacted	67-02D(7) Harzburgite Reacted	67-02D(7) Harzburgite Reacted	67-02E(3) Harzburgite Reacted
SiO_2	54.38	53.50	52.68	53.22	53.54	53.39	53.29	54.34	54.82	52.57	53.81	52.68	53.04	51.94	53.44
TiO_2	0.08	0.11	0.05	<0.05	<0.05	<0.05	<0.05	0.06	<0.05	<0.05	<0.05	0.17	0.09	0.25	<0.05
Al_2O_3	1.26	1.25	0.48	1.66	1.29	1.40	1.26	1.39	0.55	1.37	1.15	2.41	2.01	2.71	1.61
Cr_2O_3	0.71	0.68	0.24	0.74	0.69	0.62	0.71	0.56	0.81	0.73	0.57	0.90	0.76	0.59	0.67
FeO	2.17	3.24	1.53	1.57	1.54	1.89	1.86	1.70	2.82	1.68	1.98	2.97	2.32	5.04	1.92
MnO	0.07	0.13	0.09	0.06	0.12	0.09	0.05	0.07	0.10	0.12	0.08	0.05	0.07	0.14	0.06
MgO	17.76	19.07	18.28	17.79	17.87	18.24	18.10	17.88	20.22	17.99	18.39	18.18	18.47	17.23	17.77
CaO	23.55	21.65	24.97	23.73	23.56	23.94	23.84	24.08	20.37	24.10	23.22	22.17	22.69	21.43	23.88
Na_2O	0.14	0.19	0.12	0.07	0.09	0.09	0.15	0.10	0.21	0.11	0.15	0.23	0.22	0.23	0.12
NiO	<0.05	0.05	<0.05	0.05	0.05	0.05	<0.05	0.05	0.06	0.05	0.02	0.07	0.07	0.03	0.06
Total	100.12	99.82	98.44	98.88	98.72	99.67	99.29	100.22	99.98	98.69	99.37	99.82	99.74	99.63	99.48
Mg#	0.936	0.913	0.955	0.953	0.954	0.945	0.945	0.949	0.927	0.950	0.943	0.916	0.934	0.859	0.943

Table 2.2 Average major element compositions (wt. %) of olivine, spinel, orthopyroxene and clinopyroxene in Ritter samples. Mg# = Mg/Mg+Fe, Cr# = Cr/Cr+Al. Fe_2O_3 in spinel was calculated assuming ideal stoichiometry on a 3 cation basis

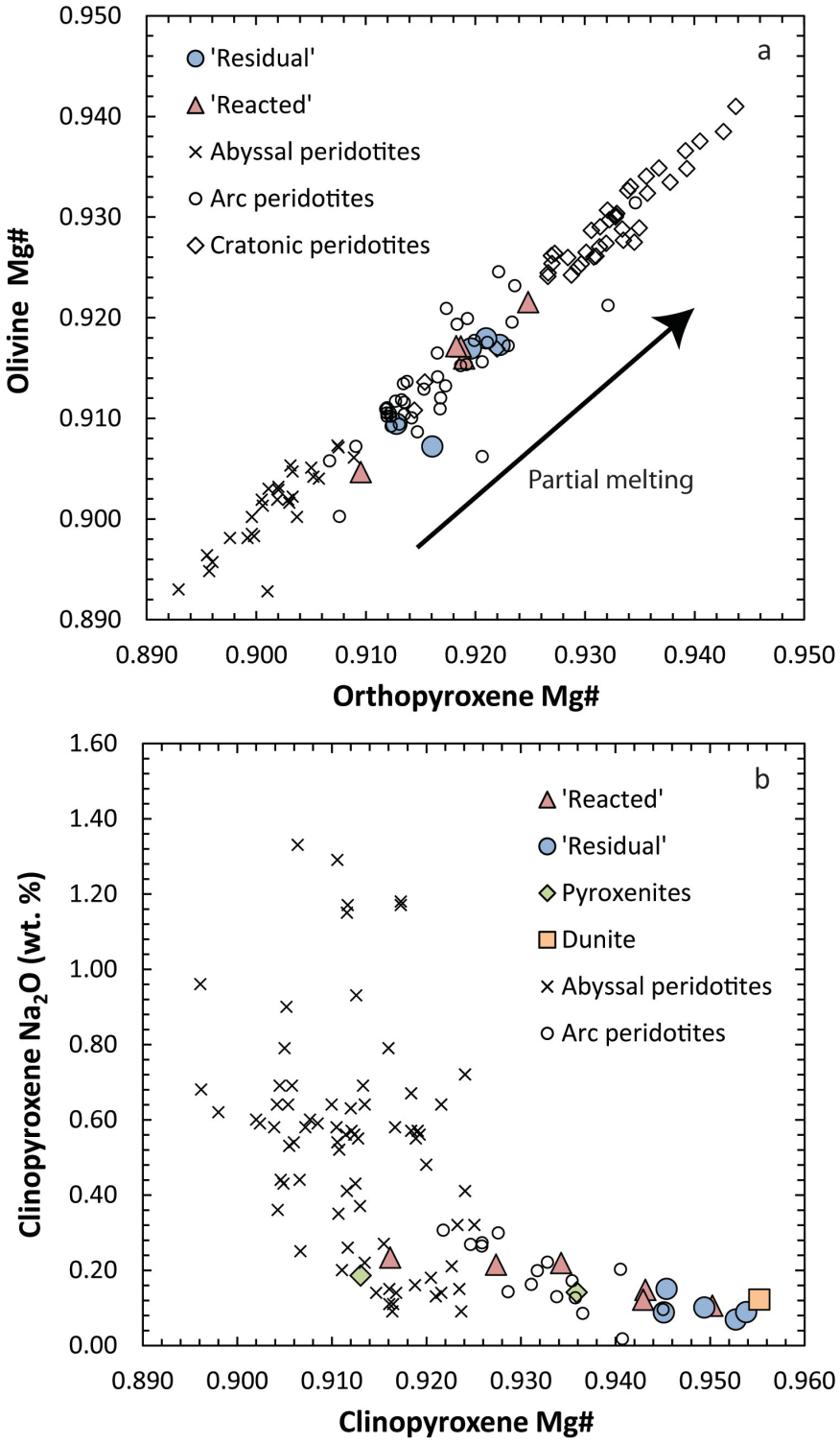

Fig. 2.3 Co-variation of; a) olivine and orthopyroxene Mg# (Mg/Mg+Fe) where arrow indicates compositional changes from increased degrees of partial melting; b) clinopyroxene Mg# and Na_2O, both compared to the abyssal (Seyler et al. 2003), arc (Parkinson and Pearce 1998, Ionov 2010) and cratonic (Bernstein et al. 2006) peridotite arrays.

2.4 Results

2.4.1 Mineral major elements

Major element compositions of mineral phases are reported in Table 2.2. Olivines in the harzburgites display a relatively restricted range of major element compositions (Mg# = 0.905-0.922, NiO = 0.39-0.46 wt. %) whilst the two dunites studied contain olivine with higher Mg# and Ni contents (Mg# = 0.922-0.940, NiO = 0.41-0.47 wt. %). The compositional variability within each sample is very small, typically <1 %. There is no systematic difference between the major element composition of olivines from 'residual' and 'reacted' samples. Spinel on the other hand displays more varied compositions, with clear, albeit overlapping distinctions between the two sample types. Spinel from 'residual' samples has lower Cr# (0.495-0.614) and TiO_2 (0.01-0.08 wt. %), compared to spinel from 'reacted' samples (Cr# 0.549-0.783 and TiO_2 0.01-0.37 wt. %). Spinel from the pyroxenites is similar to spinel from 'reacted' harzburgites, whilst spinel from the dunite is distinguished by its very high Cr# (up to 0.885). Orthopyroxene from the harzburgites has a similar compositional range to olivine, with Mg# ranging from 0.910-0.925 and $Kd^{FeO/MgO}_{orthopyroxene/olivine}$ of 0.90-0.99, and there is good correlation between forsterite content of olivine and orthopyroxene Mg# in agreement with global melt depletion trends (Fig. 2.3). Al_2O_3 and CaO contents are both very low (1.24-1.78 wt. % and 0.40-1.12 wt. % respectively). Orthopyroxene porphyroclasts from sample 67-02A(3) have uniquely low Al_2O_3 (0.89 wt. %) and higher CaO (1.23 wt. %). As with olivine, there is no clear distinction between orthopyroxene from 'residual' and 'reacted' samples. Orthopyroxene from the pyroxenites is similar in composition except for slightly lower Al_2O_3 (1.15 wt. %) compared to the majority of harzburgites and, in the case of the orthopyroxenite, lower Mg# (0.900). Harzburgitic clinopyroxene is similarly low in Al_2O_3 (1.15-2.41 wt. %) and Na_2O (0.01-0.23 wt. %) but has high CaO (typically 22.15-24.10 wt. %) and high Mg# (typically 0.943-0.954). There is a negative correlation between Na_2O and both Mg# and CaO (Fig. 2.3). Clinopyroxene neoblasts in porphyroclastic sample 67-02A(3) are compositionally distinct, with lower Al_2O_3 (0.55 wt. %) and CaO (20.37 wt. %). More compositional variation is observed in clinopyroxene than the other phases. This is most apparent for two reacted samples, 67-02B(5) and 67-02D(7). Three clinopyroxene analyses in the

former show significant variation in Mg# (0.908-0.925) which correlates negatively with TiO_2. 67-02D(7) contains two populations of clinopyroxene, one with higher Mg# and CaO (0.934 and 22.69 wt. % respectively) compared to lower values of 0.859 and 21.43 wt. % in the other population. Significantly, there is no difference between the chemistry of clinopyroxenes which constitute the vein in residual sample 67-02E(1) and any of the other clinopyroxene populations, other than the exceptions described above. There is no clear relationship between the Mg# of clinopyroxene and the forsterite content of olivine. $Kd^{FeO/MgO}_{clinopyroxene/olivine}$ values deviate significantly from unity (0.52-0.83, with the exception of 67-02B(5) which has a mean value of 1.01). Clinopyroxene in the pyroxenites is similar to those in the harzburgites but with slightly higher FeO. Clinopyroxene from dunite 67-02D(3) has lower Al_2O_3 and higher Mg# and CaO than harzburgitic clinopyroxene.

2.4.2 Major element thermometry and fO_2

The application of traditional multi-phase chemical exchange thermometers is only valid under the condition of equilibrium. Popular thermometers based on major elements utilise the exchange of temperature-sensitive components between olivine and spinel (e.g. O'Neill and Wall 1987, Ballhaus et al. 1991) and pyroxenes (e.g. Brey and Kohler 1990). In the case of olivine-spinel equilibria there is a lack of correlation between forsterite content of olivine and spinel Mg#, however this is most likely due to variations in fO_2, which would strongly affect the Mg# of spinel but not the forsterite content of olivine, since Fe^{3+} is highly incompatible in olivine (Canil and O'Neill 1996). If we assume that olivine and spinel are in major element equilibrium then temperatures calculated using the formulation of O'Neill and Wall 1987 give temperatures of 662-759 °C for 'residual' samples and 732-1131 °C for 'reacted' samples (Table 2.3, Fig. 2.4, assuming a pressure of 1.5 GPa). These temperatures are relatively well constrained, given the narrow compositional variation in spinel and olivine composition in each sample with standard deviations of typically <50 °C. Temperatures calculated using the similar thermometer of Ballhaus et al. (1991) are within uncertainty. There is a distinct positive correlation between calculated temperature and Cr# of spinel (Fig. 2.4) and weak positive correlation between temperature and TiO_2 in spinel (not shown). The clinopyroxene-orthopyroxene thermometer of Brey and Köhler (1990) was also applied to these

samples. Despite a lack of correlation between the composition of clinopyroxene and other phases, temperatures calculated with this method correlate well with the olivine-spinel temperatures, albeit offset to higher values by 60-157 °C (Fig. 2.4). This indicates that clinopyroxene is indeed in chemical equilibrium with respect to major elements. An exception is the 'reacted' sample 67-02A(5) which records a two-pyroxene temperature ~260 °C lower than the olivine-spinel temperature.

Sample	Type		T (BBG)	T (ONW)	T (BKN)	Olivine Mg#	Spinel Cr#	Spinel Fe_2O_3/FeO	fO_2(Δlog FMQ)[1]	fO_2(Δlog FMQ)[2]	± Δlog FMQ
67-02A(1)	Pyroxenite				875		0.68	0.22			
67-02B(6)	Pyroxenite				1073		0.75	0.48			
67-02B(2)	Dunite		898	913		0.940	0.88	0.40	1.2		
67-02D(3)	Dunite		670	675		0.921	0.77	0.39	1.6		
67-02A(2)	Harzburgite	Residual	772	759	840	0.917	0.56	0.20	-0.3	-1.2	0.3
67-02B(1)	Harzburgite	Residual	715	702	855	0.918	0.55	0.14	-0.7	-1.7	
67-02D(1)	Harzburgite	Residual	743	732	823	0.917	0.58	0.38	1.0	0.1	0.1
67-02D(4)	Harzburgite	Residual	708	703	793	0.909	0.61	0.13	-0.8	-2.0	0.2
67-02E(1)	Harzburgite	Residual	672	662	820	0.907	0.49	0.03	-3.1	-3.3	1.0
67-02A(3)	Harzburgite	Reacted	1114	1131	1172	0.913	0.78	0.67	1.1	0.0	0.8
67-02A(5)	Harzburgite	Reacted	971	977	714	0.916	0.68	0.45	0.6	-0.3	0.1
67-02B(3)	Harzburgite	Reacted	822	809	909	0.917	0.55	0.10	-1.9	-2.9	0.8
67-02B(5)	Harzburgite	Reacted	954	958	1018	0.917	0.68	0.52	0.9	0.0	0.4
67-02D(7)	Harzburgite	Reacted	868	871	971	0.922	0.67	0.33	0.4	-0.5	0.8
67-02E(3)	Harzburgite	Reacted	761	751	807	0.905	0.55	0.19	-0.5	-1.4	0.5

Table 2.3 Temperatures (°C) and oxygen fugacities calculated from average mineral compositions and summary of relevant mineral compositional data for comparison. 'BBG' is the olivine-spinel thermometery of Ballhaus et al. (1991), 'ONW' is the olivine-spinel thermometery of O'Neill and Wall (1987) and 'BKN' is the two-pyroxene thermometer of Brey and Köhler (1990). Variation in temperatures calculated from different mineral pairs in each sample is similar to the assumed uncertainty in the thermometry calibrations of ± 50 °C. A pressure of 1.5 GPa was assumed in all calculations. Mg# = Mg/Mg+Fe, Cr# = Cr/Cr+Al. Oxygen fugacities are expressed relative to the quartz-fayalite-magnetite buffer and are calculated using the BBG temperature estimates. [1]Estimates using Ballhaus et al. (1991), [2]estimates using O'Neill and Wall (1987). Uncertainties are 1 s.d. on repeat measurements of different spinel grains within the same sample (typically 4-6).

Oxygen fugacities calculated from olivine-orthopyroxene-spinel equilibria (Table 2.3) varied from -3.1 to 1.6 log units relative to the quartz-fayalite-magnetite buffer (QFM). However it is highly uncertain what the correct oxybarometer calibration is for highly depleted peridotites, highlighted in this dataset by substantial differences between values calculated with different calibrations. This can be demonstrated further by taking olivine, orthopyroxene and spinel compositions from literature data for peridotites of varying degrees of fertility and calculating oxygen fugacities using two commonly used methods, O'Neill and Wall (1987) and Ballhaus et al. (1991). In Fig. 2.5 we plot the difference between the values calculated with these two different calibrations and the Cr# of spinel in each sample. There is a striking positive correlation, such that for depleted peridotites with high spinel Cr#, the difference in calculated fO_2 is substantial. The O'Neill and Wall (1987) method always produces lower oxygen fugacities than Ballhaus et al. (1991). Regression of the data for global peridotites allows us to express this difference as

$$logfO_2^{BBG} = logfO_2^{ONW} + 1.70Cr\#_{Spinel} - 0.06$$

where Cr# is Cr/Cr+Al. Uncertainty is approximately ± 0.1 log units. The important implication for this is that peridotite samples from subduction zone settings and mid-ocean ridge settings are known to differ in their fertility and spinel Cr#, with spinel from arc peridotites typically having higher Cr# (Arai 1994, Arai and Ishimaru 2008). Depending on which calibration is correct, the oxygen fugacities calculated with either method may produce excessively reduced or oxidised values. For example, if the Ballhaus et al. (1991) calibration is incorrect then arc peridotites (and others with high spinel Cr#) would appear substantially more oxidised than they actually are, relative to more fertile peridotites (approximately 1 log unit for a spinel Cr# of 0.62). Hence currently we restrict the discussion to the ratio of Fe_2O_3/FeO in our spinel measurements, which is proportional to oxygen fugacity. Spinels from residual peridotites all have very low ratios of Fe_2O_3/FeO (0.03-0.20, Table 2.2) whilst spinels from reacted peridotites extend to considerably more oxidised values (0.10-0.67, Table 2.2). There is a strong positive correlation between Cr# of spinel and Fe_2O_3/FeO and also between temperature and Fe_2O_3/FeO (Fig. 2.4). Correlation between TiO_2 in spinel and Fe_2O_3/FeO is decidedly weaker (not shown).

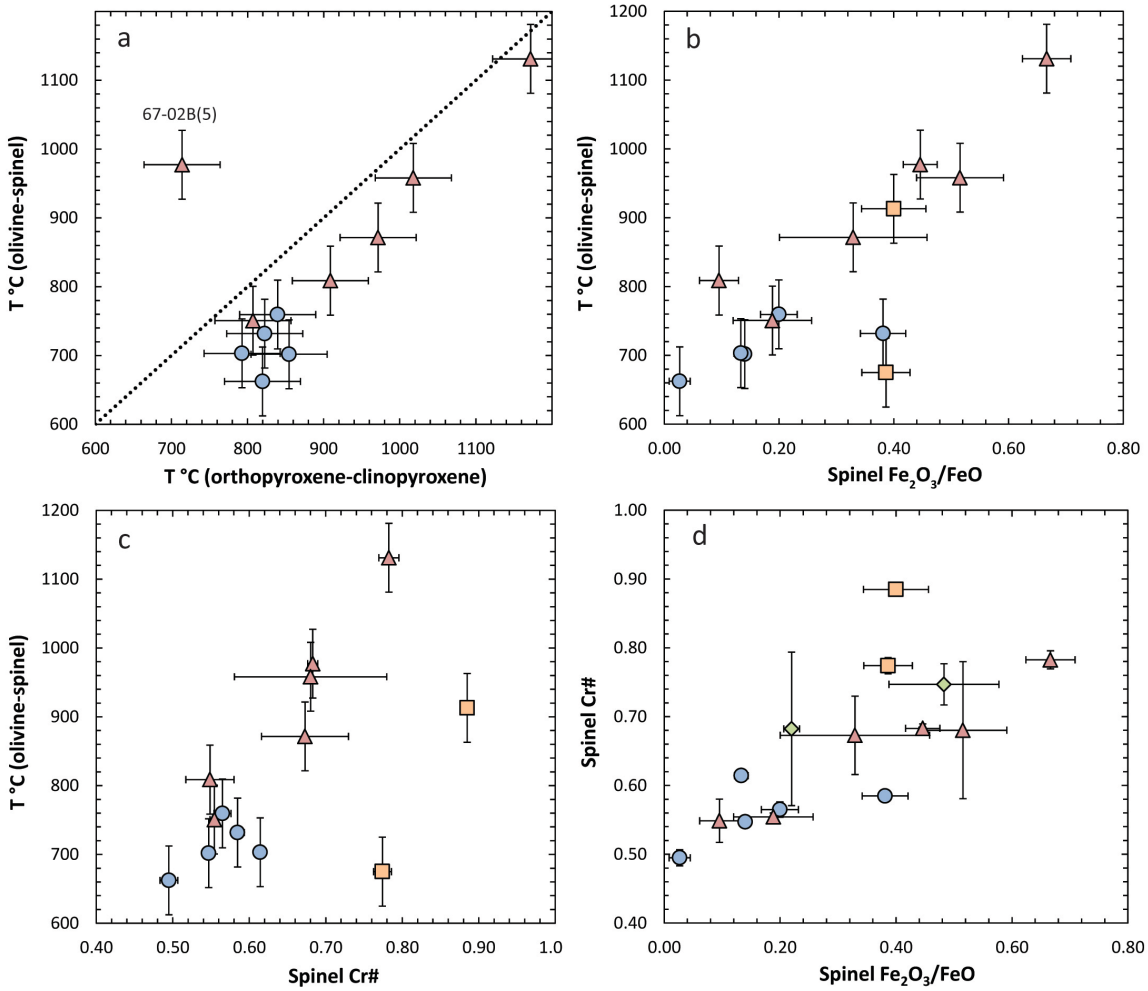

Fig. 2.4 Plots of co-variation between: (a) Temperatures calculated from olivine-spinel (O'Neill and Wall 1987) and orthopyroxene-clinopyroxene equilibria (Brey and Köhler 1990) (b) Temperature and spinel Fe_2O_3/FeO (c) Temperature and spinel Cr# and (d) Spinel Cr# and spinel Fe_2O_3/FeO. Positive correlation in (a) (b) and (c) are interpreted to reflect reaction of cold, relatively reduced ambient mantle with percolating, relatively oxidised silicate melts. Symbols as in previous figures. Uncertainties are 1 s.d. based on calculations from multiple mineral pairs. Temperature uncertainties assumed to be ± 50 °C

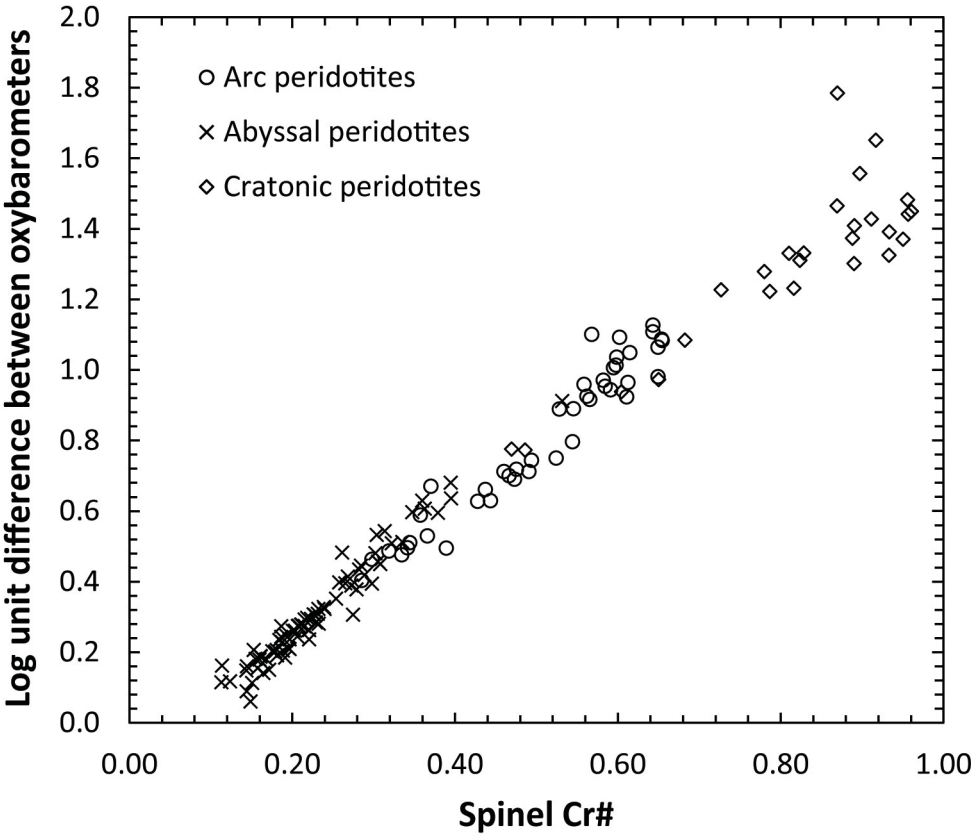

Fig. 2.5 Correlation between the difference in oxygen fugacity (relative to the fayalite-magnetite-quartz buffer) with the Cr# of spinel from the same sample. The two oxybarometers employed are both based on olivine-orthopyroxene-spinel equilibria; Ballhaus et al. 1991 and O'Neill and Wall 1987. Pressures assumed to be 1.5 GPa in all calculations, except cratonic peridotites (2.5 GPa). Data from Dick 1989, Hellebrand et al. 2001, Seyler et al. 2003, Franz et al. 2002, Parkinson et al. 2003, Ionov 2010 and Berstein et al. 2006

	67-02A(1) Pyroxenite	67-02B(6) Pyroxenite	67-02B(2) Dunite	67-02A(2) Harzburgite Residual	67-02B(1) Harzburgite Residual	67-02D(4) Harzburgite Residual	67-02E(1) Harzburgite Residual	67-02A(3) Harzburgite Reacted	67-02A(5) Harzburgite Reacted	67-02B(3) Harzburgite Reacted	67-02B(5) Harzburgite Reacted	67-02D(7) Harzburgite Reacted	67-02E(3) Harzburgite Reacted	Standards and total procedural blank						
														BHVO-1	W2	AGV-1	NBS688	BE-N	GP13	Blank
Ti (ppm)	141	215	41.4	6.00	3.00	38.4	30.0	69.5	45.6	6.00	58.2	59.2	32.2	2.74	1.06	1.03	1.16	2.63	0.100	0.000
Co	63.8	59.0	104	113	104	106	110	107	109	112	113	92.2	85.7	45.4	45.31	14.29	52.64	63.7	89.4	0.06
Ni	506	692	3394	2873	2689	2725	2751	2650	2731	2922	2826	1807	1520	130	85.1	27.6	164	279	2053	10.8
Cu	4.21	7.97	3.81	1.12	1.28	5.91	3.49	7.84	5.19	4.04	5.48	3.65	5.30	139	104	57.4	88.3	71.8	24.7	0.105
Zn	34.3	35.7	26.1	35.2	30.6	36.6	33.2	42.3	40.4	34.8	47.0	33.2	35.4	110	74.3	85.2	72.8	126	33.3	1.369
Rb	0.070	0.462	0.274	0.041	0.021	0.173	0.024	0.570	0.234	0.076	0.155	0.210	0.166	8.03	17.4	68.1	1.69	43.8	0.299	0.008
Sr	1.7	14.0	6.4	0.8	0.3	3.7	0.4	11.4	4.7	0.8	4.2	7.4	4.8	400	198	663	168	1437	9.48	0.027
Y (ppb)	360	1100	261	43.9	38.0	237	137	426	248	59.3	286	281	194	27640	22420	19870	20940	30710	3286	1.2
Zr	233	1046	544	142	157	338	145	599	444	116	339	523	239	173800	91180	229800	47460	272700	4719	10.5
Nb	33.4	56.7	73.4	45.5	54	55.5	48.3	55.5	59.4	64.6	60.5	36.7	12.8	19330	7680	14670	4235	138800	128	2.5
Cs	8.0	23.8	16.8	2.30	1.4	11.2	1.8	23.2	21.8	5.4	10.3	16.4	8.9	97	882	1251	35	752	67	0.6
Ba	225	2305	1395	208	120	774	91.9	2246	1058	227	831	2102	857	117600	154000	1225000	149700	1016000	822	49.0
La	16.9	131.1	67.8	11.2	7.8	37.1	7.4	90.9	50.7	11.3	40.2	123.1	50.6	13700	9216	39260	4330	82230	167	1.2
Ce	39.2	309.1	151.9	28.0	21.5	84.3	21.6	206.1	111.8	20.6	95.1	241.6	100.2	37710	20030	67810	9717	147200	497	3.1
Pr	6.3	53.4	23.1	3.7	3.4	13.4	3.6	32.3	17.7	2.6	15.7	34.0	16.2	4739	2656	7471	1479	15270	96	0.3
Nd	40.9	318.0	129.2	20.9	21.4	77.6	23.2	186.3	97.4	16.5	95.5	150.5	77.6	25890	13530	33370	8531	68620	655	2.6
Sm	13.3	105	33.3	5.5	5.4	20.9	9.5	51.1	25.1	3.5	27.4	34.8	19.7	6222	3337	5890	2342	12110	250	0.2
Eu	5.4	34.5	10.7	1.7	1.7	7.5	2.5	17.5	8.3	1.3	10.4	11.3	6.7	1917	1056	1881	927	3666	93	0.2
Gd	20.8	129.4	39.6	6.1	5.9	28.1	10.7	59.0	29.8	4.8	37	39.7	23.6	6117	3591	5576	2714	11520	337	0.5
Tb	5.0	24.6	6.3	1.1	0.9	5.6	2.2	9.8	5.4	0.8	6.9	6.7	4.2	957	613	721	499	1414	71	0.2
Dy	38.5	163.7	39.7	5.5	4.6	34.0	15.5	63.3	33.2	5.8	41.6	41.7	25.9	5236	3759	3703	3163	6699	490	0.2
Ho	12.0	38.9	8.7	1.4	1.2	8.0	4.4	13.8	8.3	1.4	10.0	9.4	6.0	989	795	676	714	1065	115	0.1
Er	41.2	113.3	25.5	4.3	3.5	23.4	15.4	40.7	24.7	4.7	28.9	27.3	18.5	2416	2120	1738	1984	2391	335	0.1
Tm	8.5	20.4	4.3	1.0	0.9	4.6	3.2	7.3	4.9	1.0	5.1	4.8	3.3	363	346	280	334	340	57	0.0
Yb	65.4	135.1	28.0	8.9	7.9	31.8	27.1	47.6	34.0	10.1	34.5	33.6	24.5	2016	2047	1654	2042	1873	359	0.1
Lu	12.0	23.8	5.5	2.3	2.3	5.9	5.4	8.1	6.3	2.5	6.3	6.7	5.7	306	326	268	336	280	60	0.0
Hf	14.3	41.9	21.9	12.8	9.9	15.8	9.9	27.4	20.1	8.7	16.3	15.4	6.8	4416	2456	5086	1469	5632	173	0.7
Pb	116.2	212.9	175.6	92.3	111.4	100.0	73.6	184.1	179.8	131.9	142.5	68.0	54.0	2157	7283	36150	3457	4004	435	24.3
Th	2.7	19.7	11.4	3.6	2.5	6.8	1.7	13.0	9.2	2.3	6.4	19.3	6.3	1234	2182	6442	330	10940	12	0.4
U	8.0	10.9	6.5	2.0	1.1	5.2	0.9	7.3	9.6	6.3	4.4	7.2	12.5	412	491	1894	245	2493	4.3	0.3

Table 2.4 Trace element composition of whole-rock peridotites, analytical standards and average total procedural blank. Ti to Sr reported as ppm. All other elements reported as ppb. Standard devation on each measurement is typically < 10 %

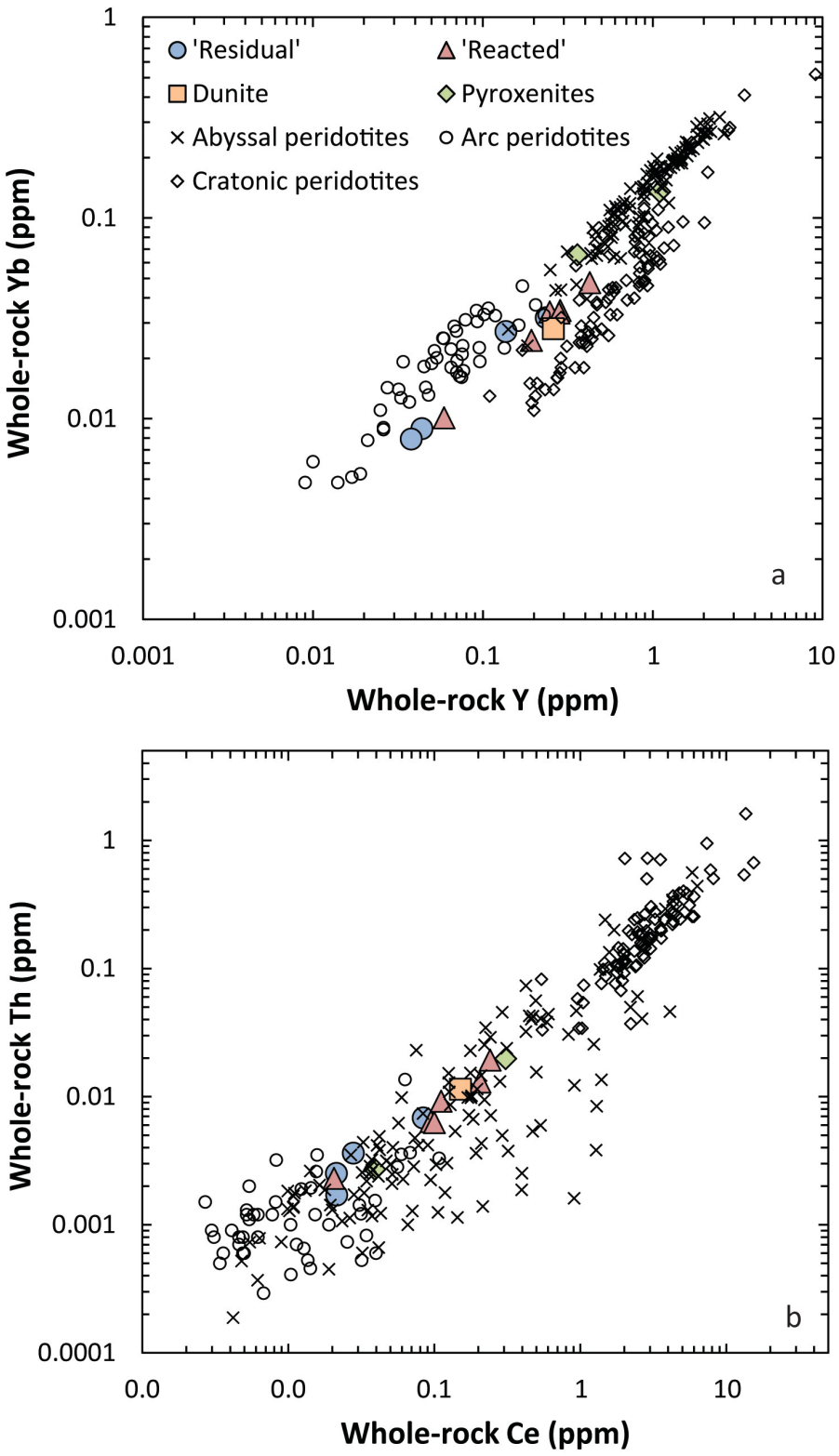

Fig. 2.6 Variations in whole-rock trace element concentration compared to abyssal (Niu 2004), arc (Parkinson and Pearce 1998, Ionov 2010) and cratonic (Wittig et al. 2008) peridotites. a) Moderately incompatible Y and Yb; b) highly incompatible Ce and Th

2.4.3 Whole rock trace elements

The compositions of all Ritter samples are reported in Table 2.4. All Ritter whole rock harzburgites are highly depleted in moderately incompatible trace elements relative to the global array of abyssal peridotites (Fig. 2.6a, Niu 2004) and display comparable depletion to other arc peridotites (Parkinson and Pearce 1998, Ionov 2010). In contrast, Ritter samples have similar concentrations of highly incompatible trace elements relative to abyssal suites (Fig. 2.6b).

The concentrations of a given element typically correlate strongly with those of neighbouring elements on extended trace element diagrams, with a few exceptions. For example, Ti correlates most strongly with Er and Tm rather than Eu and Gd, Pb shows poor correlation with Pr and Ce as do U, Nb and Ta with each other and with Th and La. Most notably, Th, Hf and Zr correlate very strongly with LREE and Sr whilst U, Pb and Nb form much weaker correlations (Fig. 2.7.).

When normalised to primitive mantle values (Palme and O'Neill 2003), there are two distinct REE patterns present in the harzburgites (Fig. 2.8). The first pattern has highly depleted HREE and steeply dipping profiles between Lu_N and Er_N. La_N to Ho_N is slightly positively sloped. The second pattern is essentially flat from Lu_N to La_N and more enriched for all elements than the first pattern with no overlap. A single 'residual' sample, 67-02E(1) has an intermediate REE pattern, with comparable HREE concentrations to the enriched group, LREE concentrations the same as the depleted group and MREE concentrations that straddle the two. There is no obvious Eu anomaly present in any of the samples, however when Hf is added to the REE plots in accordance with its relative compatibility distinct Hf anomalies emerge which correlate with overall enrichment such that the most depleted samples have the most positive Hf anomalies and the most enriched the most negative Hf anomalies. Of the four 'residual' samples, two have depleted patterns, one has an intermediate pattern and sample 67-02D(4) which shows both 'residual' and 'reacted' textures on thin section scale has an enriched REE pattern. All but one of the 'reacted' samples (67-02B(3)) has the enriched REE pattern. The single dunite measured has an REE pattern indistinguishable from the enriched 'reacted' harzburgites. The wehrlite has a very similar REE pattern to the enriched group of

harzburgites, but offset to higher concentrations. The orthopyroxenite is also relatively enriched but has a very similar REE pattern to the intermediate harzburgite 67-02E(1).

On extended primitive mantle-normalised trace element plots (Fig. 2.8) the enriched and depleted groups remain distinct for most elements. The most obvious exception is Nb has very similar concentrations in all samples, leading to positive anomalies in depleted samples but no distinct anomaly in enriched samples. Most samples have positive Sr anomalies, except the two depleted 'residual' samples. All samples have negative Ti anomalies except 67-02E(1) which has a positive Ti anomaly similar to the positive Ti anomaly in the orthopyroxenite.

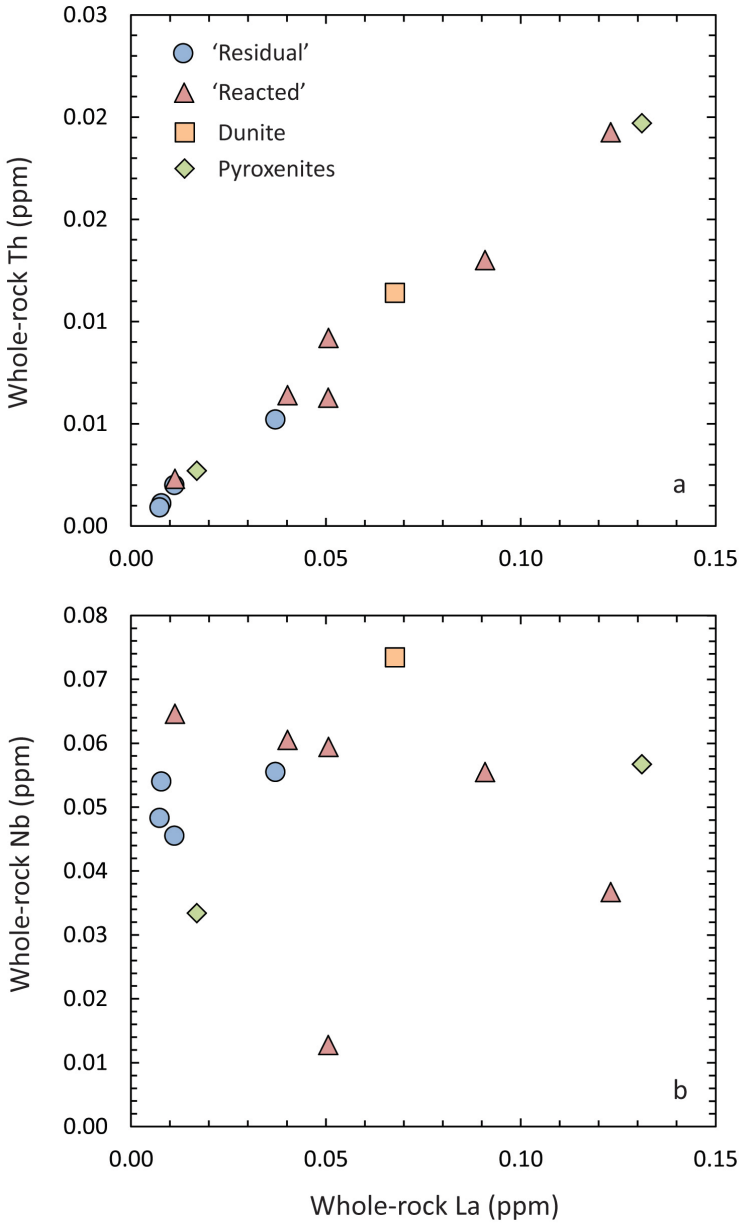

Fig. 2.7 Contrasting strong and weak correlations between a) Th and La; b) Nb and La, despite similar bulk peridotite-melt partition coefficients

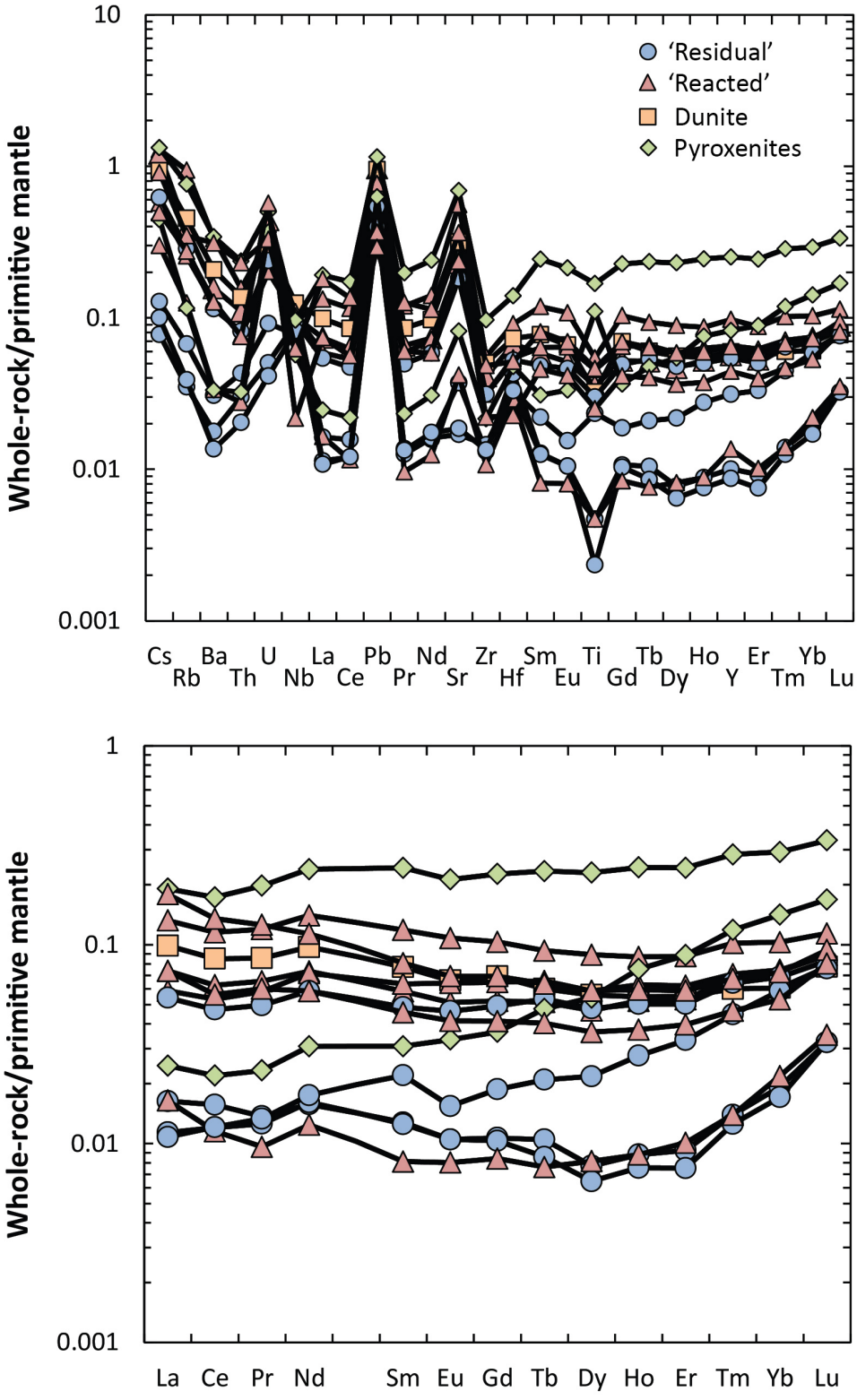

Fig. 2.8 Primitive mantle-normalised concentrations of trace elements for 'residual' and 'reacted' harzburgites, pyroxenites and a dunite. Normalising values from Palme and O'Neill (2003)

	67-02A(1) Pyroxenite		67-02B(6) Pyroxenite		67-02A(2) Harzburgite Residual		67-02B(1) Harzburgite Residual		67-02D(1) Harzburgite Residual		67-02D(4) Harzburgite Residual		67-02E(1) Harzburgite Residual	
		1 s.d. (5)		*1 s.d. (4)*		*1 s.d. (10)*		*1 s.d. (10)*		*1 s.d. (9)*		*1 s.d. (11)*		*1 s.d. (8)*
Na (ppm)					6.80	*3.84*	6.00	*3.00*	4.10	*2.21*	7.72	*2.51*	11.71	*10.72*
P (ppm)					22.59	*0.79*	20.21	*0.75*	21.90	*0.78*	20.39	*0.82*	13.10	*3.44*
Sc (ppm)	17.08	*2.60*			26.44	*1.29*	23.08	*1.03*	26.72	*2.25*	24.18	*1.95*	30.38	*0.93*
V (ppm)	44.99	*12.67*			43.07	*2.07*	47.28	*3.02*	57.80	*4.40*	42.30	*3.38*	61.02	*1.36*
Cr (ppm)					3089	*387*	3048	*501*	2954	*419*	2496	*366*	3124	*297*
Mn (ppm)					1026	*14*	1022	*17*	1102	*21*	1159	*23*	1036	*18*
Co (ppm)					50.6	*1.0*	52.7	*1.2*	52.4	*1.9*	52.7	*1.6*	52.5	*1.1*
Ni (ppm)					617	*28*	672	*35*	638	*42*	575	*27*	648	*23*
Ti (ppm)	144	*2.86*	50.3	*2.04*	10.7	*1.9*	6.8	*1.3*	27.0	*10.8*	29.5	*5.7*	82.7	*5.1*
Y (ppb)	158	*15.9*	147	*25.4*	33.2	*4.7*	48.6	*7.5*	96.8	*34.8*	101	*8.8*	187	*30.7*
Zr (ppb)	64.0	*11.2*	70.6	*4.66*	36.3	*5.7*	160	*23.5*	90.0	*23.9*	67.1	*11.6*	97.3	*15.9*
Nb (ppb)	3.67	*0.62*	1.40	*0.27*	6.15	*0.94*	7.92	*1.22*	6.24	*0.59*	6.45	*1.33*		
La (ppb)	1.00	*0.14*	0.49	*0.02*	0.31	*0.13*	0.78	*0.52*	0.54	*0.20*	0.23	*0.03*		
Ce (ppb)	3.43	*3.06*	1.88	*0.95*	0.67	*0.29*	2.49	*1.78*	1.32	*0.74*	0.53	*0.13*		
Pr (ppb)	0.53		0.36	*0.13*	0.22	*0.03*	0.58	*0.43*	0.46	*0.13*				
Nd (ppb)			4.19	*1.25*	1.66		3.63	*1.46*	3.30				4.50	
Sm (ppb)					0.80	*0.43*	2.01	*0.46*	1.35	*0.40*	0.91	*0.21*	3.05	*1.03*
Eu (ppb)	1.33	*0.12*	1.54	*0.13*			0.80	*0.29*	0.69	*0.09*	0.86			
Gd (ppb)	5.52	*0.79*	6.34	*0.57*	1.29	*0.64*	3.41	*1.21*	4.28	*1.03*	2.51	*0.19*	3.88	*0.93*
Tb (ppb)	1.32	*0.41*	1.31	*0.49*	0.32	*0.03*	0.60	*0.11*	0.98	*0.25*	0.80	*0.22*	1.45	*0.38*
Dy (ppb)	14.21	*1.39*	14.1	*2.04*	3.06	*0.79*	5.26	*1.12*	11.41	*3.45*	9.51	*1.87*	16.35	*4.47*
Ho (ppb)	5.28	*1.22*	4.76	*0.65*	1.09	*0.27*	1.56	*0.34*	3.49	*1.40*	3.58	*0.51*	6.12	*1.15*
Er (ppb)	23.42	*2.05*	20.6	*1.24*	5.83	*0.90*	6.96	*0.95*	15.99	*6.22*	15.72	*2.14*	31.68	*1.59*
Tm (ppb)	5.23	*1.40*	3.62	*0.43*	1.60	*0.26*	1.74	*0.36*	3.50	*1.12*	3.90	*0.51*	8.08	*1.32*
Yb (ppb)	50.84	*3.95*	38.1	*5.78*	23.7	*2.6*	20.7	*2.0*	39.1	*9.8*	39.6	*4.9*	78.4	*6.3*
Lu (ppb)	9.85	*0.45*	7.22	*1.12*	5.98	*0.68*	5.09	*0.64*	8.07	*1.95*	8.34	*1.21*	16.93	*3.69*
Hf (ppb)	3.74	*1.31*	2.38	*0.33*	1.01	*0.07*	3.21	*0.75*	3.55	*0.56*	1.98	*0.40*	2.58	*0.36*

	67-02A(3) Harzburgite Reacted	*1 s.d. (9)*	67-02A(5) Harzburgite Reacted	*1 s.d. (8)*	67-02B(3) Harzburgite Reacted	*1 s.d. (10)*	67-02B(5) Harzburgite Reacted	*1 s.d. (4)*	67-02D(7) Harzburgite Reacted	*1 s.d. (11)*	67-02E(3) Harzburgite Reacted	*1 s.d. (4)*	L.O.D.	BCR2G	*1 s.d. (11)*
Na (ppm)	4.85	*1.39*	53.33	*31.40*	19.49	*36.45*	37.95	*15.19*	16.19	*9.68*	21.51	*14.64*	0.35	3.15	*0.07*
P (ppm)	20.62	*0.45*	22.53	*0.78*	7.92	*0.84*	9.53	*1.54*	20.53	*0.46*	21.27	*0.67*	0.75	1589	*28.58*
Sc (ppm)	25.55	*1.25*	23.39	*0.97*	26.84	*1.71*	25.20	*0.88*	24.49	*1.43*	26.35	*1.93*	0.01	33.30	*1.69*
V (ppm)	44.36	*1.78*	51.51	*2.08*	59.37	*2.70*	39.40	*2.30*	49.07	*2.82*	55.18	*3.29*	0.00	415	*7.75*
Cr (ppm)	2862	*315*	3679	*276*	3609	*570*	3313	*403*	2714	*212*	2648	*327*	0.12	14.61	*0.41*
Mn (ppm)	1044	*19*	1006	*14*	1011	*19*	978	*27*	1011	*19*	1135	*23*	0.09	1477	*33.4*
Co (ppm)	51.1	*1.0*	53.0	*0.8*	52.5	*1.5*	51.2	*0.7*	48.3	*0.9*	52.4	*1.8*	0.01	37.22	*0.84*
Ni (ppm)	619	*28*	668	*24*	683	*43*	645	*22*	580	*27*	624	*46*	0.12	13.9	*3.75*
Ti (ppm)	10.7	*0.4*	33.8	*3.8*	23.3	*1.2*	13.1	*1.7*	44.4	*4.6*	18.1	*2.6*	0.05	12783	*238*
Y (ppb)	29.7	*2.7*	79.5	*10.4*	32.1	*7.0*	25.9	*4.6*	124	*58.2*	101	*17.0*	1.75	31.05	*1.43*
Zr (ppb)	37.6	*2.0*	93.9	*9.5*	16.7	*4.7*	58.8	*7.4*	201	*82.8*	73.1	*16.5*	2.21	174	*7.47*
Nb (ppb)	7.49	*0.82*	9.28	*1.04*					5.33	*0.82*	6.93	*0.66*	0.42	11.76	*0.25*
La (ppb)	0.46	*0.56*	2.20	*1.57*	2.71		5.18	*2.72*	0.54	*0.21*	0.67		0.20	24.4	*1.01*
Ce (ppb)	0.94	*0.66*	4.78	*2.84*	1.56	*0.66*	11.40	*5.76*	1.95	*0.66*	0.79	*0.73*	0.15	50.8	*0.88*
Pr (ppb)	0.30	*0.28*	0.76	*0.36*	0.88		1.44	*0.73*	0.47	*0.12*	0.32		0.14	6.53	*0.17*
Nd (ppb)	3.69	*2.28*	4.11	*0.39*	3.80		6.35	*4.54*	4.44	*2.02*			1.38	27.8	*0.92*
Sm (ppb)	0.87	*0.76*	1.54	*0.82*	2.20	*0.50*	2.75	*1.66*	2.41	*1.66*	1.73	*0.31*	1.36	6.54	*0.30*
Eu (ppb)									1.99	*0.43*	0.95	*0.14*	0.42	1.94	*0.06*
Gd (ppb)	2.03	*0.25*	2.50	*0.76*			3.40	*0.42*	5.28	*2.98*	6.05	*0.35*	1.14	6.45	*0.29*
Tb (ppb)	0.37	*0.04*	0.52	*0.22*	0.42	*0.09*	0.57	*0.18*	1.39	*0.69*	0.92	*0.25*	0.25	0.93	*0.01*
Dy (ppb)	2.59	*0.54*	7.63	*1.57*	2.89	*0.82*	3.25	*1.29*	14.41	*8.51*	11.39	*2.56*	0.94	6.13	*0.23*
Ho (ppb)	1.02	*0.14*	2.55	*0.44*	0.88	*0.31*	0.89	*0.36*	4.07	*2.06*	3.35	*0.67*	0.27	1.16	*0.02*
Er (ppb)	5.24	*0.53*	12.32	*1.80*	6.77	*1.51*	4.93	*0.72*	18.18	*7.10*	13.20	*1.18*	1.35	3.51	*0.17*
Tm (ppb)	1.68	*0.27*	2.92	*0.25*	2.08	*0.61*	2.10	*0.17*	4.15	*1.10*	3.01	*0.37*	0.58	0.47	*0.01*
Yb (ppb)	22.4	*2.6*	34.7	*2.6*	30.5	*5.9*	28.4	*2.1*	41.1	*8.2*	36.1	*2.3*	1.35	3.17	*0.14*
Lu (ppb)	6.04	*0.23*	7.88	*0.98*	7.57	*1.15*	7.73	*0.30*	9.12	*1.56*	7.74	*0.75*	0.38	0.46	*0.03*
Hf (ppb)	1.08	*0.07*	2.09	*0.31*	1.06		1.11		7.30	*3.53*	1.32	*0.32*	0.80	4.57	*0.11*

Table 2.5 Average trace element concentrations of orthopyroxene. Values in italics are 1 s.d. on measurements from multiple crystals (number of crystals measured in parentheses). Also reported are typical detection limits and repeat measurements of natural standard glass BCR2G during the analytical sessions

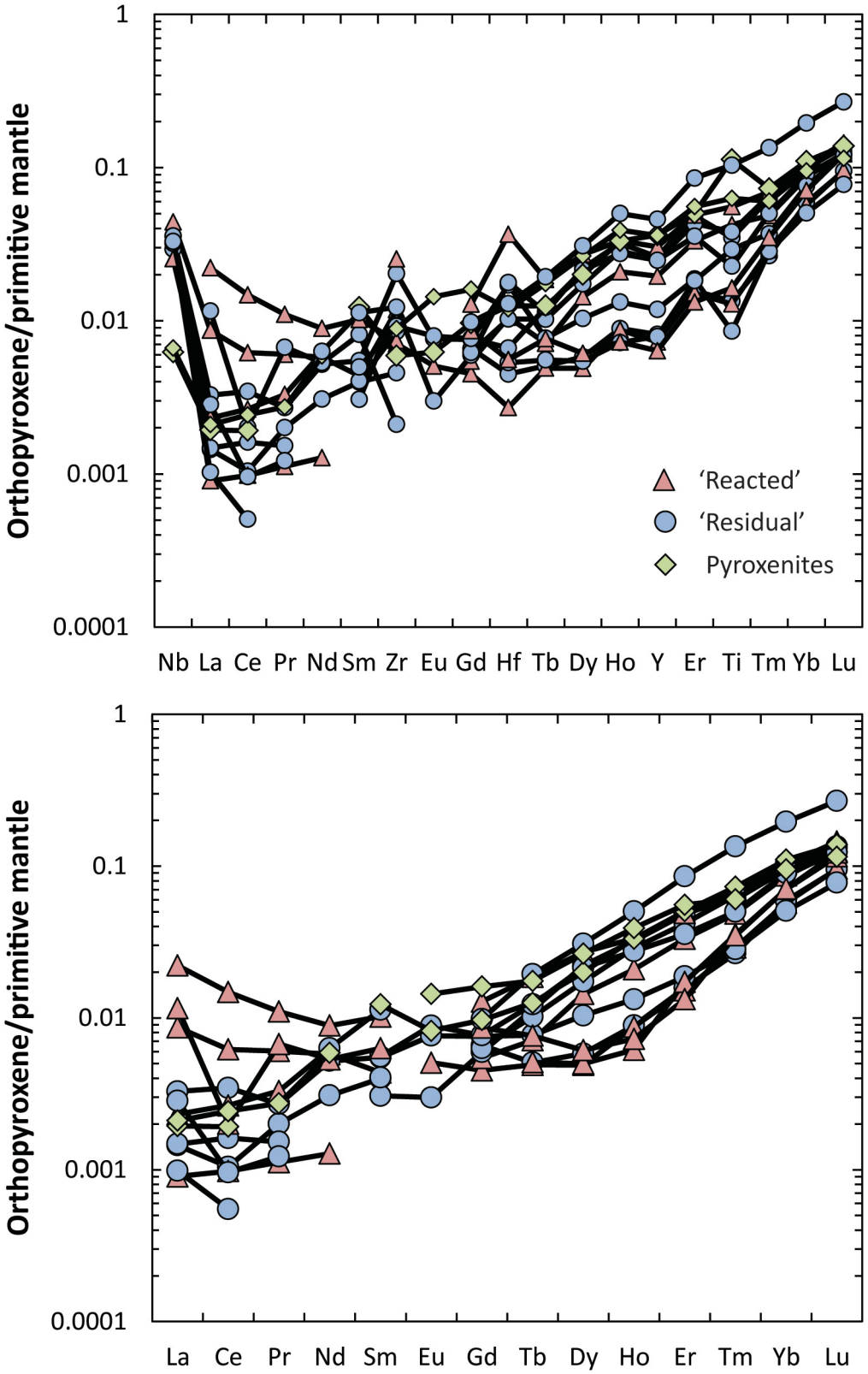

Fig. 2.9 Primitive mantle-normalised trace element concentrations of average orthopyroxene compositions. Normalising values from Palme and O'Neill (2003)

2.4.4 Orthopyroxene trace elements

The trace element compositions of orthopyroxene are reported in Table 2.5. Orthopyroxenes have very depleted trace element compositions compared to the limited data available from abyssal samples (Hellebrand et al. 2005, Seyler et al. 2011). On primitive mantle-normalised REE plots, orthopyroxenes (Fig. 2.9) typically display slightly spoon-shaped patterns, with steeply dipping HREE, relatively flat MREE and flat to slightly enriched LREE. Multiple orthopyroxenes from the same sample have similar concentrations of all REE, although a few samples have orthopyroxenes with increasingly diverging REE concentrations from the HREE through to the LREE (Fig. A2).

On a sample wide basis, orthopyroxenes have similar REE concentrations and patterns, irrespective of sample texture (Fig. 2.9). HREE concentrations overlap in a tight group, whilst LREE concentrations in average orthopyroxenes from different samples display an order of magnitude variation. The exception to this is 'residual' sample 67-02E(1) which is enriched in HREE and to a lesser extent MREE but with overlapping LREE, very similar to the unique whole rock REE pattern for this sample. On extended trace element plots, there is an obvious positive Ti anomaly for orthopyroxene from all samples, however this is due to Ti being more compatible in orthopyroxene than bulk mantle assemblages. Once Ti is assigned to its correct position according to hydrous orthopyroxene-melt partitioning experiments by McDade et al. (2003a) the positive anomaly is eradicated but replaced by slight negative Ti anomalies in a few samples (Fig. 2.9). Orthopyroxenes from some samples display strong positive Hf and Zr anomalies (Hf is also repositioned slightly in these plots, placing between Gd and Tb). Due to the lack of a complete dataset for these elements it is hard to establish whether there is any link between Hf, Zr and Ti anomalies, although it is doubtful that one exists. Orthopyroxenes from all harzburgite samples display very strong positive Nb anomalies, and concentrations of Nb do not correlate with any other measured trace element in orthopyroxene. Orthopyroxenes from the pyroxenites are similar in composition to those in the harzburgites with nearly identical normalised trace element arrays, but tend to be slightly more enriched for most elements, with LREE and Nb the exceptions (Nb anomalies are always less strongly positive).

	67-02A(1) Pyroxenite		67-02B(6) Pyroxenite		67-02A(2) Harzburgite		67-02B(1) Harzburgite		67-02D(1) Harzburgite	67-02D(4) Harzburgite		67-02E(1) Harzburgite		67-02D(7) Harzburgite	
		1 s.d. (2)		*1 s.d. (4)*	Residual	*1 s.d. (11)*	Residual	*1 s.d. (5)*	Residual	Residual	*1 s.d. (5)*	Residual	*1 s.d. (7)*	Reacted	*1 s.d. (5)*
P (ppm)			22.5	*1.92*	20.0	*1.87*	20.8	*1.93*	22.8	21.6	*2.12*	22.4	*1.84*	22.4	*2.32*
Sc (ppm)	64.1	*3.36*	56.5	*8.90*	54.5	*1.82*	60.5	*3.34*	62.9	63.7	*5.33*	93.9	*11.35*	106	*20.59*
Ti (ppm)	312	*9.5*	303	*171*	17.2	*3.63*	16	*2.97*	68	49.4	*10.8*	289	*59.6*	1504	*199*
V (ppm)	154	*2.91*	143	*63.6*	76.3	*7.19*	94.0	*10.9*	127	88.6	*16.8*	187	*38.0*	346	*43.9*
Cr (ppm)			4451	*954*	4212	*662*	4583	*250*	4604	4302	*693*	3917	*1567*	2709	*1518*
Ni (ppm)			353	*28.2*	319	*17.7*	348	*27.1*	340	310	*22.1*	349	*14.6*	352	*96.1*
Sr (ppm)			12.4	*5.49*	5.39	*1.01*	15.6	*5.25*	15.9	5.82	*1.64*	11.6	*1.54*	31.3	*0.83*
Y (ppb)	2019	*91.7*	2646	*1159*	315	*44.8*	456	*101*	1736	1066	*324*	2436	*493*	7679	*1236*
Zr (ppb)	1149	*33.6*	1539	*398*	321	*57.8*	1484	*310*	1489	728	*223*	1541	*439*	2199	*366*
Nb (ppb)	5.43	*0.86*	6.8	*1.0*	6.6	*1.6*	6.6	*0.7*	5.1	6.7	*1.5*	6.9	*2.8*	4.8	*2.4*
La (ppb)	57.7	*1.41*	116	*28.6*	47.9	*19.0*	159.6	*78.4*	167	28.7	*10.4*	94.7	*21.7*	196	*19.2*
Ce (ppb)	251	*9.03*	416	*106*	175.3	*66.1*	615.7	*314.2*	575	113	*45.6*	382	*88.5*	1010	*82.1*
Pr (ppb)	56.2	*0.72*	83.2	*24.3*	35.6	*13.9*	116.0	*55.2*	111	28.2	*11.8*	79.5	*16.4*	263.9	*28.3*
Nd (ppb)	381	*35.0*	509	*149*	200.0	*71.8*	599.0	*300.6*	725	186	*86.8*	528	*123*	1985	*267*
Sm (ppb)	177	*13.4*	204	*77.8*	66.3	*22.9*	165.7	*58.7*	268	98.0	*37.4*	244	*57.7*	914.0	*173*
Eu (ppb)	66.4	*0.9*	84.6	*23.4*	21.7	*6.4*	50.7	*19.8*	91.7	34.3	*11.2*	75.7	*17.3*	336.0	*52.7*
Gd (ppb)	291	*29.9*	357	*154*	66.4	*17.0*	141.9	*53.1*	339	141	*53.9*	342	*81.2*	1327	*202*
Tb (ppb)	47.4	*2.35*	64.3	*26.3*	8.9	*1.9*	17.0	*4.4*	51.9	25.1	*8.0*	60.3	*14.0*	224.4	*37.4*
Dy (ppb)	372	*14.4*	485	*236*	54.2	*10.4*	97.4	*37.4*	342	195	*63.4*	421	*85.7*	1558	*260*
Ho (ppb)	77.5	*8.62*	103	*49.5*	11.8	*2.0*	19.4	*5.9*	72.1	42.3	*11.4*	98.0	*20.5*	318	*51.9*
Er (ppb)	248	*30.5*	308	*138*	45.4	*8.4*	56.6	*19.2*	187	128	*33.4*	314	*61.9*	915	*154*
Tm (ppb)	31.6	*3.42*	43.9	*20.7*	8.7	*2.3*	10.8	*3.0*	30.1	19.9	*5.5*	46.6	*8.6*	116	*17.7*
Yb (ppb)	224	*5.66*	271.5	*136*	80.4	*11.5*	82.8	*16.3*	192	144	*34.6*	323	*61.9*	771	*136*
Lu (ppb)	31.5	*2.72*	38.6	*16.9*	15.5	*2.2*	15.8	*4.7*	27.8	22.4	*5.6*	50.4	*9.6*	102	*20.4*
Hf (ppb)	53.3	*6.54*	56.6	*22.3*	9.1	*1.9*	41.5	*25.1*	74.0	29.0	*10.9*	80.4	*25.4*	149	*26.4*

Table 2.6 Average clinopyroxene trace element compositions. Numbers in italics are 1 s.d. on multiple measurements from different crystals in the same sample (number of measurements in parentheses). Limit of detection and standard data as per Table 2.5.

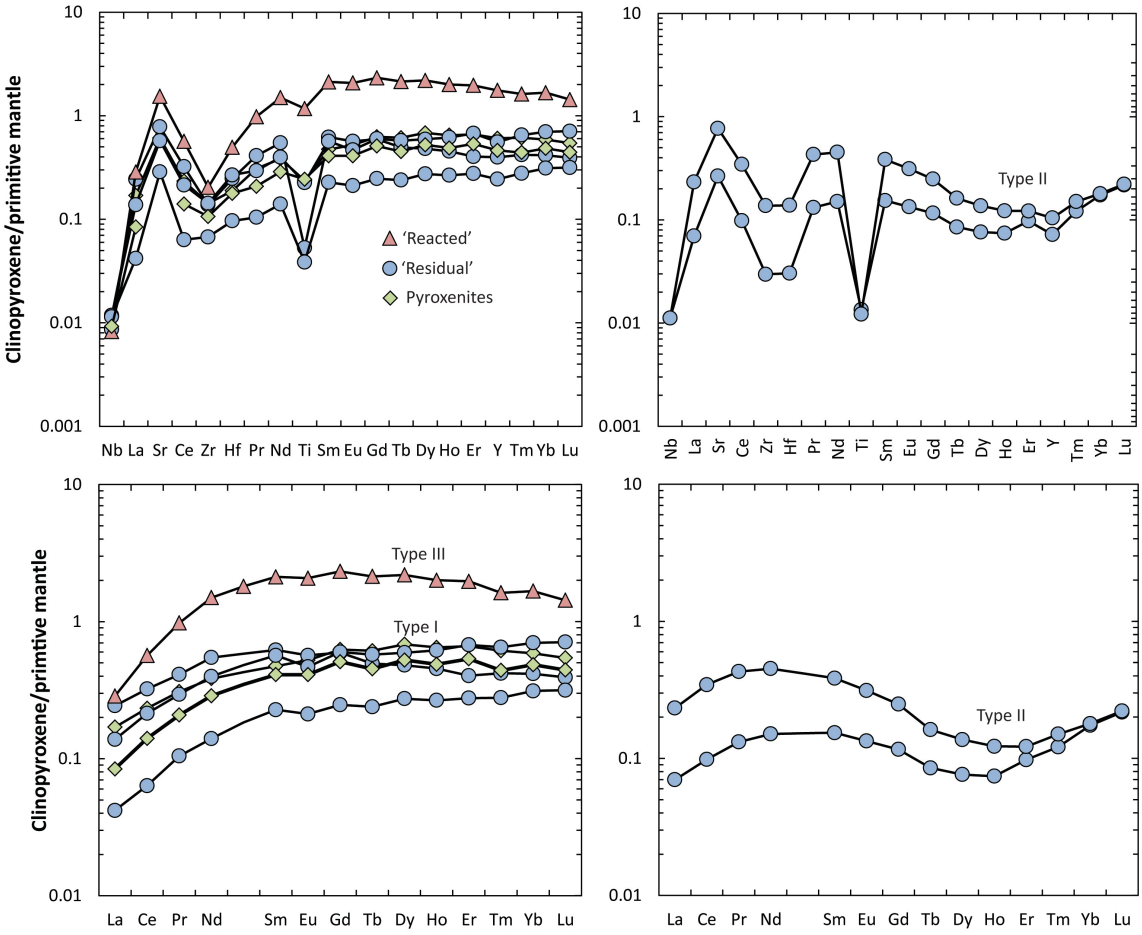

Fig. 2.10 Primitive mantle-normalised average clinopyroxene trace element compositions. Type II clinopyroxenes plotted on the right hand side figures for clarity. Normalisation values from Palme and O'Neill (2003)

2.4.5 Clinopyroxene trace elements

Due to the scarcity and fine-grained nature of clinopyroxene in these samples, analyses were restricted only to five 'residual' harzburgites, one 'reacted' harzburgite and the two pyroxenites, where grains could be clearly distinguished and appeared inclusion-free (Table 2.6). Clinopyroxene displays much greater diversity in trace element composition than orthopyroxene with three distinct primitive-mantle normalised REE patterns (Fig. 2.10,Fig. A3). Type I clinopyroxenes occur in three 'residual' harzburgites and the two pyroxenites. They display similar patterns with relatively flat HREE, gently downward-dipping LREE and La_N/Lu_N of 0.2-0.6. Two 'residual' harzburgites contain type II clinopyroxenes which display more complex sinusoidal patterns with general enrichment in LREE over HREE, peaks at Nd and Lu and a minimum at Ho. The anomalously low-Mg# type III veined clinopyroxenes from 'reacted' harzburgite 67-02D(7) are overall more enriched than any other clinopyroxenes measured, with normalised concentrations increasing from HREE through MREE before relatively steeply downward-dipping LREE. Variation between individual crystals within a sample is also apparent (Fig. A3). Type II clinopyroxenes display more variation in LREE concentration than HREE whereas the opposite is observed in type III clinopyroxenes. In pyroxenite sample 67-02B(6), type I clinopyroxenes from the clinopyroxenite layer are more enriched in MREE and HREE than clinopyroxenes from within the orthopyroxenite layer, but have the same overall shape. Type I clinopyroxenes from 67-02E(1) have distinct negative Eu anomalies, despite having similar overall REE patterns to other type I clinopyroxenes. On extended trace element plots additional diversity is observed. All clinopyroxene types display positive Sr anomalies and slightly to strongly negative Ti anomalies. Zirconium and Hf anomalies vary from strongly negative to absent whereas all clinopyroxenes have very strong negative Nb anomalies. Type II clinopyroxenes tend to have more extreme trace element anomalies compared to type I and type III clinopyroxenes, particularly the magnitude of the Ti anomaly with Ti/Eu ratios as low as 200.

	67-02B(2) Dunite *(10)*	67-02D(3) Dunite *(23)*	67-02A(2) Harzburgite Residual *(42)*	67-02B(1) Harzburgite Residual *(39)*	67-02D(1) Harzburgite Residual *(25)*	67-02D(4) Harzburgite Residual *(39)*	67-02E(1) Harzburgite Residual *(35)*	67-02A(3) Harzburgite Reacted *(23)*	67-02A(5) Harzburgite Reacted *(25)*	67-02B(5) Harzburgite Reacted *(35)*	67-02D(7) Harzburgite Reacted *(37)*	67-02E(3) Harzburgite Reacted *(20)*	L.O.D.
Na	0.75-6.18	<0.47	<0.31	<0.36 - 2.48	<0.36	<0.26	<0.28	1.44 - 22.80	<0.35 - 11.58	<0.28 - 9.61	<0.37 - 7.9	<0.17 - 2.20	0.35
Al	0.82-21	0.59 - 6.00	3.02 - 5.08	2.56 - 9.82	2.59 - 9.05	1.06 - 3.34	1.75 - 5.55	22.2 - 41.6	4.2 - 56.8	13.0 - 49.9	15.1 - 36.60	2.5 - 7.1	0.04
P	19-22	19 - 22	17 - 19	15 - 18	16 - 19	17 - 19	17 - 20	15 - 18	17 - 22	16 - 26	16 - 18	16 - 18	0.39
Ca	21-120	45- 131	41 - 90	32 - 96	39 - 140	33 - 88	26 - 104	77 - 793	29 - 166	46 - 599	22 - 302	28 - 95	1.9
Sc	3.06-4.14	3.50 - 4.29	3.26 - 3.80	3.06 - 3.40	2.90 - 3.57	3.15 - 3.50	3.26 - 3.82	3.13 - 5.30	2.77 - 3.62	3.63 - 6.57	2.83 - 4.30	2.58 - 3.15	0.004
Ti	1.89-2.93	2.28 - 4.16	0.99 - 1.28	0.88 - 1.62	1.19 - 2.01	1.28 - 2.36	2.40 - 4.04	0.75 - 5.74	1.07 - 2.96	1.21 - 10.5	1.54 - 5.55	0.80 - 1.47	0.02
V	0.02-0.34	0.08 - 0.54	0.28 - 0.42	0.27 - 0.58	0.31 - 1.02	0.23 - 0.42	0.35 - 0.63	1.82 - 3.19	0.32 - 2.43	0.39 - 3.83	0.54 - 3.00	0.31 - 0.42	0.002
Cr	5.9-13.1	3.84 - 13.8	4.0 - 10.4	4.4 - 28.6	5.5 - 18.6	4.92- 9.0	5.5 - 13.2	16 - 265	5 - 119	7 - 147	7.2 - 54.2	5.1 - 13.7	0.06
Mn	597-718	949 - 979	935 - 981	929 - 1013	975 - 1023	1022 - 1071	969 - 1028	955 - 1163	939 - 993	919 - 1289	910 - 1166	1035 - 1078	0.04
Co	89-115	126 - 135	135 - 143	140 - 148	138 -144	137 - 145	138 - 143	135 - 142	134 - 143	137 - 141	131 - 137	144 - 149	0.004
Ni	3121-3270	2740 - 2877	3079 - 3237	3166 - 3439	3112 - 3231	2835 - 2996	2971 - 3154	2792 - 3181	3013 - 3221	2753 - 3205	2875 - 3017	3069 - 3204	0.08
Y (ppb)	0.58-7.54	<0.12 - 2.10	<0.23 - 1.00	<0.26 - 3.7	<0.26 - 0.59	<0.23 - 0.82	<0.23 - 2.18	1.07 - 20.95	<0.27 - 13.69	<0.23 - 23.8	<0.25 - 20.7	<0.11 - 0.53	0.22

Table 2.7 Trace element composition of olivine (ppm). Data is displayed as maximum compositional diversity observed in each sample from many crystal measurements (number of crystals italicised and in parentheses). Representative limit of detection (L.O.D.) also reported.

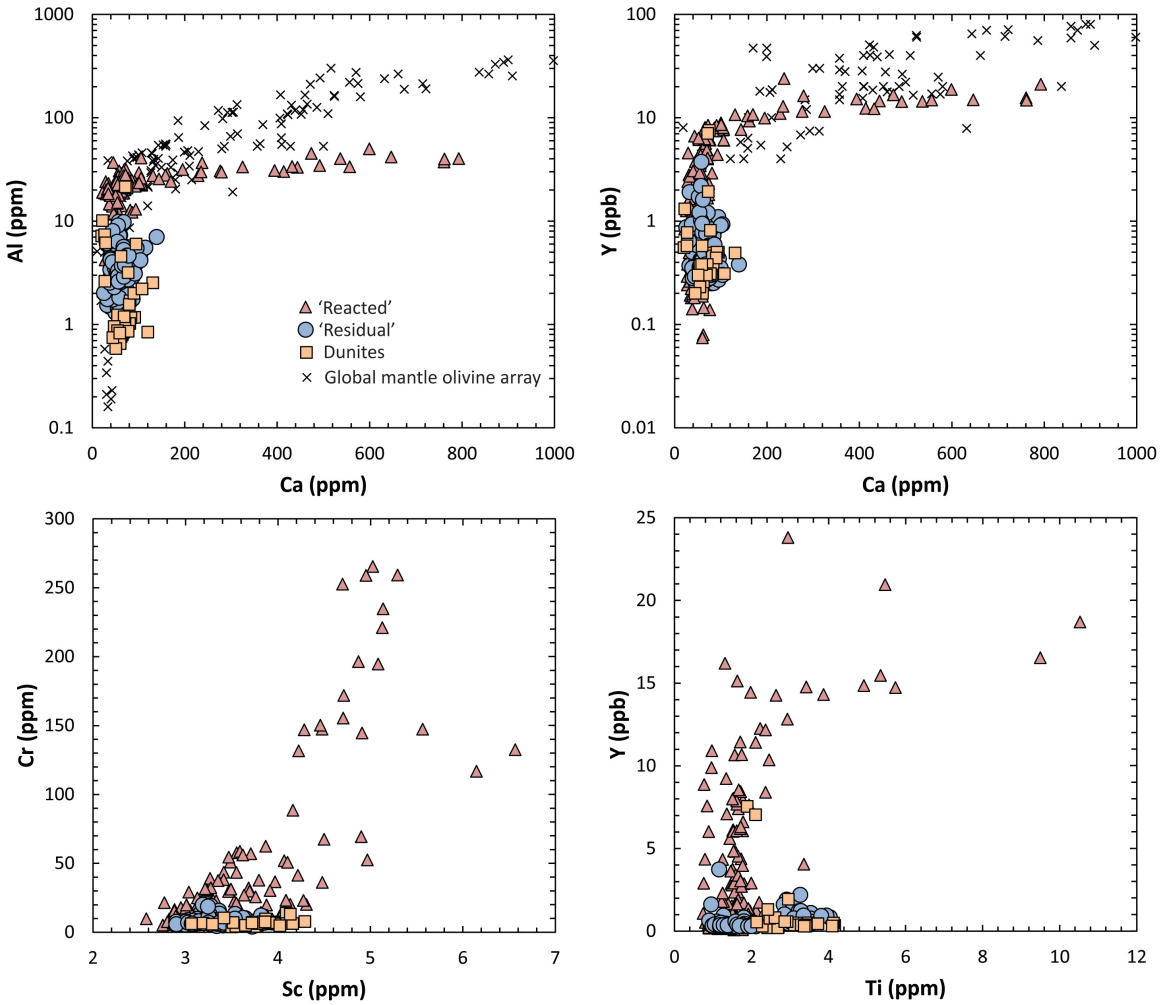

Fig. 2.11 Variation in the trace element chemistry of multiple olivines from different peridotite samples. The concentrations in the top two figures are compared with the global mantle olivine array, data from Grégoire et al. 2001, Neumann et al. 2004, Witt-Eickschen and O'Neill 2005, Zheng et al. 2005, Kaeser et al. 2006, Zheng et al. 2007, De Hoog et al. 2010, Batanova et al. 2011, Ionov 2010, Pirard et al. 2013, Smith 2013

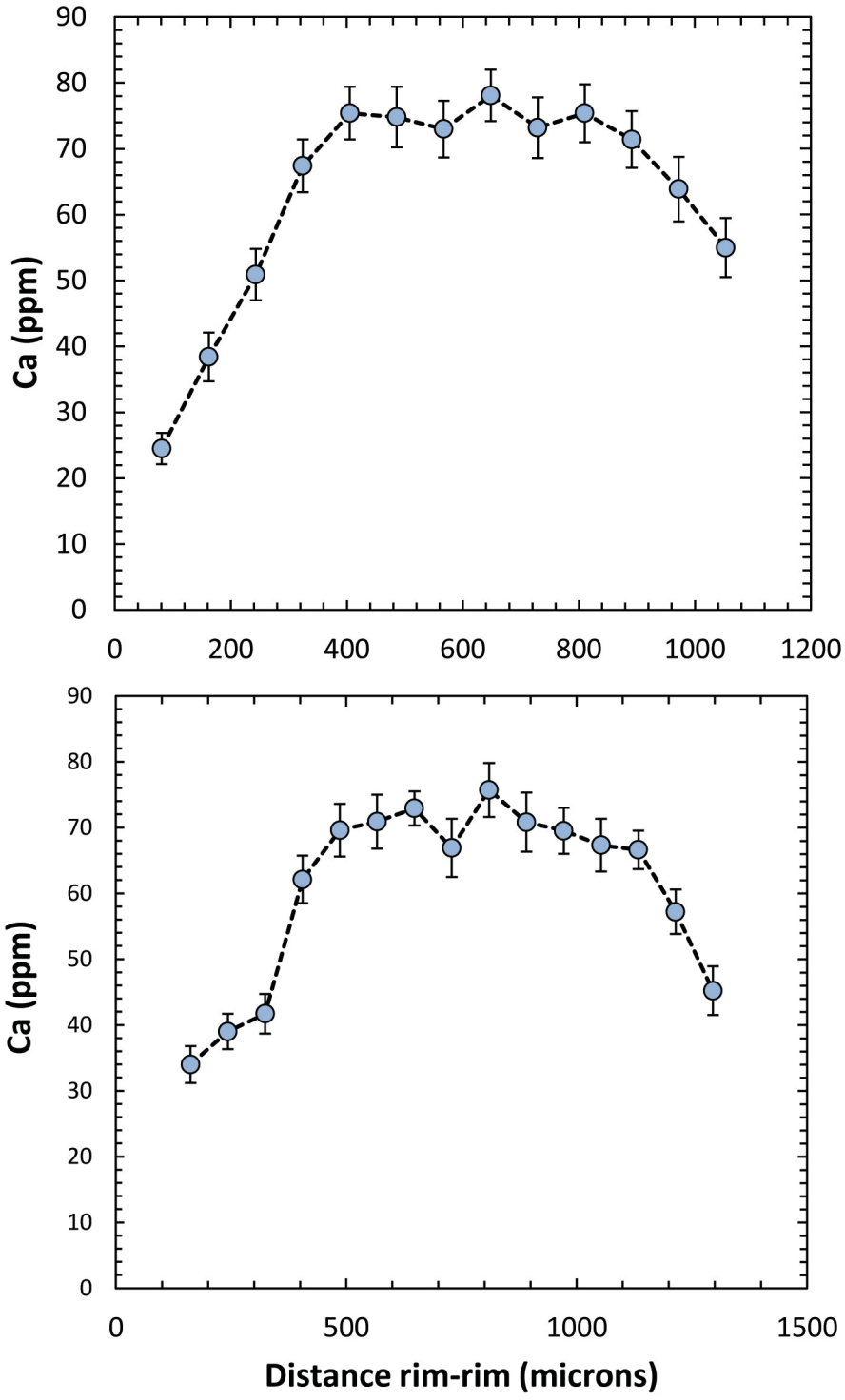

Fig. 2.12 Rim to rim zoning of Ca in olivines crystals from 'residual' samples 67-02D(4) (top) and 67-02E(1) (bottom). Error bars are 2 s.e.

2.4.6 Olivine trace elements

Trace element data is summarised in Table 2.7 and Fig. 2.11. All olivines from 'residual' harzburgite samples contain very low, concentrations of most elements (total concentration ranges in ppm; Na = <0.17–2.5, P = 14.63-20.30, Ca = 25.9-139.5, Sc = 2.578-3.820, Ti = 0.80-4.04, Mn = 929-1078, Co = 135.4-148.5, Ni = 2835-3439, Y (ppb) = <0.11-3.70). Concentrations of Al, Cr and V are particularly low (1.06-9.82 ppm, 3.99-28.60 ppm and 0.234-1.020 ppm respectively), however analyses would often produce significant spikes in these elements indicating partial ablation of the spinel exsolutions commonly observed during sample preparation (Fig. A4)**.** Sample 67-02E(1), which has higher concentrations of Ti in the whole rock, spinel, clinopyroxene and orthopyroxene also has higher concentrations in olivine, indicating all four phases are in equilibrium. There is no correlation between different trace elements in olivines, either within any given sample or on a sample-wide scale. One exception is the olivines from the dunite which show correlation between Ca and Ti, but otherwise contain similar trace element concentrations to the olivines from 'residual' harzburgites. Rim-rim traverses show no concentration gradients for the majority of elements in olivine from 'residual' samples (Fig. A4). The only notable exception is Ca which often shows distinct zoning, with lower concentrations at the rims (Fig. 2.12).

Olivines from 'reacted' harzburgite samples contain significant ranges in trace element concentrations (total concentration ranges in ppm; Na = <0.35-22.80, Al = 4.17-56.80, P = 15.45-21.90, Ca = 22.3-793.0, Sc = 2.774-6.568, Ti = 0.75-10.53, V = 0.316-3.829, Cr = 3.84-265.20, Mn = 910-1289, Co = 126.6-142.7, Ni = 2740-3221, Y (ppb) = <0.25-23.80). These variations occur both on a sample-wide scale and between olivines in individual samples, indicating a high degree of trace element disequilibrium. The concentrations overlap with, but significantly diverge from the narrow compositional space defined by olivines from 'residual' samples (Fig. 2.11)**,** with over an order of magnitude increase in some elements. Elements which show no clear distinction between olivines from the two sample groups are P and Co. There is a relationship between the apparent textural degree of reaction and the chemical enrichments. For example, olivines from sample 67-02D(7), which shows no evidence for physical reaction with a melt, only show relatively small enrichments in Na, Al, Sc, V, Cr and Y, whilst olivines from the most

texturally reacted sample, 67-02A(3), show substantial compositional variation in all elements except P. The olivine compositions from this particular sample encompass almost the entire range defined by the whole sample suite. Despite the strong correlations present when olivines from all 'reacted' samples are considered together, the relationship between particular elements is often quite complex. Plots of Y or Na against Ti or Ca define non-linear patterns, with concentrations of Y and Na increasing sharply initially at relatively constant Ti or Ca, before Ti and Ca begin to increase more substantially (Fig. 2.11).

Olivines from the two dunite samples are very similar in composition to olivines from 'residual' harzburgites, with generally very low concentrations of all incompatible trace elements. In particular, olivines from 67-02B(2) are exceptionally depleted in V containing as little as 0.03 ppm. There is no difference in the trace element composition of fine-grained olivine from the dunite vein compared to coarse dunitic olivine in sample 67-02D(3).

2.5 Discussion

2.5.1 Conditions and environment of melting

Previous studies of fore-arc peridotite xenoliths and exhumed sections of fore-arc mantle have reached various conclusions concerning melting histories, ranging from melting occurring entirely in an anhydrous, spreading centre setting followed by modification by arc melts/fluids (Parkinson and Pearce 1998; Pearce et al. 2000; McInnes et al. 2001; Jean et al. 2010; Batanova et al. 2011) to melting occurring in a hydrous, mantle wedge environment, preceded by varying degrees of melt-generation at an oceanic or back-arc spreading centre (Bizimis et al. 2000; Franz et al. 2002; Ishimaru et al. 2007; Ionov 2010; Pirard et al. 2013). In a number of cases, the complex post-melting metasomatism and ambiguous nature of the chemical systems with potential to distinguish tectonic setting prevent a clear discrimination between plausible melting scenarios (Parkinson and Arculus 2003; Vannucci et al. 2007). Nevertheless, it is clear that global occurrences of 'arc mantle' do not share common petrogenetic histories and may represent several stages of melting in a variety of different environments. This is in contrast to abyssal peridotites, which are generally regarded as the product of a single, polybaric, near-

fractional melting event (Johnson 1990; Hellebrand et al. 2002; Brunelli et al. 2006; Seyler et al. 2011).

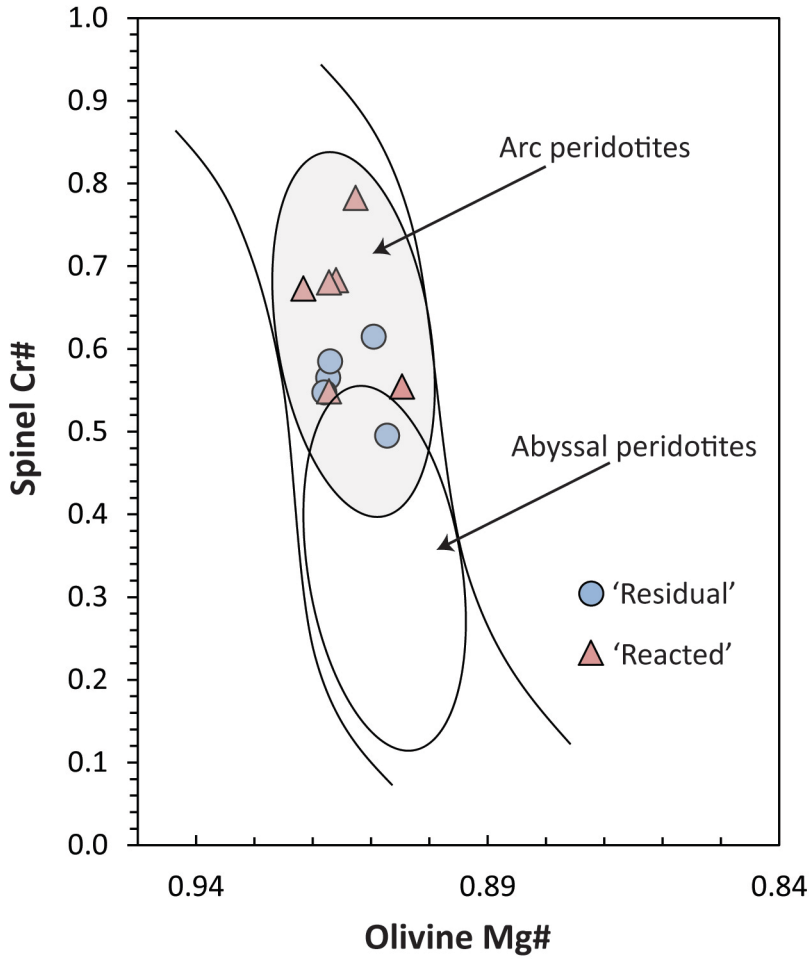

Fig. 2.13 Olivine and spinel compositions from 'residual' and 'reacted' compared to the olivine-spinel-mantle-array (OSMA) of Arai 1994

Studies of mafic and intermediate magmas erupted along the West Bismarck and New Britain (East Bismarck) Island Arcs have identified complex petrogenetic histories involving melting as part of the present-day arc systems but also evidence for a previous episode of subduction unrelated to the active arcs (Woodhead et al. 1998, Woodhead et al. 2010, Cunningham et al. 2012). Whilst the very low equilibration temperatures of the 'residual' Ritter peridotites preclude them from having experienced melting as part of the active arc, they may still preserve a memory of previous melting environments and at a resolution not possible to attain with studies of magmas erupted from the extant arc. The most simple and commonly used approach in addressing this is to compare the olivine and spinel major element compositions to the olivine-spinel mantle array (OSMA) of Arai et al. (1994) which can distinguish between peridotites formed through partial melting in a variety of environments. Ritter peridotites plot well within the arc peridotite field, although there is a degree of overlap between the most depleted (highest spinel Cr# and olivine Mg#) end of the abyssal peridotite field and the least depleted end of the arc peridotite field (Fig. 2.13). However, it is not strictly appropriate to use this as a discriminatory method for Ritter samples because the assumption that the olivine and, in particular, spinel chemistry is a product of partial melting is not satisfied. This is apparent from strong positive correlations between spinel Cr# and equilibration temperature, Fe_2O_3 in spinel, concentrations of whole-rock highly incompatible elements such as LREE, Th and Sr and the occurrence of 'reacted' textures (Fig. 2.4, Fig. 2.20). These correlations indicate that spinel Cr# has been reset to elevated values during melt-rock reaction and is thus not a primary feature in the majority of samples. Taking just 'residual' samples, which have not experienced melt-rock reaction, olivine-spinel compositions plot from the region of overlap between the arc and abyssal fields to just inside the arc-only field (Fig. 2.13). This, whilst supporting an arc origin, is not particularly conclusive.

Because of this susceptibility of spinel Cr# to secondary processes, we searched for an alternative chemical distinction. Whilst experimental studies of melting reactions and trace element partitioning in hydrous systems are relatively scarce, the limited studies so far conducted have shown some important differences from the anhydrous equivalents. Firstly, the proportion of clinopyroxene entering the melt is lower under hydrous conditions (Gaetani and Grove 1998) and secondly, the compatibility of trace

elements in clinopyroxene is lower under hydrous conditions (McDade et al. 2003). The combined effects of this is that at the point of clinopyroxene exhaustion during melting under hydrous conditions, assuming the same starting composition and closed-system fractional melting, whole rock and mineral compositions will be more depleted in incompatible trace elements then is the case for anhydrous melting. This distinction has previously been noted and used by Bizimis et al. (2000) and Jean et al. (2010) to demonstrate an origin of various ophiolites through hydrous, arc melting. We adopt a similar approach to these previous studies, however instead of utilising clinopyroxene compositions we use orthopyroxene. This is because the distribution of clinopyroxene in veins and at crystal triple junctions, and the occurrence of sinusoidal clinopyroxene REE patterns indicates that clinopyroxene is either secondary or has been metasomatically overprinted. The predominance of secondary (including exsolved) clinopyroxene over primary clinopyroxene is common in depleted peridotite samples, and therefore comparison between the compositions of orthopyroxene, which is almost universally found as a residual phase, is more appropriate. In addition to this, there is now a substantial amount of data for orthopyroxene trace element compositions from abyssal peridotites with which to compare data from arc peridotites (Hellebrand et al. 2005, Warren et al. 2009, Brunelli and Seyler 2010, Seyler et al. 2011). In order to determine peridotite melting histories it must be clearly demonstrated that the chosen melting proxy has remained undisturbed during post-melting modification by metasomatic fluids. In the Ritter samples, the very low concentrations and homogeneous distribution of mildly incompatible trace elements (HREE, Y, Sc, Ti, V etc.) in orthopyroxene cores from both the same sample and from texturally distinct samples, and the primary, equilibrated textures of the crystals analysed is strong evidence that these elements in orthopyroxene were unaffected by metasomatism and can thus be used to unravel melting histories. Our models are simple, isobaric fractional melting. In order to make the comparisons between hydrous and anhydrous melting as meaningful as possible we use partition coefficients for clinopyroxene and orthopyroxene from the same researchers/laboratories; McDade et al. (2003b) and McDade et al. (2003a) for anhydrous and hydrous values at 1.5 and 1.3 GPa and 1315 and 1245 °C respectively. Olivine partition coefficients are from Mallmann and O'Neill (2013) and are anhydrous only, although olivine D values and concentrations are so low they make very little difference to the model outcome. Our anhydrous melting

reaction is from Baker and Stolper (1994) and our hydrous melting reaction from Gaetani and Grove (1998). Our melting model utilises equation (32) from Zou (1998), which is for non-modal 'dynamic' melting (essentially fractional melting with an added porosity term to allow modelling of the effect of a small proportion of trapped melt). This equation allows calculation of the concentration of a trace element in the residue for a given degree of partial melting. From this we then calculated the concentration of the element in residual orthopyroxene using the following equation:

$$C_i^{opx} = \frac{D_i^{opx/melt}}{D_i^{bulk/melt}} C_i^{res}$$

where C_i^x is the concentration of element i in orthopyroxene or the whole rock residue and D_i^x is the partition coefficient of element i between melt and either orthopyroxene or the bulk solid. The latter is calculated from equations (A1) and (A3) from Johnson et al. (1990). For comparison between hydrous and anhydrous melting models we chose the elements Y and Yb since they are both relatively easily measured in orthopyroxene whilst displaying slightly different compatibilities (Y is chemically analogous to Ho but is easier to measure since it is present at higher concentrations). Fig. 2.14 shows the results of the models. The data for abyssal peridotites are reproduced well by the anhydrous melting model up to the point of clinopyroxene exhaustion and whilst the melting model employed here is a simplification of the actual melting process at spreading centres, it clearly shows that the exhaustion of clinopyroxene is a limiting factor to melt productivity. The data for orthopyroxene from Ritter peridotites is considerably more depleted than any of the abyssal samples or the anhydrous melting model, requiring the melting regime to be hydrous. In fact, even though the hydrous melting model predicts substantially more depleted orthopyroxene compositions, the majority of Ritter samples are more depleted still. To model these more depleted compositions, we employed the hydrous harzburgite melting reaction from Parman and Grove (2004). An additional 4 % of harzburgite melting is required to fully encompass all Ritter compositions meaning the total range of hydrous melting predicted by our models is ~26-33 %.

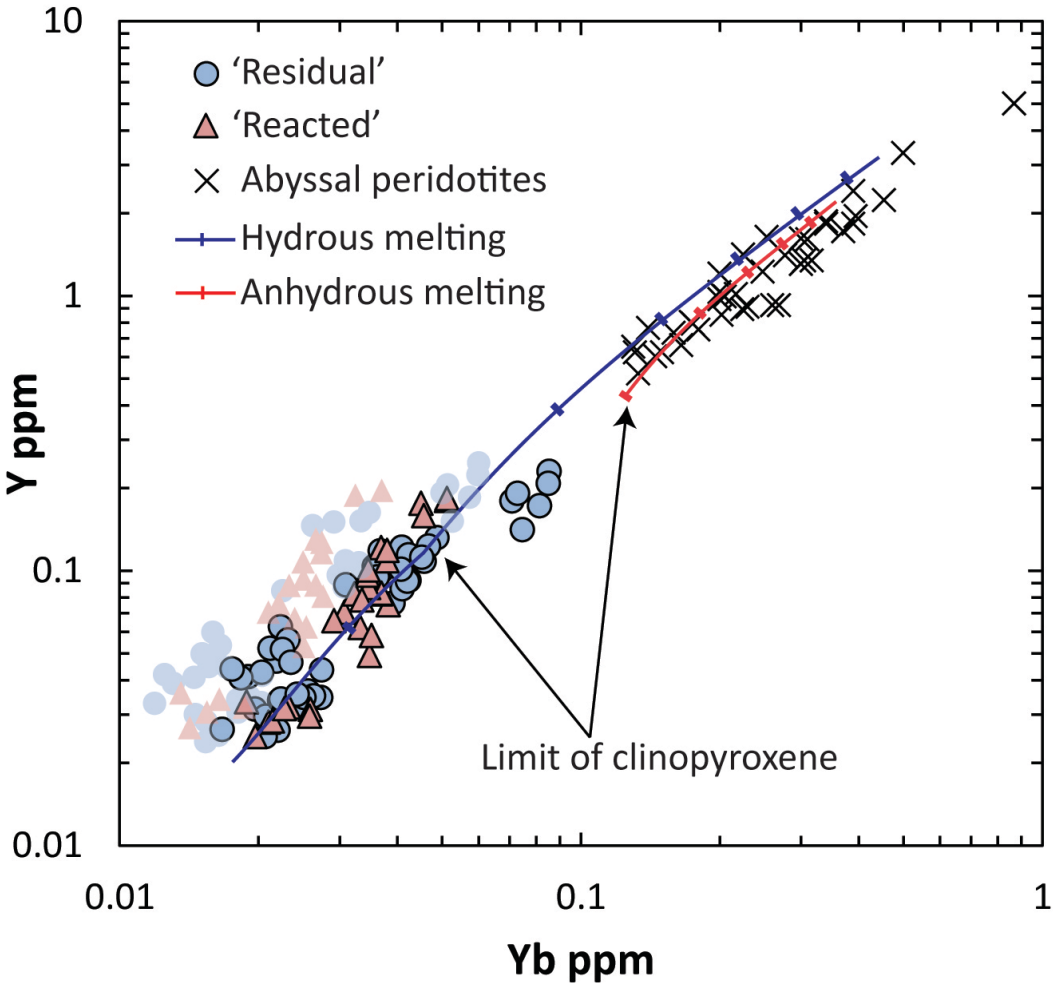

Fig. 2.14 Results of isothermal, isobaric fractional melting models under hydrous and anhydrous conditions for Y and Yb in residual orthopyroxene. Each data point represents a single crystal analysis (instead of sample averages). Pale coloured data points reflect a correction for trace element exchange during sub-solidus cooling between pyroxenes and olivine. The highly depleted trace element concentrations of orthopyroxene require a hydrous melting scenario. Sub-solidus cooling has little effect on concentrations of Y and Yb in orthopyroxene. See text for full details. Abyssal peridotite data is from Hellebrand et al. (2005), Warren et al. (2009), Brunelli and Seyler (2010) and Seyler et al. (2011).

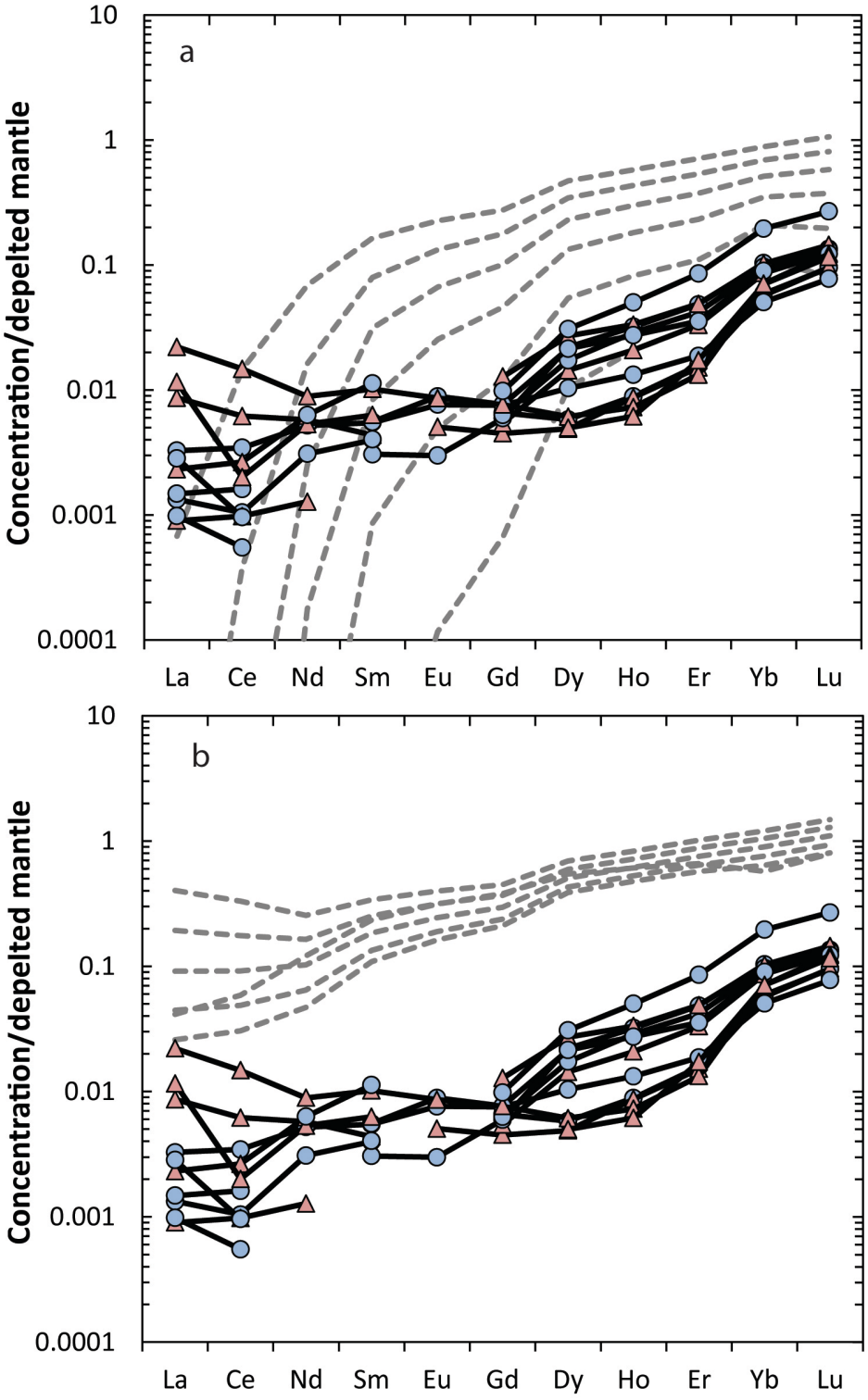

Fig. 2.15 Hydrous partial melting models for a representative suite of REE in orthopyroxene with different amounts of residual porosity. Dashed lines from top to bottom represent residual orthopyroxene after 5, 10, 15, 20, 25 and 30 % melting. a) 0 % residual porosity (perfect melt extraction); b) 5 % residual porosity (incomplete melt extraction). Residual porosity alone cannot explain the enrichment in LREE and requires an external fluid flux

Fig. 2.15 shows the results of modelling for the entire suite of REE in orthopyroxene. The hydrous partition coefficients from McDade et al. (2003a) do not include a number of important REE (Gd, Dy, Ho) so in order to model a more representative REE suite we fitted their published REE data to the lattice strain model of Blundy and Wood (1994). By performing a non-linear least squares regression, we were able to solve simultaneously for lattice site radius, Young's modulus and the strain-free partition coefficient. These values were then entered into the lattice strain model equation to produce partition coefficients for Gd, Dy and Ho. The models clearly show that the REE from Lu through to Dy are consistent with patterns predicted from our hydrous fractional melting model. Concentrations of Gd through to La however are significantly higher than our model predicts, either as a result of some trapped melt partially equilibrating with the solid residue (imperfect fractional melting) or reaction with a LREE-enriched metasomatic fluid. To test the former of these ideas, we introduced critical mass porosity values (ϕ) to the dynamic melting equation of Zou (1998) which simulates imperfect melt extraction. We found no value of ϕ could reproduce both HREE and LREE concentrations. For example, a value of 5 % reproduces well the overall shape of the REE yet at this value both HREE and LREE are approximately an order of magnitude too enriched (Fig. 2.15b). A plausible option is that the elevated concentrations of LREE are due to LREE-rich fluids present during the hydrous melting process. However without precise constraints on the composition and amount of the slab-derived fluid, which would quickly become diluted with basaltic melt as melting proceeds, we do not quantitatively model this. Therefore, we conclude that the elevated values of LREE are more consistent with addition of an externally-derived, LREE-rich fluid, either during melting or subsequent metasomatism, rather than simple imperfect melt extraction.

The combined results of both the hydrous/anhydrous Y-Yb orthopyroxene melting models and the hydrous orthopyroxene REE melting models show that the Ritter samples formed in a subduction zone environment as a result of fluid-flux melting. It is possible that both the HREE and LREE concentrations are consistent with melting in the presence of LREE-rich slab-derived fluid material, negating the need for a later discrete stage of metasomatism although we cannot presently rule this out.

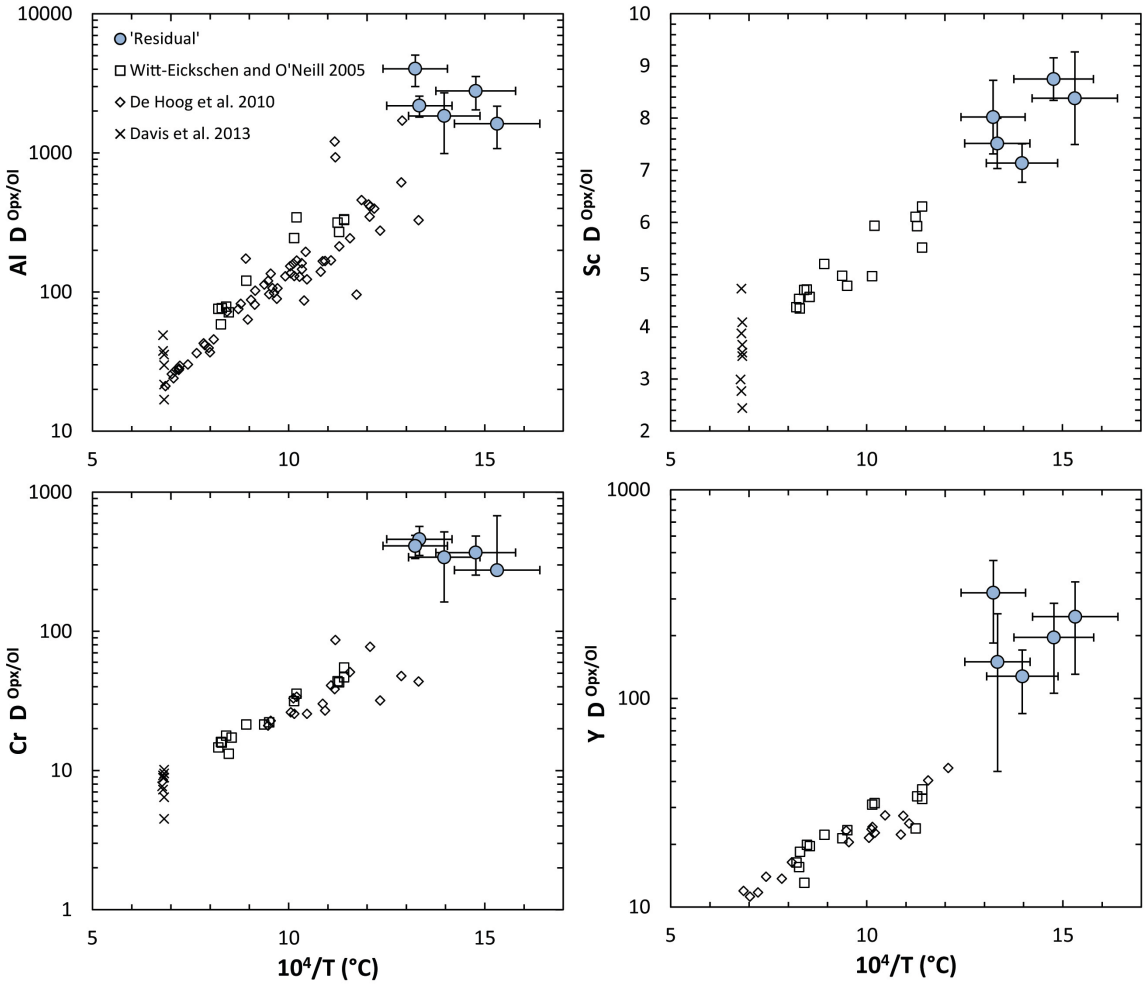

Fig. 2.16 Trace element exchange between orthopyroxene and olivine plotted against temperature calculated from olivine-spinel Fe-Mg exchange (O'Neill and Wall 1987) and compared to global data for well equilibrated peridotites and experiments

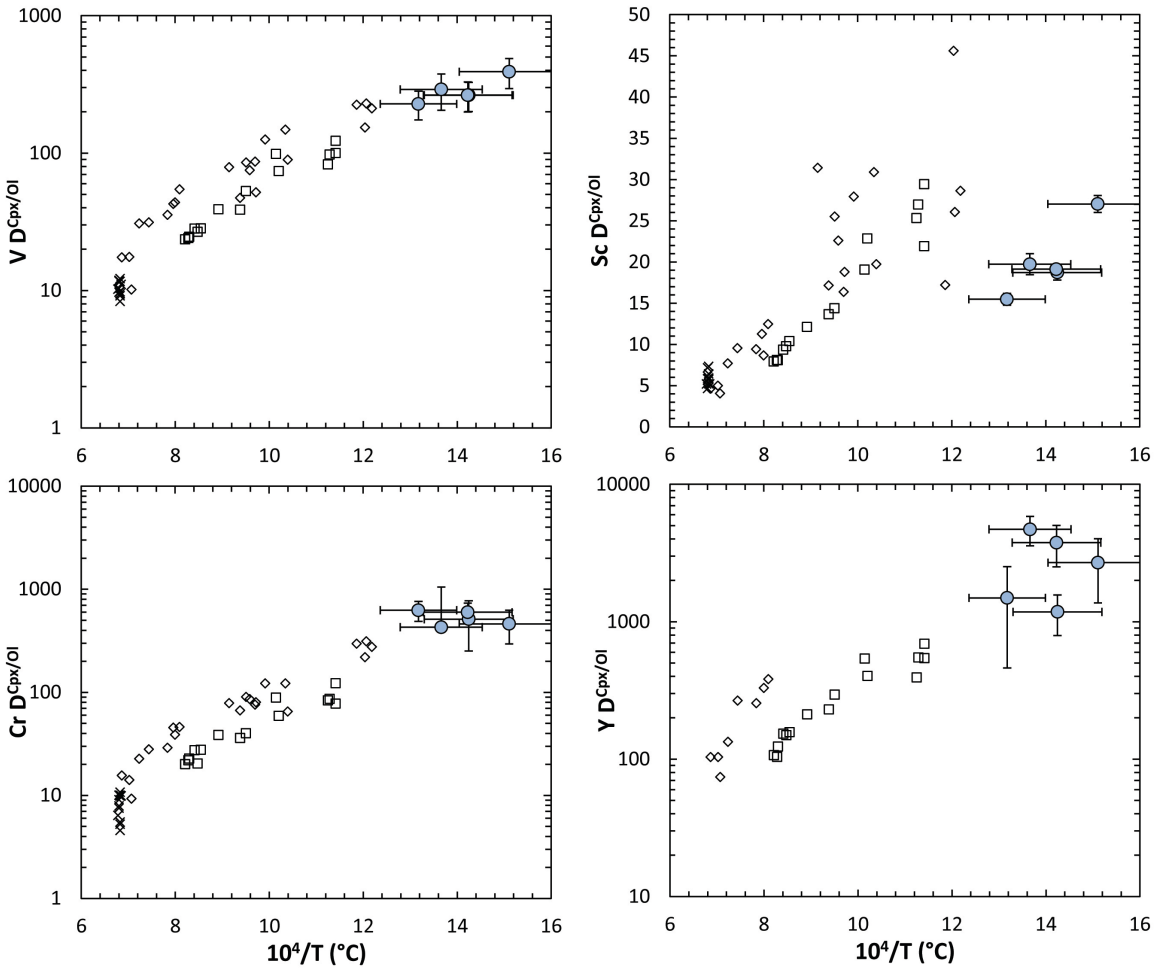

Fig. 2.17 Trace element exchange between clinopyroxene and olivine plotted against temperature calculated from olivine-spinel Fe-Mg exchange (O'Neill and Wall 1987) and compared to global data for well equilibrated peridotites and experiments

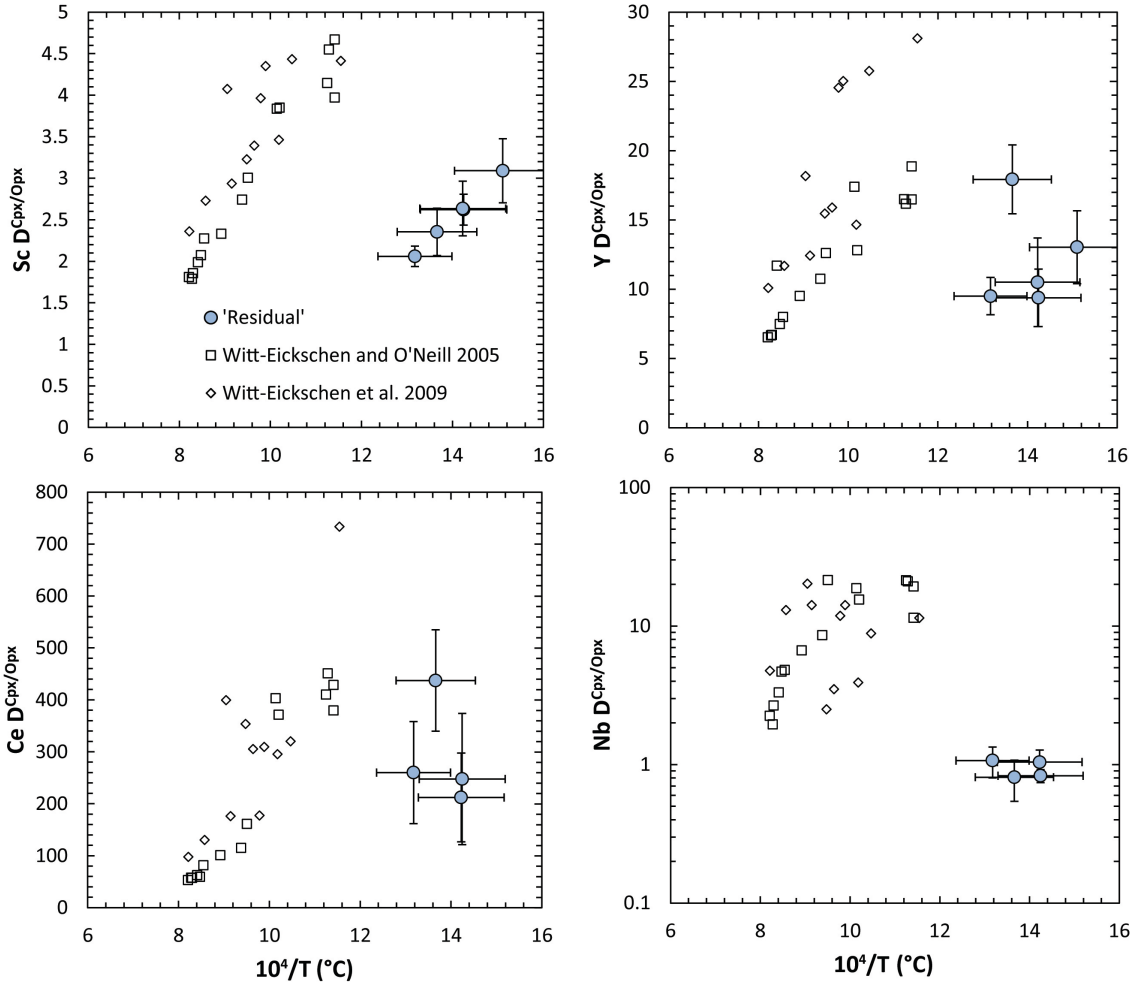

Fig. 2.18 Trace element exchange between clinopyroxene and orthopyroxene plotted against temperature calculated from olivine-spinel Fe-Mg exchange (O'Neill and Wall 1987) and compared to global data for well equilibrated peridotites and experiments

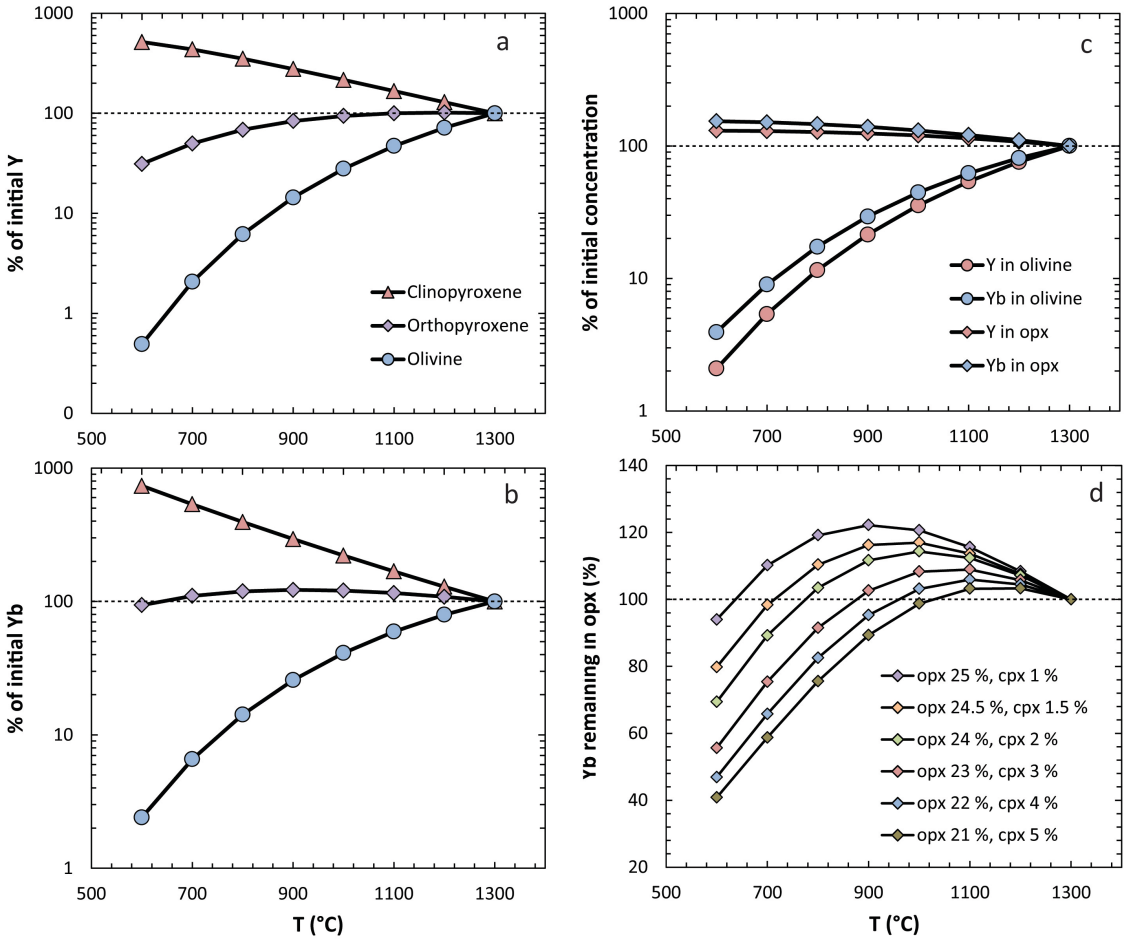

Fig. 2.19 Models calculating how the concentrations of Y and Yb in clinopyroxene, orthopyroxene and olivine would change during sub-solidus cooling. (a) and (b) are cooling with a fixed, harzburgitic mineral composition representative of the Ritter peridotites. (c) shows cooling in clinopyroxene-free harzburgite. (d) shows the effect of varying the modal proportions of orthopyroxene and clinopyroxene in a harzburgitic system on the concentration of Yb in orthopyroxene. See text for an explanation of the model

2.5.2 Sub-solidus cooling

A number of studies have shown that the partitioning of many petrologically important trace elements between olivine, orthopyroxene and clinopyroxene is a sensitive function of temperature (Witt-Eickschen and O'Neill 2005, Lee et al. 2007, Liang et al. 2013). This property of trace elements means that they have great potential as thermometers for peridotites which have cooled below their solidi, but also means that measured mineral trace element compositions no longer simply reflect the partial melting process. To investigate the effect sub-solidus cooling has had on the trace element compositions of mineral phases in the Ritter peridotites, we plotted values of $D^{opx/olivine}$, $D^{cpx/olivine}$ and $D^{cpx/opx}$ for 'residual' peridotites against temperature for a selection of temperature-sensitive trace elements, along with literature data for peridotites and experiments over a range of temperatures and compositions. Our choice of thermometer was the olivine-spinel exchange thermometer of O'Neill and Wall (1987), since the lower temperatures calculated using this calibration compared to the two pyroxene method of Brey and Köhler (1990) mean it records a more complete thermal history, implying more rapid component diffusion between olivine and spinel (lower closure temperature). Partition coefficients between olivine and both orthopyroxene and clinopyroxene are generally in good agreement with the global peridotite array (Fig. 2.16 and Fig. 2.17), with the exception of Sc partitioning between olivine and clinopyroxene, which implies that chemical equilibrium has been approximately achieved at the closure temperatures of Fe-Mg exchange between olivine and spinel. In contrast, partition coefficients between orthopyroxene and clinopyroxene are clearly not in equilibrium at the calculated temperatures, instead plotting at D values consistent with much higher temperatures of equilibration (Fig. 2.18). Applying a range of trace element exchange thermometers from Witt-Eickschen and O'Neill (2005) confirms this, with apparent temperatures ranging from 1264-1351 °C for Nb exchange down to 736-822 °C for Zr exchange. HREE and Sc exchange reveal intermediate temperatures of 887-1124 °C. Whilst temperatures calculated from MREE and LREE exchange appear broadly similar to other trace element exchange temperatures, the sinusoidal clinopyroxene patterns present in some samples preclude these being in equilibrium with orthopyroxene. It is also possible that other trace elements are not in equilibrium, however a number of trace elements show

partitioning behaviour which correlates with temperatures calculated from Fe-Mg exchange, particularly Sc (Fig. 2.18) and P (not shown). For other trace elements correlation may be obscured by analytical uncertainty. This demonstrates that at least for some elements, clinopyroxene and orthopyroxene have achieved chemical equilibrium, just at much higher closure temperatures than for element exchange with olivine and spinel. It is intriguing therefore that olivine-clinopyroxene and olivine-orthopyroxene show partitioning behaviour consistent with much lower temperatures. This appears to be a clear example of "minor's rule" (Liang 2014), whereby the time required for diffusive equilibration is dictated by the mineral which contains the lowest concentration of a particular element. In a peridotite, particularly highly depleted peridotites, olivine contains substantially lower concentrations of most incompatible trace elements than the combination of orthopyroxene and clinopyroxene, despite its greater modal abundance. Hence a much smaller element flux is required to shift the bulk composition of olivine relative to the pyroxenes. In combination with generally much more rapid element diffusion in olivine, this has facilitated equilibration to much lower temperatures.

In order to establish how the concentration of elements in olivine, orthopyroxene and clinopyroxene may have changed during the cooling process and hence whether our partial melting models of orthopyroxene composition remain valid, we constructed models for how Y and Yb concentrations in olivine, orthopyroxene and clinopyroxene would change down-temperature for the 'residual' peridotites. The basis for these models is the temperature dependency of Y and Yb partitioning which has been investigated through measurements of natural samples and theoretical treatments of experimental data (Witt-Eickschen and O'Neill 2005, Lee et al. 2007, Liang et al. 2013). For our models, we inverted and combined the orthopyroxene-melt, clinopyroxene-melt and olivine-melt Y and Yb thermometers of Liang et al. (2013) and Sun and Liang (2013) to calculate values of $D^{opx/olivine}$, $D^{cpx/olivine}$ and $D^{cpx/opx}$ over the temperature range 1300-600 °C. These thermometers are based on the lattice strain model of Blundy and Wood (1994) and require values for the lattice site radius, Young's modulus and the strain-free partition coefficient, which were calculated from average orthopyroxene and clinopyroxene major element compositions for each sample. Since pyroxene chemistry is broadly similar from sample to sample this made little difference to the model. We took a representative

harzburgitic composition for the sample suite, with modal abundances of 74 % olivine, 25 % orthopyroxene and 1 % clinopyroxene. Our model represents a 'worst case' scenario, since:

1) Clinopyroxene is clearly secondary in nature due to the presence of clinopyroxene veins and sinusoidal REE patterns. Hence it probably wasn't present under the highest temperature partial melting conditions

2) The modal proportion of clinopyroxene typically increases during cooling due to the decreasing solubility of clinopyroxene in orthopyroxene (Walter 1999). Therefore, the modal proportion observed under these low temperature equilibration conditions represents a maximum and as discussed below, the greater the proportion of clinopyroxene the more significant the impact on the composition of other phases present.

To calculate the composition of each phase at a given temperature we found a solution where all three D values matched the theoretical values for that temperature. There is no unique solution for the concentration of each phase in this methodology since whole rock concentration was not fixed in the calculation so at each stage we normalised the whole-rock composition to the initial value. This produced concentrations in each phase which satisfied both criteria of appropriate inter-mineral partitioning and whole-rock composition. The results of this exercise are shown in Fig 2.19. As anticipated, the composition of olivine is highly sensitive to temperature, retaining only 2.5 % and 0.5 % of the initial concentrations of Yb and Y respectively by 600 °C. Even at 700 °C only 2 % and 7 % of these elements remain. The important implications here are the confirmation that olivine trace element chemistry is a useful monitor of equilibration temperature (De Hoog et al. 2010), and also that at near-solidus conditions olivine can store a significant inventory of the total trace element budget (nearly 10 % of Yb at 1300 °C), not apparent from simply measuring olivine in its final equilibration state. Studies that utilise the chemistry of olivine in slowly cooled systems to infer changes in melt composition, for example in mantle-crustal layers of ophiolites, must take into account this cooling effect. Trends observed between olivines in, for example, peridotite, dunite and gabbroic layers may simply be related to differences in mineralogical environment during cooling. In

contrast to olivine, clinopyroxene becomes strongly enriched during the cooling process, gaining an additional 170-190 % of both Yb and Y by 900 °C. If kinetics permitted, by 600 °C clinopyroxene would have gained approximately 400-600 % of these elements. Orthopyroxene displays more complex behaviour. At high temperatures it becomes slightly more enriched before becoming depleted at lower temperatures. This switch from enrichment to depletion is due to the relationship between $D^{cpx/opx}$, $D^{opx/ol}$ and $D^{cpx/ol}$ changes with temperature and occurs at lower temperatures for less incompatible elements. The switchover also occurs at higher temperature at higher modal proportions of clinopyroxene, or more specifically lower orthopyroxene/clinopyroxene ratios (Fig. 2.19). By the lowest clinopyroxene/orthopyroxene closure temperatures of ~800 °C and ~900 °C for Y and Yb, in our models orthopyroxene has lost ~30 % Y and gained ~20 % Yb. With decreasing orthopyroxene/clinopyroxene ratios, the concentrations in residual orthopyroxene decrease more strongly with temperature. Following this exercise, we applied corrections to the measured orthopyroxene trace element data based on sub-solidus cooling to the Y and Yb clinopyroxene/orthopyroxene closure temperature of each sample followed by modelling cooling between just orthopyroxene and olivine down to 600 °C. The result moves the data slightly further away from the melting model vector, but has no major impact on our interpretations (Fig. 2.14), and thus demonstrates that in this case orthopyroxene is a reliable recorder of partial melting.

2.5.3 Silicate and carbonatite metasomatism

'Residual' Ritter peridotites retain both cryptic and modal evidence for metasomatism. The most obvious evidence are the occurrences of clinopyroxene veins (Fig. 2.2b), most notably in sample 67-02E(1). As noted previously, these veins have relatively well equilibrated grain boundaries with the surrounding peridotite which implies they are an older feature relative to the more recent melt-rock reaction episode. The trace element chemistry of clinopyroxenes in these veins (type I clinopyroxenes) appears very similar to randomly distributed clinopyroxenes from several other 'residual' peridotites, indicating that they share a similar metasomatic origin (Fig. 2.10). Type I patterns contain features which are typical of subduction-related fluids, such as positive Sr anomalies and negative Nb, Hf, Zr and Ti anomalies (Hawkesworth et al. 1993, Elliott et al. 1997). We therefore propose that this episode of fluid metasomatism occurred shortly after or synchronous

with the hydrous melting event, whilst the subduction system was still active. Given the flat and relatively enriched MREE to HREE, slightly depleted LREE and occurrence of negative Ti anomalies, the most likely agent is a slab-contaminated silicate mantle melt derived from super-solidus portions of the depleted mantle wedge. A similar fluid was probably responsible for the 'fossil' dunite and pyroxenite melt-rock reaction channels also preserved in the Ritter sample suite and described later. For example, the trace element composition and patterns of clinopyroxene from the pyroxenites are very similar to these harzburgitic clinopyroxenes (Fig. 2.10).

Type II clinopyroxenes display sinusoidal REE patterns which are clearly secondary in origin (Fig. 2.10). Identical sinusoidal REE patterns are commonly observed in low Ca garnets from cratonic mantle xenoliths (Stachel et al. 1998, Stachel et al. 2004, Simon et al. 2007, Klein-BenDavid and Pearson 2009, Gibson et al. 2009, Gibson et al. 2013) and to the best of our knowledge have never before been observed in clinopyroxene from off-cratonic spinel peridotites. These clinopyroxenes have distinctly lower HREE concentrations but similar LREE concentrations to those lacking sinusoidal REE patterns. The steeply dipping, highly depleted and consistent HREE concentrations indicate these clinopyroxenes may be residual to the partial melting event rather than a secondary precipitate. Extended trace element patterns are similar to those for type 1 clinopyroxenes, except typically more extreme in trace element anomalies. Sample 67-02A(2) in particular contains clinopyroxenes with very strong negative Ti and HFSE anomalies and positive Sr anomalies. We therefore suggest that the sinusoidal REE patterns are also related to subduction metasomatism which overprinted the melt depletion signature of the residual clinopyroxenes. The composition, nature and origin of the fluid responsible is difficult to constrain. Low degree melts formed in equilibrium with garnet and carbonatitic melts, both formed through partial melting of deeply subducted oceanic crust, are plausible agents. Both fluids would have the required high LREE/HREE ratio, negative anomalies for HFSE and positive Sr anomalies and have been invoked to explain similar patterns observed in garnets (Hauri et al. 1993, Rudnick et al. 1993, Stachel et al. 2004, Dasgupta et al. 2009, Aulbach et al. 2013, Gibson et al. 2013). The very low Ti/Eu ratios in these clinopyroxenes, as low as 200, are particularly indicative of metasomatism associated with carbonatitic melts (Yaxley et al. 1998, Scott et al. 2014).

The overall similarity between the normalised trace element patterns of type I and type II clinopyroxenes implies the two metasomatic agents may be linked. For example, it is possible that two end-member agents are present in the mantle wedge; a carbonate-rich fluid originating from deeply subducted lithosphere and a more silicate-rich fluid originating from shallower depths. The variation in the strength of particular trace element anomalies could thus reflect varying degrees of mixing between these end-member components.

A final distinct clinopyroxene type (type III) is present in 'reacted' sample 67-02D(7), occurring in a single coarse vein (Fig. 2.10). Such clinopyroxenes are distinguished through lower Mg#, CaO and higher Al_2O_3. Their REE and extended trace element patterns are broadly similar to type I clinopyroxenes except they are overall more enriched and overall, with less severe Ti anomalies. We interpret these to form in a similar way as type I clinopyroxenes but with a more evolved silicate melt as the metasomatising agent. Crystallisation of pyroxene within the mantle wedge (for example to form pyroxenite veins) would result in a decrease in Mg# and CaO and an increase in incompatible components in the residual melt.

2.5.4 Melt-rock reaction

Whilst 'residual' harzburgites provide insights into the ancient melting, metasomatic and cooling histories of these samples, 'reacted' harzburgites, pyroxenites and dunites record secondary textures and chemistry which are clearly attributable to a subsequent process. These features are very heterogeneous not just between samples from the same locality but also within individual hand specimens indicating that this process was localised and occurred on timescales short enough to preserve relatively unstable features such as sutured grain boundaries, partial reaction textures and fine-grained crystal domains (Fig. 2.1). Many of the features of the 'reacted' harzburgites are commonly observed in other suites of arc peridotites, most notably veins and patches of secondary orthopyroxene forming at the expense of olivine (Fig. 2.1, Franz et al. 2002, Arai et al. 2004, Bryant et al. 2007, Ionov 2010, Bénard and Ionov 2013). Combined with the observation of quenched melts in close spatial proximity to reaction textures, these features are clear physical

evidence for the involvement of olivine-undersaturated silicate melts in the petrogenesis of these textures ($Mg_2SiO_4^{Olivine} + SiO_2^{Melt} = Mg_2Si_2O_6^{Opx}$).

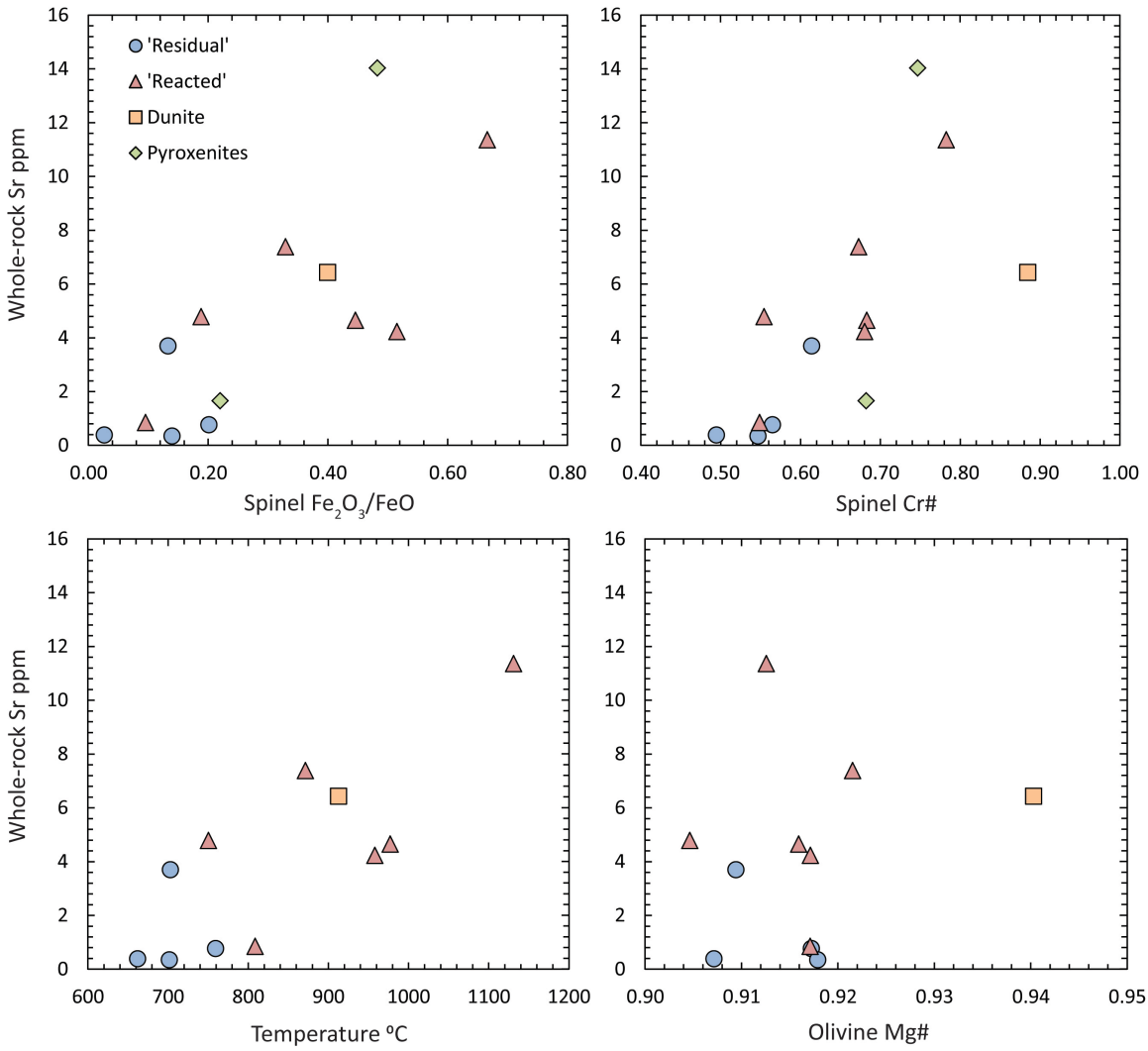

Fig. 2.20 Correlation between whole rock incompatible trace element chemistry (represented here by Sr) and spinel and olivine composition and temperature calculated from Fe-Mg exchange between olivine and spinel (O'Neill and Wall 1987).

This physical evidence is supported further by multiple lines of chemical evidence. Firstly, thermometry of 'reacted' harzburgites reveals substantial increases in temperature from ambient mantle conditions up to temperatures of 1131 °C for the porphyroclastic peridotite 67-02A(3) (Fig. 2.4, Fig. 2.19). Even this upper temperature estimate is likely to be an underestimate due to incomplete equilibration with the reacting melt (see chapter 5) and the possibility of a period of cooling following initial melt-rock reaction before xenolith formation. These temperature increases are thus consistent with incomplete chemical equilibration in response to thermal diffusion related to a percolating melt or nearby melt-channel (see chapter 5 for a thermal diffusion model). Secondly, the whole rock trace element chemistry of 'reacted' harzburgites is substantially enriched over 'residual' peridotites (Fig. 2.7., Fig. 2.8, Fig. 2.19). There are positive correlations between the degree of enrichment and temperature, which are particularly strong for more incompatible trace elements (Fig. 2.19). Fig. 2.21 compares 'reacted' harzburgites and the dunite to locally erupted lavas (Woodhead et al. 2010, Cunningham et al. 2012). The trace element patterns are very similar overall which is consistent with similar magma compositions interacting with the peridotites in the mantle, with negative Ti and Zr anomalies, positive Sr, Pb and U anomalies and enrichments in large ion lithophile elements present in both lavas and 'reacted' harzburgites. The major differences are the small or entirely absent Hf and Nb anomalies in the Ritter samples compared to the pronounced negative anomalies in the lavas. However, orthopyroxene contains distinct positive anomalies for these elements (Fig. 2.10; Fig. A2) so the difference is likely a mineralogical control in the peridotites. The relatively small change in Nb concentration between 'residual' and 'reacted' samples compared to neighbouring elements (Fig. 2.7; Fig. 2.8; Fig. A5) is consistent with very low Nb concentration in the reacting melt. The chemical enrichment reflects multiple reservoirs of trace elements within the peridotite. Since the coarse relic orthopyroxene and olivine, which make up the majority of the samples are largely unaffected chemically (at least relative to the changes in bulk-rock chemistry) by the melt-rock reaction, the dominant source of the enrichment is likely to be pockets of quenched melt, spinel-hosted melt inclusions and potentially microscopic inclusions of other phases such as rutile which may explain the absence of negative Nb anomalies. Clinopyroxene is not obviously in greater modal abundance compared to 'residual' harzburgites (in fact the

opposite is likely the case in most samples), and secondary orthopyroxene is unlikely to be abundant enough or chemically enriched enough to produce the observed differences in bulk-rock composition. Given this, it may therefore seem rather unlikely that there would be a *trend* between chemistry and temperature since the diffusional resetting of mineral thermometers in response to changes in thermal state does not require the physical presence of melt in the sample itself, just the presence of a heat source nearby. However, the remarkably broad range of equilibration temperatures from a single set of peridotite samples (which we assume were relatively closely spatially related *in-situ*) shows that the distribution of thermal anomalies associated with channelized melt networks was extremely localised and strongly dependent on proximity to physical melt. The greater the proportion of melt in a given volume of peridotite the greater the flux of heat, the shorter the length scale the heat has to diffuse over and the greater the budget of incompatible trace elements. The final line of chemical evidence is in changes to mineral chemistry. This is most apparent in the olivine trace element dataset, because the trace element composition of olivine is very sensitive to temperature (De Hoog et al. 2010, Foley et al. 2013) and trace element diffusion in olivine is much faster than in either orthopyroxene or clinopyroxene (Van Orman et al. 2001, Cherniak and Liang 2007, Spandler and O'Neill 2010). These factors mean olivine is a much more sensitive monitor of late-stage reaction processes, particularly in 'cold' ambient mantle such as the Ritter suite where the unusually large temperature gradient with the reacting melt produced distinct trends in compositional space. The very low trace element concentrations in 'residual' Ritter olivines are therefore a function of both the very low equilibration temperatures and the high degrees of melt extraction. They form a tight cluster in compositional space confirming they have experienced negligible influence from reacting melts or the host magma during ascent (Fig. 2.11). Olivines from 'reacted' peridotites fall on a narrow array which extends away from the composition of 'residual' olivines (Fig. 2.11), with over an order of magnitude enrichment in some trace elements (particularly sensitive are Na, Ca, Cr, Ti and Y). Significant variation in trace element concentration between olivines within individual samples requires that this process occurred at a late-stage prior to formation of the xenolith, hence the melt-rock reaction is inherently associated with the active magmatic system beneath the West Bismarck island arc. Chapter 5 discusses in detail the timescales and conditions associated with this melt-rock

reaction process, using the porphyroclastic sample 67-02A(3). It is interesting that the chemical trends formed by olivines in that sample are very similar to trends in other 'reacted' samples, despite significant differences in texture. This indicates a similar melt composition for the different 'reacted' samples. The difference in texture may be due to variation in the relative volumes of melt and peridotite or variation in mechanism of melt infiltration (isolated veins of melt versus grain boundary melt percolation).

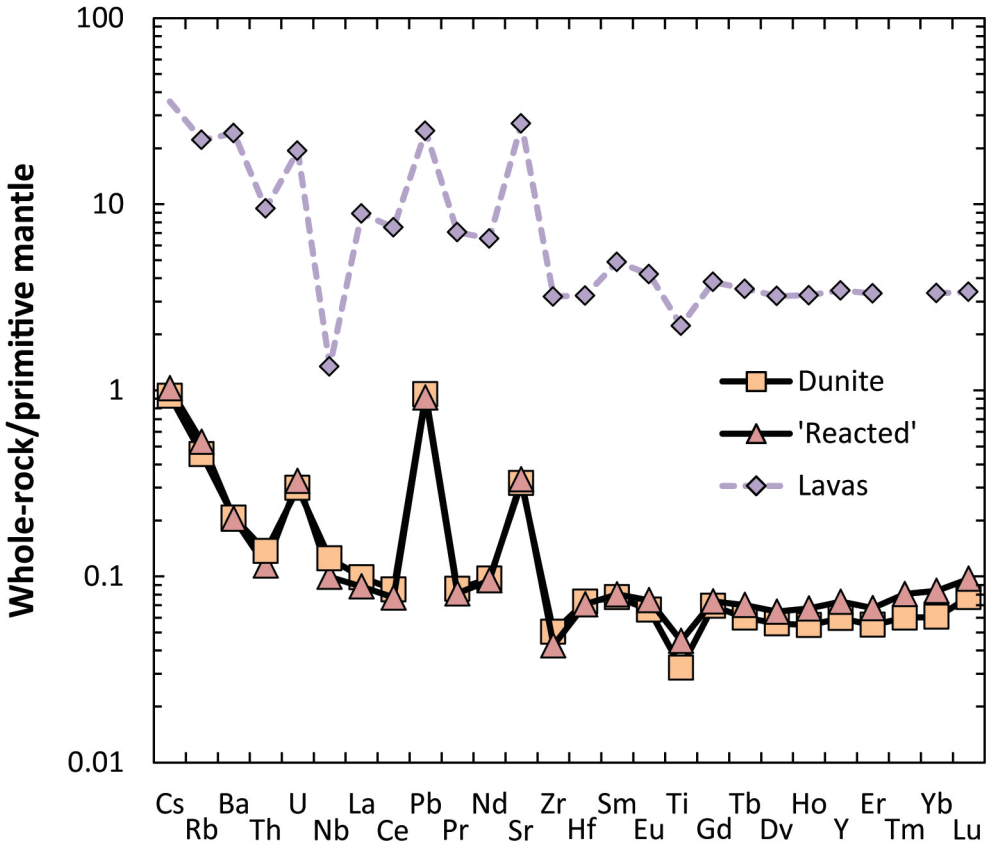

Fig. 2.21 Comparison between 'reacted' harzburgite, dunite and the average composition of lavas erupted along the West Bismarck Island Arc (Woodhead et al. 2010, Cunningham et al. 2012)

The increasingly oxidised redox state of iron in spinel during melt-rock reaction (Fig. 2.4; Fig. 2.20) indicates that the reacting melt was relatively oxidised compared to the ambient mantle, confirmed with oxybarometry of the host magma in chapter 5 which reveals values up to 2 log units above the fayalite-magnetite-quartz redox buffer. Such oxidised values are typical of arc basalts (Evans et al. 2012) and many other examples of arc peridotites that have experienced metasomatism and melt-rock reaction (e.g. Brandon and Draper 1996, Parkinson and Arculus 1999, Franz et al. 2002, Parkinson et al. 2003, Bryant et al. 2007). That such redox changes are occurring within the upper mantle wedge and over timescales short enough to preserve trace element disequilibria in olivine (chapter 5) supports studies arguing for oxidation of arc magmas at source rather than during transit through the crust. Without better constraints on the absolute values of oxygen fugacity recorded by the Ritter samples however, we refrain from making broad comparisons with other studies.

Whilst the 'reacted' harzburgites reflect partial equilibration between small veins or pools of melt, the presence of pyroxenites and dunites representing end-member stages of melt-rock reaction indicates larger veins or channels of melt in close proximity to the 'reacted' harzburgites. That both pyroxenites and dunites exist in the same xenolith suite indicates substantial variations in the conditions of melt-rock reaction, since dunites require reaction of harzburgite with a melt with low silica activity compared to a melt capable of forming a pyroxenite from the same starting material (Kelemen et al. 1992, Smith et al. 1999, Tursack and Liang 2012). Of particular significance are the equilibration temperatures, which, given the high degrees of melt-rock reaction, are lower than the temperatures of partially reacted harzburgites (Table 2.3). Sample 67-02D(3), a dunite, records an olivine-spinel temperature as low as the 'residual' harzburgites. One possibility is that the dunite and pyroxenite samples reflect earlier stages of melt-rock reaction and have subsequently cooled to intermediate temperatures. That dunitic sample 67-02D(3) is as 'cold' as the 'residual' harzburgites indicates that it may have formed much earlier, and may even be a fossil melt channel from the earlier partial melting event. This is supported further by the highly depleted trace element chemistry of olivines from this sample (Table 2.7) and the identical chemistry of olivine from the dunite vein and the surrounding 'primary' dunite. Since the process of melt-rock

reaction results in enrichment of incompatible trace elements in olivine, a significant period of time must have passed in order for the dunite vein and 'primary' dunite to equilibrate not just with each other but also with the surrounding ambient mantle. If this is indeed the case, then this demonstrates that fine-grained domains in otherwise coarse-grained mantle rocks may be able to survive during sustained periods of residence in the mantle. The survival of this heterogeneous texture may have been facilitated by the intermixed spinel since the presence of a second phase in an otherwise homogeneous fine-grained matrix is known to inhibit crystal coarsening (Olgaard and Evans 1986, Evans et al. 2001, Linckens et al. 2011).

2.5.5 Summary of the petrological evolution of Ritter peridotites

Our detailed geochemical study here reveals a complex, multi-stage history to the mantle underlying the West Bismarck island arc which is not initially obvious in its entirety through simple petrographic inspection of the peridotites or through geochemical studies of lavas (Woodhead et al. 1998, Woodhead et al. 2010, Cunningham et al. 2012). The earliest stage of petrogenesis which can be clearly identified is a hydrous melting episode within an 'ancient' subduction system (Fig. 2.22), which generated the highly depleted HREE compositions of orthopyroxene (relative to melting at spreading centre settings), high Mg# and low Al_2O_3 content of orthopyroxene, highly forsteritic olivine and high Cr# of spinel in 'residual' samples. It is unclear from major and trace element systematics where this subduction system was in relation to the present day West Bismarck arc, however a possibility is that the melting episode was caused by subduction in the north associated with the now extinct Manus/Kilinailau trench. This would be in agreement with Woodhead et al. (1998) who studied lavas erupted along the neighbouring New Britain island arc and interpreted anomalously radiogenic Sr and Pb isotope signatures to reflect tapping of a mantle source enriched by this previous subduction event. This possibility is discussed further in chapter 4. Following, or synchronous with, this melting event, the mantle wedge was exposed to a variety of distinct fluid compositions resulting in modal and cryptic metasomatism. This is most obvious in the presence of 'fossil' dunite melt channels and relatively well-equilibrated veins of clinopyroxene and sinusoidal clinopyroxene REE patterns in 'residual' harzburgites. The trace element composition of these different clinopyroxene populations likely requires mixing of fluids originating from

different slab and mantle depths. Of particular interest, sinusoidal REE patterns require interaction with fluids with very high LREE/HREE such as carbonate-rich deep slab melts (Rudnick et al. 1993, Hauri et al. 1993, Yaxley et al. 1998, Dasgupta et al. 2004, Scott et al. 2014). After melting and metasomatism, the mantle cooled rapidly from initial temperatures above the wet peridotite solidus down to unusually cold equilibration temperatures of ~600 °C. This cooling episode was rapid enough to preserve high closure temperatures calculated from clinopyroxene-orthopyroxene chemical equilibria, but slow enough to allow diffusive equilibration of rapidly diffusing components in olivine and spinel, and was largely responsible for the highly depleted trace element concentrations in olivine from 'residual' peridotites. After this period of gestation, the ambient mantle entered the present day West Bismarck arc system. The activity related to this period of petrogenesis is clearly observed texturally and chemically in the 'reacted' peridotites, which experienced variable degrees of silicate melt-rock reaction producing veins of secondary orthopyroxene and recrystallization to form porphyroclastic textures. Chemical changes associated with this process are substantial increases in whole rock trace element concentration and trace element disequilibria in olivine. Geothermometry and oxybarometry show that the reacting melt was in excess of 1130 °C and oxidised relative to the ambient mantle. The preservation of ambient mantle chemistry and textures in the Ritter peridotite suite, alongside the 'reacted' samples indicates that melt infiltration was isolated mainly to channels and veins and likely occurred on a timescale shortly before formation and entrainment of the xenoliths in the host magma.

2.5.6 Implications for the formation of cratonic mantle

Many of the geochemical features of cratonic mantle have been attributed to subduction-related processes. For example, kimberlites erupted in continental cratons often yield peridotite xenoliths with elevated orthopyroxene contents and Si/Mg whole-rock ratios relative to melt depletion trends which have been interpreted to reflect metasomatism within a subduction zone by Si-rich, slab-derived fluids, alongside competing theories (Parman et al. 2004, Simon et al. 2007, Pearson and Wittig 2008, Tappe et al. 2011). The Ritter peridotites, similar to other arc-related peridotites, contain clear evidence for the formation of secondary orthopyroxene and clinopyroxene through melt-rock reaction and associated increases in whole-rock incompatible element composition. An additional and

important feature, perhaps unique amongst previously studied off-craton peridotites to the Ritter peridotite suite is the occurrence of sinusoidal clinopyroxene REE patterns which are commonly observed in cratonic mantle mineral phases (Stachel et al. 1998, Stachel et al. 2004, Simon et al. 2007, Klein-BenDavid and Pearson 2009, Gibson et al. 2009, Gibson et al. 2013). Both of these features indicate that similar styles of metasomatism have influenced the petrogenesis of cratonic mantle domains and the Ritter peridotite suite. Despite these similar metasomatic features, notable differences exist between the Ritter peridotites and typical cratonic peridotite. For example, cratonic mantle is inferred to have undergone greater extents of partial melting than the Ritter peridotites. This is most clearly seen in the forsterite content of olivine, which in cratonic mantle is typically 92.5-92.8 (Bernstein et al. 2007, Pearson and Wittig 2008), compared to values of 90.5-92.1 for Ritter peridotites (average 91.5). These differences can be best reconciled, at least in a qualitative way, by the timing and conditions of melt extraction. Os isotope model ages for cratonic mantle are often in excess of 3 Ga, at which time the higher mantle potential temperatures may have facilitated the production of greater volumes of melt. Nevertheless, even with higher mantle potential temperatures, melting must have occurred in the presence of a hydrous fluid for similar reasons as we have inferred here for the Ritter peridotites (Pearson and Wittig 2008). In conclusion, whilst our data here does not provide a conclusive link between the compositions of peridotites formed in subduction zone settings and cratonic mantle, we add to the body of evidence that silica enrichment is a common process active in the mantle wedge and provide new evidence of a similar style of metasomatism involved in the petrogenesis of both mantle environments.

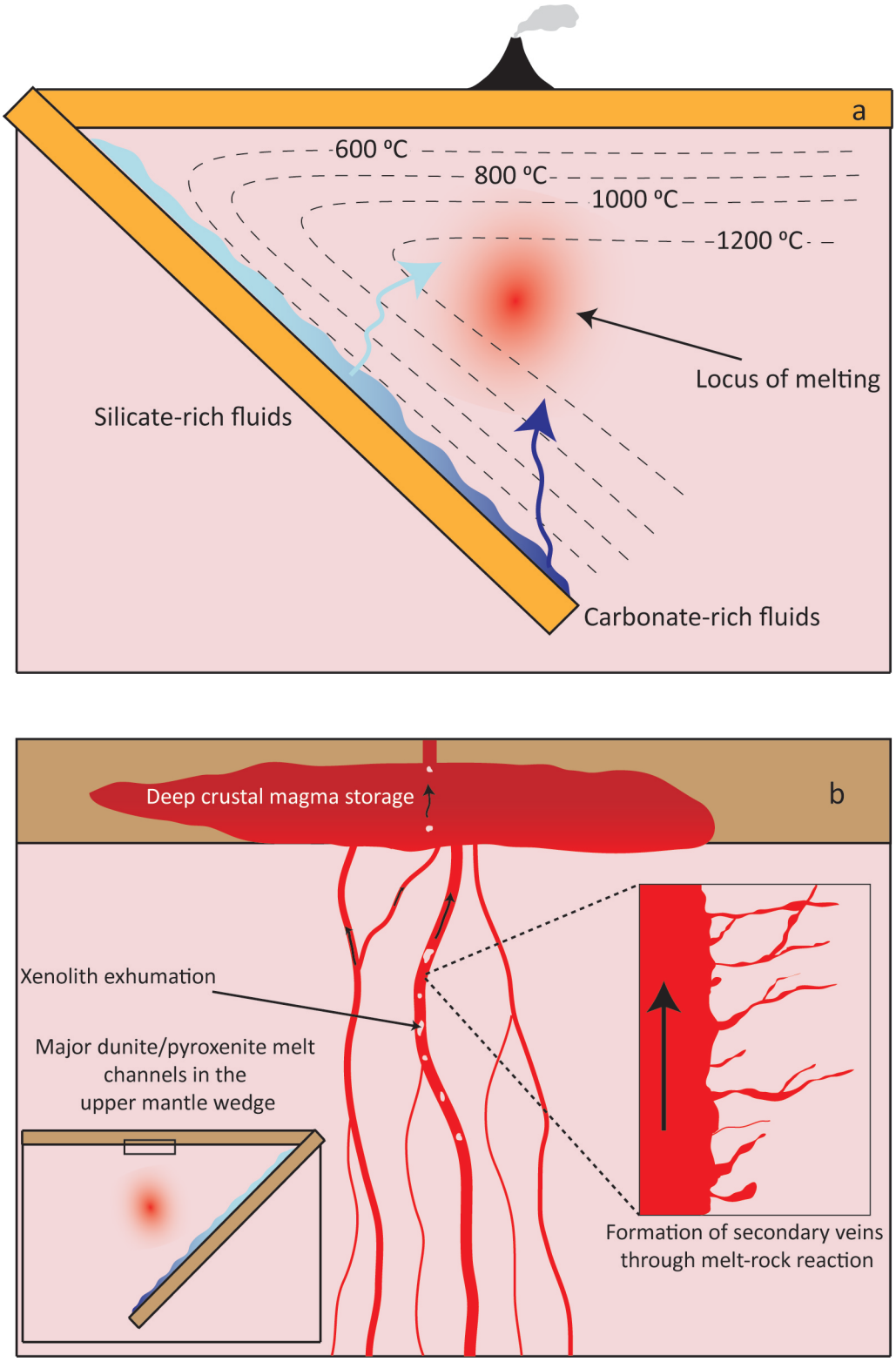

Fig. 2.22 Summary of the petrological evolution of the Ritter peridotites. (a) Melting and metasomatism by multiple slab-derived fluids as part of an 'ancient' arc system (b) A period of cooling to low ambient mantle temperatures followed by melt-rock reaction in the upper mantle wedge as part of the modern West Bismarck arc. See text for full details

2.6 References

Annen, C., Blundy, J.D., Sparks, R.S.J., 2006. The Genesis of Intermediate and Silicic Magmas in Deep Crustal Hot Zones. J. Petrol. 47, 505-539

Arai, S., 1994. Characterization of spinel peridotites by olivine-spinel compositional relationships: Review and interpretation. Chemical Geology 113, 191-204

Arai, S., Takada, S., Michibayashi, K., Kida, M., 2004. Petrology of Peridotite Xenoliths from Iraya Volcano, Philippines, and its Implication for Dynamic Mantle-Wedge Processes. J. Petrol. 45, 369-389

Arai, S., Ishimaru, S., 2008. Insights into Petrological Characteristics of the Lithosphere of Mantle Wedge beneath Arcs through Peridotite Xenoliths: a Review. J. Petrol. 49, 665-695

Aulbach, S., Griffin, W.L., Pearson, N.J., O'Reilly, S.Y., 2013. Nature and timing of metasomatism in the stratified mantle lithosphere beneath the central Slave craton (Canada). Chemical Geology 352, 153-169

Baker, M.B., Stolper, E.M., 1994. Determining the composition of high-pressure mantle melts using diamond aggregates. Geochim. Cosmochim. Acta 58, 2811-2827

Ballhaus, C., Berry, R.F., Green, D.H., 1991. High pressure experimental calibration of the olivine-orthopyroxene-spinel oxygen geobarometer: implications for the oxidation state of the upper mantle. Contrib. Mineral. Petrol. 107, 27-40

Batanova, V.G., Belousov, I.A., Savelieva, G.N., Sobolev, A.V., 2011. Consequences of Channelized and Diffuse Melt Transport in Supra-subduction Zone Mantle: Evidence from the Voykar Ophiolite (Polar Urals). J. Petrol. 52, 2483-2521

Bénard, A., Ionov, D.A., 2013. Melt- and Fluid-Rock Interaction in Supra-Subduction Lithospheric Mantle: Evidence from Andesite-hosted Veined Peridotite Xenoliths. J. Petrol. 54, 2339-2378

Bernstein, S., Hanghøj, K., Kelemen, P.B., 2006. Ultra-depleted, shallow cratonic mantle beneath West Greenland: dunitic xenoliths from Ubekendt Ejland. Contrib. Mineral. Petrol. 152, 335-347

Bernstein, S., Kelemen, P.B., Hanghøj, K., 2007. Consistent olivine Mg# in cratonic mantle reflects Archean mantle melting to the exhaustion of orthopyroxene. Geology 35, 459-462

Bizimis, M., Salters, V.J.M., Bonatti, E., 2000. Trace and REE content of clinopyroxenes from supra-subduction zone peridotites. Implications for melting and enrichment processes in island arcs. Chemical Geology 165, 67-85

Blundy, J., Wood, B., 1994. Prediction of crystal-melt partition-coefficients from elastic-moduli. Nature 372, 452-454

Brandon, A.D., Draper, D.S., 1996. Constraints on the origin of the oxidation state of mantle overlying subduction zones: An example from Simcoe, Washington, USA. Geochim. Cosmochim. Acta 60, 1739-1749

Brey, G.P., Köhler, T., 1990. Geothermobarometry in Four-phase Lherzolites II. New Thermobarometers, and Practical Assessment of Existing Thermobarometers. J. Petrol. 31, 1353-1378

Brunelli, D., Seyler, M., Cipriani, A., Ottolini, L., Bonatti, E., 2006. Discontinuous Melt Extraction and Weak Refertilization of Mantle Peridotites at the Vema Lithospheric Section (Mid-Atlantic Ridge). J. Petrol. 47, 745-771

Brunneli, D., Seyler, M., 2010. Asthenospheric percolation of alkaline melts beneath the St. Paul region (Central Atlantic Ocean). Earth Planet. Sci. Lett. 289, 393-405

Bryant, J.A., Yogodzinski, G.M., Churikova, T.G., 2007. Melt-mantle interactions beneath the Kamchatka arc: Evidence from ultramafic xenoliths from Shiveluch volcano. Geochem. Geophys. Geosys. 8, doi:10.1029/2006GC001443

Canil, D., O'Neill, H.St.C., 1996. Distribution of Ferric Iron in some Upper-Mantle Assemblages. J. Petrol. 37, 609-635

Cherniak, D.J., Liang, Y., 2007. Rare earth element diffusion in natural enstatite. Geochim. Cosmochim. Acta 71, 1324-1340

Cunningham, H., Gill, J., Turner, S., Caulfield, J., Edwards, L., Day, S., 2012. Rapid magmatic processes accompany arc-continent collision: the Western Bismarck arc, Papua New Guinea. Contrib. Mineral. Petrol. 164, 789-804

Dasgupta, R., Hirschmann, M.M., McDonough, W.F., Spiegelman, M., Withers, A.C., 2009. Trace element partitioning between garnet lherzolite and carbonatite at 6.6 and 8.6 GPa with applications to the geochemistry of the mantle and of mantle-derived melts. Chemical Geology 262, 57-77

De Hoog, J.C.M., Gall, L., Cornell, D.H., 2010. Trace-element geochemistry of mantle olivine and application to mantle petrogenesis and geothermobarometry. Chemical Geology 270, 196-215

Dick, H.J.B., 1989. Abyssal peridotites, very slow spreading ridges and ocean ridge magmatism. *In* "Magmatism in the Ocean Basins', Saunders, A.D., Norry, M.J., Geol. Soc. Sp. Pub. 42, 71-105"

Dungan, M.A., Davidson, J., 2004. Partial assimilative recycling of the mafic plutonic roots of arc volcanoes: An example from the Chilean Andes. Geology 32, 773-776

Elliott, T., Plank, T., Zindler, A., White, W., Bourdon, B., 1997. Element transport from slab to volcanic front at the Mariana arc. J. Geophys. Res. 102, 14991-15019

Evans, B., Renner, J., Hirth, G., 2001. A few remarks on the kinetics of static grain growth in rocks. Int. J. Earth Sci. 90, 88-103

Evans, K.A., Elburg, M.A., Kamenetsky, V.S., 2012. Oxidation state of subarc mantle. Geology 40, 783-786

Foley, S.F., Prelevic, D., Rehfeldt, T., Jacob, D.E., 2013. Minor and trace elements in olivines as probes into early igneous and mantle melting processes. Earth Planet. Sci. Lett. 363, 181-191

Franz, L., Becker, K-P., Kramer, W., Herzig, P.M., 2002. Metasomatic Mantle Xenoliths from the Bismarck Microplate (Papua New Guinea)- Thermal Evolution, Geochemistry and Extent of Slab-induced Metasomatism. J. Petrol. 43, 315-343

Gaetani, G., Grove, T., 1998. The influence of water on melting of mantle peridotite. Contrib. Mineral. Petrol. 131, 323-346

Grove, T.L., Till, C.B., Krawczynski, M.J., 2012. The Role of H_2O in Subduction Zone Magmatism. Ann. Rev. Earth Planet. Sci. 40, 413-439

Handley, H.K., Turner, S., Macpherson, C.G., Gertisser, R., Davidson, J.P., 2011. Hf-Nd isotope and trace element constraints on subduction inputs at island arcs: Limitations of Hf anomalies as sediment input indicators. Earth Planet. Sci. Lett. 304, 212-223

Hauri, E.H., Shimizu, N., Dieu, J.J., Hart, S.R., 1993. Evidence for hotspot-related carbonatite metasomatism in the oceanic upper mantle. Nature 365, 221-226

Hawkesworth, C.J., Gallagher, K., Hergt, J.M., McDermott, F., 1993. Mantle and slab contributions in arc magmas. Annu. Rev. Earth Planet. Sci. 21, 175-204

Hellebrand, E., Snow, J.E., Dick, H.J.B., Hofmann, A.W., 2001. Coupled major and trace elements as indicators of the extent of melting in mid-ocean-ridge peridotites. Nature 410, 677-681

Hellebrand, E., Snow, J.E., Hoppe, P., Hofmann, A.W., 2002. Garnet-field Melting and Late-stage Refertilization in 'Residual' Abyssal Peridotites from the Central Indian Ridge. J. Petrol. 43, 2305-2338

Hellebrand, E., Snow, J.E., Mostefaoui, S., Hoppe, P., 2005. Trace element distribution between orthopyroxene and clinopyroxene in peridotites from the Gakkel Ridge: a SIMS and NanoSIMS study. Contrib. Mineral. Petrol. 150, 486-504

Hermann, J., Spandler, C.J., 2008. Sediment Melts at Sub-arc Depths: an Experimental Study. J. Petrol. 49, 717-740

Gibson, S.A., Malarkey, J., Day, J.A., 2008. Melt Depletion and Enrichment beneath the Western Kaapvaal Craton: Evidence from Finsch Peridotite Xenoliths. J. Petrol. 49, 1817-1852

Gibson, S.A., McMahon, S.C., Day, J.A., Dawson, J.B., 2013. Highly Refractory Lithospheric Mantle beneath the Tanzanian Craton: Evidence from Lashaine Pre-metasomatic Garnet-bearing Peridotites. J. Petrol. 54, 1503-1546

Grégoire, M., McInnes, B.I.A., O'Reilly, S.Y., 2001. Hydrous metasomatism of oceanic sub-arc mantle, Lihir, Papua New Guinea Part 2. Trace element characteristics of slab-derived fluids. Lithos 59, 91-108

Ionov, D.A., 2010. Petrology of Mantle Wedge Lithosphere: New Data on Supra-Subduction Zone Peridotite Xenoliths from the Andesitic Avacha Volcano, Kamchatka. J.Petrol. 51, 327-361

Ishimaru, S., Arai, S., Ishida, Y., Shirasaka, M., Okrugin, V.M., 2007. Melting and Multi-stage Metasomatism in the Mantle Wedge beneath a Frontal Arc Inferred from Highly Depleted Peridotite Xenoliths from the Avacha Volcano, Southern Kamchatka. J. Petrol. 48, 395-433

Jean, M.M., Shervais, J.W., Choi, S-H., Mukasa, S.B., 2010. Melt extraction and melt refertilization in mantle peridotite of the Coast Range ophiolite: an LA-ICP-MS study. Contrib. Mineral. Petrol. 159, 113-136

Johnson, K.T.M., Dick, H.J.B., Shimizu, N., 1990. Melting in the Oceanic Upper Mantle; An Ion Microprobe Study of Diopsides in Abyssal Peridotites. J. Geophys. Res. 95, 2661-2678

Kaeser, B., Kalt, A., Pettke, T., 2006. Evolution of the Lithospheric Mantle beneath the Marsabit Volcanic Field (Northern Kenya): Constraints from the Textural, *P-T* and Geochemical Studies on Xenoliths. J. Petrol. 47, 2149-2184

Kamenov, G.D., Perfit, M.R., Mueller, P.A., Jonasson, I.R., 2008. Controls on magmatism in an island arc environment: study of lavas and sub-arc xenoliths from the Tabar-Lihir-Tanga-Feni island chain, Papua New Guinea. Contrib. Mineral. Petrol. 155, 635-656

Kelemen, P.B., Dick, H.J.B., Quick, J.E., 1992. Formation of harzburgite by pervasive melt rock reaction in the upper mantle. Nature 358, 635-641

Kepezhinskas, P.K., Defant, M.J., Drummond, M.S., 1995. Na Metasomatism in the Island-Arc Mantle by Slab Melt-Peridotite Interaction: Evidence from Mantle Xenoliths in the North Kamchatka Arc. J. Petrol. 36, 1505-1527

Klein-BenDavid, O., Pearson, D.G., 2009. Origins of subcalcic garnets and their relation to diamond-forming fluids-Case studies from Ekati (NWT-Canada) and Murowa (Zimbabwe). Geochim. Cosmochim. Acta 73, 837-855

Liang, Y., Sun, C., Yao, L., 2013. A REE-in-two-pyroxene thermometer for mafic and ultramafic rocks. Geochim. Cosmochim. Acta 102, 246-260

Liang, Y., 2014. Time scales of diffusive re-equilibration in bi-mineralic systems with and without a fluid or melt phase. Geochim. Cosmochim. Acta 132, 274-287

Lee, C.T.A., Harbert, A., Leeman, W.P., 2007. Extension of lattice strain theory to mineral/mineral rare-earth element partitioning: An approach for assessing disequilibrium and developing internally consistent partition coefficients between olivine, orthopyroxene, clinopyroxene and basaltic melt. Geochim. Cosmochim. Acta 71, 481-496

Linckens, J., Herwegh, M., Müntener, O., Mercolli, I., 2011. Evolution of a polymineralic mantle shear zone and the role of second phases in the localisation of deformation. J. Geophys. Res. 116 (B6)

Mallmann, G., O'Neill, H.St.C., 2013. Calibration of an Empirical Thermometer and Oxybarometer based on the Partitioning of Sc, Y and V between Olivine and Silicate Melt. J. Petrol. 54, 933-949

Maury, R.C., Defant, M.J., Joron, J-L., 1992. Metasomatism of the sub-arc mantle inferred from trace elements in Philippine xenoliths. Nature 360, 661-663

McDade, P., Blundy, J.D., Wood, B.J., 2003a. Trace element partitioning between mantle wedge peridotite and hydrous MgO-rich melt. Am. Mineral. 88, 1825-1831

McDade, P., Blundy, J.D., Wood, B.J., 2003b. Trace element partitioning on the Tinaquillo Lherzolite solidus at 1.5 GPa. Phys. Earth Planet. Int. 139, 129-147

McInnes, B.I.A., Gregoire, M., Binns, R.A., Herzig, P.M., Hannington, M.D., 2001. Hydrous metasomatism of oceanic sub-arc mantle, Lihir, Papua New Guinea: petrology and geochemistry of fluid-metasomatised mantle wedge xenoliths. Earth Planet. Sci. Lett. 188, 169-183

Neumann, E-R., Griffin, W.L., Pearson, N.J., O'Reilly, S.Y., 2004. The Evolution of the Upper Mantle beneath the Canary Islands: Information from Trace Elements and Sr isotope Ratios in Minerals in Mantle Xenoliths. J. Petrol. 45, 2573-2612

Niu, Y., 2004. Bulk-rock Major and Trace Element Compositions of Abyssal Peridotites: Implications for Mantle Melting, Melt Extraction and Post-melting Processes Beneath Mid-Ocean Ridges. J. Petrol. 45, 2423-2458

O'Neill, H.S., Wall, V.J., 1987. The Olivine-Orthopyroxene-Spinel Geobarometer, the Nickel Precipitation Curve, and the Oxygen Fugacity of the Earth's Upper Mantle. J. Petrol. 28, 1169-1191

Olgaard, D.L., Evans, B., 1986. Effect of second-phase particles on grain growth in calcite. J. Am. Ceram. Soc. 69, C272-C277

Palme, H., O'Neill, H.St.C., 2003. Cosmochemical Estimates of Mantle Composition: Treatise on Geochemistry

Parkinson, I.J., Pearce, J.A., 1998. Peridotites from the Izu-Bonin-Mariana Forearc (ODP Leg 125): Evidence for Mantle Melting and Melt-Mantle Interaction in a Supra-Subduction Zone Setting. J. Petrol. 39, 1577-1618

Parkinson, I.J., Hawkesworth, C.J., Cohen, A.S., 1998. Ancient Mantle in a Modern Arc: Osmium Isotopes in Izu-Bonin-Mariana Forearc Peridotites. Science 281, 2011-2013

Parkinson, I.J., Arculus, R.J., 1999. The redox state of subduction zones: insights from arc-peridotites. Chemical Geology 160, 409-423

Parkinson, I.J., Arculus, R.J., Eggins, S.M., 2003. Peridotite xenoliths from Grenada, Lesser Antilles Island Arc. Contrib. Mineral. Petrol. 146, 241-262

Parman, S.W., Grove, T.L., Dann, J.C.,de Wit, M.J., 2004. A subduction origin for komatiites and cratonic lithospheric mantle. S. African J. Geol. 107, 107-118

Pearce, J.A., Barker, P.F., Edwards, S.J., Parkinson, I.J., Leat, P.T., 2000. Geochemistry and tectonic significance of peridotites from the South Sandwich arc-basin system, South Atlantic. Contrib. Mineral. Petrol. 139, 36-53

Pearson, D.G., Canil, D., Shirey, S.B., 2003. Mantle Samples Included in Volcanic Rocks: Xenoliths and Diamonds. Treatise on Geochemistry

Pearson D.G., Wittig, N., 2008. Formation of Archaean continental lithosphere and its diamonds: the root of the problem. J. Geol. Soc. 165, 895-914

Pirard, C., Hermann, J., O'Neill, H.St.C., 2013. Petrology and Geochemistry of the Crust-Mantle Boundary in a Nascent Arc, Massif du Sud Ophiolite, New Caledonia, SW Pacific. J. Petrol. 54, 1759-1792

Poli, S., Schmidt, M.W., 1995. H_2O transport and release in subduction zones: Experimental constraints on basaltic and andesitic systems. J. Geophys. Res. 100, 22299-22314

Rudnick, R.L., McDonough, W.F., Chappell, B.W., 1993. Carbonatite metasomatism in the northern Tanzanian mantle: petrographic and geochemical characteristics. Earth Planet. Sci. Lett. 114, 463-475

Scott, J.M., Hodgkinson, A., Palin, J.M., Waight, T.E., Van der Meer, Q.H.A., Cooper, A.F., 2014. Ancient melt depletion overprinted by young carbonatitic metasomatism in the New Zealand lithospheric mantle. Contrib. Mineral. Petrol. 167, doi:10.1007/s004-10-014-0963-0

Seyler, M., Cannat, M., Mével, C., 2003. Evidence for major-element heterogeneity in the mantle source of abyssal peridotites from the Southwest Indian Ridge (52° to 68°E). Geochem. Geophys. Geosys. 4, doi:10.1029/2002GC000305

Seyler, M., Brunelli, D., Toplis, M.J., Mével, C., 2011. Multiscale chemical heterogeneities beneath the eastern Southwest Indian Ridge (52°E-68°E): Trace element compositions of

along-axis dredged peridotites. Geochem. Geophys. Geosys. 12, doi:10.1029/2011GC003585

Simon, N.S.C., Carlson, R.W., Pearson, D.G., Davies, G.R., 2007. The Origin and Evolution of the Kaapvaal Cratonic Lithospheric Mantle. J. Petrol. 48, 589-625

Skora, S., Blundy, J., 2010. High-pressure Hydrous Phase Relations of Radiolarian Clay and Implications for the Involvement of Subducted Sediment in Arc Magmatism. J. Petrol. 51, 2211-2243

Smith, D., Riter, J.C.A., Mertzman, S.A., 1999. Water-rock interactions, orthopyroxene growth, and Si-enrichment in the mantle: evidence in the xenoliths from the Colorado Plateau, south-western United States. Earth Planet. Sci. Lett. 165, 45-54

Smith, D., 2013. Olivine thermometry and source constraints for mantle fragments in the Navajo Volcanic Field, Colorado Plateau, southwest United States: Implications for the Mantle Wedge. 14 doi:10.1002/ggge.20065

Spandler, C., O'Neill, H.St.C., 2010. Diffusion and partition coefficients of minor and trace elements in San Carlos olivine at 1,300 °C with some geochemical implications. Contrib. Mineral. Petrol. 159, 791-818

Stachel, T., Viljoen, K.S., Brey, G., Harris, J.W., 1998. Metasomatic processes in lherzolitic and harzburgitic domains of diamondiferous lithospheric mantle: REE in garnets from xenoliths and inclusions in diamonds. Earth Planet. Sci. Lett. 159, 1-12

Stachel, T., Aulbach, S., Brey, G.P., Harris, J.W., Leost, I., Tappert, R., Viljoen, K.S., 2004. The trace element composition of silicate inclusions in diamonds: a review. Lithos 77, 1-19

Stolper, E., Newmann, S., 1994. The role of water in the petrogenesis of Mariana trough magmas. Earth Planet. Sci. Lett. 121, 293-325

Sun, C., Liang, Y., 2013. The importance of crystal chemistry on REE partitioning between mantle minerals (garnet, clinopyroxene, orthopyroxene, and olivine) and basaltic melts. Chemical Geology 358, 23-36

Tappe, S., Smart, K.A., Pearson, D.G., Steenfelt, A., Simonetti, A., 2011. Craton formation in Late Archean subduction zones revealed by first Greenland eclogites. Geology 39, 1103-1106

Thirlwall, M.F., Graham, A.M., Arculus, R.J., Harmon, R.S., Macpherson, C.G., 1996. Resolution of the effects of crustal assimilation, sediment subduction, and fluid transport in island arc magmas: Pb-Sr-Nd-O isotope geochemistry of Grenada, Lesser Antilles. Geochim. Cosmochim. Acta 60, 4785-4810

Turner, S., Caulfield, J., Turner, M., van Keken, P., Maury, R., Sandiford, M., Prouteau, G., 2012. Recent contribution of sediments and fluids to the mantle's volatile budget. Nat. Geosci. 5, 50-54

Tursack, E., Liang, Y., 2012. A comparative study of melt-rock reactions in the mantle: laboratory dissolution experiments and geological field observations. Contrib. Mineral. Petrol. 163, 861-876

Vannucci, R., Tiepolo, M., Defant, M.J., Kepezhinskas, P., 2007. The metasomatic record in the shallow peridotite mantle beneath Grenada (Lesser Antilles arc). Lithos 99, 25-44

Van Orman, J.A., Grove, T.L., Shimizu, N., 2001. Rare earth element diffusion in diopside: influence of temperature, pressure, and ionic radius, and an elastic model for diffusion in silicates. Contrib. Mineral. Petrol. 141, 687-703

Walter, M.J., 1999. Comments on 'mantle melting and melt extraction processes beneath ocean ridges: Evidence from abyssal peridotites' by Yaoling Niu. J. Petrol. 40, 1187-1193

Warren, J.M., Shimizu, N., Sakaguchi, C., Dick, H.J.B., Nakamura, E., 2009. An assessment of upper mantle heterogeneity based on abyssal peridotite isotopic compositions. J. Geophys. Res. 114, doi:10.1029/2008JB006186

Widom, E., Kepezhinskas, P., Defant, M., 2003. The nature of metasomatism in the sub-arc mantle wedge: evidence from Re-Os isotopes in Kamchatka peridotite xenoliths. Chemical Geology 196, 283-306

Witt-Eickschen, G., O'Neill, H.St.C., 2005. The effect of temperature on the equilibrium distribution of trace elements between clinopyroxene, orthopyroxene, olivine and spinel in upper mantle peridotite. Chem. Geol. 221, 65-101

Wittig, N., Pearson, D.G., Webb, M., Ottley, C.J., Irvine, G.J., Kopylova, M., Jensen, S.M., Nowell, G.M., 2008. Origin of cratonic lithospheric mantle roots: A geochemical study of peridotites from the North Atlantic Craton, West Greenland. Earth Planet. Sci. Lett. 274, 24-33

Woodhead, J.D., Eggins, S.M., Johnson, R.W., 1998. Magma Genesis in the New Britain Island Arc: Further Insights into Melting and Mass Transfer Processes. J. Petrol. 39, 1641-1668

Woodhead, J., Hergt, J., Sandiford, M., Johnson, W., 2010. The big crunch: Physical and chemical expressions of arc/continent collision in the Western Bismarck arc. J. Volc. Geotherm. Res. 190, 11-24

Yaxley, G.M., Green, D.H., Kamenetsky, V., 1998. Carbonatite Metsomatism in the Southeastern Australian Lithosphere. J. Petrol. 39, 1917-1930

Zheng, J.P., Zhang, R.Y., Griffin, W.L., Liou, J.G., O'Reilly, S.Y., 2005. Heterogeneous and metasomatized mantle recorded by trace elements in minerals of the Donghai garnet peridotites, Sulu UHP terrane, China. Chem. Geol. 221, 243-259

Zheng, J.P., Griffin, W.L., O'Reilly, S.Y., Yu, C.M., Zhang, H.F., Pearson, N., Zhang, M., 2007. Mechanism and timing of lithospheric modification and replacement beneath the eastern North China Craton: Peridotitic xenoliths from the 100 Ma Fuxin basalts and a regional synthesis. Geochim. Cosmochim. Acta 71, 5203-5225

Zou, H., 1998. Trace element fractionation during modal and nonmodal dynamic melting and open-system melting: A mathematical treatment. Geochim. Cosmochim. Acta 62, 1937-1945

Chapter 3

Chemical and physical controls on mechanisms of water incorporation and loss in olivine and orthopyroxene from arc peridotite xenoliths

3.1 Introduction

It is now well-established that the nominally anhydrous minerals (NAMs) that constitute the majority of Earth's mantle are capable of incorporating small quantities of hydrogen as hydroxyl ions (OH^-), colloquially termed "water" (Bell and Rossman 1992, Hirschmann 2006). Despite behaving as a trace component, water has a disproportional influence on many of the key geophysical and geochemical properties of the mantle. Perhaps most significantly, water in NAMs will reduce the mechanical strength of the mantle increasing the propensity for mantle convection and will also lower the peridotite solidus (Hirth and Kohlstedt 1996, Mei and Kohlstedt 2000, Gaetani and Grove 1998, Costa and Chakraborty 2008, Hirschmann et al. 2009, Green et al. 2010, Till et al. 2011). Since realising the importance of water for Earth's mantle and crustal evolution, a number of studies attempted to constrain the factors controlling water solubility and partitioning in and between olivine and pyroxene (e.g., Hirth and Kohlstedt 1996, Zhao et al. 2004, Lemaire et al. 2004, Matveev et al. 2005, Berry et al. 2005, Hauri et al. 2006, Berry et al. 2007, Ardia et al. 2012, Férot and Bolfan-Casanova 2012, Kovacs et al. 2012, Gaetani et al. 2014). Despite the relatively simple chemistry of these phases, particularly olivine, it is now apparent that there is no single parameter which controls the incorporation of water in NAMs, with pressure, temperature, oxygen fugacity, water fugacity, silica activity and major/trace element composition of both crystal and melt all playing a role. It is thus important to consider how the interplay between these parameters influences water incorporation particular to different mantle domains in order to fully understand the behaviour of water on a global scale.

At subduction zones, water is a major component of fluids generated during dehydration and melting of subducted crust and melting of the overlying mantle wedge (Elliott et al. 1997, Schmidt and Poli 1998, Wallace 2005, Hirschmann 2006, Till et al. 2011). It is vital therefore that we understand how the water content of NAMs in arc mantle responds to the process of hydrous melting and subsequent sub-solidus processes such as melt-rock reaction, both of which are responsible for substantial water transport through the mantle. This however is made difficult due to uncertainty and variability in the composition of 'typical' mantle wedge peridotite, in the composition and nature of water-bearing fluids, in the thermal structure of the mantle wedge and in the physical

mechanisms by which recycled components and arc melts migrate away from the loci of fluid-production. These uncertainties limit the applicability of experimental hydration studies beyond relatively simple, narrowly defined systems which may not fully reflect the complexity of the mantle wedge. Ideally, samples of mantle wedge material should be measured and carefully compared to experimental hydration studies, however this approach has been limited due to the scarcity and representativeness of arc peridotite xenoliths and difficulty in discerning equilibrium water contents in natural samples. In particular, the rapid diffusivity and low solubility of water in olivine under typical upper crustal magmatic conditions often results in significant water-loss during even rapid rates of ascent from the mantle (Demouchy et al. 2006, Peslier et al. 2008, Denis et al. 2013).

Here we report *in-situ* measurements of water by fourier transform infrared spectroscopy (FTIR) in olivine and orthopyroxene from a suite of unaltered, highly depleted harzburgite xenoliths from Ritter Island in the West Bismarck Island Arc (Fig. 1.1, Fig. 1.2). We demonstrate that despite suffering ascent-induced dehydration, the xenoliths preserve equilibrium water contents. We combine our water data with previous measurements of major and trace elements and a novel set of "hydroxylation" experiments to discern the mechanisms by which water is incorporated into olivine and orthopyroxene in the upper mantle wedge. Our data shows that the highly depleted chemistry of arc mantle is the major limiting factor for the water storage capacity of NAMs in subduction systems.

3.2 Methods

3.2.1 Sample preparation and FTIR analysis

Sections 300-600 µm thick were cut from each sample and doubly-polished to 1 µm grade in order to facilitate analysis by infra-red spectroscopy. This sample preparation method has the advantages of allowing rapid *in-situ* analysis of multiple crystals and permitting determination of the spatial distribution of water in a given sample. It also ensures that crystal boundaries are intact, vital for assessing ascent-induced water exchange. The disadvantage is that crystals are randomly orientated; preventing precise determination of water by measuring crystals perfectly orientated to the three principle crystallographic axes.

After cutting and polishing, sections were checked carefully using optical microscopy and suitable crystals were selected and marked onto sample maps. Olivine crystals were selected to cover a wide range of crystal sizes and proximity to patches of reacted sample. In samples which contained the host magma-peridotite contact, crystals were selected to cover the entire section to investigate any water loss/gain due to interaction with the host magma could be investigated. Importantly, these same spots were subsequently measured for trace elements (chapter 2) allowing direct comparison between water content, IR spectra and trace element composition. The spot size for olivine was typically ~100x100 µm; however in reacted samples where clear crystal paths were limited in visible area and water content was higher, spot sizes down to 20x20 µm were used. Large numbers of olivine crystals (n=20-40) were analysed in each sample so that the degree of equilibration between individual olivine crystals could be assessed and also to check for relationships between trace element concentration and water content in an effort to determine trace element substitution mechanisms. In 'residual' samples where olivine crystal boundaries could be identified, analyses were performed as close to the crystal core as possible. Olivine crystal boundaries were typically not determinable in the 'reacted' samples and clear crystal paths suitable for analysis often limited, so analyses were performed on the largest suitable crystal areas. In samples with large, clear crystals with clearly defined crystal boundaries, transects in two perpendicular directions were taken in order to examine homogeneity and anisotropy of water within individual crystals.

Analyses of orthopyroxene crystals were only conducted on entirely transparent patches, free of cloudy textures and exsolution, and as close to the core of the crystal as possible (although crystal boundaries were often hard to reliably identify). This restricted the number of analyses to ~10/sample, which is enough to quantify water content using the method of Kovacs et al. (2008). Where possible, the crystal rim was also analysed to check for homogeneous distribution of water, a prerequisite for applying the aforementioned methodology. In sample 67-02A(3), no suitable orthopyroxene was present in the thick section, so individual crystals were picked from crushed sample and polished into crystal wafers ~300 µm thick and analysed separately. The spot size used for orthopyroxene was usually limited by the transparent area of each crystal. Where

possible, a spot size of 50x50 µm was used, although a smaller size of 20x20 µm was more typical.

Water contents were determined using FTIR spectroscopy at the Research School of Earth Sciences, Australian National University using a Bruker TENSOR 27 spectrometer equipped with a KBr beamsplitter, and attached to a Bruker Hyperion 1000 microscope with automated stage. The microscope was mounted with a nitrogen-cooled MCT-detector and the sample chamber purged with dry air to minimise atmospheric contamination. All analyses were processed using the OPUS 7 software package. Spectra were acquired in the wavenumber range 600-4000 cm^{-1} using 64 scans at a resolution of 4 cm^{-1}. Background spectra were recorded regularly and subtracted from olivine spectra before further processing. Transects on individual crystals were performed by photographing the crystal target and programing two perpendicular transect lines. A spot size of 50x50 µm was used for transects, with overlapping spots to increase spatial resolution. All analyses were performed using unpolarised light. Spectra were corrected for atmospheric contamination using the 'Atmospheric compensation' software algorithm, before being baseline corrected. The baseline correction for olivine spectra was always performed using the 'Concave rubberband correction' method, with 10 iterations and 4 baseline points. The same method was used for orthopyroxene, except 3 instead of 4 baseline points were used. The thickness of each crystal measured was determined using a Mitotuyo analogue micrometer, which has a nominal accuracy of 2 µm.

Water contents for olivine were calculated by integrating beneath peaks in the wavelength region 3600-3000 cm^{-1}. However, due to the association of peaks (or groups of peaks) with different water substitution mechanisms, integration was performed over the appropriate wavelength ranges so that water concentrations associated with each substitution mechanism could be calculated separately. The total integration was converted to the approximate total water content for each crystal using equation (10) from Kovacs et al. (2008):

$$C_{OH} = \frac{\sum_{n=0}^{i} A_i}{n} \cdot k_{pol} \cdot 3$$

where C_{OH} is the concentration of hydroxyl ("water") in parts per million, A_i is the unpolarised absorbance of a randomly orientated crystal normalised to 1 cm and n is the number of crystals measured. k_{pol} is the site-specific calibration factor to convert total absorbance into water concentration and its value depends on the substitution mechanism of water in olivine, determined by comparison of peak position with experimental studies (Kovacs et al. 2010). The factor 3 is used to convert the unpolarised partial absorbance measured in a single crystal orientation into a total absorbance. This procedure only gives an estimate of the total water content of the crystal measured, because the anisotropic distribution of water in olivine means that a truly quantitative measurement can only be made by determining absorption perpendicular to each of the crystal's principle crystallographic axes. However, this procedure can be used to calculate total water content for a sample comprising many crystals in random orientations by summing C_{OH} for each crystal measured and dividing by the number of measurements, with a minimum of 10 measurements necessary to give errors of < ±20 % (Sambridge et al. 2008).

Water contents for orthopyroxene were calculated by integrating beneath peaks in the wavelength region 3650-3250 cm^{-1}. These integration values were normalised to 1 cm and converted to water concentration using the method of Bell et al. (1995):

$$C_{OH} = A_i * 3 / \mu_i$$

This formulation is similar to that used for olivine, but utilises μ_i the integrated molar absorption coefficient (14.84 ppm^{-1} cm^{-2} for orthopyroxene). As with olivine these measurements were performed on randomly orientated crystals and hence an estimate of the total water content of orthopyroxene in a sample can only be achieved by measuring many crystals in random orientations, summing their absorbance and dividing by the number of analyses (Sambridge et al. 2008).

Total uncertainties in the values for water contents reported are comprised of uncertainties in:

1. The integration beneath each peak, defined by the choice of wavenumbers between which the integration is performed and any interferences on the peaks,

such as uncorrected atmospheric contamination. This is negligible in these samples due to the consistency of baseline correction procedures and integration periods chosen, and due to the absence of major atmospheric contamination at the low wavenumbers involved

2. The thickness of each point analysed. This is <1 % since the error in the micrometer used (2 μm) is much smaller than the thickness of the samples (300-600 μm)
3. The anisotropic distribution of water in silicate minerals means calculations of water content from single measurements on randomly orientated crystals are subject to large errors. This is difficult to estimate because it will vary depending on how water is substituted into the crystal lattice. We estimate it for these samples by taking the standard deviation of core measurements from the 10 largest crystals from 3 'residual' samples which show no evidence for water loss (see discussion). Assuming the variation in water content is only due to anisotropy gives differences between the most water-rich and water-poor crystals of up to 40 %, which we take as a conservative estimate for the uncertainty associated with anisotropy
4. The calibration factor used. This is thought to be < ± 15 % (Bell et al. 1995; Kovacs et al. 2010)

Given these individual uncertainties, a total uncertainty on each value is likely to be ~40 %, and in many cases will be less than this. Reproducibility of the analyses was tested by measuring the same olivine spot throughout the analytical period, returning values of 6.2, 6.4 and 6.5 ppm. In addition, multiple orthopyroxenes in one sample were measured twice on separate days returning average values of 59 ppm and 61 ppm. Reproducibility is therefore taken as better than 5 %.

3.2.2 Experimental methodology

Two sets of 'hydroxylation' experiments were conducted to investigate the incorporation mechanisms of water in olivines from 'residual' and 'reacted' Ritter samples. The first experiment was designed to investigate the role of Fe^{3+} which as we discuss later may play an important role in water incorporation by charge balancing H^+ (Berry et al. 2005,

Berry et al. 2007, Grant et al. 2007b). It was conducted in two stages; an annealing stage at 1 atm. under reducing conditions to eliminate water and Fe^{3+} followed by re-addition of water (hydroxylation) at 1 GPa. The olivines selected for this experiment were picked from a 'residual' sample 67-02B(1) and a 'reacted' sample 67-02B(5). Crystals of San Carlos olivine were included since the 'raw' crystals are water under-saturated, show no absorbance and thus acted as tracers to ensure our hydroxylation experiments were successful. In addition to this we also included crystals of olivine from a gabbroic arc cumulate (Tollan et al. 2012) and hydrothermal olivines from Zabargad, Egypt (Miller et al. 1987). Both of these samples contain measureable water but do not display evidence for water bonded with Fe^{3+}. They were included to act as monitors in case unwanted oxidation occurred, which would be reflected in new IR peaks in the region 3400-3300 cm^{-1}.

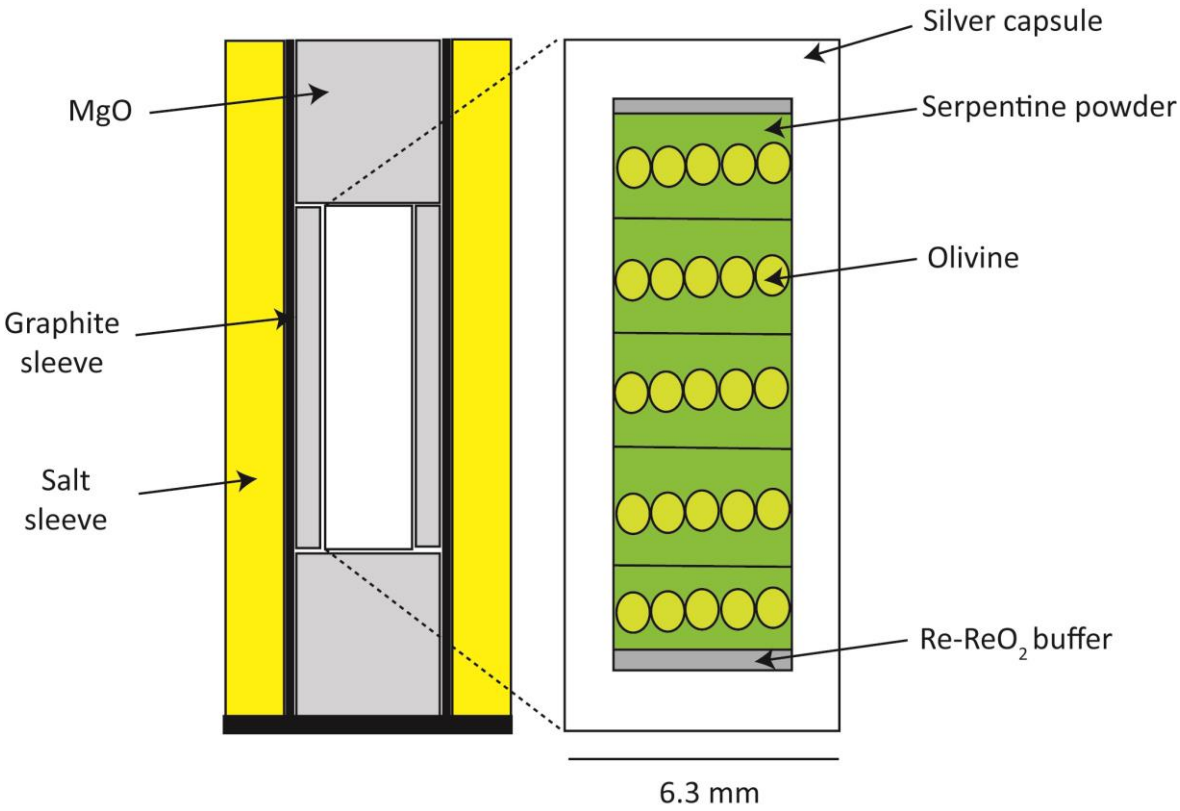

Fig. 3.1 Capsule design for the first 'hydroxylation' experiment. Outer capsule design on the left and inner capsule design on the right. Each layer of five olivines represents a different sample divided by a silver film (see text)

First, individual crystals were selected from each sample and checked under optical microscope for any unwanted surface impurities. Five crystals from each sample were then measured by FTIR. These measurements were conducted on whole (i.e. unpolished) crystals and were done to ensure that they contained representative defect structures for that particular sample. For the annealing stage, crystals from each sample were loaded in individual platinum crucibles which were then suspended from platinum wire to form a chandelier arrangement, allowing annealing of all crystals at identical P-T-$ƒO_2$ conditions. Annealing was conducted in 1 atm. gas mixing furnaces at 1400 °C for 24 hours. Oxygen fugacity was controlled through CO-CO_2 equilibria and was set to a value equal to -2.5 log units below the nickel-nickel oxide (NNO) buffer at which essentially all Fe should be Fe^{2+} (Mallmann and O'Neill 2009). The redox conditions were maintained at a constant value throughout the annealing process, including during cooling of the samples to low temperature before removal from the experimental apparatus. After this stage, each crystal was again measured by FTIR, this time to ensure that all water had been eliminated from the crystal structure. Following this, the olivine crystals were hydroxylated at elevated temperature and pressure in a piston cylinder apparatus. The capsule design involved an inner and outer capsule (Fig. 3.1). The inner capsule was composed of a single silver tube 6.3 mm in diameter which was divided into compartments using thin silver film dividers and sealed with a silver lid. Each of the compartments contained crystals from an individual sample, surrounded by powdered serpentine which acted as the water source. The top and bottom compartments also contained a solid-state Re-ReO_2 buffer which is substantially more oxidised than the redox conditions imposed during annealing. The purpose of the buffer was to test whether the crystal defect structures remained unaltered during hydroxylation, which would be indicated by the appearance of peaks between 3400-3300 cm^{-1} in olivines in the cumulate and Zabargad olivines. The outer capsule consisted of sleeves of MgO, graphite and salt to maintain an even distribution of temperature and pressure. Hydroxylation was conducted at 1 GPa and 800 °C for 48 hours, with temperature measured using a Pt-PtRh thermocouple. These conditions were chosen so that serpentine would break down, releasing free water to diffuse into the olivine structure decorating defect sites

equilibrated during the annealing stage. The low temperature and short run time also ensured point defect populations equilibrated during the annealing stage would be un-affected. After cooling, the inner capsule was removed from the assembly and a small hole drilled to identify the presence of free water, confirming the breakdown of serpentine. Removal of individual crystals from the capsule was not possible, so the whole capsule was cut and polished on both sides to facilitate subsequent measurement of the new IR spectra by FTIR. All FTIR measurements done during the experimental routine followed the same methodology as the *in-situ* analyses described above.

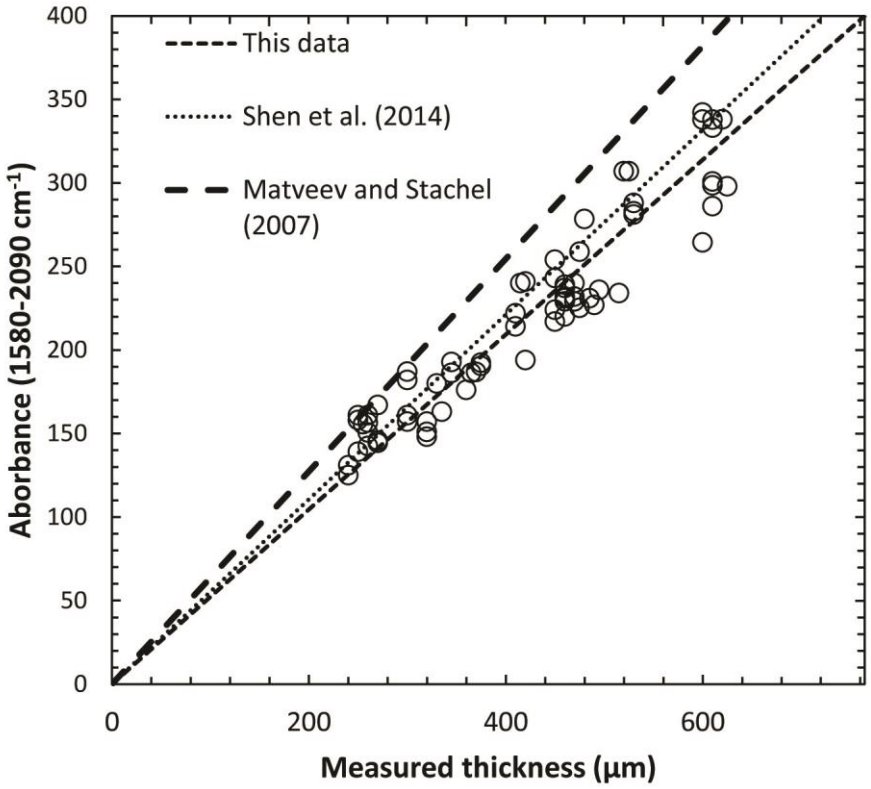

Fig. 3.2 Calibration of the silicate overtone region (1580-2090 cm^{-1}) of olivine as an 'internal micrometer'. Data are for olivines in this study measured *in-situ* on double-polished thick sections of variable thickness, with thickness pre-determined with a micrometer. Dashed lines represent a regression of this dataset and comparisons with previous calibrations

The second hydroxylation experiment was performed with 'residual', 'reacted' and San Carlos olivines but without the initial annealing stage and was designed to test further whether the annealing at low fO_2 changed the solubility of water in the Ritter olivines. The capsule design was similar to the first hydroxylation experiment but lacked dividers. Crystals were photographed before being placed in the capsule to ensure they could be identified after the experimental run. The run conditions were identical to the first experiment, however the water source in this case was de-ionised H_2O, pipetted into the capsule before sealing. Crystals were removed whole from the capsule after the experiment and bore no visible signs of deformation, such as cracks or surface alteration. Since the spectra for olivines from this experiment were obtained on whole crystals (i.e., not cut and polished) thickness could not be directly measured reliably with a micrometer. To obtain thickness information we used the absorption in the silicate overtone region, which is strongly dependent on thickness, as in 'internal micrometer', similar to the methods of Matveev and Stachel (2007) and Shen et al. (2014). We used the measured thickness and IR spectra of olivines from the polished thick sections as our calibration since they span a large range of thicknesses (~200-600 μm), integrating the silicate overtones between 1580 cm^{-1} and 2090 cm^{-1}. The results are displayed in Fig. 3.2 and compared to the calibrations of Matveev and Stachel (2007) and Shen et al. (2014). Regression of our data yields the relationship $A_{overtones} = 0.523t$, where A is the integrated absorption in the region 1580-2090 cm^{-1} and t is thickness in μm with an uncertainty of <15 %. This result is within uncertainty of the slope found by Shen et al. (2014) of 0.553. Using this method we were able to normalise and directly compare all experimentally hydroxylated olivines.

3.3 Results

3.3.1 Olivine

Olivine crystals from 'residual' and 'reacted' samples display similar IR spectra, with three distinct peak groups identified (Fig. 3.3). Almost all absorption in olivine crystals from each sample is associated with a double peak at intermediate wavenumbers of 3354-6 cm^{-1} and 3328 cm^{-1}, with a small shoulder at ~3310 cm^{-1} occurring on the lower wavenumber peak occasionally. In both the dunite, 67-02D(3), and a 'residual' peridotite

(67-02E(1)) a double peak at wavenumbers 3572 cm^{-1} and 3525 cm^{-1} with much lower intensity is observed (in other samples this double peak is rarely observed or below the limit of detection). The final peak identified is a much broader single peak centred at approximately 3170 cm^{-1}, also with low intensity.

Despite the position of peaks being similar in crystals from texturally contrasting samples, there are some important differences. Firstly, the total absorption is generally greater in crystals from 'reacted' harzburgites corresponding to higher concentrations of water. Secondly, the lower wavenumber peak (3328 cm^{-1}) often contributes more to the total absorbance in olivines from 'reacted' harzburgites. In particular, the most water-rich olivines from sample 67-02A(3) often display spectra where the intensity of this lower wavenumber peak is greater than the higher wavenumber peak. This increase in relative intensity of the lower wavenumber peak is strongly correlated with total water and may indicate a change in substitution mechanism (see Chapter 5 for discussion).

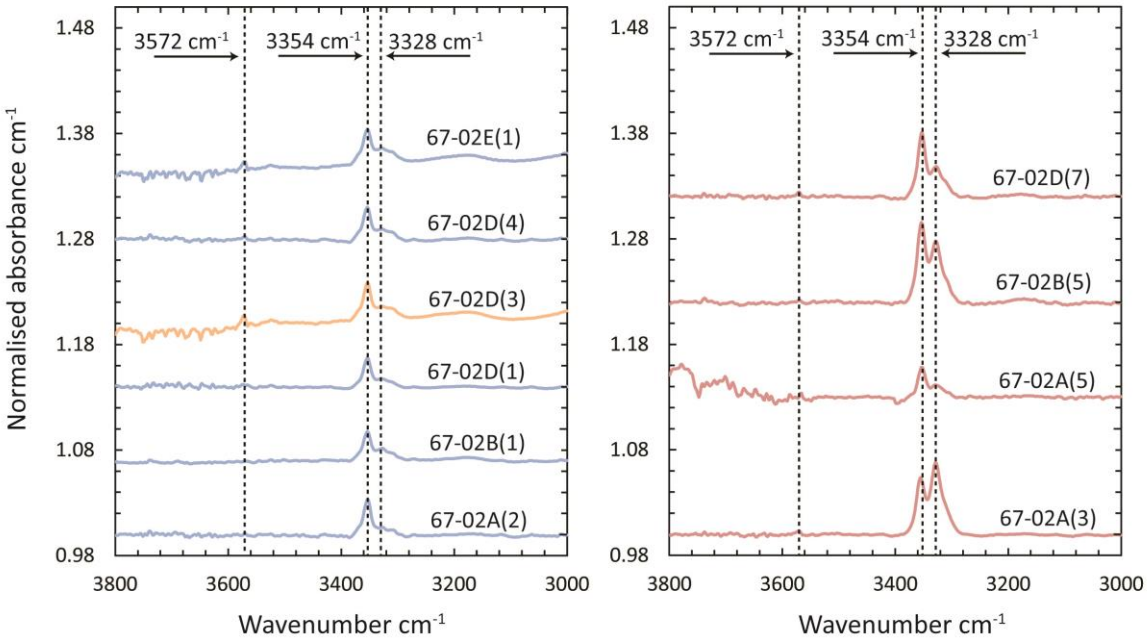

Fig. 3.3 Averaged IR spectra for olivines from samples in this study. Samples on the left are from 'residual' peridotites (blue lines) and a dunite (orange line). Samples on the right are from 'reacted' peridotites (red lines). Note generally greater absorbance in olivines from 'reacted' samples and greater contribution from the peak at 3328 cm^{-1}. All spectra are normalised to 1 cm and offset for clarity.

Sample	Type	No. of crystals	Average normalised absorbance 3300-3400 cm^{-1}	Average normalised absorbance 3500-3600 cm^{-1}	Average water (ppm) 3300-3400 cm^{-1}	Average water (ppm) 3500-3600 cm^{-1}	Max. total water (ppm)	Min. total water ppm
67-02A(2)	Residual	42	30.2		5.4		9.3	2.4
67-02A(3)	Reacted	23	89.9		16.2		28.0	7.0
67-02A(5)	Reacted	42	32.9		5.9		7.8	3.8
67-02B(1)	Residual	39	25.7		4.6		7.4	2.1
67-02B(5)	Reacted	35	61.7		11.1		16.4	5.9
67-02D(1)	Residual	25	24.7		4.5		5.9	3.1
67-02D(3)	Dunite	24	28.4	5.2	5.1	0.9	9.8	3.5
67-02D(4)	Residual	39	31.8		5.7		10.7	2.5
67-02D(7)	Reacted	37	61.2		11.0		15.1	7.7
67-02E(1)	Residual	35	30.8	6.3	5.5	1.1	10.1	1.5
67-02E(3)	Reacted	20	21.9		3.9		5.1	8.4

Table 3.1 Summary of FTIR data for olivine. Averaged normalised absorbance is the measured absorbance in the wavelength region noted for all crystals multiplied by three to take into account anisotropy. All data is normalised to a thickness of 1 cm. Uncertainty on individual randomly orientated crystals is <40 %.

Sample	Type	No. of crystals	Average normalised absorbance	Average water (ppm)	Max. water (ppm)	Min. water (ppm)
67-02A(2)	Residual	20	873	59	90	24
67-02A(3)	Reacted	13	755	51	88	23
67-02B(1)	Residual	11	829	56	70	41
67-02D(1)	Residual	9	947	64	84	51
67-02D(4)	Residual	11	474	32	47	22
67-02D(7)	Reacted	11	1214	82	102	64
67-02E(1)	Residual	12	444	30	36	24

Table 3.2 Summary of FTIR data for orthopyroxene. Average normalised absorbance is the measured absorbance in the wavelength region 3650-3250 cm^{-1} for all crystals multiplied by three to take into account anisotropy. All data is normalised to 1 cm. Uncertainty due to anisotropy is approximately the difference between the max. and min. values, since variation within crystals is typically <15 %.

The absorption beneath the trivalent peaks was converted to water content, using the method described in the methods section. Absorption associated with the 3170 cm^{-1} peak was variable, but typically small which, combined with the very low value for the calibration factor for this substitution mechanism (0.03 ± 0.03; Kovacs et al. 2010), meant it was unnecessary to include it in calculations of total water. The absence of any significant absorption at higher wavenumbers therefore means total water content is proportional to absorbance at intermediate wavenumber peaks. Water contents in olivines from 'residual' samples varied from 1.5-10.7 ppm (Table 3.1). However there was still substantial variation between olivines within individual samples, often covering much of this total range and outside the estimated uncertainties due to analytical error and anisotropic distribution of water (Fig. 3.4). Water contents in olivines from 'reacted' samples varied from 3.8-28.0 ppm (Table 3.2), tending to be higher than those from 'residual' samples. Again, substantial ranges are present in individual samples well outside the estimated uncertainties (Fig. 3.4). To determine the origin of this crystal-crystal variation, we measured the distribution of water on a single crystal scale. FTIR profiles were measured on multiple olivines from 5 'residual' samples where crystal boundaries were clearly defined. All profiles show significant normal zoning, with maximum water contents in the crystal cores, occasionally forming a plateau, decreasing to minimum values close to the crystal rims to form 'bell-shaped' concentration distributions (Fig. 3.5). Such profiles are consistent with water-loss profiles described in other studies of mantle olivine (Peslier et al. 2006, Demouchy et al. 2006, Peslier et al. 2008, Denis et al. 2013). To investigate the role of internal fractures on the distribution of water, traverses on strongly fractured olivines from sample 67-02A(2) were conducted. These profiles show minima in absorption at both the true crystal edges and also either side of internal fractures (Fig. 3.5a).

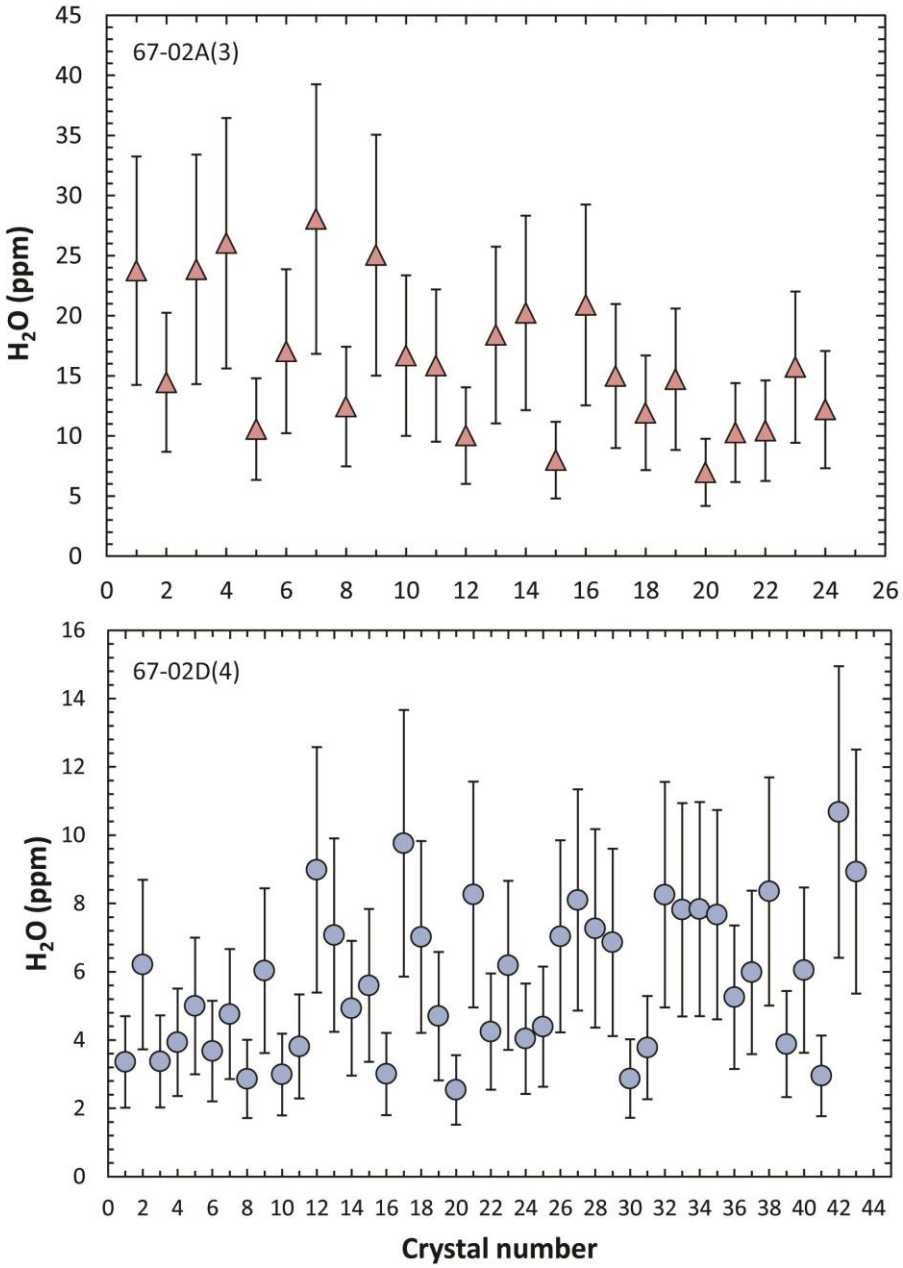

Fig. 3.4 Crystal to crystal variation in total water content for cores of olivine in 67-02A(3) and 67-02D(4). Error bars reflect a conservative estimate of uncertainty (<40 %) due to crystal anisotropy. Variation is clearly observed outside this maximum uncertainty illustrating real differences between the water content of individual crystals

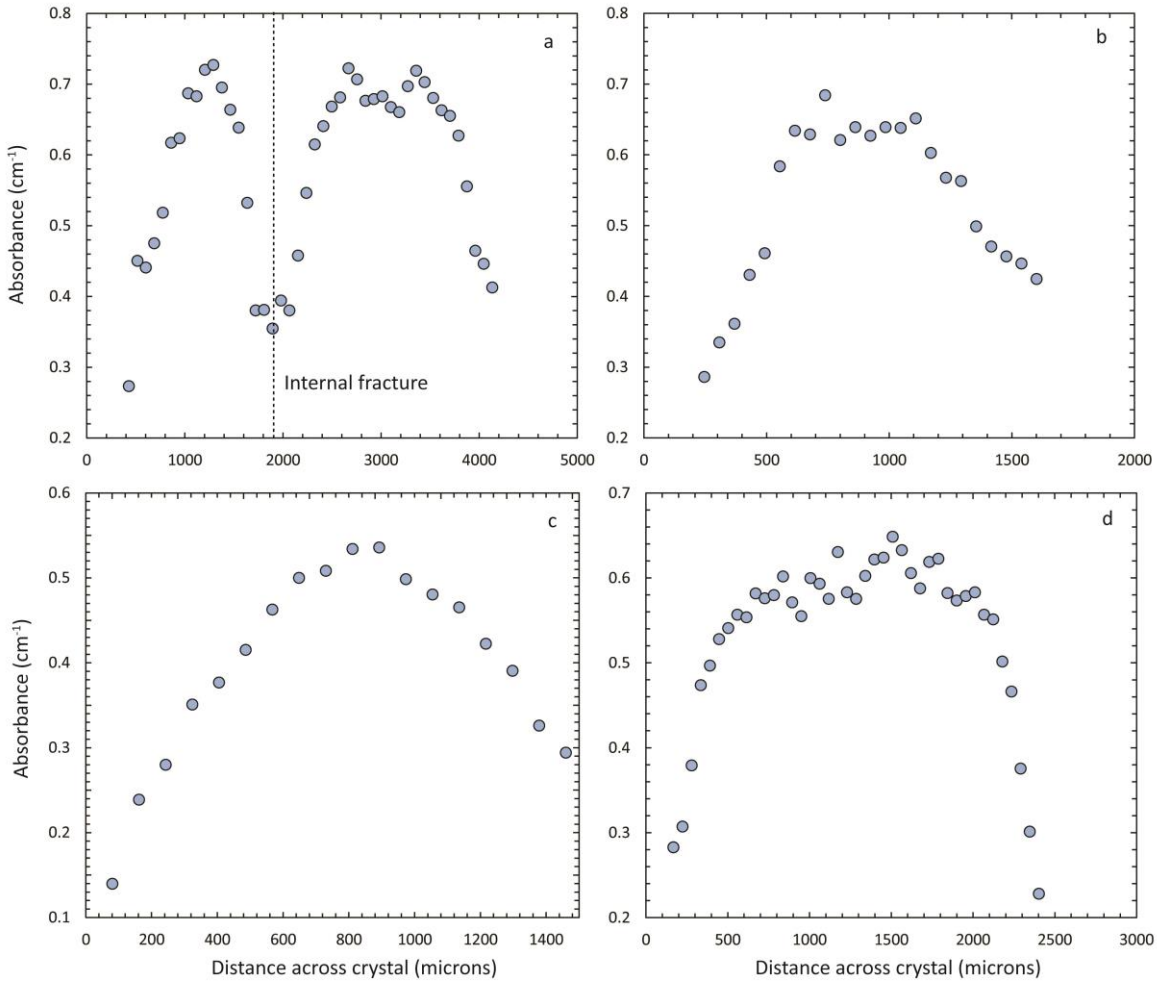

Fig. 3.5 Substantial rim to rim variation in infrared absorption of olivine crystals from four different 'residual' samples. a) 67-02A(2); b) 67-02B(1); c) 67-02D(4); d) 67-02E(1). Highly fractured olivines in sample 67-02A(2) display drops in absorbance both at crystal rims but also at the internal fractures.

3.3.2 Orthopyroxene

IR spectra were measured and water contents calculated for orthopyroxene from 7 samples (5 'residual' harzburgites and 2 'reacted' harzburgites). The smaller number of 'reacted' samples used is due to an absence of transparent orthopyroxene crystals in several samples. Orthopyroxene spectra were consistent between samples, with 5 peaks identified (Fig. 3.6). The most intense peak is located at 3600 cm^{-1}, followed by a double peak at 3545 and 3522 cm^{-1}. Lower intensity, broader peaks occur at ~3400 cm^{-1} and occasionally at ~3060 cm^{-1}. There is substantial variation between the relative intensity of peaks in different orthopyroxene crystals in a given sample, particularly the intensity of the double peak (3545 and 3522 cm^{-1}) resulting in differences in water content. This is most probably due to the anisotropic distribution of water of the randomly orientated crystals measured, as evidenced by associated variations in the peaks in the orientation-specific silicate overtone region (1500-2200 cm^{-1}).

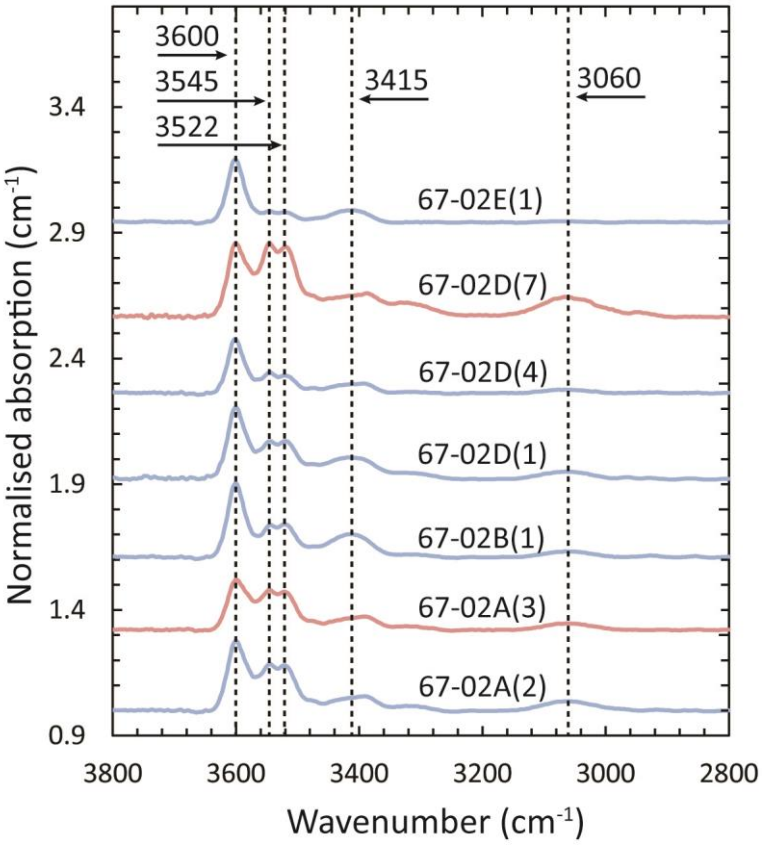

Fig. 3.6 Average FTIR spectra for multiple orthopyroxenes from each sample with sufficient transparent crystal paths. Blue and red lines are for orthopyroxenes from 'residual' and 'reacted' peridotites respectively. All spectra are normalised to 1 cm.

Average core water contents varied from 30-82 ppm (Table 3.2), with no clear distinction between orthopyroxenes from 'residual' and 'reacted' samples although comparison is limited due to the lack of transparent orthopyroxenes in 'reacted' samples. Notably, the water content of orthopyroxene in sample 67-02A(3), which hosted the most water-rich olivines, was indistinguishable from 'residual' samples, although water for orthopyroxene from this sample was measured in picked crystals from crushed hand sample and so may have originated from an unreacted part of the sample. The limited amount of transparent zones in most crystals prevented a thorough investigation into inter-crystal variation. The limited core-rim analyses conducted were generally consistent with each other, although there were exceptions (Fig. 3.7). Several orthopyroxenes from sample 67-02A(2) showed slight (15 %) reverse zoning, whilst an orthopyroxene from sample 67-02B(1) showed greater variation (38 %). This is however substantially less than the zoning measured in olivine, which was typically > 50 % and often > 70 %.

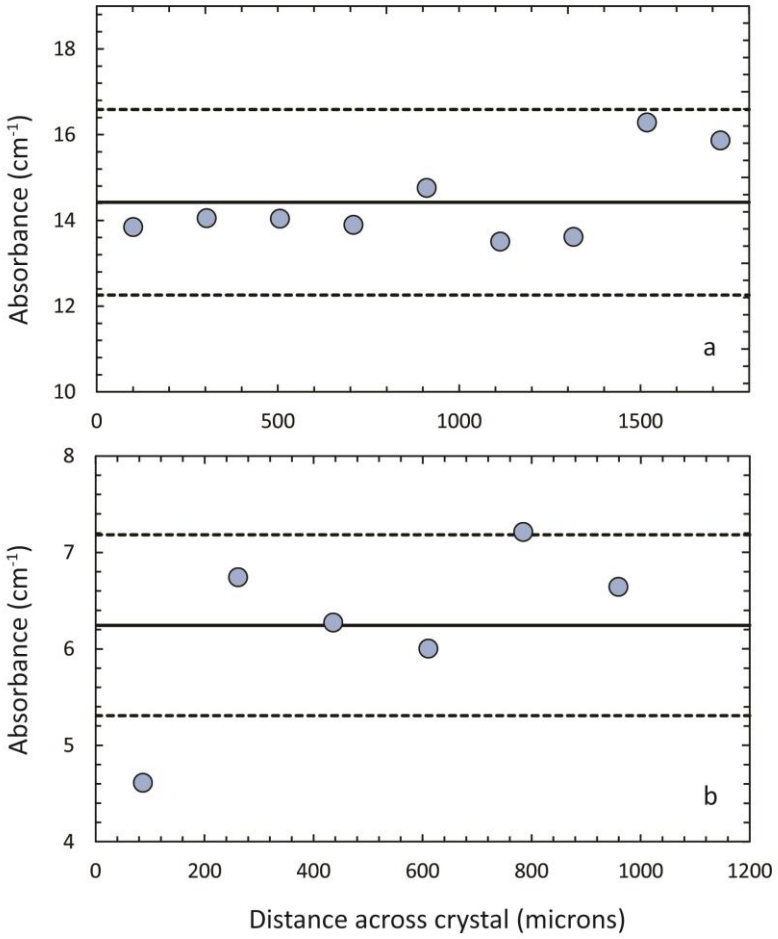

Fig. 3.7 Rim to rim profiles across orthopyroxenes from two different samples. a) 67-02A(2); b) 67-02B(1). Solid line is the average absorption for the crystal, whilst dashed lines represent plus and minus 15 % of this value. Variation is not systematic and is substantially less than observed in olivine

3.3.3 Hydroxylation experiments

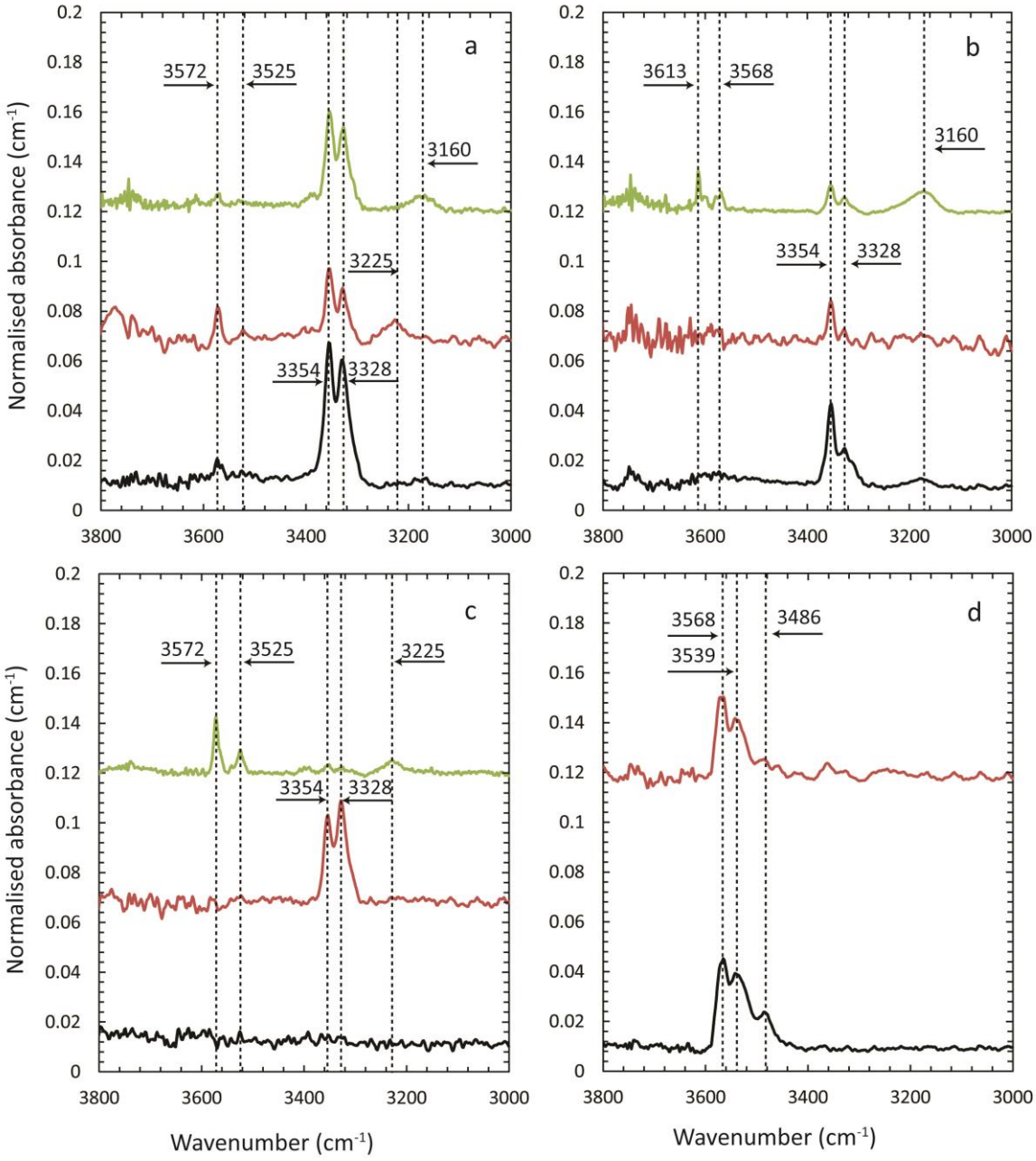

Fig. 3.8 Results of the olivine hydroxylation experiments. FTIR spectra in each diagram represent from bottom to top; 'raw' olivine crystals (pre-experiment); hydroxylation with an annealing stage at low fO_2; hydroxylation without an annealing stage. Samples are: a) 67-02B(5) ('reacted' peridotite), b) 67-02B(1) ('residual' peridotite), c) San Carlos olivine, d) Cumulus olivine (Tollan et al. 2012); this sample was only hydroxylated with an annealing stage. All spectra offset for clarity. See text for a discussion of these results

Fig. 3.8 shows the spectra of crystals before and after hydroxylation with/without the annealing stage. After both experiments the peaks at 3354 cm^{-1} and 3328 cm^{-1} observed in the pre-experimental 'raw' crystals returned. This was irrespective of whether they experienced an annealing stage at low fO_2 or not. Calculated absorbance in this wavenumber region for hydroxylated olivines was always lower than the 'raw' crystals, outside the variation anticipated from just anisotropic distribution of water (Table 3.3). The water contents of hydroxylated olivines from the 'residual' sample, both with and without annealing at low fO_2, were within uncertainty of each other. The water content of hydroxylated olivines from the 'reacted' sample without the annealing stage however were higher than the annealed and hydroxylated olivines by a value close to the limit of our estimated uncertainty. The San Carlos olivines contained no detectable absorbance in the 'raw' crystals. After hydroxylation absorbance was measured in both pre-annealed and un-annealed crystals confirming further the hydroxylation was successful, although the peaks were in different positions (3354 cm^{-1} and 3328 cm^{-1} in the pre-annealed olivine and 3572 cm^{-1} and 3525 cm^{-1} in the un-annealed olivine). Finally no absorbance could be resolved from background noise associated with peaks between 3400-3300 cm^{-1} in either the Zabargad olivine or the cumulate olivine, despite the use of an oxidising buffer, thus demonstrating that the point defect structure was preserved during the hydroxylation stage.

	Raw		Anneal + hydr		Hydr	
Sample	Absorption/cm	Water (ppm)	Absorption/cm	Water (ppm)	Absorption/cm	Water (ppm)
67-02B(5)	70.2 *(5)*	12.7	27.9 *(1)*	5.0	40.8 *(3)*	7.3
67-02B(1)	33 *(8)*	5.9	8.7 *(2)*	1.6	11.1 *(2)*	2.0

Table 3.3 Summary of the olivine hydroxylation experiments. Data shown is for olivines from a 'reacted' sample, 67-02B(5) and a 'residual' sample, 67-02B(1). Absorption is calculated by integrating only the peaks in the region 3400-3300 cm^{-1} and is the average of the number of crystals measured (italicised parentheses). The value for measured absorbance has been multiplied by three to take into account anisotropy. Maximum uncertainties for individual crystals are approximately 40 %. Water content calculated as described in the methods section.

3.4 Discussion

3.4.1 Equilibrium mantle water contents

The well equilibrated textures and major and trace element compositions of olivine and orthopyroxene from 'residual' Ritter peridotites indicate that the samples preserve conditions representative of the upper mantle (chapter 2). In addition the highly depleted orthopyroxene compositions, bulk rock trace element compositions, high Cr# spinels and radiogenic Sr isotope compositions (chapter 4) imply they were residues of hydrous melting in a subduction zone environment. Equilibrium water contents of olivine and orthopyroxene may therefore retain important information regarding the water content of NAMs that constitute the mantle wedge, the recycling of water in subduction zones and the storage capacity of water in highly depleted mantle domains.

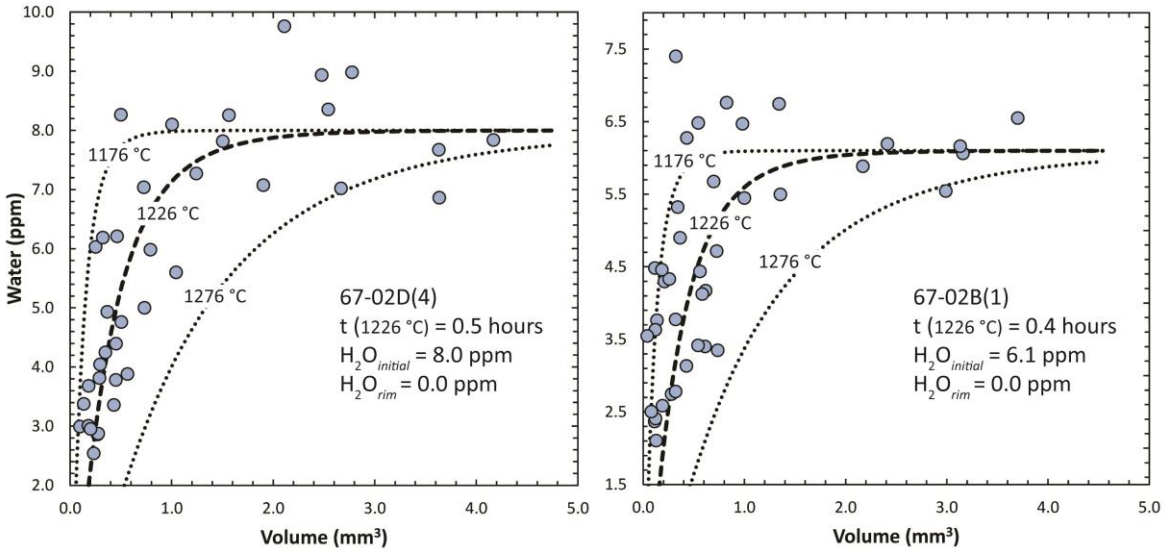

Fig. 3.9 Variation in the water content of the cores of multiple olivines from two 'residual' samples, plotted against estimated volume for each crystal calculated from observed crystal area and assuming spherical geometry. Positive correlation at small volumes/water contents reflects diffusive water-loss on ascent. Plateau values of water at large crystal volumes are interpreted to represent values unaffected by water-loss (equilibrium mantle values). Dashed lines are models of water-loss at magmatic temperatures (see text for model details). Short timescales most likely reflect diffusive loss associated with shallow level magmatic degassing.

Studies attempting to calculate the equilibrium water content of mantle olivine are often hampered by the rapid diffusivity of water, resulting in significant degrees of water-exchange (typically water-loss) during xenolith transport in the host magma (Demouchy et al. 2006, Peslier and Luhr 2006, Peslier et al. 2008, Denis et al. 2013). In order to provide an accurate estimate of equilibrium concentrations either crystals which have been unaffected must be measured, or the water-loss event must be understood and quantified in order to back-calculate to initial values. Alternatively pyroxenes, whose water contents tend to remain unaffected during ascent, can be used to calculate the composition of equilibrium olivine assuming the partitioning of water between minerals is well known at the conditions of interest (Denis et al. 2013).

Olivines from Ritter xenoliths show clear evidence for water-loss (Fig 3.5.). Equilibrium water contents were estimated by plotting the core olivine water contents against crystal volume (calculated from visible crystal area and assuming spherical geometry) for 3 'residual' samples where crystal boundaries could be clearly identified (Fig. 3.9). Errors on each data point will be due not only to uncertainty in the water content but also uncertainty in how close each measurement was to the true core of the crystal, since observations could not be made in 3 dimensions. Firstly, it is clear from these plots that the cores of smaller olivines contain less water, consistent with diffusive exchange with the host magma. Secondly in both of these plots, beyond a critical crystal size (~1.1 mm^3), the positive correlation between water and crystal size ends and water content appears to plateau (within error) at the largest crystal sizes. We interpret this plateau to reflect cores of larger crystals unaffected by water exchange during exhumation, and therefore equilibrium water contents. Furthermore, since multiple crystals exceed this critical size, the method of Kovacs et al. (2008) can be applied to calculate water content. For samples 67-02B(1), 67-02D(4) and 67-02E(1) an average of 10 crystals in each produces values of 6.1 ± 0.5 ppm, 8.2 ± 1.1 and 6.1 ± 1.3 ppm respectively, where the error represents 1 s.d. on the average of these 10 largest crystals.

Knowledge of the partitioning behaviour of water between mantle minerals is vital for calculations of the bulk distribution and concentrations of water in the upper mantle and also for assessing water equilibrium in upper mantle assemblages. Previous studies have found that orthopyroxene typically retains equilibrium mantle concentrations in

samples where olivine displays significant evidence for post-exhumation modification (Demouchy et al. 2006, Peslier et al. 2008, Peslier 2010, Denis et al. 2013). Our measurements of water distribution in orthopyroxene confirm this, with relatively small variations compared to olivine and no evidence for similar diffusion profiles (Fig. 3.7). We infer from this that orthopyroxene retains concentrations reflecting upper mantle equilibrium. Since we also know the equilibrium water content of olivine from the plateau values discussed above, we can combine this information to calculate values of $D_{H_2O}^{opx/ol}$ for the conditions at which the 'residual' peridotites last equilibrated (~1 GPa, ~600 °C). We calculate values of 9.2 ± 1.6, 4.0 ± 1.3 and 4.9 ± 1.2 for the three samples listed above respectively, where uncertainty consists of uncertainty in both the average olivine and orthopyroxene compositions. Our values are very similar to those calculated from experiments by Kovacs et al. (2012), who used the same baseline-correction procedures as this study (4.7 ± 1.1 and 6.7 ± 2 at 2.5 and 4 GPa respectively). The elevated pressures and temperatures (1000-1200 °C) of their experiments however were quite dissimilar to the conditions of equilibration for the Ritter samples. Variations in $D_{H_2O}^{opx/ol}$ may depend on a complex combination of parameters which are presently not fully understood, such as water activity in a co-existing fluid phase, pressure, temperature and mineral composition. The latter is particularly important since the concentrations of Al and Cr are known to strongly influence water solubility in pyroxenes (Stalder 2004, Stalder et al. 2005, Hauri et al. 2006), whilst concentrations of Ti and trivalent species such as Cr^{3+} and Fe^{3+} have important controls on water solubility in olivine (Berry et al. 2005, Hauri et al. 2006, Berry et al. 2007, Peslier 2010). The trace element composition of experimentally hydrated olivines in Kovacs et al. (2012) are not reported, however the San Carlos olivines used in their experiments typically contain significantly higher concentrations of incompatible trace elements than the Ritter olivines (Spandler and O'Neill 2010), although it is possible that the chemistry and thus point defect structures of olivine may have changed over the duration (1-7 days) of the high temperature experiments. The Al_2O_3 content of orthopyroxenes however are very similar to the values measured in Ritter orthopyroxenes (1.27-2.78 wt. % compared to 1.25-1.69 wt. %), and may be a dominant reason why the values of $D_{H_2O}^{opx/ol}$ calculated here and in Kovacs et al. (2012) are lower than other experimental studies which utilised much more aluminous

orthopyroxene (Aubaud et al. 2004, Hauri et al. 2006). This is illustrated in plots of $D_{H_2O}^{opx/ol}$ against Al_2O_3 in orthopyroxene for equilibrium experiments and Ritter samples which show a broad positive correlation (Fig. 3.10). Scatter may be due to competing charge balance of Al by variable amounts of Cr and Fe^{3+} (Stalder et al. 2005); for example, as will be shown later, Fe^{3+} may also play an important role in controlling the water content of orthopyroxene in the samples studied here. Plots of $D_{H_2O}^{opx/ol}$ against both pressure and temperature show no correlation, indicating they may have little effect (Fig. 3.10).

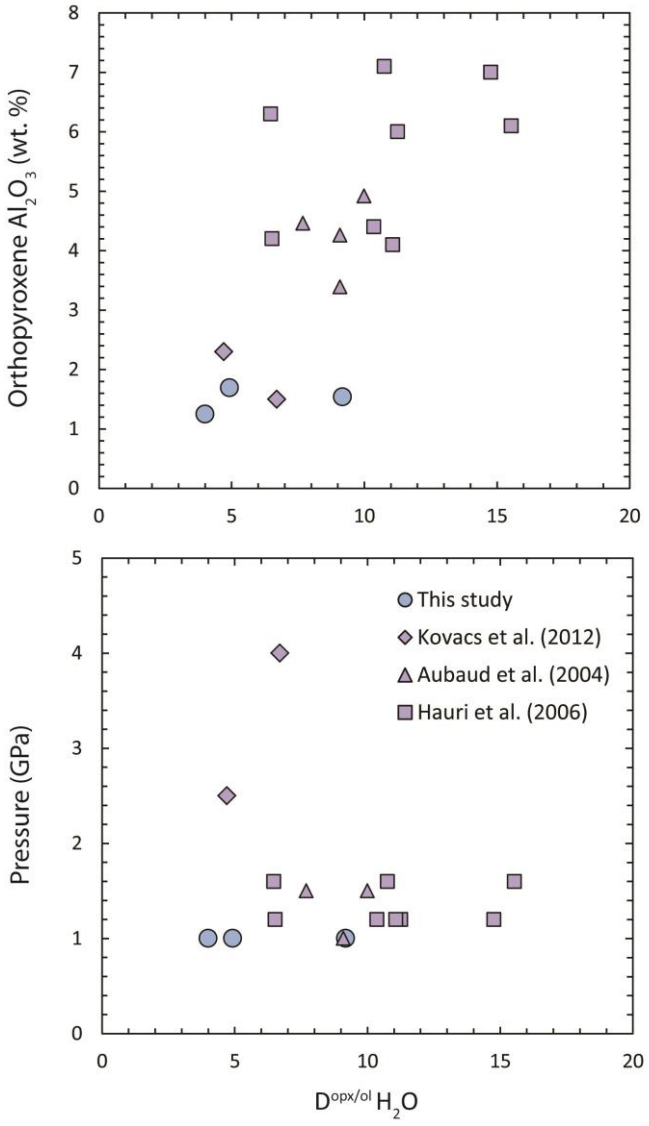

Fig. 3.10 Comparison of $D^{opx/ol}$ H_2O values calculated for Ritter orthopyroxenes compared to experimental partitioning studies (Aubaud et al. 2004, Hauri et al. 2006, Kovacs et al. 2012). There is a broad correlation with Al_2O_3 indicating the importance of this component in controlling the distribution and concentrations of water in the upper mantle. No correlations with pressure or temperature (not shown) indicate they have relatively little control . Pressure for Ritter samples assumed to be 1 GPa.

3.4.2 Comparison to global dataset

Whilst there is currently a substantial dataset for water in mantle olivine and orthopyroxene from a range of tectonic settings, the scarcity of mantle xenoliths from subduction zones has prevented the acquisition of an equivalently large dataset. Our work here therefore adds significantly to the few previous studies of water in NAMs of a purported subduction-related origin (Peslier et al. 2002, Peslier and Luhr 2006, Soustelle et al. 2010, Turner et al. 2012, Soustelle et al. 2013). Of these studies, only Soustelle et al. (2010) and Soustelle et al. (2013) report a sizeable quantity of data for both olivine and orthopyroxene from equivalent highly depleted, oceanic fore-arc mantle.

Our best estimates for the water content of equilibrium arc mantle olivine (6-8 ppm) are similar to these previous studies. Meaningful comparisons with literature data are only possible where diffusive water-loss is absent or corrected for. Both the studies of Peslier and Luhr (2006) and Soustelle et al. (2010) document clear evidence for water-loss from olivine, so we only compare their maximum measured values. The highest water contents for Mexican, subduction-related mantle olivines measured by Peslier and Luhr (2006) is 7.5 ppm, identical to our estimate. These mantle samples are from sub-continental lithospheric mantle and are erupted in alkaline magmas, so whilst they are subduction-related their precise tectonic and magmatic origin means they may not be suitable analogues to compare with the Ritter samples. The mantle xenoliths studied by Soustelle et al. (2010) are very similar to the Ritter samples petrographically, chemically and tectonically (Ionov 2010). The average measured water contents for their coarsest olivine fraction was 6.1 ppm, again identical to our estimate. Perhaps more significantly though, the unusual IR spectra for olivines from this study, which is dominated by absorbance at 3400-3300 cm^{-1}, is very similar to the olivines measured by Soustelle et al. (2010), indicating similar substitution mechanisms which may be compositionally and perhaps even tectonically related. Identical spectra are also observed in olivines from arc peridotite xenoliths from Tubaf Island in the Tabar-Lihir-Tanga-Feni Island Chain (Soustelle et al. 2013 and Tollan, unpublished data). Our estimate of equilibrium mantle water is lower than mantle olivines from other tectonic environments (Fig. 3.11). The most well studied sample types are cratonic mantle (e.g. Grant et al. 2007a, Peslier et al. 2008, Peslier et al. 2010, Baptiste et al. 2012) and off-cratonic (continental) mantle (e.g.

Grant et al. 2007a, Denis et al. 2013, Schmädicke et al. 2013). Estimates for equilibrium mantle values for olivines from these studies (either through direct measurement or calculated assuming equilibrium with coexisting pyroxene) are typically in excess of 15 ppm and in the case of cratonic mantle, often >50 ppm. Crucially though, in the majority of these samples studied the dominant IR absorption occurs at high wavenumbers (3650-3400 cm^{-1}) in contrast to olivines from sub-oceanic arc xenoliths from this study, Soustelle et al. (2010) and Soustelle et al. (2013), implying a distinctly different water incorporation method in olivines from these mantle domains.

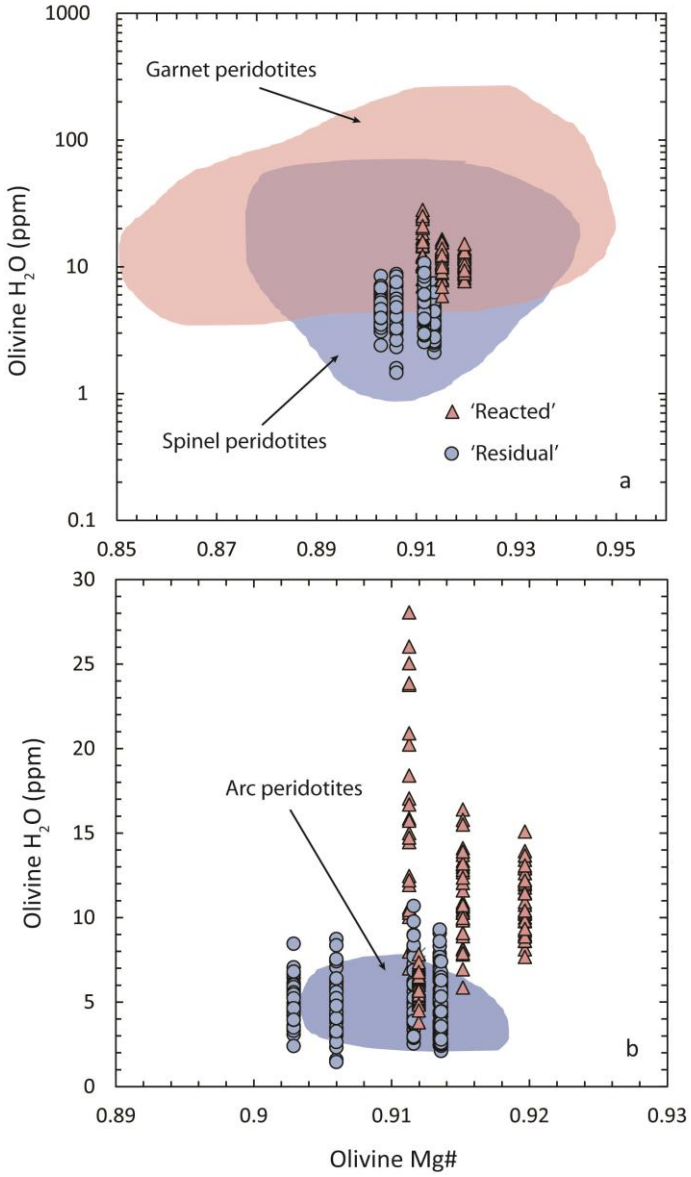

Fig. 3.11 Comparison of water contents of olivines from 'reacted' and 'residual' Ritter samples with a) global data for olivine from cratonic, off-cratonic and oceanic settings (Peslier 2010, Soustelle et al. 2010, Soustelle et al. 2013, Denis et al. 2013, Schmädicke et al. 2013); b) data from other arc peridotites (Soustelle et al. 2010, Soustelle et al. 2013) Note literature data for olivines, particularly from spinel peridotites, may have been affected by water-loss.

Our estimates for orthopyroxene water contents (30-80 ppm) are low compared to both arc data and the global dataset (Soustelle et al. 2010, Peslier 2010, Turner et al. 2012). However, we caution against direct comparisons of orthopyroxene from different studies unless the same baseline correction procedure is applied. For example, both Soustelle et al. (2010) and Turner et al. (2012) report generally much higher orthopyroxene water contents (and in the former case where olivine was also measured, $D_{H_2O}^{opx/ol}$). Close inspection of their IR spectra reveals significant differences in baseline correction though. For example, our method fixes the spectrum to the baseline at ~3200 cm^{-1}, whilst the aforementioned studies apply a correction which fixes the spectrum to the baseline at much lower wavenumbers (as low as 2800 cm^{-1}). This more liberal correction results in a much greater area to integrate and therefore greater total absorbance/water content. Consequently, we restrict ourselves only to comparisons with olivine for which similar issues are relatively minor.

3.4.3 Diffusive water-loss and magma ascent time

It is clear from the relationship between crystal size and water content (Fig. 3.9), from traverses on individual crystals (Fig. 3.5) and from a lack of correlation between water and other incompatible elements within individual samples that olivine has been affected by diffusive water-loss. It should be noted that it is possible that apparent water-loss features could actually be due to gain of water. This could occur if water diffusing into the crystal decorates defect site vacancies present due to a pre-existing concentration gradient of a co-substituting element (see chapter 5). We can rule this out however since no trivalent elements show any such variations. Fe^{3+} wasn't measured, however since the 'reacted' samples have elevated oxygen fugacities, Fe^{3+} concentrations in olivine should be greater at the crystal rims, not lower.

Water-loss in olivine is usually attributed to the low water fugacity of the host magma (Demouchy et al. 2006, Denis et al. 2013). However in this case, the magma is hydrous, with a water fugacity high enough to hydrate olivine at mantle pressures (see discussion below and chapter 5). The cause of the observed water-loss must therefore be due to a drop in the water fugacity of the melt during ascent to surface. The solubility of water in melt and crystals is known to be a sensitive function of pressure, with lower

pressures inducing both degassing of hydrous magmas and a drop in the solubility of water in olivine (e.g., Newman and Lowenstern 2002, Lloyd et al. 2013). It is most likely that the water-loss was initiated at lower pressures where arc magmas reach vapour saturation. The diffusion profiles measured should thus reflect the time between the initiation of this degassing stage and final eruption and quenching of the xenoliths. The observation that water-loss is not only controlled by true crystal rims, but also by internal fractures (Fig. 3.5a) implies that crystal fracturing either preceded water-loss or was coincidental. We calculated the time for this water-loss event by comparing diffusion models to the multi-crystal data, which has two main advantages over modelling diffusion in individual crystals (e.g. Demouchy et al. 2006). Firstly water-loss is expressed on a sample-wide scale, albeit with a loss of resolution. Secondly, assuming there is no preferential crystal alignment in these samples, the random orientation of each crystal negates the need for orientation-specific diffusion modelling. Errors are introduced due to the simplification of olivine morphology to a sphere and the uncertainty over the precise location of the crystal core. The temperature of the host magma is constrained in chapter 5 to be 1226 °C however we also bracket this with temperatures ± 50 °C to illustrate the effect of uncertainties in this calculation. Recently, Padrón-Navarta et al. (2014) showed that rate of water diffusion is different depending on the type of defect it is associated with. Therefore, accurate modelling of water diffusion in natural crystals can only be achieved when the diffusion coefficient for the observed point defect is chosen. The diffusion coefficient used in the models was from Demouchy and Mackwell (2006), which is appropriate since their pre-exponential diffusion coefficient was derived using experimentally-hydrated olivines with similar FTIR spectra to the olivines in this study and hence diffusion of the same hydrous defect type. Due to the random crystal orientations, a 'bulk' diffusion coefficient was calculated by averaging diffusion in each orientation. The diffusion profiles measured in individual crystals could not be modelled since crystallographic orientation was not determined. The equation used to model diffusion was taken from Crank (1956) for diffusion in a sphere, solved to the 10th term:

$$\frac{C - C_1}{C_0 - C_1} = 1 + 2 \sum_{n=1}^{\infty} (-1)^n \, exp\,(-Dn^2\pi^2 \frac{t}{a^2})$$

where C_1 is the initial concentration at the core of the crystal, C_0 is the concentration at the crystal rim, D is the diffusion coefficient, t is time and a is the diffusion length. We could not measure the precise rim concentrations in the olivines since the low water concentrations prevented us from using suitably low spot sizes during analysis and so we therefore assume an equilibrium concentration of 0.0 ppm. The timescales we estimate using the multi-crystal approach are 0.2-0.8 hours for both samples 67-02D(4) and 67-02B(1) over the temperature range 1276-1176 °C (Fig. 3.9). These timescales are much shorter than other estimates of xenolith ascent time (see Denis et al. 2013 for a summary). We suggest that the short times are consistent with water-loss triggered by degassing at shallow magmatic depths, since the high water contents of the host arc magma (3.8 wt. % H_2O, see chapter 5) will limit dehydration of olivine at greater depths by maintaining a higher water fugacity. Water fugacity (and therefore water solubility in olivine) would decrease as the magma rises, however this would be buffered to some degree by earlier degassing of CO_2.

3.4.4 Water incorporation mechanisms in olivine and an experimental test

One of the principle advantages of using FTIR to measure water in NAMs is that the position of peaks at different IR wavenumbers can be used to extract information regarding methods of water incorporation within crystal structures. Since the incorporation of water at specific defect sites is known to change many of the physical properties of olivine, this information can, in turn, be used to constrain the physical and chemical controls on mantle hydration and geodynamics. The relatively simple chemistry of olivine compared to other mantle phases and its modal dominance in most mantle rocks has led to a number of experimental and computational studies which have attempted to associate specific chemical and thermodynamic system properties to unique IR peaks (Kohlstedt et al. 1996, Lemaire et al. 2004, Zhao et al. 2004, Berry et al. 2005, Mosenfelder et al. 2006, Berry et al. 2007, Grant et al. 2007b, Walker et al. 2007, Kovacs et al. 2010, Férot and Bolfan-Casanova 2012, Gaetani et al. 2014). Peaks at higher wavenumbers (3650-3400 cm^{-1}) are usually attributed to hydrogen charge-balancing ('decorating') silicon vacancies created in the olivine structure either due to low silica activity of the system and/or presence of hydrated Ti point defects (Ti-clinohumite) which shifts the site occupancy of Ti from tetrahedral to octahedral (Walker et al. 2007). The

latter incorporation method is identified by a double peak at 3572 and 3525 cm^{-1}, and may be the dominant substitution mechanism in typical shallow upper mantle (Berry et al. 2005, Walker et al. 2007, Schmädicke et al. 2013). In contrast to these studies, Gaetani et al. (2014) proposed that the intensities of these peaks are predominantly a function of water fugacity, with minimal contribution from Ti-clinohumite point defects. This latter study however compared bulk absorbance with Ti concentration, rather than absorption associated only with Ti-related peaks, as in Schmädicke et al. 2013 where a relationship between Ti and Ti-related absorbance was found. A broad peak at low wavenumbers (3100-3250 cm^{-1}) is sometimes observed in off-craton mantle olivines, typically in combination with the Ti-clinohumite peaks due to the decoration of Mg-vacancies on octahedral sites formed in response to high silica activity. Finally, peaks at intermediate wavenumber (3400-3300 cm^{-1}) are occasionally observed in both upper mantle olivines and also magmatic olivines (Matveev et al. 2005). These are attributed to a coupled substitution involving hydrogen and a trivalent trace cation in the olivine structure. Of the many trivalent trace elements which may substitute into olivine, only those occurring at the ppm or greater level will have any substantial impact on the water content, since the substitution operates on a 1:1 molar basis. The most likely candidates under typical mantle conditions are therefore Fe^{3+}, Al^{3+}, Cr^{3+} and Sc^{3+} (Berry et al. 2005, Berry et al. 2007, De Hoog et al. 2010). However in natural upper mantle olivines these 'trivalent' peaks, when present, typically only contribute a minor component of the total spectral absorbance and have previously been considered to form due to late stage oxidation during magmatic transport and thus not a primary mantle signature (Berry et al. 2005).

The IR spectra of all Ritter olivine crystals are unusual compared to the global database of olivine measurements in having almost all absorption associated with the trivalent cation substitution peaks (Fig. 3.3). Since these peaks are ubiquitous in Ritter olivines, including those crystals which retain equilibrium mantle values, we propose that they are an inherent part of the local upper mantle. Whilst absorption for olivines from both 'reacted' and 'residual' samples is at the same wavenumbers approximately, the shift in the intensity ratio for the two IR peaks in some olivines from 'reacted' samples suggests a different trace element (or combination of different trace elements) is responsible for water incorporation in olivine from these samples (Fig 3.3 and chapter 5).

We designed a series of 'hydroxylation' experiments to try and identify the element(s) involved in these subtly different substitution reactions and also to establish whether the 'raw' (pre-experimental) crystals are at water saturation. The essence of these experiments was to saturate the crystals with water in order to reveal the full defect structure, which can then be compared to the 'raw' olivine data. The experiments were performed on olivine separates picked from 'residual' and 'reacted' Ritter samples, as well as olivines from 3 other unrelated samples (see methods section for detailed information). Since Ritter olivines contain substantial amounts of FeO (8-9 wt. %), Fe^{3+} may be concentrated relative to other trivalent trace elements in olivine and therefore a strong possible candidate for the coupled substitution with water (Berry et al. 2005, Berry et al. 2007, Grant et al. 2007). Our first experiment was designed to test this by annealing the olivines at low oxygen fugacity (2.5 log unites below NNO) to significantly reduce the concentration of Fe^{3+} before hydroxylation at low temperature, saturating the altered point defect structure with water. The hydroxylation stage takes advantage of the much faster diffusion of H relative to other elements in olivine (Demouchy and Mackwell 2006, Padrón-Navarta et al. 2014), hence the experiment could be run at temperatures and durations low enough to retain the annealed point defect structure. Our second experiment excluded the annealing step, instead decorating the 'raw' point defect chemistry. The difference in absorption and spectra between this experiment and the first would reveal the full role of Fe^{3+} in water incorporation and also show whether the 'raw' olivines are at water saturation.

The results of the hydroxylation experiment are displayed in Fig. 3.8 and Table 3.3. Initially olivines from the 'residual' and 'reacted' samples displayed IR spectra and water contents consistent with our *in-situ* measurements (Fig. 3.3 and Table 3.1). For example, the water content of olivines from 67-02B(1) (average of 8 crystals) is 5.9 ppm (Table 3.3), very similar to the value of 6.1 ppm calculated from *in-situ* measurements (Fig. 3.9). The most striking result from the hydroxylation experiments is that peaks return in the same positions irrespective of whether the olivines were annealed at low oxygen fugacity or not. This means that Fe^{3+} does not play a substantial role in water incorporation, which is instead accommodated by one or more other trivalent cations. Berry et al. (2007) synthesised and then hydrated olivines doped with a variety of different trivalent cations,

and found a strong relationship between wavenumber of the dominant absorption peak and ionic radius. Comparison of our data with this study shows that Cr^{3+} is the most likely substituting element, forming a reaction such as $Mg_2SiO_4 + Cr^{3+} + H^+ = CrHSiO_4 + 2Mg^{2+}$. This is consistent with the higher concentrations of Cr and associated water contents of 'reacted' olivines (chapter 5). Further scrutiny of the hydroxylated olivines shows that the absorption of hydroxylated 'reacted' olivines without the annealing stage is 32 % higher, whilst hydroxylated 'residual' olivines contain approximately the same amount, with or without annealing at low fO_2. This 32 % difference for 'reacted' olivines is close to the maximum difference that could be anticipated from anisotropy (40 %). We suggest that this reflects an increased contribution from Fe^{3+}, since the higher Fe_2O_3/FeO of spinels from this 'reacted' sample shows it equilibrated at higher oxygen fugacity. Another important observation from these experiments is that despite being hydroxylated with a pure fluid, hence very high water fugacity, the crystals never reach the total absorption measured in the 'raw' crystals, even after taking into account possible differences in crystal orientation. The reason for this is not obvious and will require further investigation. Nevertheless, given the thermodynamically favourable conditions under which the crystals were hydroxylated it is clear that, despite low overall water contents, the olivines in the Ritter xenoliths must be at or very close to water saturation.

Finally, Ti-related peaks are either absent (in the case of 'residual' olivines) or only a minor feature (in the case of 'reacted' olivines) both before and after hydroxylation. This result disagrees with the findings of Gaetani et al. (2014) who concluded that absorption at wavelengths of 3572 cm^{-1} and 3525 cm^{-1} was associated with high water fugacities and not related to substitution with Ti. If their conclusions were correct then these peaks would appear strongly in all of our hydroxylated olivines. Instead this result provides further evidence that these peaks are indeed due to Ti-related defects, particularly since the Ti concentration of olivines from the 'reacted' sample used here are higher (1.2-10.5 ppm) than olivines from the 'residual' sample (0.9-1.6 ppm). In addition, olivines from samples 67-02D(3) and 67-02E(1) both contain slightly higher concentrations of Ti and correspondingly show quantifiable absorption at 3572 cm^{-1} and 3525 cm^{-1} (Fig. 3.3, Table 3.1). The Ti contents measured in Ritter olivines are lower than typical upper mantle olivine (> 10 ppm, De Hoog et al. 2010), which explains why

relatively little absorption is measured at these wavenumbers compared to the majority of olivines from spinel peridotite (Schmädicke et al. 2013). Titanium has special significance since the formation of Ti-clinohumite results in hydrated Si vacancies which are considered to be the dominant weakening mechanism in olivine and therefore play may play an important role in dictating the geodynamic properties of the upper mantle (Walker et al. 2007), which we will discuss in more detail subsequently.

3.4.5 Role of redox on water in orthopyroxene

Oxygen fugacity has been suggested to play a role in the incorporation of water in both olivine and orthopyroxene (Peslier et al. 2002, Stalder 2004, Stalder et al. 2005). Our experimental results show that increased oxygen fugacity (and associated increased concentrations of Fe^{3+} in olivine) may play a role in incorporation of water in 'reacted' Ritter olivines. However, orthopyroxene also contains appreciable amounts of Fe, hence it is possible that oxygen fugacity/Fe^{3+} is an additional control on solubility of water alongside Al and Cr (Fig. 3.10). There are strong negative trends between the water content of orthopyroxene and orthopyroxene FeO opposite to what would be anticipated for partial melting since both water and Fe behave incompatibly (Fig. 3.12). We also find a positive correlation between water content of orthopyroxene and the Fe_2O_3/FeO ratio of spinel (Fig. 3.12). One possible interpretation is that these trends reflect water substituting into orthopyroxene as part of a coupled substitution with Fe_2O_3, $2Fe_2Si_2O_6 + H_2O + \frac{1}{2}O_2 = 2FeHSi_2O_6 + 2FeO$. Such a reaction results in a decrease in the number of moles of Fe in orthopyroxene but an increase in the number of defect sites available for H to bond with. The trends we observe here however are opposite to trends observed by Peslier et al. (2002) and Stalder (2004). Additionally, inspection of the results of experimental studies by Stalder (2004) and Stalder et al. (2005) shows that water incorporated onto octahedral sites, as implied by the above substitution reaction, results in IR absorption at lower wavenumbers than the FTIR spectra of Ritter orthopyroxenes (Fig. 3.6). An alternative explanation for the trends in Fig. 3.12 is that two Fe^{3+} cations are substituting onto octahedral sites, charge-balanced by water on a tetrahedral site. The increasing Fe^{3+} content of the system as a whole during this oxidation event could stabilise spinel, leading to an overall decrease in the Fe content of coexisting phases (but

increase in Fe^{3+}/Fe^{2+}). Assuming one of the above interpretations is correct, and if our data is representative of the upper mantle, it may indicate that the water content of orthopyroxene, in addition to olivine, is sensitive to changes in oxygen fugacity such that in more oxidised environments such as the mantle wedge (Parkinson and Arculus 1999) the water storage capacity of bulk peridotite is greater (when all other factors are constant).

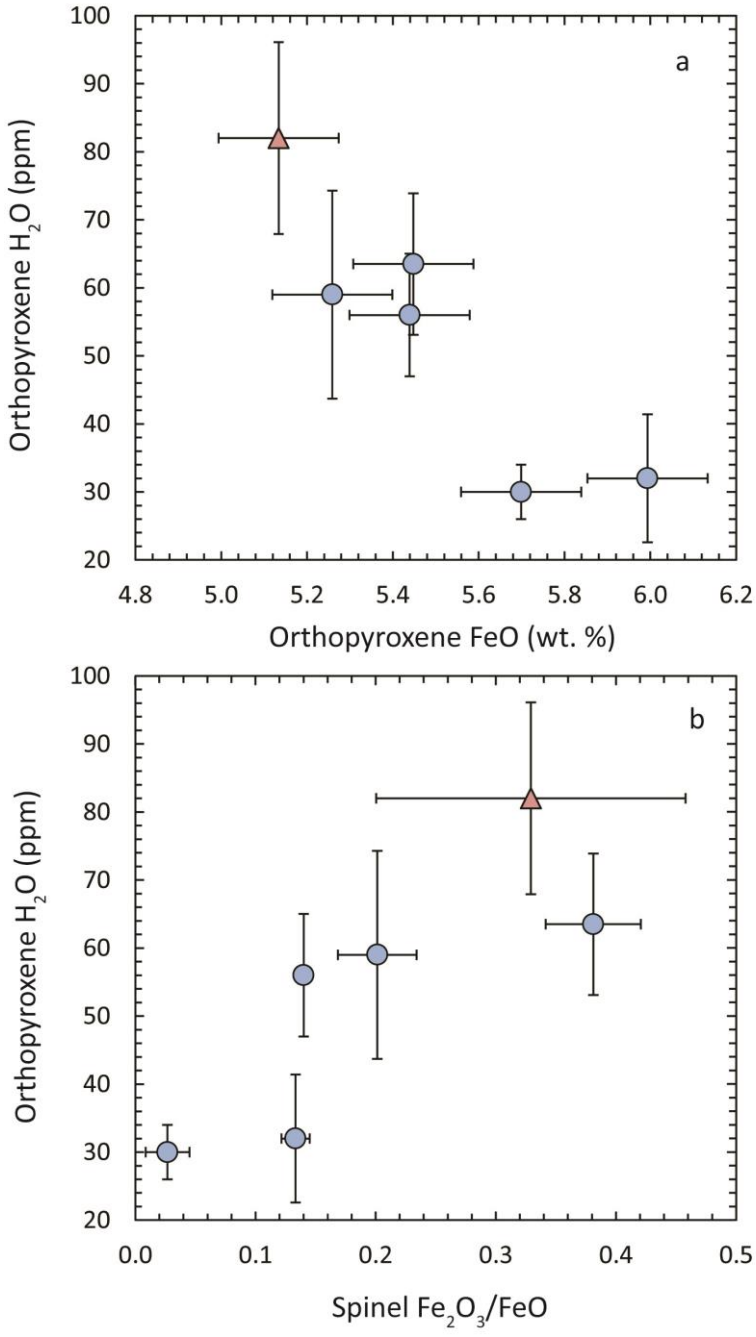

Fig. 3.12 Correlation between the water content of orthopyroxene and a) FeO; b) spinel Fe_2O_3/FeO, indicating a dependence on redox for water incorporation. Uncertainties represent 1 s.d. of multiple measurements

3.4.6 Effects of partial melting and sub-solidus cooling on water content

Our results and discussion so far have shown that the chemical composition of both olivine and orthopyroxene has a significant effect on water incorporation. It is therefore important to consider the processes which have contributed to the chemical composition of these phases. An early hydrous partial melting event contributed significantly to the depleted trace and major element composition of the mineral phases in the Ritter peridotites (chapter 2). Important consequences of this are that incompatible trace and major elements in both olivine and orthopyroxene, which control the solubility of water, will be lowered, particularly Al in orthopyroxene and Ti in olivine (Aubaud et al. 2004, Stalder et al. 2005, Berry et al. 2005, Hauri et al. 2006, Kovacs et al. 2012). The residues of hydrous partial melting therefore, despite the presence of water-rich fluids, may be depleted in water owing to the concomitant decrease in the concentrations of co-substituting elements. Following the partial melting event, the samples subsequently cooled to very low ambient mantle temperatures of ~600 °C (chapter 2). Whilst the direct influence of temperature on $D_{H_2O}^{opx/ol}$ is minimal (Fig 3.13), it is well understood that cooling can change the chemical composition of solid phases at equilibrium (Witt-Eickschen and O'Neill 2005). The main consequence is that the concentration of most trace elements in olivine decreases substantially with decreasing temperature, whilst the concentration of trace and major elements in orthopyroxene remains relatively constant, particularly in systems with little or no clinopyroxene (chapter 2). Previous studies (Witt-Eickschen and O'Neill 2005, De Hoog et al. 2010, Mallmann and O'Neill 2013) and chapter 2 have shown that whilst Cr is only mildly incompatible (or even slightly compatible) between olivine and basaltic melt at high temperature, it becomes strongly incompatible during cooling and is preferentially incorporated into neighbouring pyroxenes. Since we have shown here that Cr may have an important role in water incorporation in olivine, this change in concentration during cooling will have a major effect on how much water can be stored at the associated defect site. The major consequence of this is that at the conditions of partial melting, the solubility of water in olivine may be much higher. We can quantify this through a simple model; an equation which expresses the concentration of Cr in olivine or orthopyroxene as a function of bulk concentration, modal proportions of the two phases and the temperature-dependent partitioning of Cr between olivine and

orthopyroxene. To calculate $D_{Cr}^{opx/ol}$ for a range of temperatures, we performed a non-linear least squares regression of literature data for Cr in olivine and orthopyroxene from well-equilibrated spinel peridotites (Witt-Eickschen and O'Neill 2005, De Hoog et al. 2010). The data were fitted to the equation $D_{Cr}^{opx/ol} = (T/A)^B$, where A and B are constants and T is in °C (Fig. 3.14). Whilst spinel is likely to impact on this relationship, the good correlation observed in the data implies it is negligible compared to the effect of temperature. Our regression resulted in the formulation $D_{Cr}^{opx/ol} = (T/2114)^{-4.42}$ which could be combined with the following equation to calculate concentrations of Cr in olivine and orthopyroxene as a function of temperature (assuming modal proportions of 75 % olivine, 25 % orthopyroxene):

$$C_{Cr}^{ol} = \frac{C_{Cr}^{wr}}{\left(\frac{X^{opx}}{D_{Cr}^{opx/ol}} + X^{ol}\right)}$$

where C refers to the concentration of Cr in olivine or the whole rock (which should be calculated from known mineral composition and modal proportions) and X is the modal proportion of each phase. The results are displayed in Fig. 3.14 and show that at 1300 °C olivine contains over 23 times more Cr than at 600 °C, whilst orthopyroxene contains 1.3 times less. Thus cooling greatly reduces the solubility of water in olivine by reducing the number of available point defect sites. The opposite is true for orthopyroxene, since cooling increases the concentration of Cr (and also, similarly Al). However these changes are relatively minor and so should not impact as substantially on the solubility of water in orthopyroxene.

Unlike Al and Cr, Ti partitioning between olivine and pyroxenes is not particularly temperature sensitive (Fig. 3.14, Witt-Eickschen et al. 2005). Instead, olivine Ti contents are mainly controlled by bulk-rock Ti concentration, itself dominantly a function of the degree of partial melting (Hermann et al. 2005, De Hoog et al. 2010). Consequently the Ti content of olivine from even significantly cooled peridotite is likely to be a close approximation to the solidus Ti contents following partial melting and can therefore be used to estimate the maximum storage capacity of water in olivine associated with the Ti-clinohumite point defect (e.g. Schmädicke et al. 2013).

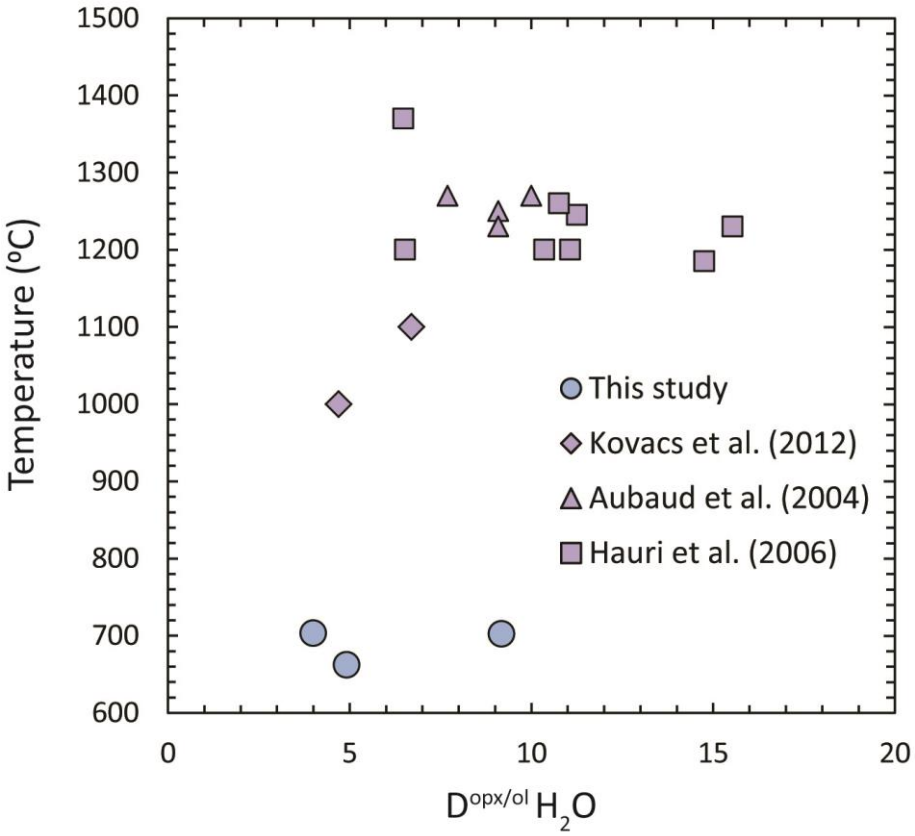

Fig. 3.13. Comparison of $D^{opx/ol}$ H_2O values and temperature calculated for Ritter peridotites compared to experimental partitioning studies (Aubaud et al. 2004, Hauri et al. 2006, Kovacs et al. 2012). Temperature for Ritter samples calculated from Fe-Mg exchange between olivine and spinel (O'Neill and Wall 1987)

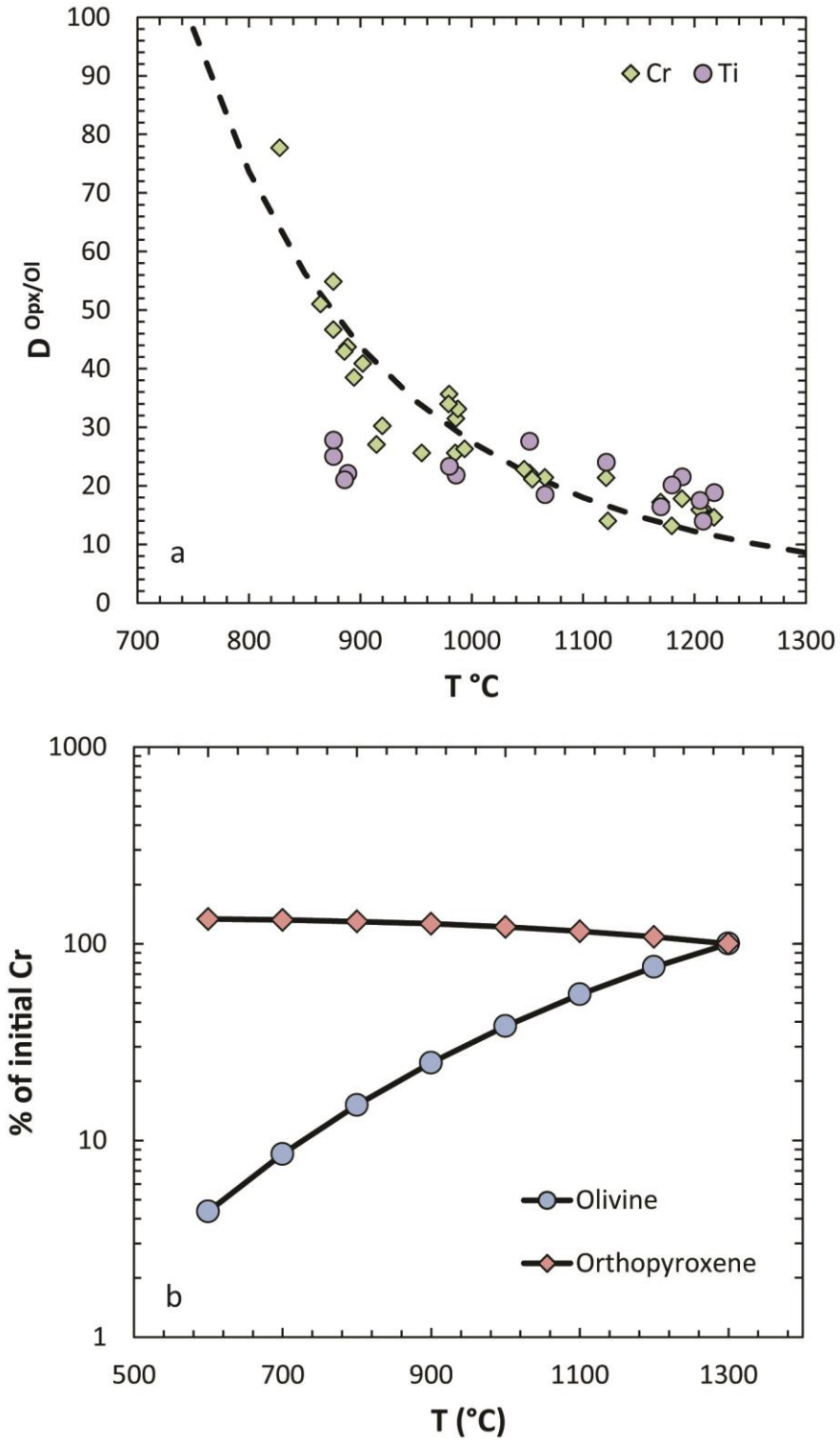

Fig. 3.14 a) Variations in $D^{opx/ol}$ for Cr and Ti with temperature. Data is from well-equilibrated peridotites from Witt-Eickschen et al. 2005 and De Hoog et al. 2010. The dashed line represents a regression of the Cr partitioning data. b) Model for Cr exchange between olivine and orthopyroxene in a harzburgite (75 % olivine, 25 % orthopyroxene) during sub-solidus cooling from melting temperatures (1300 °C) down to equilibration temperatures similar to the Ritter peridotites.

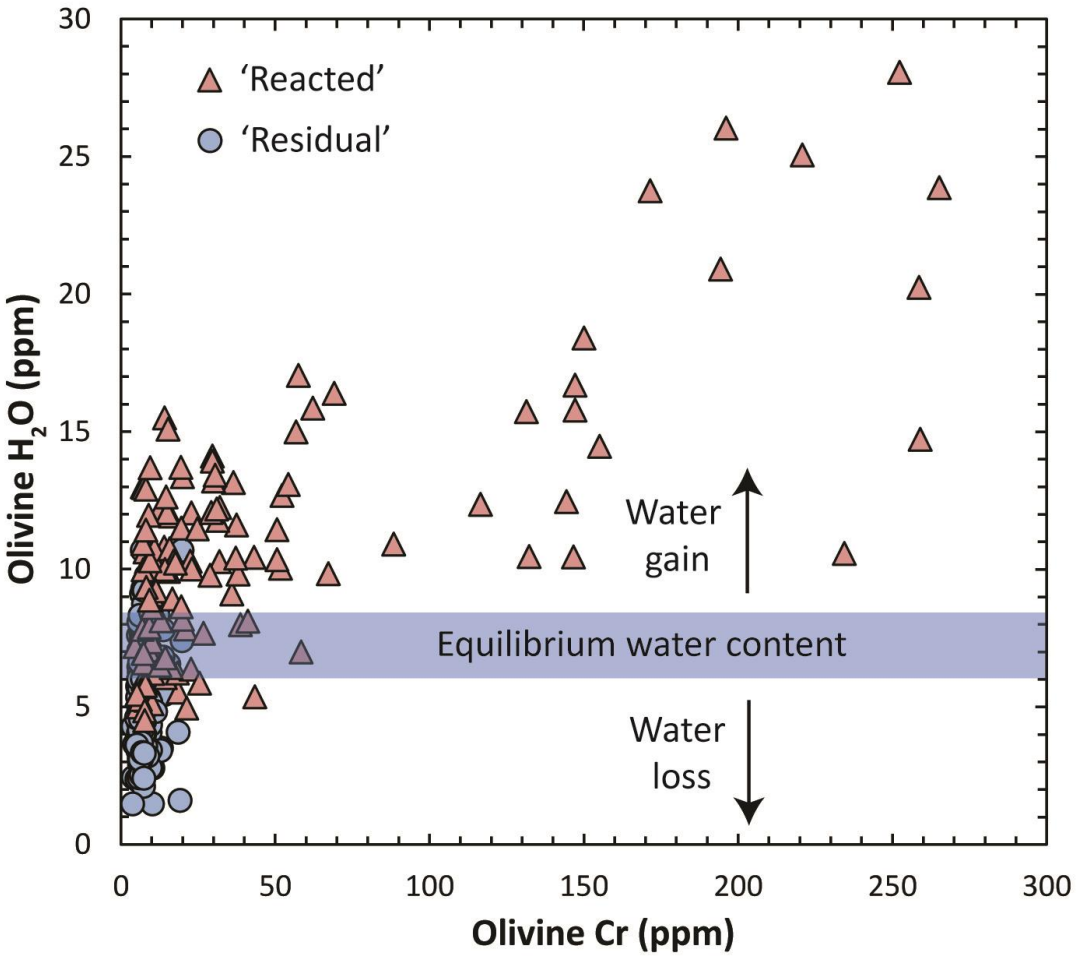

Fig. 3.15 Correlation between the water content of olivine from 'residual' and 'reacted' peridotites and Cr content, measured on the same spot for each crystal. Since Cr is sensitive to the process of melt-rock reaction (see Chapters 2 and 5) the correlation with water shows that reaction between hydrous melts and ambient mantle wedge peridotite causes local hydration. Equilibrium water content (6.1-8.2 ppm) calculated from 'plateau' values (see discussion)

3.4.7 Effect of melt-rock reaction

'Reacted' Ritter samples show textural and chemical evidence for interaction of ambient mantle (represented by the 'residual' peridotites) with silicate melts in the upper mantle wedge (chapter 2). A key question is whether such reactions increase or decrease the water content of the surrounding mantle, as this will impact on estimates of the efficiency of water recycling in subduction zones and the bulk water storage capacity and rheology of the upper mantle. Our data shows that three of the four 'reacted' peridotites studied here show increases in the total amount of water which, on a sample-wide scale, correlates with the concentrations of incompatible trace elements inferred to reflect diffusion from percolating melts (Fig. 3.15, chapters 2 and 5). We propose that the increase in water is facilitated by an increase in available defect sites caused by the influx of trivalent cations, principally Cr which also shows the most substantial increases in concentration of plausible co-substituting trivalent elements, but also Fe^{3+} since the spinels in the 'reacted' samples have elevated values of Fe_2O_3/FeO indicating an increase in oxygen fugacity. Without a flux of elements and associated change in vacancy concentrations, simply equilibrating in the presence of a fluid would not raise the water content of olivine as is shown clearly through our hydroxylation experiments performed at mantle pressures in the presence of pure water (Fig. 3.8, Table 3.3). The absence of correlation between concentrations of water and trace elements in individual samples reflects mainly the rapid diffusive loss of water during ascent which would disturb any correlations originally present pre-exhumation. The reader is directed to chapter 5 for a further discussion of the effect of melt-rock reaction.

3.4.8 Implications for mantle wedge dynamics and recycling of water in subduction zones

Our results here, combined with other data from samples of fore-arc mantle (Soustelle et al. 2010, 2013), show that the upper mantle wedge is a region of cold, highly depleted and 'dry' peridotite. The very low water contents of olivine and orthopyroxene are consistent with high degrees of partial melting at low pressure. Water contents of olivine may have been further lowered during cooling, due to significant re-distribution of trivalent cations into orthopyroxene lowering the solubility of water, although this may be countered slightly by an increase in water solubility in orthopyroxene by the same

process. The much lower water contents for our natural residues compared to the majority of experimental data are best reconciled by a combination of the overall more chemically depleted composition of the natural peridotites and the anticipated lower water fugacities of more solute- and CO_2-rich natural mantle fluids which interacted with the peridotites. Therefore it is possible that residues of shallow pressure melting even under vapour-saturated conditions are depleted in water compared to nominally anhydrous, low degree (fertile) melting residues formed in other tectonic settings.

The absence of any significant absorption associated with the Ti-clinohumite point defect in Ritter, Tubaf (Soustelle et al. 2013) and Kamchatkan (Soustelle et al. 2010) arc mantle olivines is particularly important for the mechanical behaviour of the mantle wedge. A number of studies have shown that the viscosity of the mantle is dependent on the rate of Si self-diffusion in olivine, itself a function of the concentration of Si vacancies which is enhanced significantly under hydrous conditions. The formation of Ti-clinohumite point defects results in increased Si vacancies due to the switching of Ti from a tetrahedral to an octahedral position (Walker et al. 2007), and thus IR absorption at the higher wavenumbers characteristic of this defect type (and also Si vacancies formed as a direct consequence of low silica activity) is indicative of mechanically weaker olivine structures. The very low Ti concentrations in such highly depleted mantle, and the presence of orthopyroxene buffering silica activity has resulted in low concentrations of hydrated Si vacancies. In addition to this, the chemically depleted composition of mantle wedge olivine and orthopyroxene may act as a 'barrier' to water incorporation during interaction with hydrous slab-derived fluids. The 'reacted' Ritter peridotites show that even substantial amounts of reaction between hydrous melts and depleted peridotite do not significantly alter the water content of mantle olivine and orthopyroxene, and that the increased water content is still almost all associated with an octahedral defect site which does not result in the formation of Si vacancies. Interaction between aqueous fluids and mantle wedge are even less likely to overcome this chemical 'barrier' irrespective of whether the water fugacity is higher since the concentrations of incompatible elements is substantially less compared to hydrous melts (Hermann and Rubatto 2009). The ultimate consequence of this is that the 'dry', stiff upper mantle wedge residues are likely to be detached from the bulk convecting mantle which will

promote the preservation of the chemical and isotopic fingerprints of subduction over geological time.

3.5 References

Ardia, P., Hirschmann, M.M., Withers, A.C., Tenner, T.J., 2012. H_2O storage capacity of olivine at 5-8 GPa and consequences for dehydration partial melting of the upper mantle. Earth Planet. Sci. Lett. 345-348, 104-116

Aubaud, C., Hauri, E.H., Hirschmann, M.M., 2004. Hydrogen partition coefficients between nominally anhydrous minerals and basaltic melts. Geophys. Res. Lett. 31, L20611

Baptiste, V., Tommasi, A., Demouchy, S., 2012. Deformation and hydration of the lithospheric mantle beneath the Kaapvaal craton, South Africa. Lithos 149, 31-50

Bell, D.R., Rossman, G.R., 1992. Water in Earth's Mantle: The Role of Nominally Anhydrous Minerals. Science 255, 1391-1397

Bell, D.R., Ihinger, P.D., Rossman, G.R., 1995. Quantitative analysis of trace OH in garnet and pyroxenes. Am. Mineral. 80, 465-474

Berry, A.J., Hermann, J., O'Neill, H.St.C., Foran, G.J., 2005. Fingerprinting the water site in olivine. Geology 33, 869-872

Costa, F., Chakraborty, S., 2008. The effect of water on Si and O diffusion rates in olivine and implications for transport properties and processes in the upper mantle. Phys. Earth Planet. Int. 166, 11-29

Crank, J., 1975. The Mathematics of Diffusion. Oxford University Press

De Hoog, J.C.M., Gall, L., Cornell, D.H., 2010. Trace-element geochemistry of mantle olivine and application to mantle petrogenesis and geothermobarometry. Chemical Geology 270, 196-215

Demouchy, S., Jacobsen, S.D., Gaillard, F., Stern, C.R., 2006. Rapid magma ascent recorded by water diffusion profiles in mantle olivine. Geology 34, 429-432

Demouchy, S., Mackwell, S., 2006. Mechanisms of hydrogen incorporation and diffusion in iron-bearing olivine. Phys. Chem. Minerals 33, 347-355

Denis, C.M.M, Demouchy, S., Shaw, C.S.J., 2013. Evidence of dehydration in peridotites from Eiffel Volcanic Field and estimates of the rate of magma ascent. J. Volc. Geotherm. Res. 258, 85-99

Elliott, T., Plank, T., Zindler, A., White, W., Bourdon, B., 1997. Element transport from slab to volcanic front at the Mariana arc. J. Geophys. Res. 102, 14,991-15,019

Evans, K.A., Elburg, M.A., Kamenetsky, V.S., 2012. Oxidation state of subarc mantle. Geology 40, 783-786

Férot, A., Bolfan-Casanova, N., 2012. Water storage capacity in olivine and pyroxene to 14 GPa: Implications for the water content of Earth's upper mantle and nature of seismic discontinuities. Earth Planet. Sci. Lett. 349-350, 218-230

Gaetani, G.A., Grove, T.L., 1998. The influence of water on melting of mantle peridotite. Contrib. Mineral. Petrol. 131, 323-346

Gaetani, G.A., O'Leary, J.A., Koga, K.T., Hauri, E.H., Rose-Koga, E.F., Monteleone, B.D., 2014. Hydration of mantle olivine under variable water and oxygen fugacity conditions. Contrib. Mineral. Petrol. 167, 965-979

Grant, K., Ingrin, J., Lorand, J.P., Dumas, P., 2007a. Water partitioning between mantle minerals from peridotite xenoliths. Contrib. Mineral. Petrol. 154, 15-34

Grant, K.J., Kohn, S.C., Brooker, R.A., 2007b. The partitioning of water between olivine, orthopyroxene and melt synthesised in the system albite-forsterite-H_2O. Earth Planet. Sci. Lett. 260, 227-241

Green, D.H., Hibberson, W.O., Kovacs, I., Rosenthal, A., 2010. Water and its influence on the lithosphere-asthenosphere boundary. Nature 467, 448-451

Hauri, E.H., Gaetani, G.A., Green, T.H., 2006. Partitioning of water during melting of Earth's upper mantle at H_2O-undersaturated conditions. Earth Planet. Sci. Lett. 248, 715-734

Hermann, J., O'Neill, H.S.C., Berry, A.J., 2005. Titanium solubility in olivine in the system TiO_2-MgO-SiO_2: no evidence for an ultra-deep origin of Ti-bearing olivine. Contrib. Mineral. Petrol. 148, 746-760

Hermann, J., Rubatto, D., 2009. Accessory phase control on the trace element signature of sediment melts in subduction zones. Chemical Geology 265, 512-526

Hirschmann, M.M., 2006. Water, Melting, and the Deep Earth H_2O Cycle. Annu. Rev. Earth Planet. Sci. 34, 629-653

Hirschmann, M.M., Tenner, T., Aubaud, C., Wither., A.C., 2009. Dehydration melting of nominally anhydrous mantle: The primacy of partitioning. Phys. Earth Planet. Int. 176, 54-68

Hirth, G., Kohlstedt, D.L., 1996. Water in the oceanic upper mantle: implications for rheology, melt extraction and the evolution of the lithosphere. Earth Planet. Sci. Lett. 144, 93-108

Ionov, D.A., 2010. Petrology of Mantle Wedge Lithosphere: New Data on Supra-Subduction Zone Peridotite Xenoliths from the Andesitic Avacha Volcano, Kamchatka. J. Petrol. 51, 327-361

Köhler, T.P., Brey, G.P., 1990. Calcium exchange between olivine and clinopyroxene calibrated as a geothermobarometer for natural peridotites from 2 to 60 kb with applications. Geochim. Cosmochim. Acta 54, 2375-2388

Kovacs, I., Hermann, J., O'Neill, H.St.C., Fitz Gerald, J., Sambridge, M., Horvath, G., 2008. Quantitative absorbance spectroscopy with unpolarized light: Part II. Experimental evaluation and development of a protocol for quantitative analysis of mineral IR spectra. Am. Mineral. 93, 765-778

Kovacs, I., O'Neill, H.St.C., Hermann, J., Hauri, E.H., 2010. Site-specific infrared O-H absorption coefficients for water substitution into olivine. Am. Mineral. 95, 292-299

Kovacs, I., Green, D.H., Rosenthal, A., Hermann, J., O'Neill, H.St.C., Hibberson, W.O., Udvardi, B., 2012. An Experimental Study of Water in Nominally Anhydrous Minerals in the Upper Mantle near the Water-saturated Solidus. J. Petrol. 53, 2067-2093

Lemaire, C., Kohn, S.C., Brooker, R.A., 2004. The effect of silica activity on the incorporation mechanisms of water in synthetic forsterite: a polarised infrared spectroscopic study. Contrib. Mineral. Petrol. 147, 48-57

Lloyd, A.S., Plank, T., Ruprecht, P., Hauri, E.H., Rose, W., 2013. Volatile loss from melt inclusions in pyroclasts of differing sizes. Contrib. Mineral. Petrol. 165, 129-153

Mallmann, G., O'Neill, H.St.C., 2009. The Crystal/Melt Partitioning of V during Mantle Melting as a Function of Oxygen Fugacity Compared with some other Elements (Al, P, Ca, Sc, Ti, Cr, Fe, Ga, Y, Zr, Nb). J. Petrol. 50, 1765-1794

Mallmann, G., O'Neill, H.St.C., 2013. Calibration of an Empirical Thermometer and Oxybarometer based on the Partitioning of Sc, Y and V between Olivine and Silicate Melt. J. Petrol. 54, 933-949

Matveev, S., Portnyagin, M., Ballhaus, C., Brooker, R., Geiger, C.A., 2005. FTIR Spectrum of Phenocryst Olivine as an Indicator of Silica Saturation in Magmas. J. Petrol. 46, 603-614

Mei, S., Kohlstedt, D.L., 2000. Influence of water on plastic deformation of olivine aggregates 1. Diffusion creep regime. J. Geophys. Res. 105, 21457-21469

Miller, G.H., Rossman, G.R., Harlow, G.E., 1987. The natural occurrence of hydroxide in olivine. Phys. Chem. Min. 14, 461-472

Mosenfelder, J.D., Deligne, N.I., Asimow, P.D., Rossman, G.R., 2006. Am. Mineral. 91, 285-294

Newman, S., Lowenstern, J.B., 2002. VOLATILECALC: a silicate melt-H_2O-CO_2 solution model written in Visual Basic for excel. Comp. Geosci. 28, 597-604

O'Neill, H.St.C., Wall, V.J., 1987. The Olivine-Orthopyroxene-Spinel Oxygen Geobarometer, the Nickel Precipitation Curve, and the Oxygen Fugacity of the Earth's Upper Mantle. J. Petrol. 28, 1169-1191

Padrón-Navarta, J.A., Hermann, J., O'Neill, H.St.C., 2014. Site-specific hydrogen diffusion rates in forsterite. Earth Planet. Sci. Lett. 392, 100-112

Parkinson, I.J., Arculus, R.J., 1999. The redox state of subduction zones: insights from arc-peridotites. Chemical Geology 160, 409-423

Parkinson, I.J., Arculus, R.J., Eggins, S.M., 2003. Peridotite xenoliths from Grenada, Lesser Antilles Island Arc. Contrib. Mineral. Petrol. 146, 241-262

Peslier, A.H., Luhr, J.F., Post, J., 2002. Low water contents in pyroxenes from spinel-peridotites of the oxidized, sub-arc mantle wedge. Earth Planet. Sci. Lett. 201, 69-86

Peslier, A.H., Luhr, J.F., 2006. Hydrogen loss from olivines in mantle xenoliths from Simcoe (USA) and Mexico: mafic alkali magma ascent rates and water budget of the sub-continental lithosphere. Earth Planet. Sci. Lett. 242, 302-319

Peslier, A.H., Woodland, A.B., Wolff, J.A., 2008. Fast kimberlites ascent rates estimated from hydrogen diffusion profiles in xenolithic olivines from Southern Africa. Geochim. Cosmochim. Acta 72, 2711-2722

Peslier, A.H., Woodland, A.B., Bell, D.R., Lazarov, M., 2010. Olivine water contents in the continental lithosphere and the longevity of cratons. Nature 467, 78-81

Peslier, A.H., 2010. A review of water contents of nominally anhydrous natural minerals in the mantles of Earth, Mars and the Moon. J. Volc. Geotherm. Res. 197, 239-258

Sambridge, M., Fitz Gerald, J.D., Kovacs, I., O'Neill, H.St.C., Hermann, J., 2008. Quantitative IR spectroscopy with unpolarized light. Part 1: Physical and mathematical development. Am. Mineral. 93, 751-764

Schmädicke, E., Gose, J., Witt-Eickschen, G., Brätz, H., 2013. Olivine from spinel peridotite xenoliths: Hydroxyl incorporation and mineral composition. Am. Mineral. 98, 1870-1880

Schmidt, M.W., Poli, S., 1998. Experimentally based water budgets for dehydrating slabs and consequences for arc magma generation. Earth Planet. Sci. Lett. 163, 361-379

Soustelle, V., Tommasi, A., Demouchy, S., Ionov, D.A., 2010. Deformation and Fluid-Rock Interaction in the Supra-Subduction Zone Mantle: Microstructures and Water Contents in Peridotite Xenoliths from the Avacha Volcano, Kamchatka. J. Petrol. 51, 363-394

Soustelle, V., Tommasi, A., Demouchy, S., Franz, L., 2013. Melt-rock interactions, deformation, hydration and seismic properties in the sub-arc lithospheric mantle inferred from xenoliths from seamounts near Lihir, Papau New Guinea. Tectonophysics 608, 330-345

Stalder, R., 2004. Influence of Fe, Cr and Al on hydrogen incorporation in orthopyroxene. Eur. J. Mineral. 16, 703-711

Stalder, R., Klemme, S., Ludwig, T., Skogby, H., 2005. Hydrogen incorporation in orthopyroxene: interaction of different trivalent cations. Contrib. Mineral. Petrol. 150, 473-485

Till, C.B., Grove, T.L., Withers, A.C., 2012. The beginnings of hydrous mantle wedge melting. Contrib. Mineral. Petrol. 163, 669-688

Tollan, P.M.E., Bindeman, I., Blundy, J.D., 2012. Cumulate xenoliths from St. Vincent, Lesser Antilles Island Arc: a window into upper crustal differentiation of mantle-derived basalts. Contrib. Mineral. Petrol. 163, 189-208

Turner, S., Caulfield, J., Turner, M., van Keken, P., Maury, R., Sandiford, M., Prouteau, G., 2012. Recent contribution of sediments and fluids to the mantle's volatile budget. Nat. Geosci. 5, 50-54

Walker, A.M., Hermann, J., Berry, A.J., O'Neill, H.St.C., 2007. Three water sites in upper mantle olivine and the role of titanium in the water weakening mechanism. J. Geophys. Res., Solid Earth 112, B05211

Wallace, P.J., 2005. Volatiles in subduction zone magmas: concentrations and fluxes based on melt inclusion and volcanic gas data. J. Volc. Geotherm. Res. 140, 217-240

Witt-Eickschen, G., O'Neill, H.St.C., 2005. The effect of temperature on the equilibrium distribution of trace elements between clinopyroxene, orthopyroxene, olivine and spinel in upper mantle peridotite. Chemical Geology 221, 65-101

Zhao, Y-H., Ginsberg, S.B., Kohlstedt, D.L., 2004. Solubility of hydrogen in olivine: dependence on temperature and iron content. Contrib. Mineral. Petrol. 147, 155-161

Chapter 4

Roles of partial melting and melt-rock reaction on highly siderophile element abundances and Os, Sr, O isotope systematics in highly-depleted peridotite xenoliths sampling the upper mantle wedge beneath the West Bismarck Island Arc

4.1 Introduction

The highly siderophile nature of Re and the platinum group elements (PGE; Os, Ir, Ru, Pt and Pd) is in contrast to the dominantly lithophile behaviour of most elements in the mantle. This fundamental difference in chemical affinity means that they have the potential to yield information on a range of processes inaccessible through measurements of 'traditional' suites of elements. Principally, the concentrations of highly siderophile elements (HSE) in peridotite and mantle-derived basalts reflect the segregation of Earth's Fe-rich core during early planetary differentiation. However numerous studies have shown that the concentrations of these elements in the mantle are higher than would be anticipated from core formation alone, most plausibly explained by a synchronous or subsequent addition to the primitive mantle from undifferentiated and Fe-rich meteorites (Chou 1978, Palme and O'Neill 2003, Becker et al. 2006, Walker 2009, Mann et al. 2012)

Determining the magnitude of this extraneous addition of HSE requires an intimate knowledge of how these elements fractionate during mantle processes. It is now well understood that the concentrations of palladium-group PGE (PPGE; Pd and Pt) and Re are highly fractionated from iridium-group PGE (IPGE; Os, Ir and Ru) during partial melting, owing to their overall incompatible behaviour (Handler and Bennett 1999, Pearson et al. 2004, Mungall et al. 2005, Bockrath et al. 2004, Becker et al. 2006). The resultant peridotite residues will be variably depleted in PPGE and Re relative to melts, which facilitates the calculation of the ages of partial melting events using Os isotope systematics of residual peridotite, events not recorded by more established but dominantly incompatible lithophile isotope systems (Shirey and Walker 1998, Parkinson et al. 1998, Pearson et al. 2004, Rudnick and Walker 2009). However, the incompatible behaviour of PPGE also means that their absolute and relative concentrations in peridotites are susceptible to alteration through metasomatism and melt-rock reaction (Handler and Bennett 1999, Büchl et al. 2002, Büchl et al. 2004, Lorand et al. 2004, Resiberg et al. 2005, Uysal et al. 2009, Ackerman et al. 2009, Ackerman et al. 2012, Lorand et al. 2013). The influence of these processes is not well known. This is mainly

because the transport of HSE in mantle fluids is controlled by the concentrations of sulphur and complex phase relations of trace sulphide and platinum group minerals in the ambient mantle, which in turn are dependent on numerous poorly constrained variables such as fluid composition, melt-rock ratio, oxygen fugacity, temperature and pressure (Mavrogenes and O'Neill 1999, Luguet et al. 2004, Bockrath et al. 2004, Luguet et al. 2007, Jugo 2009, Lorand et al. 2010, Lorand et al. 2013). For example, previous studies have documented both decreasing and increasing concentrations of PPGE in peridotite during melt-rock reaction (Zhou et al. 1998, Büchl et al. 2002, Büchl et al. 2004, Ackerman et al. 2009, Uysal et al. 2009, Ackerman et al. 2012 O'Driscoll et al. 2012). Even IPGE, which are compatible during partial melting, may become highly fractionated during these secondary processes (Büchl et al. 2002, Ackerman et al. 2009). The impact that this has on the Os isotope composition and the reliability of Os isotope ages is consequently highly variable between mantle systems, even those which appear broadly similar in terms of petrography and lithophile element composition.

The behaviour of HSE in subduction zones is particularly poorly understood, due to uncertainties in the flux of sulphur and HSE from subducted lithosphere into the mantle wedge and uncertainties in the fugacities of oxygen, sulphur and key volatile species in the mantle wedge and in magmas during ascent to the surface (Parkinson and Arculus 1999, Wallace 2005, Dale et al. 2009, Jugo 2009, Dale et al. 2012, Evans 2012). This lack of understanding is compounded by a dearth of peridotite xenoliths erupted from island arc volcanoes. Previous studies of arc mantle xenoliths have documented significant enrichments in PPGE which were attributed to the influence of slab-derived fluids (McInnes et al. 1999, Kepezhinskas et al. 2002). However it's not clear whether the enrichments reflect remobilisation and subsequent concentration of material already present in the mantle wedge by percolating fluids or whether addition directly from the slab is necessary. Brandon et al. (1996) and Wisdom et al. (2003) measured radiogenic Os isotope compositions in arc mantle xenoliths, interpreted to reflect mobilisation of Os from the subducting slab, whilst studies of relatively un-differentiated arc lavas and supra-subduction zone ophiolites have documented evidence both for and against (Büchl et al. 2002, Woodland et al. 2002, Suzuki et al. 2011, Aldanmaz et al. 2012, Aulbach et al. 2012, Dale et al. 2012, Liu et al. 2012). Taken together, the current body of evidence for

subduction-related peridotites and lavas implies that the behaviour of HSE varies significantly between subduction zones, highlighting the need for more data to develop a fuller understanding of the fundamental parameters controlling HSE in the mantle wedge.

In this study we report the Os isotope compositions and concentrations of HSE in xenoliths of harzburgite, pyroxenite and dunite, exhumed fragments of upper mantle wedge beneath Ritter Island in the West Bismarck Island arc (Fig. 1.1, Fig. 1.2). By comparing this new dataset to previously determined petrography, major and trace lithophile element compositions (chapter 2) we demonstrate the relative influences of partial melting and melt-rock reaction on HSE and Os isotope systematics as part of a subduction system. Combined with Sr isotope measurements which clearly track both flux of subducted material and melt-rock reaction, we show that HSE were largely unaffected by input from the slab. Their systematics were instead dictated by partial melting and re-mobilisation during silicate melt-rock reaction. Differences between the HSE concentrations (particularly Os and Pt) of olivine separates and whole-rocks indicates an important role for Pt- and Os-rich alloy nuggets, and demonstrates the highly heterogeneous distribution of HSE-bearing phases in depleted peridotite. Osmium isotopes are decoupled from HSE concentrations and lithophile elements, except for P concentrations in olivine and orthopyroxene indicating preservation of an ancient high temperature Os isotope signature unrelated to the currently active subduction.

4.2 Methods

Strontium isotope compositions were determined on 200 mg aliquots of powdered sample. The chemistry procedures followed closely the methods described in Charlier et al. (2006). Powders were dissolved in triple-distilled, concentrated HF (29 M) and HNO_3 (16 M) acids and centrifuged to remove particulate matter. Chromatographic columns and Sr-spec resin were cleaned with 6M HCl, rinsed with ultra-pure water and pre-conditioned with 3M HNO_3. Dissolved samples were then brought up in 3M HNO_3 and passed through the columns to separate Sr from the peridotite matrix. Eight samples with higher concentrations of Sr were brought up in 3 % HNO_3 and analysed on a Thermo Scientific Neptune plasma ionisation multi-collector mass-spectrometer (MC-ICPMS) in the Department of Earth Sciences, Durham University. The multi-collection analytical

routine consisted of 50 cycles with an integration time of 4 seconds per cycle and washout in between to return the signal to background level. Sample voltages varied from 6.38 to 36.28 V of ^{88}Sr. The $^{88}Sr/^{86}Sr$ ratio was monitored and corrected for instrumental mass bias using an exponential law and an $^{88}Sr/^{86}Sr$ ratio of 0.1194. Throughout the run, standard NBS987 was measured and returned a mean value of 0.710256 ± 0.000020 (2σ, n = 7), which was then used to correct the standard data assuming a value for NBS987 of 0.710240. The remaining 6 samples contained too little Sr to be run using the Neptune so instead were analysed on a Thermo Scientific Triton thermal ionisation mass-spectrometer (TIMS) also at Durham University. The Sr cuts were taken up in 1 µl of concentrated HNO_3 and loaded on to Re filaments using 1 µl of TaF_5 activator to increase ionisation efficiency. Analyses were conducted in blocks of 20 cycles, with 135-210 ratios used to calculate the final data. Similar instrument mass-fractionation corrections to the Neptune routine were applied. Six measurements of standard NBS987 returned an average value of 0.710248 ± 0.000019, identical to the value obtained with the Neptune.

Oxygen isotope compositions were determined using a MAT 253 mass spectrometer with gas extraction and purification achieved with a custom-built laser fluorination line at the Department of Geological Sciences, University of Oregon. Inclusion-free separates of olivine and orthopyroxene were picked from crushed whole rock samples under an optical microscope and weighed using a microbalance before being loaded into the sample cell. Where possible, individual crystals of mass 1-1.5 mg were selected so that isotopic variability between crystals could be assessed. When this wasn't possible, 2-3 crystals of smaller mass were selected. Occasionally, olivine crystals exhibited violent reactions to laser heating which resulted in 'jumping' and loss of sample from the reaction cell. To try and minimise this, crystals were crushed to a coarse powder before laser heating. Prior to analysis, samples were pre-treated overnight with BrF_5 to increase the efficiency of vaporisation, before being vaporised by laser under an atmosphere of BrF_5. The lasing procedure consisted of a relatively rapid increase in laser power and strafing of the laser spot to heat the crystal(s) evenly. Complete vaporisation is a pre-requisite for accurate oxygen isotope determination since any remaining oxygen-bearing material is likely to be isotopically fractionated. Complete vaporisation of

silicates, particularly olivine and clinopyroxene, may be hindered by the formation of fluoride melt which shields residual silicate material (Tollan et al. 2012). This was circumvented by applying rapid bursts of laser energy, causing rapid heating and bubbling of MgF_2 liquid which allowed any remaining vapour to escape. The extracted vapour was passed through a series of cryogenic traps held at liquid nitrogen temperatures and a mercury diffusion pump to isolate and purify oxygen gas which was then converted to CO_2 by reacting with a heated platinum-graphite filament. The volume of CO_2 produced was measured before being fed directly into the mass spectrometer. Blanks were measured at the start of each day by loading an aliquot of BrF_5 into an empty sample cell, leaving for 5 minutes before following the standard analytical procedure. Blank contribution was typically <2 % of the total extracted vapour. Standards of University of Oregon Garnet (calibrated against Gore Mountain garnet) were measured throughout the analytical sessions, producing average $\delta^{18}O$ values of 7.240 ± 0.006 ‰ (3), 7.265 ± 0.056 ‰ (3) and 7.238 ± 0.007 ‰ (4) on each of the 3 days, where errors represent one standard deviation on the total number of standards (parentheses) and $\delta^{18}O = [(^{18}O/^{16}O_{Sample})/(^{18}O/^{16}O_{VSMOW})-1]*1000$. Duplicates and triplicates of samples were typically in excellent agreement with each other, with standard deviation always better than 0.1 ‰, and typically 0.05 ‰ or better.

Osmium isotope and highly siderophile element (HSE) analyses were conducted at the Department of Earth Sciences, Durham University, closely following the methods described in Dale et al. (2009). Approximately 1.5 g of each sample powder was weighed out and transferred to a quartz high pressure asher (HPA) vessel, before addition of a mixed spike enriched in ^{190}Os, ^{185}Re, ^{191}Ir, ^{99}Ru, ^{194}Pt and ^{106}Pd. This mixture was then dissolved using inverse aqua regia (2.5 ml 12M HCl + 5 ml 16M HNO_3) as a reagent in an Anton-Paar HPA held at 300 °C for at least 12 hours. The HPA vessels were allowed to cool under confining pressure to limit volatile-loss, before removal from the asher and dilution with ultra-pure water and extraction of Os from the inverse aqua regia through reaction with CCl_4. Osmium was then back-extracted into HBr. This HBr aliquot was dried down and the residue transferred to a clean aliquot of HBr by micro-distillation with H_2SO_4 and Cr (dissolved in H_2SO_4) to remove impurities (Birck et al., 1997). This was then dried down to a volume of approximately 1 µl and loaded onto outgassed Pt filaments

along with ~0.5 µl of a $Ba(OH)_2$ in 0.1 M NaOH activator for analysis. The other HSE were extracted from the residue by transferring the inverse aqua regia and any remaining solid residue to Teflon® vials and drying down before dissolving in concentrated HF and HCl. This was then dried down, and 1 ml of 10 % H_2O_2 added to reduce Cr, increasing the efficiency of Cr elution during column chemistry, which can otherwise form polyatomic interferences on Ru isotope masses. This was dried down again and brought up in 10 ml of 0.5 M HCl ready for chromatographic separation of the HSE, Ir, Ru, Pd, Pt and Re using AGX1-8 (100–200 mesh) anion-exchange resin and a column procedure similar to that of Pearson and Woodland (2000). Rhenium, Ir, Pt and Ru were collected in 13.5M HNO_3, and Pd subsequently eluted in 9M HCl. To identify the phase(s) hosting the budget of HSE in the samples and investigate the effect of slab metasomatism on $^{187}Os/^{188}Os$, olivine separates were also measured. Approximately 0.1 g of optically pure but not necessarily sulphide-free olivine crystals were picked from three samples under optical microscope, ensuring minimal contribution from other phases such as spinel. The crystals were cleaned in ultra-clean water and ethanol to remove any trace surficial material, dried, crushed to a fine powder and then prepared for chemical purification and analysis using the same method as detailed above.

Osmium isotopes were measured by thermal ionisation mass spectrometry (TIMS) on a Thermo Scientific Triton at Durham University. The measurements were performed in negative ionisation mode, with Os measured as OsO_3^- ions, with counts collected by a secondary electron multiplier ion detector. Raw data was processed offline to correct for O isotope interferences, mass fractionation (using $^{192}Os/^{188}Os = 3.08271$) and spike un-mixing. Aliquots of Durham Romil Os Standard (DROsS) solution (0.1 ng and 0.01 ng) were run during each analytical session, producing a (Re-corrected) value of 0.16071 ± 0.00023 (1 s.d., n = 8), in agreement with the value of 0.160924 ± 0.00004 for 10-100 ng/g aliquots measured by Faraday Cup detectors on the same instrument (Luguet et al. 2008). It is also consistent with the long-term average over the analytical period for multiple users in the Durham lab for multiple loads of 0.16064 ± 0.00037. Concentrations of HSE; Re, Ir, Ru, Pt and Pd, were determined by inductively-coupled plasma mass spectrometry (ICP-MS), using a Thermo Scientific Element 2 at Durham University. Instrument tuning and optimisation was performed at the start of each session using a 1 ppb solution of Ce.

Standard 1 ppb solutions of multi-HSE, Hf, Zr, Y, Cd and Mo were measured at regular intervals throughout the analytical sessions in order to monitor sensitivity and to correct for mass fractionation and polyatomic interferences (< 1 %). Total procedural blanks produced on average 2.3 pg , 1.7 pg, 39 pg, 34 pg, 3.2 pg and 2.0 pg for Os, Ir, Ru, Pt, Pd and Re respectively, contributing typically <1 %, but occasionally as much as 6 % (in the case of Re) of the total measured concentration. Dissolutions of ~1 g of the peridotite standard GP13 were processed and measured to test for accuracy and reproducibility of the procedures described. Estimated reproducibility (1 s.d.) was 0.8 % (Os), 2.4 % (Ir), 1.5 % (Ru), 8.2 % (Pt), 7.2 % (Pd), 1.8 % (Re) and 0.3 % ($^{187}Os/^{188}Os$), for 3 separates analyses of GP13. Values measured here agree, within uncertainty, with those obtained from both Durham and other labs (Pearson et al. 2004).

4.3 Results

4.3.1 Sr, O and Os isotope compositions

The Sr isotope composition ($^{87}Sr/^{86}Sr$, Table 4.1) of whole rock peridotites, both 'reacted' and 'residual' types, varies from relatively isotopically enriched values of up to 0.704871 down to values slightly more radiogenic than typical mid-ocean ridge basalts (MORB) of 0.703427 (Workman and Hart 2005). The dunite also has a value within the broad MORB range of 0.703383, whilst the pyroxenites have both enriched and MORB-like values of 0.704444 and 0.703412. The oxygen isotope composition of olivine separates from all samples varies from 5.06 to 5.23 ‰ $\delta^{18}O$ (Table 4.2), well within the typical mantle range of 5.18 ± 0.28 ‰ (Mattey et al. 1994). The recrystallized olivine neoblasts of sample 67-02A(3) yielded an almost identical $\delta^{18}O$ to the olivine porphyroclasts from the same sample (5.22 and 5.20 ‰ respectively). Similarly, cloudy olivine from samples 67-02A(5), 67-02B(3) and 67-02D(4) have indistinguishable oxygen isotope compositions to transparent olivine from the same samples, differing by 0.00 to 0.07 ‰. Orthopyroxene has a wider compositional range than olivine of 5.67 to 5.99 ‰ $\delta^{18}O$ (Table 4.2), but still typical of the upper mantle (5.69 ± 0.28 ‰, Mattey et al. 1994). The lowest value is recorded by orthopyroxene from a pyroxenite (5.67 ‰), although this is very close to the lowest value for harzburgitic orthopyroxene (5.75 ‰). There is no correlation between $\delta^{18}O_{Olivine}$ and $\delta^{18}O_{Opx}$. Oxygen isotope fractionation between orthopyroxene and olivine

Sample	Mass (g)	Type	Os	Ir	Ru	Pt	Pd	Re	$^{187}Os/^{188}Os$	1 s.e.	T_{RD} (Ga)	$^{87}Sr/^{86}Sr$	1 s.e.
Whole-rocks													
A1	1.49	Pyroxenite	0.79	2.01	0.59	322	99.3	0.156	0.12601	0.00004	0.3	*0.704444*	*0.000015*
B6	1.50	Pyroxenite	0.08	0.85	3.58	9.60	6.79	0.166	0.12479	0.00016	0.5	0.703412	0.000015
B2	1.51	Dunite	1.30	2.07	15.8	0.16	0.21	0.060	0.12346	0.00008	0.7	0.703383	0.000009
A2	1.50	Residual	5.91	4.57	5.92	1.84	0.12	0.007	0.12141	0.00010	1.0	*0.704473*	*0.000010*
B1	1.50	Residual	2.72	4.91	5.24	6.05	0.04	0.005	0.12630	0.00009	0.3	*0.704208*	*0.000020*
D4	1.51	Residual	1.74	2.92	3.82	0.81	0.18	0.063	0.12793	0.00007	0.1	0.703556	0.000012
E1	1.50	Residual	1.54	1.52	3.56	1.67	0.41	0.010	0.12128	0.00008	1.0	*0.703860*	*0.000010*
A3	1.50	Type II reacted	5.00	4.18	8.95	10.5	5.32	0.026	0.12650	0.00007	0.3	0.703427	0.000010
A5	1.50	Type II reacted	3.56	0.52	2.41	1.09	0.68	0.032	0.12039	0.00020	1.1	0.703557	0.000007
A5 (duplicate)	1.49	Type II reacted	-	0.85	2.13	1.41	0.78	0.033					
B3	1.50	Type I reacted	2.72	1.70	3.40	1.91	0.28	0.071	0.12348	0.00013	0.7	*0.704871*	*0.000009*
B5	1.48	Type II reacted	0.07	0.57	4.44	2.22	1.08	0.038	0.12564	0.00012	0.6	0.703531	0.000009
B5 (duplicate)	1.50	Type II reacted	0.06	0.54	4.15	2.05	0.96	0.034					
D7	1.50	Type I reacted	3.80	3.30	4.33	5.68	0.44	0.032	0.12581	0.00005	0.4	0.703888	0.000008
E3	1.51	Type I reacted	3.54	4.81	7.10	5.84	0.43	0.078	0.12491	0.00009	0.5	0.703676	0.000008
Olivine separates													
A2 olivine	0.116	Residual	21.0	5.87	11.0	0.14	1.22	0.020	0.1218	0.0002	0.9		
A5 olivine	0.106	Type II reacted	0.02	0.32	6.96	0.24	8.76	0.276	0.1248	0.0010	0.5		
A5 olivine	0.125	Type II reacted	0.01	0.02	0.10	0.04	1.06	0.040					
D4 olivine	0.101	Residual	0.50	10.2	3.31	1.49	0.05	0.032	0.1273	0.0001	0.2		
Total procedural blank and reference standard													
TPB	-		2.30	1.69	38.7	33.7	3.18	2.04					
GP13	1.0		3.54	3.39	5.94	6.94	5.25	0.261	0.12607	0.00007			

Table 4.1 HSE concentrations (ppb) and Os and Sr isotope compositions of whole-rock harzburgites, pyroxenites and dunite. Sample masses refer to masses used for HSE (including Os isotope) measurements. Also reported are the HSE concentrations and Os isotope compositions of olivine separates. Rhenium-depletion age (T_{RD}) calculated using the primitive mantle estimates of Meisel et al. (2001). Italicised Sr isotope data was measured by TIMS

Sample	Mass (g)	Type	Os	Ir	Ru	Pt	Pd	Re	$^{187}Os/^{188}Os$	1 s.e.	T_{RD} (Ga)	$^{87}Sr/^{86}Sr$	1 s.e.
Whole-rocks													
A1	1.49	Pyroxenite	0.79	2.01	0.59	322	99.3	0.156	0.12601	0.00004	0.3	*0.704444*	*0.000015*
B6	1.50	Pyroxenite	0.08	0.85	3.58	9.60	6.79	0.166	0.12479	0.00016	0.5	0.703412	0.000015
B2	1.51	Dunite	1.30	2.07	15.8	0.16	0.21	0.060	0.12346	0.00008	0.7	0.703383	0.000009
A2	1.50	Residual	5.91	4.57	5.92	1.84	0.12	0.007	0.12141	0.00010	1.0	*0.704473*	*0.000010*
B1	1.50	Residual	2.72	4.91	5.24	6.05	0.04	0.005	0.12630	0.00009	0.3	*0.704208*	*0.000020*
D4	1.51	Residual	1.74	2.92	3.82	0.81	0.18	0.063	0.12793	0.00007	0.1	0.703556	0.000012
E1	1.50	Residual	1.54	1.52	3.56	1.67	0.41	0.010	0.12128	0.00008	1.0	*0.703860*	*0.000010*
A3	1.50	Type II reacted	5.00	4.18	8.95	10.5	5.32	0.026	0.12650	0.00007	0.3	0.703427	0.000010
A5	1.50	Type II reacted	3.56	0.52	2.41	1.09	0.68	0.032	0.12039	0.00020	1.1	0.703557	0.000007
A5 (duplicate)	1.49	Type II reacted	-	0.85	2.13	1.41	0.78	0.033					
B3	1.50	Type I reacted	2.72	1.70	3.40	1.91	0.28	0.071	0.12348	0.00013	0.7	*0.704871*	*0.000009*
B5	1.48	Type II reacted	0.07	0.57	4.44	2.22	1.08	0.038	0.12564	0.00012	0.6	0.703531	0.000009
B5 (duplicate)	1.50	Type II reacted	0.06	0.54	4.15	2.05	0.96	0.034					
D7	1.50	Type I reacted	3.80	3.30	4.33	5.68	0.44	0.032	0.12581	0.00005	0.4	0.703888	0.000008
E3	1.51	Type I reacted	3.54	4.81	7.10	5.84	0.43	0.078	0.12491	0.00009	0.5	0.703676	0.000008
Olivine separates													
A2 olivine	0.116	Residual	21.0	5.87	11.0	0.14	1.22	0.020	0.1218	0.0002	0.9		
A5 olivine	0.106	Type II reacted	0.02	0.32	6.96	0.24	8.76	0.276	0.1248	0.0010	0.5		
A5 olivine	0.125	Type II reacted	0.01	0.02	0.10	0.04	1.06	0.040					
D4 olivine	0.101	Residual	0.50	10.2	3.31	1.49	0.05	0.032	0.1273	0.0001	0.2		
Total procedural blank and reference standard													
TPB	-		2.30	1.69	38.7	33.7	3.18	2.04					
GP13	1.0		3.54	3.39	5.94	6.94	5.25	0.261	0.12607	0.00007			

Sample	Type	$\delta^{18}O_{Olivine}$	n	1 s.d.	$\delta^{18}O_{Orthopyroxene}$	n	1 s.d.	Δ_{Opx-ol}
A2	Residual	5.26	2	0.06	5.91	2	0.06	0.64
		5.20	2	0.06	5.84	3	0.01	
A3	Type II reacted	5.19	3	0.02	5.96	1	0.02	0.77
		5.21	2	0.02	5.97	1	0.02	
A3 neoblasts	Type II reacted	5.21		0.02				
		5.22		0.02				
A5	Type II reacted	5.14	3	0.02	5.77	1	0.02	0.67
		5.10	3	0.02				
		5.10	Powdered	0.01				
		5.05	Powdered	0.01				
B1	Residual	5.12	Powdered	0.01	5.93	1	0.02	0.76
		5.19	1	0.02	5.91	1	0.02	
		5.17	Powdered	0.01				
B3	Type I reacted	5.14	Powdered	0.01	5.75	2	0.06	0.58
		5.20	Powdered	0.01				
		5.17	Powdered	0.01				
B5	Type II reacted	5.18	1	0.02	5.83	3	0.01	0.65
		5.12	1	0.02	5.69	3	0.01	
					5.89	2	0.06	
B6	Pyroxenite				5.67	3	0.01	
					5.67	3	0.01	
D4	Residual	5.19	Powdered	0.01	5.85	2	0.06	0.75
		5.06	1	0.06				
		5.01	Powdered	0.01				
		5.12	Powdered	0.01				
D7	Type I reacted	5.14	1	0.02	5.74	3	0.01	0.71
		5.06	2	0.02	5.87	1	0.02	
E1	Residual				5.97	3	0.01	
					6.01	3	0.01	
E3	Type I reacted	5.14	1	0.06	5.76	2	0.06	0.72
		5.11	2	0.06	5.91	2	0.06	
					5.84	3	0.01	

Table 4.2 Oxygen isotope composition ($\delta^{18}O$) of olivine and orthopyroxene, expressed as per mil. 'n' refers to the number of crystals analysed, with 'powdered' denoting multiple finely crushed crystals which mediated problems with crystals jumping during vaporisation. 1 s.d. is the standard deviation of three standards measured on the day of analysis. Δ_{Opx-ol} is the isotopic fractionation between the average composition of orthopyroxene and olivine for each sample where both phases were measured. A3 neoblasts were clusters of fine-grained olivine matrix and hence the number of crystals could not be determined.

($\Delta^{18}O_{Opx\text{-}Olivine}$) varies from 0.580 to 0.792 ‰. There is no correlation between either $\delta^{18}O$ or $\Delta^{18}O$ and $^{87}Sr/^{86}Sr$. Orthopyroxene from 'reacted' samples tends to have slightly lower $\delta^{18}O$ compared to orthopyroxene from 'residual' samples however these differences are generally within the uncertainty of the measurements. The Os isotope compositions ($^{187}Os/^{188}Os$) of whole rock peridotites defines a broad range of values between 0.12039 and 0.12793 (Table 4.1) which mirrors the range of values for the convecting oceanic mantle (Harvey et al., 2006; Snow and Reisberg, 1995). There is no systematic distinction between the $^{187}Os/^{188}Os$ of harzburgites, pyroxenites and the dunite, nor is there any correlation with either O or Sr isotope composition. The Os isotope compositions of olivine separates from two samples were nearly identical to their respective whole-rock values for those samples (0.1217 compared to 0.1214 and 0.1273 compared to 0.1279 for samples 67-02A(2) and 67-02D(4) respectively).

4.3.2 Highly siderophile elements

Concentrations of Os, Ir, Ru, Pd, Pt and Re in the harzburgites show substantial variations (Table 4.1; total ranges are 0.07-5.91 ng/g, 0.52-4.91 ng/g, 2.41-8.95 ng/g, 0.81-10.55 ng/g, 0.04-5.32 ng/g and 0.01-0.08 ng/g respectively). Where present, correlations between HSE are poorly defined (Fig. 4.1), with weak positive correlations between Os and Ir, Ru and both Ir and Pt and, with the exception of one sample (67-02A(3)), a weak negative correlation between Ir and Pd. Concentrations of HSE in 'residual' harzburgites show less variation than observed in 'reacted' harzburgites, particularly concentrations of PPGE (Pt to Pd). When normalised to the primitive mantle values of Becker et al. (2006), 'residual' harzburgites display typical 'depleted' patterns (Fig. 4.2) with approximately flat Os to Ru (IPGE), albeit at concentrations sometimes only half those of the primitive mantle, and steeply downward dipping PPGE. Values of Pd_N/Ir_N (where subscript N indicates normalisation to primitive mantle values) range from 0.004 to 0.132. Rhenium is highly depleted relative to primitive mantle but is generally positively inflexed relative to Pd. Primitive mantle-normalised HSE patterns for 'reacted' harzburgites (Fig. 4.2) vary both from sample to sample and when compared to 'residual' harzburgite patterns. The differences from 'residual' harzburgites can be summarised by; 1) More variable concentrations and fractionation of IPGE, particularly Ir and Ru; 2) Less steeply dipping PPGEs and general relative enrichment in Re. Osmium is relatively homogeneous except

for one sample (67-02B(5)) which is substantially depleted in Os and has highly fractionated IPGE (Os_N/Ru_N = 0.03). Pd_N/Ir_N values fall into two sub-groups; three 'reacted' samples (type I) are similarly fractionated to 'residual' samples (0.044-0.080) whilst the remaining three 'reacted' samples (type II) have relatively unfractionated ratios (0.628-0.874).

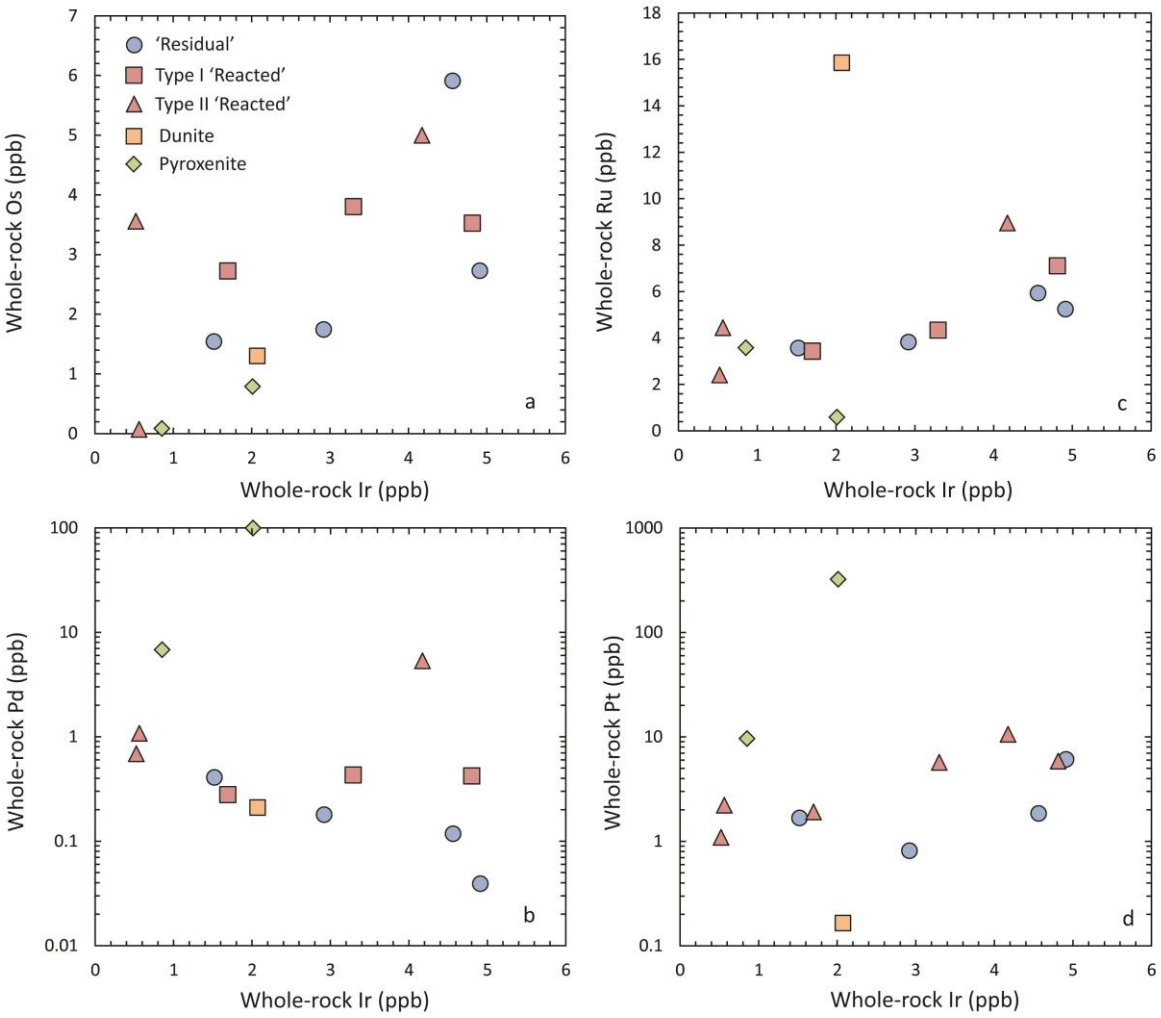

Fig. 4.1 Co-variation between highly siderophile elements in whole-rock peridotites; a) Os vs. Ir; b) Pd vs. Ir; c) Ru vs. Ir; d) Pt vs. Ir

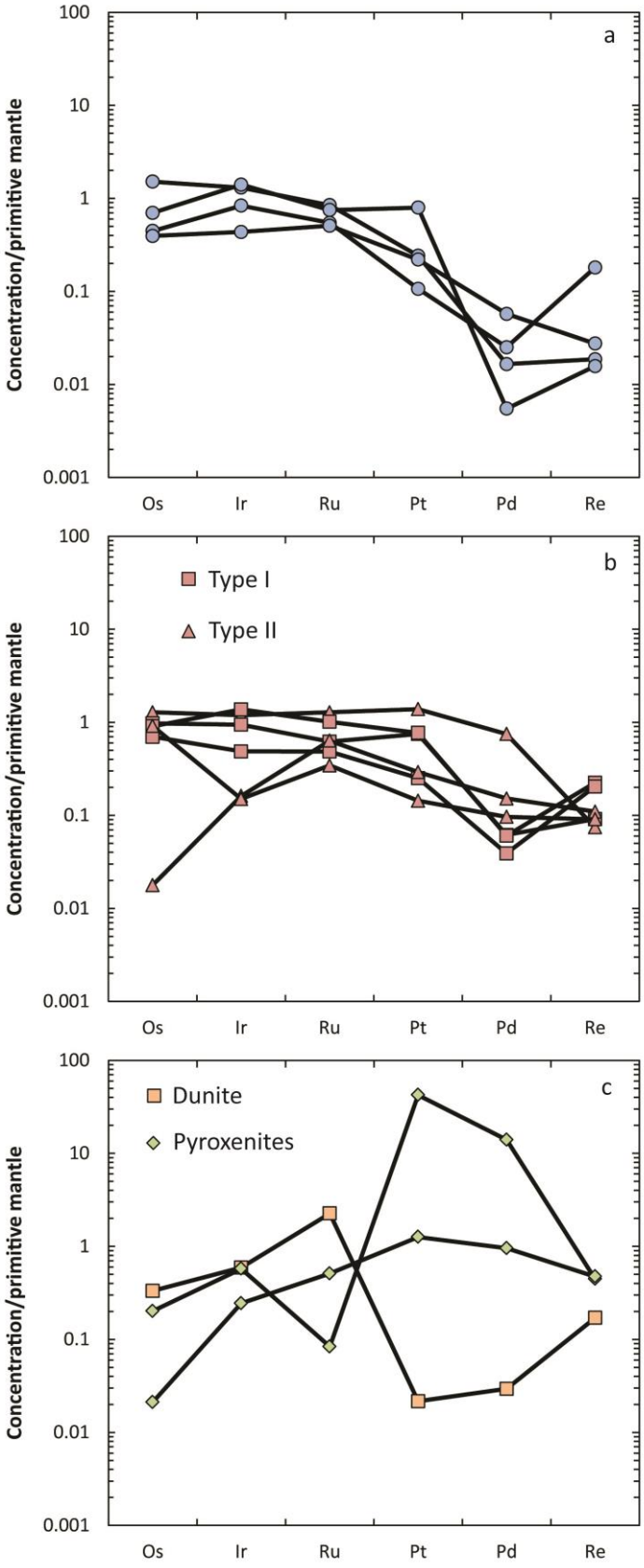

Fig. 4.2 Primitive mantle-normalised HSE concentrations of; a) 'residual' harzburgites; b) type I and type II 'reacted' harzburgites; c) dunite and pyroxenites. Normalising values from Becker et al. (2006)

The two pyroxenites and the dunite display very different normalised HSE patterns (Fig 4.2c). The dunite has fractionated IPGE, with a positive Ru anomaly (Ru_N/Os_N = 6.8) but concentrations of Os and Ir similar to the harzburgites. PPGE on the other hand are highly depleted relative to primitive mantle, but with a positive Re_N/Pt_N (7.9) compared to (with one exception) sub-chondritic values of Re_N/Pt_N for the harzburgites. One of the pyroxenites (67-02B(6)) has an HSE pattern which is strongly complementary to the dunite, with a negative Ru anomaly (Ru_N/Os_N = 0.4) and enriched concentrations of Pt and Pd (322 and 97 ppb respectively). Re_N/Pt_N is very low (0.01), amongst the lowest reported for non-residual terrestrial rocks. The other pyroxenite (67-02B(6)) displays general enrichment in PPGE and Re over IPGE, with Pt_N/Os_N of 59.8. Re_N/Pt_N however is again subchondritic (0.38). There are no correlations between concentrations of HSE and Os isotope composition.

Olivine separates from three samples produced primitive mantle-normalised HSE patterns which showed both similarities and differences to their respective whole-rock compositions (Fig. 4.3). Olivines from 'residual' sample 67-02A(2) share the high IPGE/PPGE ratios of the whole-rock data for this sample but are overall more enriched in Os, Ir, Ru, Pd and Re than the whole-rock. The major difference is the concentration of Pt, which is much more enriched in the whole-rock such that the olivine has a pronounced negative Pt anomaly (Pt_N/Ir_N = 0.01, Pt_N/Pd_N = 0.11). An olivine separate from the other 'residual' sample (67-02D(4)) shares a similar overall normalised HSE pattern to the whole-rock but are slightly more depleted in Pd and Re and have much more fractionated IPGE (Os_N/Ir_N = 0.04 in the olivines compared to 0.54 in the whole-rock). Olivines in this sample do not have a negative Pt anomaly, and in fact are slightly more enriched in Pt compared to the whole-rock. Duplicate olivine measurements from 'reacted' sample 67-02A(5) have similar normalised HSE patterns to each other but with very different concentrations (for example, Ru differs in concentration by nearly two orders of magnitude). The normalised HSE pattern of the whole-rock is similar (for example, both olivines and whole-rock have Ru_N/Ir_N >1), but with two important differences. Firstly, both olivine separates have Os_N/Ir_N <1 (0.05 and 0.57) whereas the whole-rock has a positive Os_N/Ir_N (6.1). Secondly, the olivine separates have negative Pt anomalies not present in the whole-rock data, similar to those found in 67-02A(2).

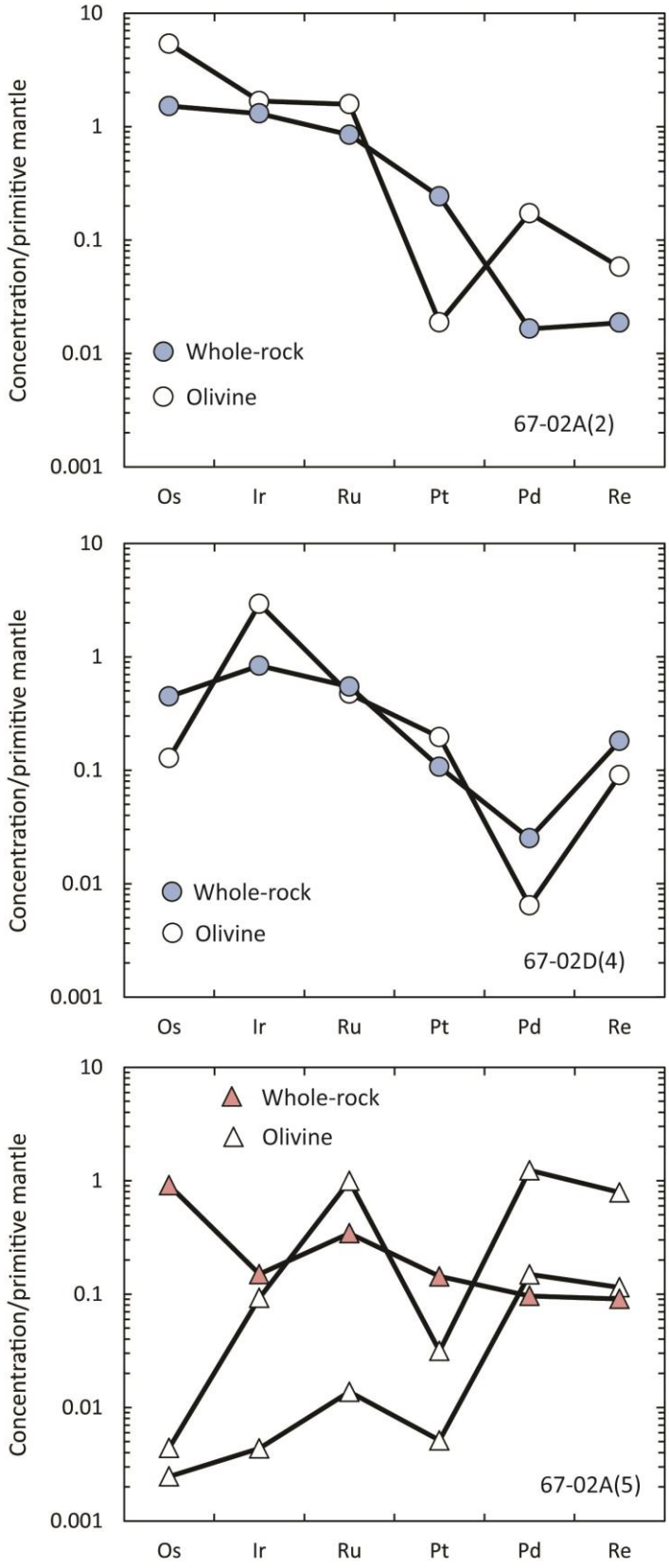

Fig. 4.3 Primitive mantle-normalised HSE concentrations of olivine separates and respective whole-rocks from two 'residual' peridotites, 67-02A(2) and 67-02D(4), and one 'reacted' peridotite, 67-02A(5). Normalising values from Becker et al. (2006)

Thin sections were inspected closely using reflected light microscopy to determine the presence of sulphides. 'Residual' samples have very low sulphide abundances, with only rare inclusions in olivine (2-5 per section). Intergranular sulphides were less abundant but occasionally observed in a number of samples. 'Reacted' samples often contain slightly greater abundances of sulphide grains which are associated with secondary orthopyroxene patches and veins. A number of larger grains showed exsolution of a second sulphide phase. Pyroxenite 67-02B(6) contains similarly low overall abundances, whilst the other pyroxenite 67-02A(1) containS much more abundant, relatively large sulphides typically as inclusions in pyroxene. Dunite 67-02B(2) also contains abundant sulphides, although they are smaller and typically occur as inclusions in spinel and olivine with occasional intergranular examples.

4.4 Discussion

4.4.1 Effect of partial melting on HSE concentrations

It is now well established that HSE are fractionated during partial melting, owing to the differences in compatibility between IPGE (Os, Ir, Ru) and PPGE (Pt, Pd) + Re (e.g. Barnes et al., 1985 Pearson et al. 2004, Mungall et al. 2005, Bockrath et al. 2004, Mungall et al. 2005, Ballhaus et al. 2006, Mungall and Barnes 2014). Previous studies have found that the dominant hosts for HSE in mantle samples are base metal sulphides (BMS) in which HSE are highly compatible (Lorand et al. 2013 are references within). The BMS observed in such samples however (e.g. chalcopyrite, pentlandite and pyrrhotite) are not primary mantle phases and instead form through exsolution of high temperature BMS during sub-solidus cooling. These high temperature BMS consist of monosulphide solid solution (MSS; Fe-Ni-S) and intermediate solid solution (ISS; Cu-Fe-S). During melting, the more fusible ISS tend to dissolve more readily to form Cu-rich sulphide melt, preferentially removing PPGE from the residue, before being removed from the residue along with the extraction of silicate melt (Bockrath et al. 2004, Ballhaus et al. 2006). Monosulphide solid solution, in which IPGE are more compatible than PPGE, will remain in the residue until greater degrees of melting, particularly at low oxygen fugacity and at lower melting temperatures (e.g. during fluid-fluxed melting, Bockrath et al. 2004, Mungall et al. 2006). This physical behaviour of ISS and MSS and the different compatibilities of IPGE and PPGE

between MSS and Cu-sulphide melt results in the general order of compatibility for HSE; $D^{Os} \approx D^{Ir} \approx D^{Ru} > D^{Pt} > D^{Pd} > D^{Re}$ (Luguet et al. 2003, Bockrath et al. 2004, Pearson et al. 2004, Mungall et al. 2005, Ballhaus et al. 2006, Mungall et al. 2014) and is responsible for the lower concentrations of PPGE, compared to IPGE, observed in peridotites after moderate to large degrees of partial melting. This produces highly fractionated HSE patterns with low PPGE/IPGE, and typically low Pd/Pt, yet relatively unfractionated and primitive mantle-like IPGE.

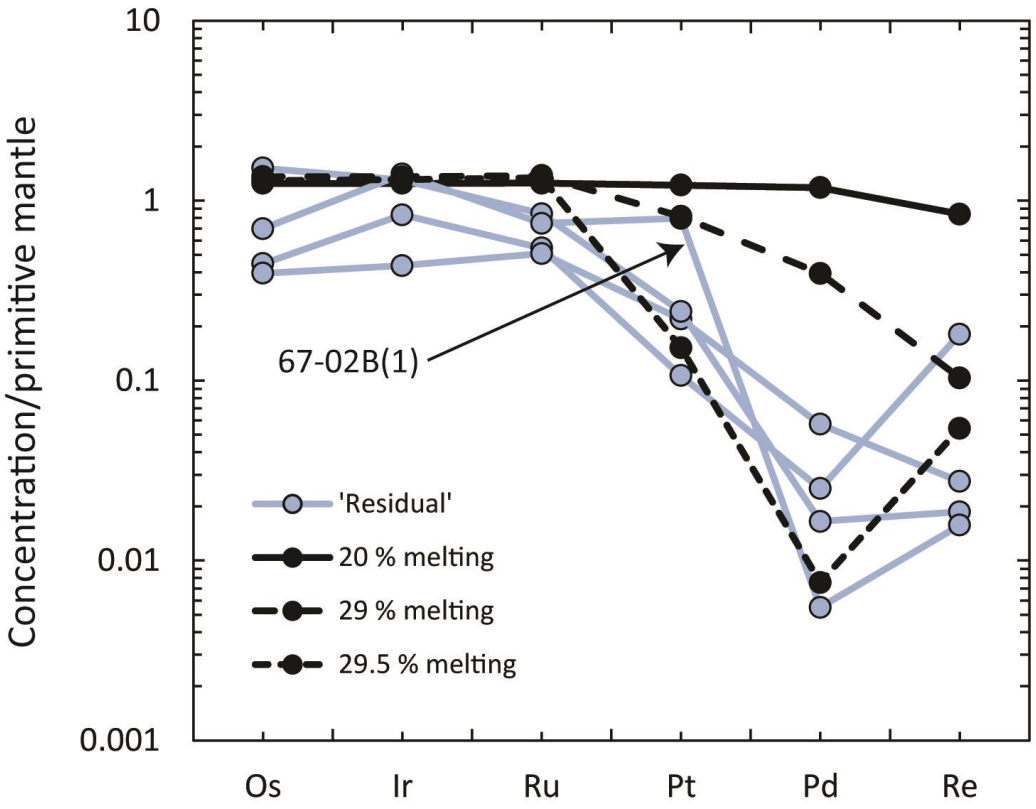

Fig. 4.4 The results of modal fractional melting models attempting to reconstruct the primitive mantle-normalised HSE concentrations of 'residual' harzburgites. 67-02B(1) with exceptionally low Pd_N/Pt_N labelled individually. See text and Table 4.3 for methodology and parameters used and complete discussion. The extreme fractionation of Pd from Ir can only be achieved close to the point of sulphide exhaustion (~ 30 %) over a narrow range of partial melting degrees, with MSS present in the residue. Alternatively, sulphide melt may be preferentially stripped from the residue, removing PPGE preferentially over IPGE which may also explain the observed fractionations. Variation in concentrations of IPGE are best explained by heterogeneous distribution of Os-Ir-Ru nuggets on hand sample scale (10-30 cm)

Estimates for the degree of partial melting based on mildly incompatible trace elements in orthopyroxene are high for the Ritter samples (29-33 %, see chapter 2). At such degrees of partial melting it may be anticipated that sulphide would be completely exhausted from the solid residue (Lorand et al. 2004, Luguet et al. 2007), in which case HSE concentrations would be controlled by other phases, such as platinum group minerals which may form as breakdown products of MSS and sequester residual HSE (Luguet et al. 2004, Luguet et al. 2007), and residual silicates or spinel. Sulphides, however, are observed in all samples, albeit in very low abundances, typically as inclusions in olivine or in 'reacted' samples in secondary orthopyroxene veins and patches. Their inclusion in mineral hosts may have acted as a shield from physical removal from the residue and thus the partitioning systematics discussed above would still apply, although an additional control by un-characterised HSE-rich phases can't be discounted. Sulphides included in secondary phases may reflect redistribution of residual sulphides or may be entirely secondary, which would result in changes to HSE concentrations, particularly PPGE which are enriched in melts (although this would also depend on the composition of the sulphide). A simple modal fractional partial melting model was constructed to ascertain whether the HSE concentrations and fractionations are consistent with the degrees and conditions of partial melting deduced through lithophile trace element systematics (chapter 2). In our model we assumed partial melting at 1250 °C and 2 GPa (consistent with a subduction zone setting), under which conditions sulphide would remain in the residue until ~30 % melting (Mavrogenes and O'Neill 1999), although if the oxygen fugacity was significantly greater than the fayalite-magnetite quartz buffer sulphide-out would potentially occur much earlier in the melting process due to hugely increased S solubility (Jugo 2009). Under these conditions, MSS is still stable in the residue (Bockrath et al. 2004), hence we assume 80 % of sulphide is MSS and the remainder sulphide liquid. Bulk partition coefficients were calculated for equilibrium between silicate melt, sulphide melt, MSS and silicate restite with partition coefficients listed in Table 4.3. Mungall and Brenan (2014) recently reported updated sulphide melt/silicate melt partition coefficients which were substantially higher than previous studies (e.g. Peach et al. 1990, Andrews and Brenan 2002). Our model is significantly impacted by this when compared to similarly-constructed partial melting models prior to Mungall and Brenan (2014). The result is that until a point very close to (within 1 % of)

sulphide-out in the residue the concentrations of HSE in the bulk residue remain much higher and unfractionated relative to the Ritter harzburgites (Fig. 4.4). The Ritter HSE data (in particular the very low Pd_N/Ir_N) can only be reconciled with the partial melting model if melting proceeded right up until sulphide-out at ~30 % melting, which would be consistent with our lithophile partial melting model (chapter 2). It may seem fortuitous that melting ended at such a precise stage, without any thermodynamic barrier such as exhaustion of a major silicate phase. It is plausible that the shielding of sulphides described above may have prevented physical removal of sulphides at/beyond the point of sulphide-exhaustion, hence the highly fractionated and depleted HSE signature would be preserved over a broader partial melting range. Alternatively, the sulphide melt in equilibrium with residual MSS could have been preferentially stripped from the residue, hence our model would overestimate the concentrations of PPGE and underestimate the degree of HSE fractionation.

	Os	Ir	Ru	Pt	Pd	Re
Primitive mantle[a]	3.9	3.5	7.0	7.6	7.1	0.35
D MSS/sulphide melt[b]	2	1	4	0.004	0.012	3
D sulphide melt/silicate melt[c]	3.5.E+05	4.9.E+05	3.0.E+05	2.4.E+05	1.0.E+05	9.6.E+02
D MSS/silicate melt (calculated)	7.0.E+05	4.9.E+05	1.2.E+06	9.6.E+02	1.2.E+03	2.9.E+03
D solid silicates/silicate melt[d]	2	3	3	0.017	0.007	0.1
Proportion of sulphide as MSS	0.8					
Initial sulphur	200 ppm					

Table 4.3 Parameters used in the modal fractional melting model:
[a]Becker et al. (2006)
[b]IPGE and Re from Ballhaus et al. (2006), PPGE from Mungall et al. (2005)
[c]Mungall and Brenan (2014)
[d]IPGE and PPGE from Mungall and Brenan (2014), calculated assuming an oxygen fugacity of -7 log bars. Re is from Mallmann and O'Neill (2007) assuming an 80:20 mixture of olivine and orthopyroxene and an oxygen fugacity equivalent to the fayalite-magnetite-quartz buffer

There are two main discrepancies when comparing the melting model to the Ritter data. Firstly sample 67-02B(1) has very low Pd_N/Pt_N which cannot be reconciled with any degree of melting (Fig. 4.4). This sample also shows a slight positive Ir anomaly, and we thus attribute this relative enrichment in Pt and Ir to Pt-rich Pt-Ir alloy nuggets which have been previously invoked to explain broad ranges in IPGE concentrations, and enhanced compatibility of Pt, in continental peridotites (Luguet et al. 2007, Lorand et al. 2013). A second discrepancy between the measured data and the melting model is the greater variation and fractionations in IPGE. We also attribute this to a nugget effect, with heterogeneously distributed Os-Ir-Ru phases variably diluted by IPGE-poor silicates. These nugget effects are evaluated in more detail further in the discussion.

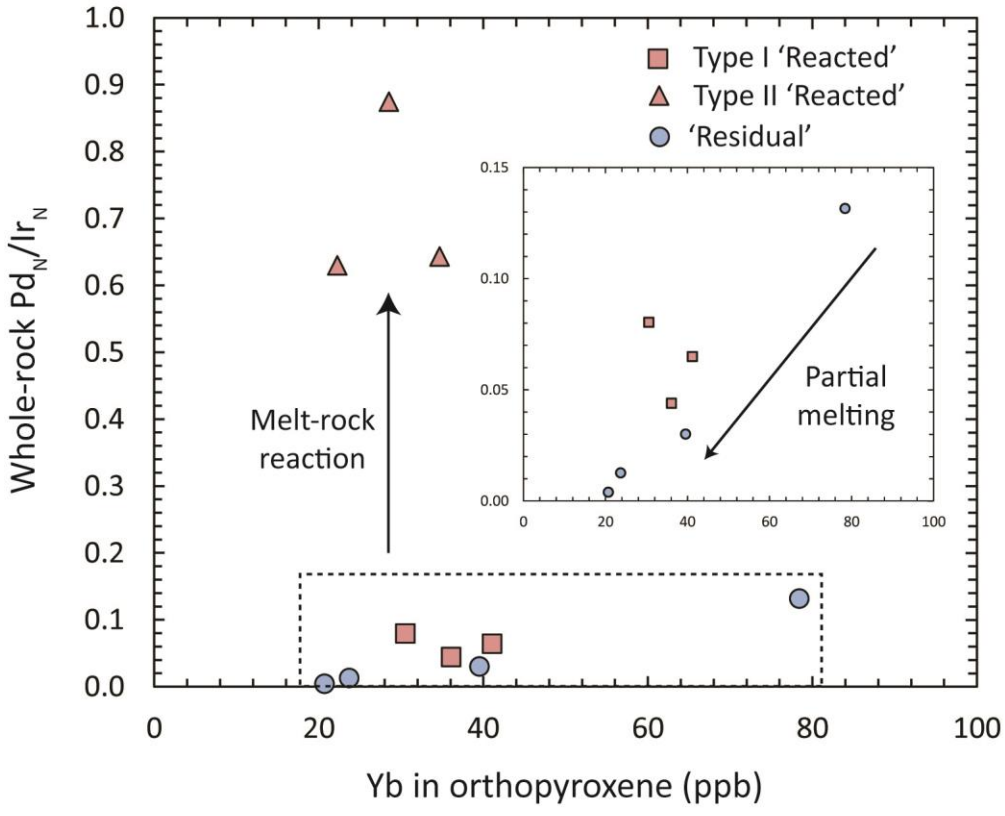

Fig. 4.5 Correlation between Pd_N/Ir_N and the concentration of Yb in orthopyroxene for Ritter harzburgites. Samples with low Pd_N/Ir_N define a partial melting trend whereas samples with high Pd_N/Ir_N are interpreted to reflect melt-rock reaction

To further investigate whether the HSE concentrations in 'residual' samples do indeed reflect the partial melting process we compared concentrations and ratios of HSE to the concentrations of HREE in orthopyroxene, which have been shown to reliably retain partial melting histories (chapter 2). The 'residual' harzburgites and the three low Pd/Ir 'reacted' harzburgites produce a positive trend between concentrations of Yb in orthopyroxene and whole rock Pd_N/Ir_N (Fig. 4.5), which is consistent with expected trends given the greater incompatibility of Pd relative to Ir and incompatibility of Yb during partial melting. It is possible that this trend reflects metasomatism, with addition of more incompatible Pd in addition to Yb. However we observe no trends between Pd_N/Ir_N and other elements in orthopyroxene more sensitive to metasomatism, such as LREE and Na. We also note the much higher Pd_N/Ir_N of the other three 'reacted' harzburgites, at similar Yb in orthopyroxene contents, which we ascribe to melt-rock reaction (see below). We therefore propose that Pd_N/Ir_N in seven of the ten of the harzburgites is indeed related to partial melting in these samples. This is in spite of the observed textural variability, since two type II 'reacted' samples which record low Pd_N/Ir_N also show substantial textural evidence for silicate melt-rock reaction with numerous veins and patches of secondary orthopyroxene with which sulphide grains are often associated. Our data therefore show that Pd_N/Ir_N, whilst clearly disturbed in type II 'reacted' samples, may be able to survive secondary processes operating in the upper mantle. The sulphides associated with secondary phases and any secondary nuggets of HSE-bearing alloys clearly must be sufficiently low in Pd and Ir to preserve such a trend. Concentrations and ratios of other HSE display no such correlations with Yb in orthopyroxene which, combined with the general lack of correlation between HSE themselves, implies that they have been disturbed by subsequent processes or that HSE concentrations are influenced by heterogeneously located MSS or alloy nuggets. With the exception of Pt however, these were not sufficient to obscure the overall residue-like depleted normalised HSE patterns (Fig. 4.2).

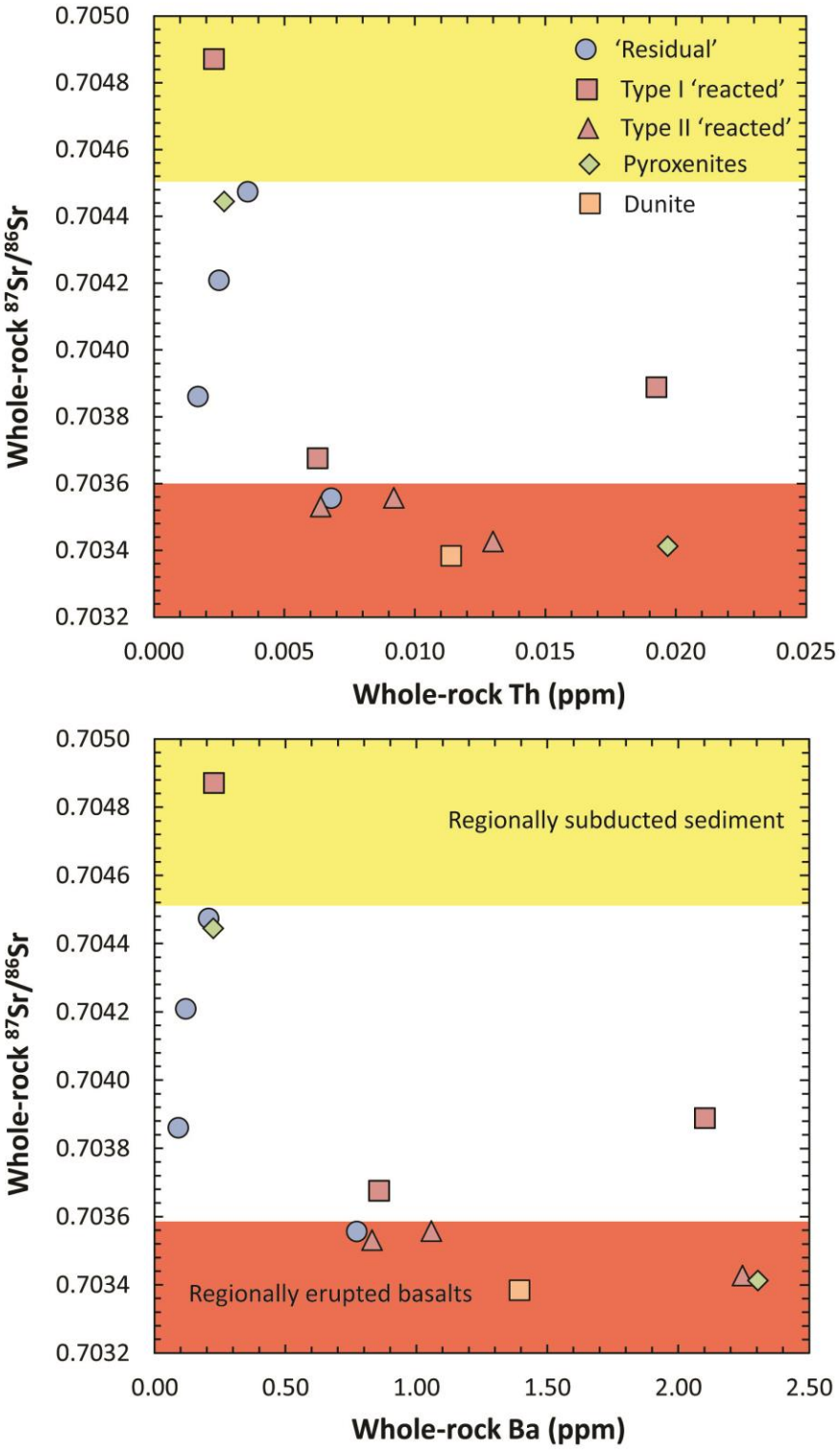

Fig. 4.6 Correlation between whole-rock $^{87}Sr/^{86}Sr$ and concentration of highly incompatible trace elements. Shaded areas at the top of each plot represents the range of $^{87}Sr/^{86}Sr$ values for Solomon Sea sediment (Woodhead et al. 1998). Shaded areas at the bottom of each plot represents the average $^{87}Sr/^{86}Sr$ values for lavas erupted along the West Bismarck and New Britain Island Arcs ± 1 s.d. (Woodhead et al. 1998, Woodhead et al. 2010, Cunningham et al. 2012). Uncertainties in measured data are similar to or smaller than symbol size.

4.4.2 Response of Sr and O isotopes to open-system processes

Whole-rock and *in-situ* geochemistry of 'residual' and 'reacted' harzburgites is consistent with melting and metasomatism as part of a previous arc system, followed by variable degrees of melt-rock reaction with silicate melts as part of the present day mantle wedge underlying the active West Bismarck Island Arc (chapter 2). To assess the involvement of slab-derived material in the petrogenesis of these geochemical signatures, we plotted whole-rock $^{87}Sr/^{86}Sr$ against parameters sensitive to open-system processes, such as whole-rock incompatible trace element concentrations and Fe_2O_3/FeO in spinel (Fig. 4.6, Fig. 4.7). Strontium isotopes are a well-established tracer of slab-derived material, since both continent-derived and oceanic sediments typically inherit highly radiogenic Sr from old continental material and seawater, distinct from the substantially less radiogenic values of the mantle. 'Residual' samples with very low concentrations of whole-rock trace elements and low Fe_2O_3/FeO in spinel have elevated values of $^{87}Sr/^{86}Sr$ that are not only significantly outside the MORB range but also elevated compared to the majority of arc basalts erupted along the lengths of both the New Britain and West Bismarck Island Arcs (Woodhead et al. 1998, Woodhead et al. 2010, Cunningham et al. 2012). These elevated $^{87}Sr/^{86}Sr$ ratios approach the compositions of regionally subducted sediment (Woodhead et al. 1998), and are thus interpreted to reflect a peridotite protolith fluxed with crustal-derived sedimentary material, supporting the conclusion from trace element systematics that they formed in an 'ancient' mantle wedge. This further supports the conclusions of Woodhead et al. (1998) that the mantle beneath the New Britain Island Arc experienced a prior episode of subduction resulting in 'palaeo-enrichments' and observed in rare instances of lavas with more radiogenic Sr and Pb isotope compositions, such as from Rabaul volcano. Similarly radiogenic lavas are occasionally erupted along the West Bismarck Arc (Woodhead et al. 2010, Cunningham et al. 2012) indicating that these palaeo-enrichments may be a more widespread feature of the mantle beneath the Bismarck Archipelago. Our data demonstrate that this radiogenic component is present at least in the upper mantle wedge. It is possible therefore that these rarer, more radiogenic magmas inherit this signature through melt-rock interactions between arc magmas generated with MORB-like Sr isotopic composition and this enriched portion of the mantle. The scarcity of lavas reflecting this radiogenic mantle may be largely due to the

fact that the signature is contained within very depleted material (< 1 ppm Sr). Therefore, substantial amounts of interaction with peridotite and perhaps assimilation of more Sr-rich pyroxenite veins carrying this radiogenic signature would be required to satisfy mass-balance constraints, allowing the MORB-like signature to dominate the isotopic composition of the majority of lavas erupted along the Bismarck Arcs. In agreement with Woodhead et al. (1998), it seems that the most likely source of these palaeo-enrichments is the now extinct Vitiaz-West Melanesian trench system currently situated to the north. We note that both lavas and lava-hosted mantle xenoliths erupted from this arc system bear similarly radiogenic Sr isotope compositions to the 'residual' Ritter xenoliths (0.70306 to 0.70474 for peridotite residues, 0.70397 for lavas; Kamenov et al. 2008).

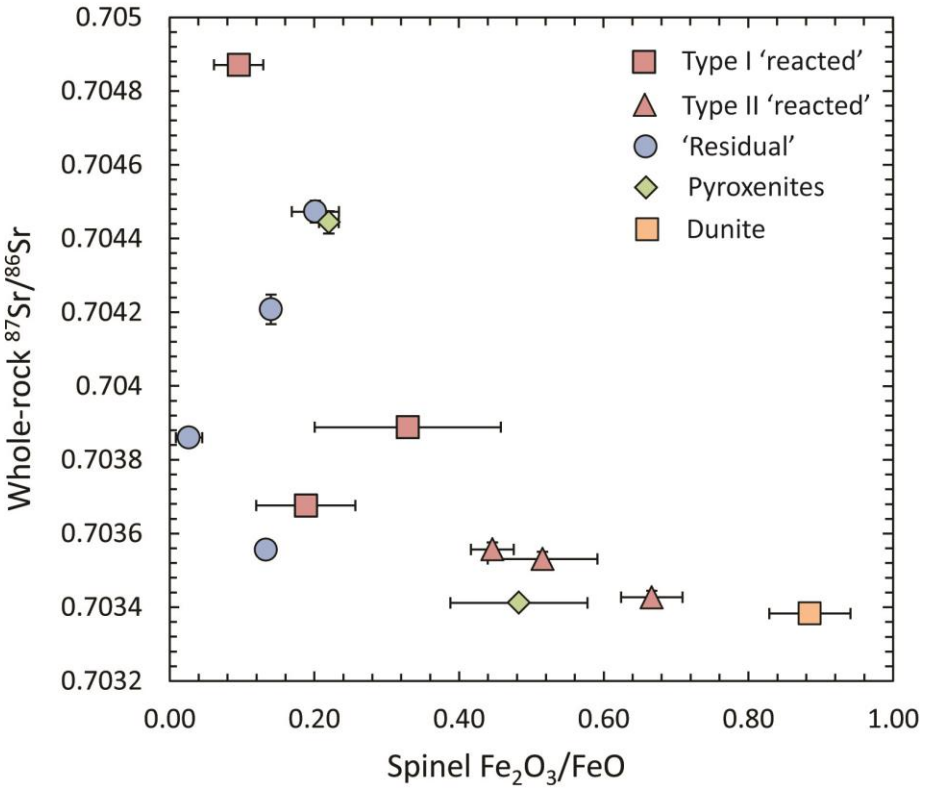

Fig. 4.7 Correlation between spinel Fe_2O_3/FeO (redox state) and whole-rock $^{87}Sr/^{86}Sr$. Fe_2O_3/FeO calculated assuming idea spinel stoichiometry (chapter 2). Error bars for Fe_2O_3/FeO represent 1 s.d. of multiple spinel measurements. Uncertainties on Sr isotope composition, where visible, are for 2 s.e.

When the Sr isotope composition of 'residual' samples is compared with 'reacted' samples, which have elevated incompatible trace element concentrations and Fe_2O_3/FeO in spinel, a broad mixing trend is apparent, with 'reacted' samples yielding identical $^{87}Sr/^{86}Sr$ to the majority of local/regional arc lavas (Fig. 4.4, Fig. 4.5). This supports the conclusion that the textural observations and trace element systematics were induced through interaction of ambient mantle material with basaltic melts in the present day upper mantle wedge. Of significance is that one clearly texturally reacted sample, 67-02B(3), yields the most elevated $^{87}Sr/^{86}Sr$ even compared to 'residual' samples. Combined with the similar trace element systematics and low equilibration temperature to 'residual' samples, this supports our conclusions in chapter 2 that a number of Ritter samples carry the signature of melt-rock reaction associated with the previous episode of subduction.

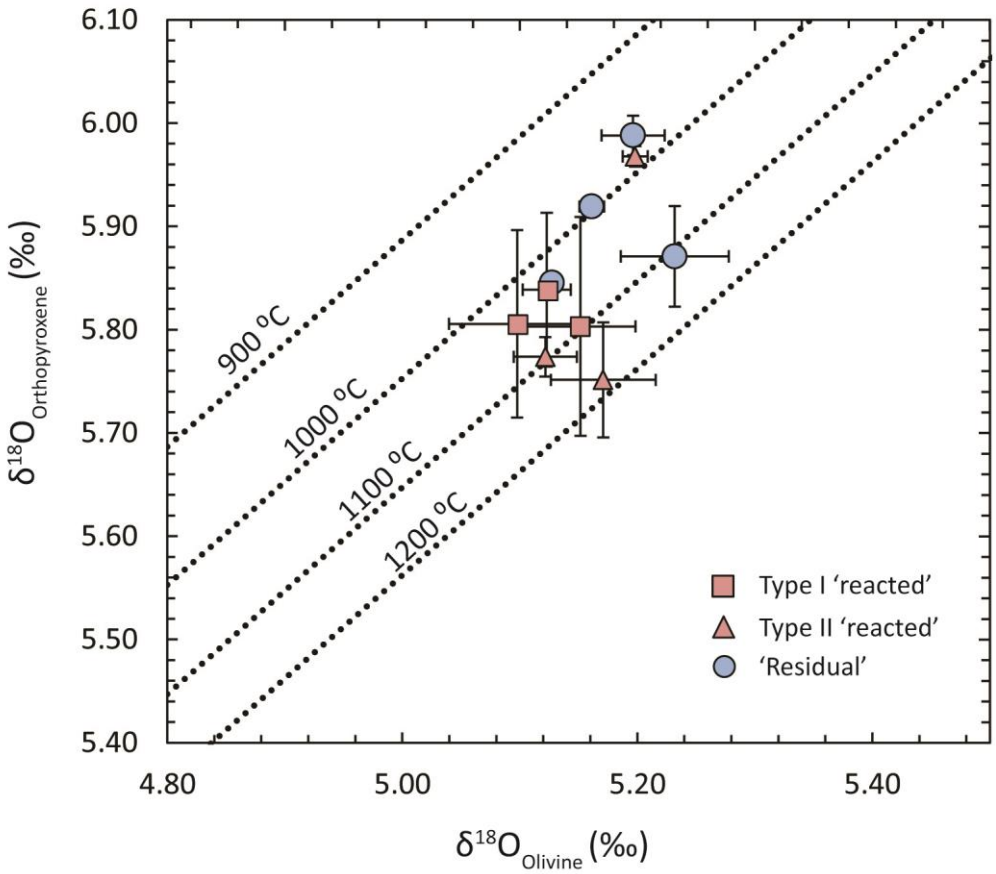

Fig. 4.8 Oxygen isotope composition ($\delta^{18}O$) of olivine and orthopyroxene mineral separates. Error bars represent variation in 2-4 repeat analyse. Isotherms calculated from the fractionation of oxygen isotopes between olivine and orthoypyroxene, with fractionation factors from Zheng et al. (1993) for forsterite and enstatite

Oxygen isotope variation in olivine and orthopyroxene between samples in the Ritter suite (Fig. 4.8) are well within the range of typical mantle values (Mattey et al. 1994) and show no correlation with whole-rock $^{87}Sr/^{86}Sr$ or other tracers of open-system processes. In particular, the $\delta^{18}O$ of the olivine neoblast matrix in porphyroclastic sample 67-02A(3) is identical to the $\delta^{18}O$ of olivine porphyroclasts, despite comprehensive trace element and isotopic evidence for interaction with hydrous arc magmas (chapters 2, 3 and 5). This may reflect interaction with fluids possessing mantle-like $\delta^{18}O$, since the MORB-like Sr isotope composition of 'reacted' peridotites and erupted lavas precludes a major subducted sedimentary component present in the primary melts. Alternatively this could simply reflect kinetic limitations on the inheritance of an anomalous $\delta^{18}O$ signature during melt-rock reaction. Very short timescales, on the order of a year, for the interaction of melts with the ambient mantle prior to xenolith exhumation are described in Chapter 5. Since the diffusion rate of O in olivine is several orders of magnitude slower than other trace elements from which this timescale was constrained (Spandler and O'Neill 2010), it is possible that the timescale was insufficient for the ambient mantle $\delta^{18}O$ to be disturbed during migration of melts in the upper mantle. The slow kinetics of O diffusion are apparent in this dataset from temperatures calculated from the fractionation of oxygen isotopes between olivine and orthopyroxene, which are considerably higher than other estimates from faster diffusing chemical components (chapter 2). The typically lower $\delta^{18}O$ values of orthopyroxene from 'reacted' samples, when $\delta^{18}O$ of olivine is nearly identical between 'reacted' and 'residual' samples, results in slightly higher average temperatures, although the level of uncertainty on duplicate analyses is too high to establish whether this is a real difference or not (Fig. 4.8).

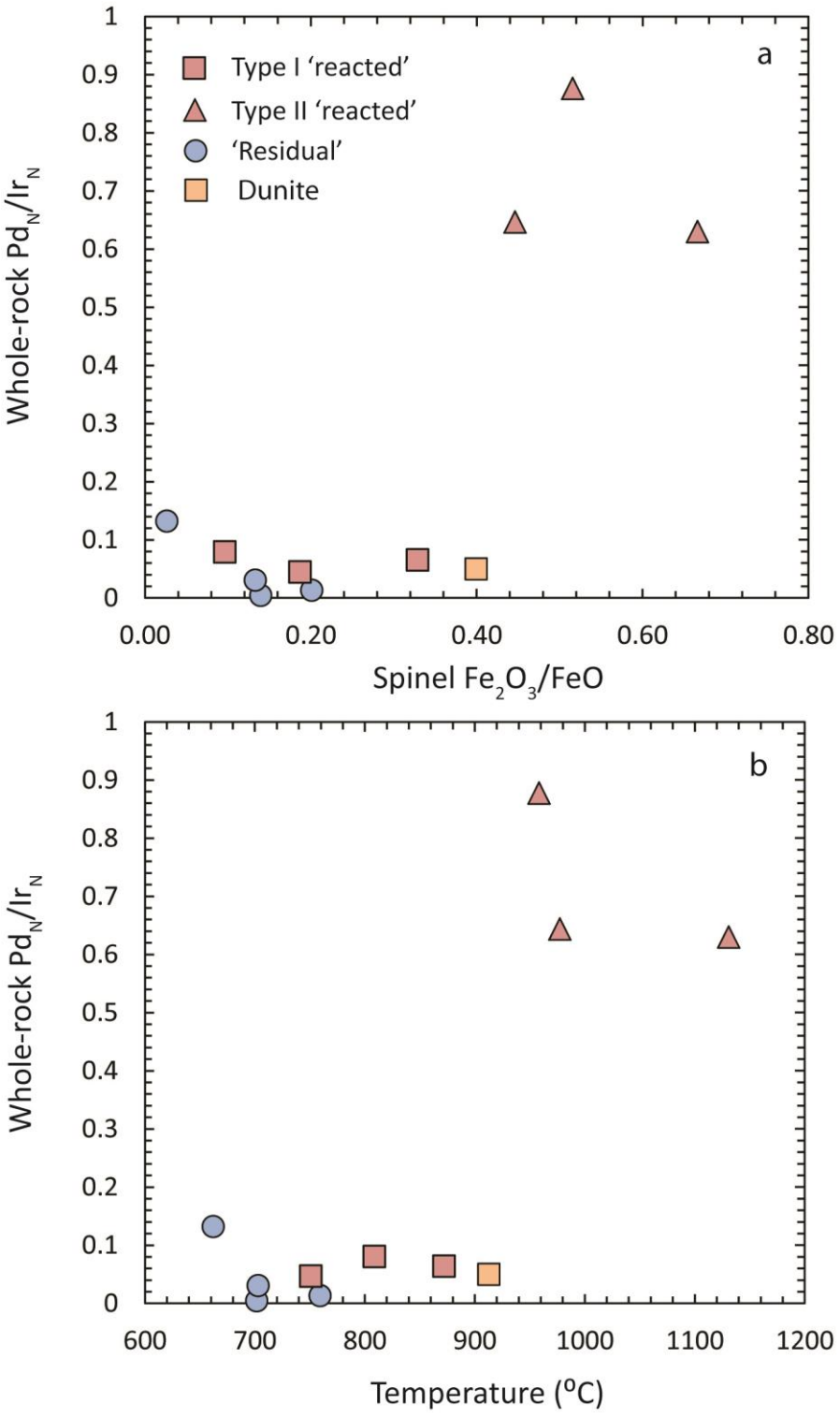

Fig. 4.9 Variation between whole-rock Pd_N/Ir_N (where subscript 'N' denotes normalisation to primitive mantle values of Becker et al. 2006) and a) spinel Fe_2O_3/FeO and b) temperature. Temperature calculated from Fe-Mg exchange between spinel and olivine (see chapter 2)

4.4.3 Response of highly siderophile elements to open-system processes

Given the multiple lines of chemical and isotopic evidence for involvement of slab-derived components and melt-rock reaction in the petrogenesis of both 'residual' and 'reacted' samples, the Ritter samples provide a rare opportunity to assess how highly siderophile elements behave during such processes. A number of previous studies of mantle xenoliths and ophiolites have shown strong evidence for alteration of HSE systematics of the mantle during melt-rock reaction (Handler and Bennett 1999, Rehkämper et al. 1999, Büchl et al. 2002, Büchl et al. 2004, Lorand et al. 2004, Resiberg et al. 2005, Ackerman et al. 2009, Ackerman et al. 2013, Lorand et al. 2013). The consequences for HSE concentrations and fractionations, however, vary significantly between studies, highlighting the complex behaviour of HSE in systems differing in key parameters controlling HSE solubility and partitioning such as sulphur, oxygen and water fugacity, temperature, melt composition and melt/rock ratio. For example, Büchl et al. (2002) reported increasing ratios of IPGE/PPGE in peridotite with proximity to dunite melt channels, showing that in contrast to partial melting, IPGE can behave incompatibly during melt-rock reaction and may become fractionated. Similarly, Ackerman et al. (2009) reported depletion and fractionation of IPGE in spinel peridotite xenoliths, consistent with dissolution of residual monosulphide solid solution (MSS) in which IPGE are compatible (Lorand et al. 2004). In contrast to these studies, Ackerman et al. (2013) reported enrichment in IPGE at only mild levels of PPGE depletion in Mg-lherzolites, interpreted to reflect precipitation of IPGE alloys during melt-rock reaction. This same study, however, also reported dunites and wehrlites with similar PPGE enrichments to equivalent rocks studied by Büchl et al. (2002) and Büchl et al. (2004), illustrating complex, variable behaviour of HSE in response to different styles of melt-rock reaction operating in the same mantle section. Likewise, Reisberg et al. (2005) showed that interaction of spinel peridotite with two different melt compositions (one sulphur-undersaturated, and another lower-degree/more evolved melt) resulted in either removal of Os and Re or addition of Re with no change in Os.

In general, there is no clear relationship between lithophile trace element evidence for melt-rock reaction and the concentrations and fractionations of the chalcophile HSE, in the Ritter samples, reflecting the different chemical affinities of these

elements in the mantle. In detail, 'reacted' Ritter harzburgites show a range of HSE patterns (Fig. 4.2). Type II 'reacted' samples display strongly elevated Pd_N/Ir_N ratios (though Pd/Ir remains sub-chondritic) compared to 'residual' samples, which is at odds with the highly depleted orthopyroxene compositions and distinct from the partial melting trend discussed above (Fig. 4.5). These type II 'reacted' samples also have the highest equilibration temperatures and most oxidised spinel compositions (Fig. 4.9). Two of these samples contain both lower concentrations of Ir and higher concentrations of Pd than 'residual' harzburgites (Table 4.1). We interpret this to reflect percolation of S-undersaturated melts into ambient mantle which would dissolve residual IPGE-rich sulphides, depleting IPGE in the surrounding peridotite but also raising the concentrations of PPGE due to their relative enrichment in the melt. IPGE are also highly fractionated in these samples (Fig. 4.2b) with low Ir_N/Ru_N of 0.25 and 0.45. Values of Os_N/Ir_N show contrasting fractionations with values of 6.1 and 0.1. Given the similarity in the concentrations of other HSE, this could be due to different stages of incongruent dissolution of residual sulphides or platinum group minerals, which may initially retain Os at low degrees of reaction whilst Ru and Ir are lost to the melt before the remaining Os-rich fraction is liberated. A possible alternative for the sample with very low Os_N/Ir_N is loss of Os through volatilisation during ascent in oxidised magmas (Lorand et al. 2003). The oxygen fugacity of the host magma is FMQ +2 (see chapter 5) which is similar to the values for devolatilised peridotite xenoliths measured by Lorand et al. 2003. However, if this was the case then we might expect similar Os-loss from other xenoliths in this suite which share similar textures. The other type II 'reacted' sample has a distinctly different HSE pattern with flat Os_N to Pt_N, at broadly PUM-like concentrations, and only slightly lower Pd_N (Fig. 4.2). The similarity in IPGE concentrations to 'residual' samples indicates that the result of melt-rock reaction in this case has been to increase PPGE concentrations, possibly through deposition of a PPGE-bearing sulphide melt phase.

The HSE pattern of the dunite is distinctly different from any of the 'reacted' harzburgites, with positively sloping Os_N to Ru_N, and depleted but positively sloping PPGE and Re (Fig. 4.2c). The patterns are, however, very similar to whole-rock measurements of the global occurrences of chromitites (Zhou et al. 1998, Büchl et al. 2004, Uysal et al. 2009, O'Driscoll et al. 2012), particularly the severe depletion of Pt relative to Ru and Pd.

We note that the petrology of the dunite, with a high modal abundance of coarse-grained Cr-rich spinel (~10 % by observable area), is similar to chromitites found in ophiolites. These chemical and lithological similarities therefore support ideas that chromitites formed as part of a subduction zone system. The petrochemical origin of the dunite HSE signature must be considered in combination with pyroxenite sample 67-02A(1), which displays a complementary HSE signature with depletions in Ru and strong enrichments in Pt and Pd. Considering both samples together, we suggest that the low Pt and Pd of the dunite are due to preferential stripping of these elements during melt-rock reaction, either as droplets of sulphide melt or potentially Pt-Pd alloys (O'Driscoll et al. 2012). These elements were subsequently deposited during formation of the pyroxenite, consistent with the much higher abundance of sulphides observed in this sample. Thus the concentration of Pt and Pd in subduction zones may be achieved simply through melt-rock reaction and doesn't necessarily require a flux from subducted lithosphere (McInnes et al. 1999). The anomalously low Ru contents of this pyroxenite may be related to the high modal abundance of Cr-spinel in the dunite, which could retain Ru either due to elevated partition coefficients of this element in spinel at relatively oxidising conditions (Park et al. 2012) such as those of dunite formation (chapter 2), or due to micro-inclusions of a Ru-bearing phase, such as laurite (Uysal et al. 2009) which are commonly observed in chromites from chromitite deposits. Such platinum-group minerals are thought to form on the boundaries of chromites due to a localised reduction in oxygen fugacity, due to the preferential incorporation of Fe^{3+} into chromite, which results in reduced solubility of PGEs in silicate melt (Finnigan et al. 2008). The remaining pyroxenite sample (67-02B(6)) has an HSE pattern which shows similarities with basaltic melts, with elevated concentrations of PPGE relative to IPGE (Fig. 4.2), albeit with higher Ir, Ru, Pt and Pd, and lower Re, probably reflecting its precursor mantle-like signature. The pattern is most similar to 'reacted' harzburgite 67-02B(5) except for overall greater enrichment in PPGE indicating that the pyroxenite represents a higher degree of melt-rock reaction compared to the harzburgite.

4.4.4 Mineral-scale control on highly siderophile element systematics

One of the major challenges with interpreting the behaviour of HSE in mantle samples is that these elements dominantly reside in sulphide phases which constitute only a minor

or trace proportion of the total solid assemblage. In addition, the distribution of such sulphide phases can be much more heterogeneous than modally dominant silicate phases, leading to the 'nugget' effect documented here and in numerous previous studies (Luguet et al. 2007, Lorand et al. 2013). Sulphide phases can be grouped into two types: intergranular (located along grain boundaries) and included (located within mineral hosts such as olivine). Based on petrographic inspection, intergranular sulphides are scarcer than included sulphides from both 'residual' and 'reacted' samples implying that whole-rock HSE systematics are controlled largely by included sulphides. Olivine is the dominant host of sulphides in most samples, except the pyroxenites and two samples with abundant secondary orthopyroxene veins/patches, where orthopyroxene is the dominant host. The extent to which olivine-hosted sulphides control the whole-rock HSE budget can thus be estimated by comparing whole-rock HSE abundances and fractionations with those of olivine separates and their included sulphides. This comparison is only justified if olivine itself is not a major host for HSE but since HSE are strongly incompatible in olivine relative to sulphides or platinum group minerals, the contribution from HSE bonded within the olivine crystal lattice should be minor. For example, assuming that olivine contains ~0.05 ppb Os (Burton et al. 2002) and sulphide contains 6000 ppb (Luguet et al. 2004), then for a modal abundance of only 0.01 % sulphide (99.99 % olivine), the contribution from olivine to the total Os budget would be 8 %. For a sulphide abundance of 0.1 % (which approaches a total concentration of Os similar to whole-rock values reported here), the difference would be essentially imperceptible.

Duplicate 0.1 g aliquots of multiple olivine crystals from sample 67-02A(5) show similar overall HSE patterns but substantially different concentrations (Table 4.1, Fig. 4.3). This suggests that the 'nugget' effect has an important control in dictating HSE abundances certainly at total dissolved masses of < 1g. The similar sense of fractionations however suggests that whilst sulphides are hetereogeneously distributed in their mineral hosts, they have all been subjected to the same petrogenetic processes. The different scale of fractionations in olivines from this 'reacted' sample show that the melt-rock reaction process responsible for the fractionations was spatially variable on a hand-sample (10-30 cm) scale. Comparing data from olivine separates with their respective whole-rock concentrations yields further insights into HSE storage (Fig. 4.3). In 67-02A(5),

olivine separates have much lower Os_N/Ir_N than the whole-rock, implying that Os is controlled by a separate Os-rich alloy phase not sampled in the ~0.2 g of olivines dissolved from this sample. This Os-rich phase may be formed during breakdown of an IPGE-rich precursor phase, as suggested earlier in the discussion, and either subsequently included in a separate mineral phase, located in intergranular spaces or simply extremely hetereogeneously distributed even compared to sulphides. Another major difference between olivine separate data and whole-rock data for 'residual' sample 67-02A(2) and 'reacted' sample 67-02A(5) is pronounced Pt anomalies for olivine separates. This shows that Pt is also being controlled by a separate Pt-rich phase and supports our earlier assertion that elevated Pt concentrations in whole-rock 'residual' sample 67-02B(1) is probably the result of Pt-rich platinum group minerals. Olivines from 'residual' sample 67-02D(4) do not contain such a Pt anomaly, presumably demonstrating that this olivine separate contained some of the very sparsely distributed Pt 'nuggets' which were not sampled in other separates. A final important observation is that despite being enclosed ('shielded') in olivine, all HSE patterns are fractionated which, once the nugget effect is discounted, is consistent with the sense of fractionations anticipated during partial melting in the presence of residual MSS. This may reflect either diffusion of HSE through the olivine structure to equilibrate with surrounding sulphide melt or partial melting of enclosed sulphides, forming sulphide melt which subsequently migrates out of the olivines through permeable micro-fracture networks. Both processes would preferentially strip PPGE from the enclosed residual sulphides assuming the kinetic rates of diffusion or sulphide melt migration are rapid enough.

4.4.5 Mobility and control of Os in subduction systems

Studies of mantle samples of a purported subduction origin and arc lavas have reached contrasting conclusions regarding the mobility of Os in subduction zones and thus whether the Os isotope composition of arc magmas and peridotites reflects the timing of melt extraction (Brandon et al. 1996, McInnes et al. 1999, Woodland et al. 2002, Widom et al. 2003, Dale et al. 2012). The $^{187}Os/^{188}Os$ values of Ritter samples are all less radiogenic than the primitive mantle value of 0.1296 (Meisel et al. 2001) and most chondrites (Walker et al., 2002) and there is no systematic distinction between the Os isotope composition of 'residual' samples and 'reacted' samples, pyroxenites or the

dunite (Table 4.1). Despite this, however, there is a significant range of $^{187}Os/^{188}Os$ values which translates to rhenium depletion model ages for the harzburgites of 0.08-1.14 Ga, based on estimates of primitive upper mantle evolution (Table 4.1, Meisel et al. 2001). Many studies investigating Os isotope systematics of peridotite suites have found correlations between partial melting indices such as whole-rock Al_2O_3 and $^{187}Os/^{188}Os$, attributed to variations in Re/Os and consequently $^{187}Os/^{188}Os$ over time (Rudnick and Walker 2009). We found no correlation between $^{187}Os/^{188}Os$ and Yb in orthopyroxene implying that the Os isotope systematics reflect a process either prior to the melting event or subsequent to it (Fig. 4.10c). However, we find no correlations between $^{187}Os/^{188}Os$ and $^{87}Sr/^{86}Sr$, concentrations of highly fluid-mobile incompatible trace elements or any other tracers of slab-derived material and melt-rock reaction (Fig. 4.10d). Neither do we find any correlations between $^{187}Os/^{188}Os$ and concentrations or ratios of HSE, including Re/Os (Fig. 4.10a). This indicates that in the case of the Ritter samples $^{187}Os/^{188}Os$ was largely unaffected by input of subducted material through metasomatism or melt-rock reaction, in contrast to a number of other studies of melt-peridotite reaction channels and sub-arc mantle xenoliths (Brandon et al. 1996, McInnes et al. 1999, Büchl et al. 2002, Widom et al. 2003) and has been decoupled from HSE systematics. This decoupling with lithophile and chalcophile tracers may indicate a complex and fortuitous combination of processes such as partial melting and subsequent metasomatism and melt-rock reaction which have had similar but competing effects on Os isotope composition, however our data shows that Os is predominantly lost from rather than added to the residue during melt-rock reaction, as IPGE become fractionated.

The only correlation with $^{187}Os/^{188}Os$ identified in this extensive geochemical dataset was with the concentrations of phosphorous in olivine and orthopyroxene, which show clear negative correlations (Fig. 4.10b). Phosphorous is unique amongst the lithophile trace elements in that it tends to be concentrated in olivine over other silicate minerals (Witt-Eickschen and O'Neill 2005). It diffuses very slowly compared to other elements owing to its high charge and small ionic radius, limiting it to diffusion through silicon vacancies with perhaps additional requirements of maintaining charge balance with the neighbouring octahedral site (Spandler and O'Neill 2010). This slow diffusion potentially allows P to trace ancient processes which would otherwise be completely

overprinted by diffusive re-equilibration. This slow diffusion, however, has also limited our understanding of the partitioning behaviour of P in mantle systems, since it is difficult to achieve equilibration in experimental partitioning studies, even at high temperatures. Witt-Eickschen and O'Neill (2005) found a weak correlation between $D_P^{opx/ol}$ and temperature which would imply that P preferentially partitions into orthopyroxene over olivine ($D_P^{opx/ol}$ >1) at temperatures of 1200-1300 °C. Since $D_P^{opx/ol}$ is both uniform and greater than 1 (1.23) in the Ritter harzburgites (chapter 2), this indicates that P and by association $^{187}Os/^{188}Os$ is uniquely recording an ancient high temperature process. The very narrow range of P concentrations and homogeneous P distribution within crystals (chapter 2 and chapter 5) means that metasomatism is an unlikely cause. The negative correlation between $^{187}Os/^{188}Os$ and P also precludes partial melting, since P is thought to behave incompatibly under mantle conditions (Konzett et al. 2012, Grant and Kohn 2013). Residual apatite present during partial melting may substantially change the behaviour of P in the residue during melting, however the stability of apatite in the mantle during partial melting is poorly understood at present (Konzett et al. 2012). It is also perhaps significant that comparison between the HSE concentrations of olivine and the whole-rock data indicate that Os concentrations may be controlled by a separate Os-rich mineral phase. Such Os-rich phases are thought to be chemically-inert and thus more likely to preserve an 'ancient' high-temperature (Luguet et al. 2007, Fonseca et al. 2012), lending credence to the trend we observe with P in olivine. Without a more developed understanding of how P behaves in the mantle though we do not attempt to interpret this trend further with regards to a petrogenetic process. However we suggest that this trend demonstrates significant preservation potential for Os isotope signatures in the mantle in spite of processes which clearly disrupt both other HSE and lithophile element and isotope systematics, consistent with the apparently preserved record of mantle depletion events spanning the last 2 Ga (e.g. Harvey et al. 2006, Pearson et al. 2007).

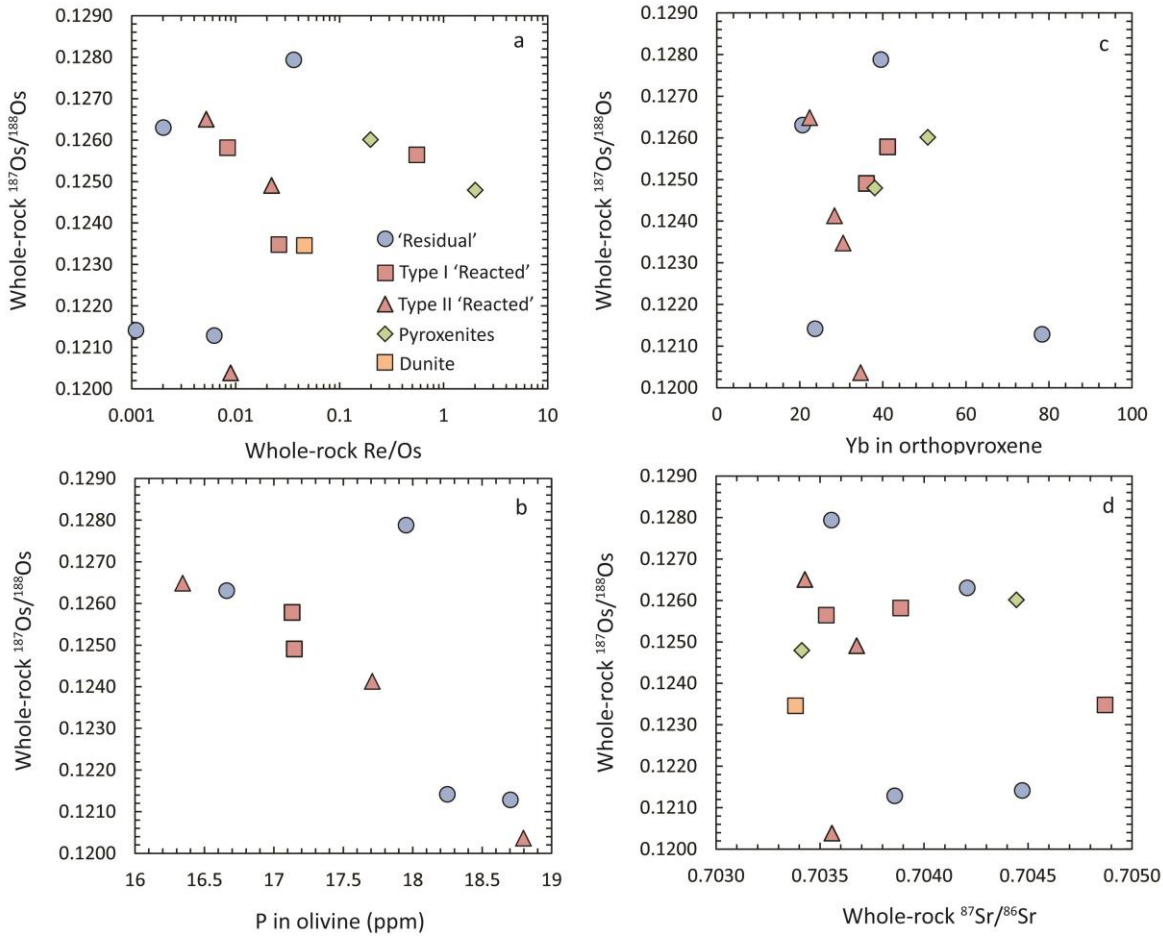

Fig. 4.10 a) Lack of correlation between whole-rock $^{187}Os/^{188}Os$ and Re/Os indicates decoupling of HSE and Os isotope systematics; b) Negative correlation of $^{187}Os/^{188}Os$ with P in olivine and orthopyroxene (not shown) likely reflects control by a previous, high-temeperature event; c) absence of correlation between $^{187}Os/^{188}Os$ and Yb in orthopyroxene (partial melting indicator); d) absence of correlation between $^{187}Os/^{188}Os$ and $^{87}Sr/^{86}Sr$ shows that Os is not mobilised substantially by slab-

4.5 References

Ackerman, L., Walker, R.J., Puchtel, I.S., Pitcher, L., Jelínek, E., Strnad, L., 2009. Effects of melt percolation on highly siderophile elements and Os isotopes in subcontinental lithospheric mantle: A study of the upper mantle profile beneath Central Europe. Geochim. Cosmochim. Acta 73, 2400-2414

Ackerman, L., Pitcher, L., Strnad, L., Puchtel, I.S., Jelínek, E., Walker, R.J., Rohovec, J., 2013. Highly siderophile element geochemistry of peridotites and pyroxenites from Horní Bory, Bohemian Massif: Implications for HSE behaviour in subduction-related upper mantle. Geochim. Cosmochim. Acta 100, 158-175

Aldanmaz, E., Meisel, T., Celik, O.F., Henjes-Kunts, F., 2012. Osmium isotope systematics and highly siderophile element fractionation in spinel-peridotites from the Tethyan ophiolites in SW Turkey: Implications for multi-stage evolution of oceanic upper mantle. Chem. Geol. 294-295, 152-164

Andrews, D.R.A., Brenan, J.M., 2002. The solubility of ruthenium in sulphide liquid: implications for platinum group mineral stability and sulphide melt-silicate melt partitioning. Chem. Geol. 192, 163-181

Aulbach, S., Stachel, T., Seitz, H.M., 2012. Chalcophile and siderophile elements in sulphide inclusions in eclogitic diamonds and metal cycling in a Paleoproterozoic subduction zone. Geochim Cosmochim. Acta 93, 278-299

Ballhaus, C., Bockrath, C, Wohlgemuth-Ueberwasser, C., 2006. Fractionation of the noble metals by physical processes. Contrib. Mineral. Petrol. 152, 667-684

Barnes, S.-J., Naldrett, A.J., Gorton, M.P., 1985. The Origin of the Fractionation of Platinum-Group Elements in Terrestrial Magmas. Chemical Geology 53, 303-323

Becker, H., Horan, M.F., Walker, R.J., Gao, S., Lorand, J.-P., Rudnick, R.L., 2006. Highly sideorphile element composition of the Earth's primitive upper mantle: Constraints from new data on peridotite massifs and xenoliths. Geochim. Cosmochim. Acta 70, 4528-4550

Birck, J.L., Barman, M.R., Capmas, F., 1997. Re-Os isotopic measurements at the femtomole level in natural samples. Geostand. Newsl. 20, 19-27

Bockrath, C., Ballhaus, C., Holzheid, A., 2004. Fractionation of the Platinum-Group Elements During Mantle Melting. Science 305, 1951-1953

Brandon, A.D., Creaser, R.A., Shirey, S.B., Carlson, R.W., 1996. Osmium recycling in subduction zones. Science 272, 861-864

Büchl, A., Brügmann, G., Batanova, V.G., Münker, C., Hofmann, A.W., 2002. Melt percolation monitored by Os isotopes and HSE abundances: a case study from the mantle section of the Troodos Ophiolite. Earth Planet. Sci. Lett. 204, 385-402

Büchl, A., Brügmann, G., Batanova, V.G., 2004. Formation of podiform chromitite deposits: implications from PGE abundances and Os isotopic compositions of chromites from the Troodos complex, Cyprus. Chem. Geol. 208, 217-232

Burton, K.W., Gannoun, A., Birck, J.L., Allegre, C.J., Schiano, P., Clocchiatti, R., Alard, O., 2002. The compatability of rhenium and osmium in natural olivine and their behaviour during mantle melting and basalt genesis. Earth Planet. Sci. Lett. 198, 63-76

Charlier, B.L.A., Ginibre, C., Morgan, D., Nowell, G.M., Pearson, D.G., Davidson, J.P., Ottley, C.J., 2006. Methods for the microsampling and high-precision analysis of strontium and rubidium isotopes at single crystal scale for petrological and geochronological applications. Chem. Geol. 232, 114-133

Chou, C.-L., 1978. Fractionation of siderophile elements in the Earth's upper mantle and lunar samples. Proc. 9th Lunar Planet. Sci. Conf. 9, 163-165

Cunningham, H., Gill, J., Turner, S., Caulfield, J., Edwards, L., Day, S., 2012. Rapid magmatic processes accompany arc-continent collision: the Western Bismarck arc, Papua New Guinea. Contrib. Mineral. Petrol. 164, 789-804

Dale, C.W., Burton, K.W., Pearson, D.G., Gannoun, A., Alard, O., Argles, T.W., Parkinson, I.J., 2009. Highly siderophile element behaviour accompanying subduction of oceanic crust: Whole rock and mineral-scale insights from a high-pressure terrain. Geochim. Cosmochim. Acta 73, 1394-1416

Dale, C.W., Macpherson, C.G., Pearson, D.G., Hammond, S.J., Arculus, R.J., 2012. Inter-element fractionation of highly siderophile elemenets in the Tonga Arc due to flux melting of a depleted source. Geochim. Cosmochim. Acta 89, 202-225

Evans, K.A., 2012. The redox budget of subduction zones. Earth-Sci. Rev. 113, 11-32

Finnigan, C.S., Brenan, J.M., Mungall, J.E., McDonough, W.F., 2008. Experiments and Models Bearing on the Role of Chromite as a Collector of Platinum Group Minerals by Local Reduction. J. Petrol. 49, 1647-1665

Fonseca, R.O.C., Laurenz, V., Mallmann, G., Luguet, A., Hoehne, N., Jochum, K.P., 2012. New constraints on the genesis and long-term stability of Os-rich alloys in the Earth's mantle. Geochim. Cosmochim. Acta 87, 227-242

Grant, T.B., Kohn, S.C., 2013. Phosphorous partitioning between olivine and melt: An experimental study in the system Mg_2SiO_4-$Ca_2Al_2Si_2O_9$-$NaAlSi_3O_8$-$Mg_3(PO_4)_2$. Am. Mineral. 98, 1860-1869

Handler, M.R., Bennett, V.C., 1999. Behaviour of Platinum-group elements in the subcontinental mantle of eastern Australia during variable metasomatism and melt depletion. Geochim. Cosmochim. Acta 63, 3597-3618

Harvey, J., Gannoun, A., Burton, K.W., Rogers, N.W., Alard, O., Parkinson, I.J., 2006. Ancient melt extraction from the oceanic upper mantle revealed by Re-Os isotopes in abyssal peridotites from the Mid-Atlantic ridge. Earth Planet. Sci. Lett. 244, 606-621

Jugo, P.J., 2009. Sulfur content at sulfide saturation in oxidised magmas. Geology 37, 415-418

Kamenov, G.D., Perfit, M.R., Mueller, P.A., Jonasson, I.R., 2008. Controls on magmatism in an island arc environment: study of lavas and sub-arc xenoliths from the Tabar-Lihir-Tanga-Feni island chain, Papua New Guinea. Contrib. Mineral. Petrol. 155, 635-656

Kepezhinskas, P., Defant, M.J., Widom, E., 2002. Abundance and distribution of PGE and Au in the island-arc mantle: implications for sub-arc metasomatism. Lithos 60, 113-128

Konzett, J., Rhede, D., Frost, D.J., 2012. The high PT stability of apatite and Cl partiitoning between apatite and hydrous potassic phases in peridotite: an experimental study to 19 GPa with implications for the transport of P, Cl and K in the upper mantle. Contrib. Mineral. Petrol. 163, 277-296

Liu, C.-Z., Wu, F.-Y., Chu, Z.-Y., Ji, W.-Q., Yu, L.-J., Li, J.-L., 2012. Preservation of ancient Os isotope signatures in the Yungbwa ophiolite (southwestern Tibet) after subduction modification. J. Asian Earth Sci. 53, 38-50

Lorand, J.-P., Alard, O., Luguet, A., Keays, R.R., 2003. Sulfur and selenium systematics of the subcontinetal lithospheric mantle: Inferences from the Massif Central xenolith suite (France). Geochim. Cosmochim. Acta 67, 4137-4151

Lorand, J.-P., Delpech, G., Grégoire, M., Moine, B., O'Reilly, S.Y., Cottin, J.-Y., 2004. Platinum-group elements and the multistage metasomatic history of Kerguelen lithospheric mantle (South Indian Ocean). Chem. Geol. 208, 195-215

Lorand, J.-P., Alard, O., Luguet, A., 2010. Platinum-group element micronuggets and refertilization process in the Lherz peridotite (northeastern Pyrenees, France). Earth Planet. Sci. Lett. 289, 298-310

Lorand, J.-P., Delpech, G., Grégoire, M., Moine, B., O'Reilly, S.Y., Cottin, J.-Y., 2004. Platinum-group elements and the multistage metasomatic history of Kerguelen lithospheric mantle (South Indian Ocean). Chem. Geol. 208, 195-215

Luguet, A., Lorand, J.-P., Alard, O., Cottin, J.Y., 2004. A multi-technique study of platinum-group element systematics in some Ligurian ophiolitic peridotites, Italy. Chem. Geol. 208, 175-194

Luguet, A., Shirey, S., Lorand, J.-P., Horan, M.F., Carlson, R.C., 2007. Residual platinum group minerals from highly depleted harzburgites of the Lherz massif (France) and their role in HSE fractionation of the mantle. Geochim. Cosmochim. Acta 71, 3082-3097

Luguet, A., Nowell, G.M., Pearson, D.G., 2008. $^{184}Os/^{188}Os$ and $^{186}Os/^{188}Os$ measurements by Negative Thermal Ionisation Mass Spectrometry (N-TIMS): Effecs of interfering

element and mass fractionation corrections on data accuracy and precision. Chem. Geol. 248, 342-362

Mallmann, G., O'Neill, H.St.C., 2007. The effect of oxygen fugacity on the partitioning of Re between crystals and silicate melt during mantle melting. Geochim. Cosmochim. Acta 71, 2837-2857

Mann, U., Frost, D.J., Rubie, D.C., Becker, H., Audétat, A., 2012. Partitioning of Ru, Rh, Pd, Re, Ir and Pt between liquid metal and silicate at high pressure and high temperature - Implications for the origin of highly siderophile element concentrations in the Earth's mantle. Geochim. Cosmochim. Acta 84, 593-613

Mattey, D., Lowry, D., Macpherson, C., 1994. Oxygen isotope composition of mantle peridotite. Earth Planet. Sci. Lett. 128, 231-241

Mavrogenes, J., O'Neill, H.St.C., 1999. The relative effects of pressure, temperature and oxygen fugacity on the solubility of sulfide in mafic magmas. Geochim. Cosmochim. Acta 63, 1173-1180

McInnes, B.I.A., McBride, J.S., Evans, N.J., Lambert, D.D., Andrew, A.S., 1999. Osmium isotope constraints on ore metal recycling in subduction zones. Science 286, 512-516

Meisel, T., Walker, R.J., Irving, A.J., Lorand, J.-P., 2001. Osmium isotopic compositions of mantle xenoliths: A global perspective. Geochim. Cosmochim. Acta 65, 1311-1323

Mungall, J.E., Andrews, D.R.A., Cabri, L.J., Sylvester, P.J., Tubrett, M., 2005. Partitioning of Cu, Ni, Au, and platinum-group elements between monosulfide solid solution and sulfide melt under controlled oxygen and sulfur fugacities. Geochim. Cosmochim. Acta 69, 4349-4360

Mungall, J.E., Hanley, J.J., Arndt, N.T., Debecdelievre, A., 2006. Evidence from meimechites and other low-degree mantle melts for redox controls on mantle-crust fractionation of platinum-group elements. Proc. Nat. Ac. Sci. 103, 12695-12700

Mungall, J.E., Brenan, J.M., 2014. Partitioning of platinum-group elements and Au between sulfide liquid and basalt and the origins of mantle-crust fractionation of the chalcophile elements. Geochim. Cosmochim. Acta 125, 265-289

O'Driscoll, B., Day, J.M.D., Walker, R.J., Daly, J.S., McDonough, W.F., Piccoli, P.M., 2012. Chemical heterogeneity in the upper mantle recorded by peridotites and chromitites from the Shetland Ophiolite Complex, Scotland. Earth Planet. Sci. Lett. 333-334, 226-237

Palme, H., O'Neill, H.St.C., 2003. Cosmochemical Estimates of Mantle Composition: Treatise on Geochemistry

Park, J.-W., Campbell, I.H., Eggins, S.M., 2012. Enrichment of Rh, Ru, Ir and Os in Cr spinels from oxidised magmas: Evidence from the Ambae volcano, Vanuatu. Geochim. Cosmochim. Acta 78, 28-50

Parkinson, I.J., Hawkesworth, C.J., Cohen, A.S., 1998. Ancient Mantle in a Modern Arc: Osmium Isotopes in Izu-Bonin-Mariana Forearc Peridotites. Science 281, 2011-2013

Parkinson, I.J., Arculus, R.J., 1999. The redox state of subduction zones: insights from arc-peridotites. Chemical Geology 160, 409-423

Peach, C.L., Mathez, E.A., Keays, R.R., 1990. Sulfide melt silicate melt distribution coefficients for noble-metals and other chalcophile elements as deduced from MORB-implications for partial melting. Geochim. Cosmochim. Acta 54, 3379-3389

Pearson, D.G., Woodland, S.J., 2000. Solvent extraction/anion exchange separation and determination of PGEs (Os, Ir, Pt, Pd, Ru) and Re-Os isotopes in geological samples by isotope dilution ICP-MS. Chem. Geol. 165, 87-107

Pearson, D.G., Irvine, G.J., Ionov, D.A., Boyd, F.R., Dreibus, G.E., 2004. Re-Os isotope systematics and plantinum group element fractionation during mantle melt extraction: a study of massif and xenolith peridotite suites. Chem. Geol. 208, 29-59

Pearson, D.G., Parman, S.W., Nowell, G.M., 2007. A link between large mantle melting events and continental growth seen in osmium isotopes. Nature 449, 202-205

Rehkämper, M., Halliday, A.N., Alt, J., Fitton, J.G., Zipfel, J., Takazawa, E., 1999. Non-chondritic platinum-group element ratios in oceanic mantle lithosphere: petrogenetic signature of melt percolation? Earth Planet. Sci. Lett. 172, 65-81

Resiberg, L., Zhi, X., Lorand, J.-P., Wagner, C., Peng, Z., Zimmermann, C., 2005. Re-Os and S systematics of spinel peridotite xenoliths from east central China: Evidence for contrasting effects of melt percolation. Earth Planet. Sci. Lett. 239, 286-308

Rudnick, R.L., Walker, R.J., 2009. Interpreting ages from Re-Os isotopes in peridotites. Lithos 1125, 1083-1095

Shirey, S.B., Walker, R.J., 1998. The Re-Os isotope system in cosmochemistry and high-temperature geochemistry. Ann. Rev. Earth Planet. Sci. 26, 423-500

Snow, J.E., Reisberg, L., 1995. Os isotopic systematics of the MORB mantle: results from altered abyssal peridotites. Earth Planet. Sci. Lett. 133, 411-421

Spandler, C., O'Neill, H.St.C., 2010. Diffusion and partition coefficients of minor and trace elements in San Carlos olivine at 1,300 °C with some geochemical implications. Contrib. Mineral. Petrol. 159, 791-818

Suzuki, K., Senda, R., Shimizu, K., 2011. Osmium behaviour in a subduciton system elucidated from chromian spinel in Bonin island beach sands. Geology 39, 999-1002

Tollan, P.M.E., Bindeman, I., Blundy, J.D., 2012. Cumulate xenoliths from St. Vincent, Lesser Antilles Island Arc: a window into upper crustal differentiation of mantle-derived basalts. Contrib. Mineral. Petrol. 163, 189-208

Uysal, I., Tarkian, M., Sadiklar, M.B., Zaccarini, F., Meisel, T., Garuti, G., Heidrich, S., 2009. Petrology of Al- and Cr-rich ophiolitic chromitites from Muğla, SW Turkey: implications from composition of chromite, solid inclusions of platinum-group mineral, silicate, and base-metal mineral, and Os-isotope geochemistry. Contrib. Mineral. Petrol. 158, 659-674

Walker, R.J., Horan, M.F., Morgan, J.W., Becker, H., Grossman, J.N., Rubin, A.E., 2002. Comparative Re-187-Os-187 systematics of chondrites: Implications regarding early solar system processes. Geochim. Cosmochim. Acta 66, 4187-4201

Walker, R.J., 2009. Highly siderophile elements in the Earth, Moon and Mars: update and implications for planetary accretion and differentiation. Chemie der Erde - Geochemistry 69, 101-125

Wallace, P., 2005. Volatiles in subduction zones: concentrations and fluxes based on melt inclusion and volcanic gas data. J. Volc. Geotherm. Res. 140, 217-240

Widom, E., Kepezhinskas, P., Defant, M., 2003. The nature of metasomatism in the sub-arc mantle wedge: evidence from Re-Os isotopes in Kamchatka peridotite xenoliths. Chem. Geol. 196, 283-306

Witt-Eickschen, G., O'Neill, H.St.C., 2005. The effect of temperature on the equilibrium distribution of trace elements between clinopyroxene, orthopyroxene, olivine and spinel in upper mantle peridotite. Chem. Geol. 221, 65-101

Woodhead, J.D., Eggins, S.M., Johnson, R.W., 1998. Magma Genesis in the New Britain Island Arc: Further Insights into Melting and Mass Transfer Processes. J. Petrol. 39, 1641-1668

Woodhead, J., Hergt, J., Sandiford, M., Johnson, W., 2010. The big crunch: Physical and chemical expressions of arc/continent collision in the Western Bismarck arc. J. Volc. Geotherm. Res. 190, 11-24

Woodland, S.J., Pearson, D.G., Thirlwall, M.F., 2002. A platinum group element and Re-Os isotope investigation of siderophile element recyling in subduction zones: comparison of Grenada, Lesser Antilles arc, and the Izu-Bonin arc. J. Petrol. 43, 171-198

Workman, R.K., Hart, S.R., 2005. Major and trace element composition of the depleted MORB mantle (DMM). Earth Planet. Sci. Lett. 231, 53-72

Zheng, Y.-F., 1993. Calculation of oxygen isotope fractionation in anhydrous silicate minerals. Geochim. Cosmochim. Acta 57, 1079-1091

Zhou, M.-F., Sun, M., Krays, R.R., Kerrich, R.W., 1998. Controls on platinum-group elemental distributions of podiform chromitites: A case study of high-Cr and high-Al chromitites from Chinese orogenic belts. Geochim. Cosmochim. Acta 62, 677-688

Chapter 5

The development of porphyroclastic texture in a peridotite xenolith from sub-arc mantle: physicochemical conditions and timescale

5.1 Introduction

Xenoliths of mantle peridotite hosted in a variety of volcanic rocks offer a direct insight into the nature of the upper mantle, due to their rapid exhumation and quenching from upper mantle conditions (Pearson et al. 2003). Element partitioning between peridotite phases reflect the intensive properties of the mantle and allow reconstruction of the local mantle geotherm and redox state (e.g. Mather et al. 2011, Parkinson and Arculus 1999, Parkinson and Pearce 1998). However, many xenoliths display chemical disequilibrium and secondary textures unrelated to the ambient mantle. Secondary features such as veins or aggregates of secondary minerals and the development of porphyroclastic textures are often interpreted to reflect infiltration of melt shortly before magmatic entrainment, or localisation of strain in ductile shear zones with or without melt present (Drury et al. 1991, Kelemen et al. 1992, Franz et al. 2002, Arai et al. 2004, Kaczmarek and Müntener 2008, Falus et al. 2011, Bénard and Ionov 2013). These secondary textures may provide insights into the deformation history of the upper mantle or the nature of fluid phases, but it is often unclear whether these textures are caused by the magmatism that exhumed the xenoliths, or by previous events in the mantle.

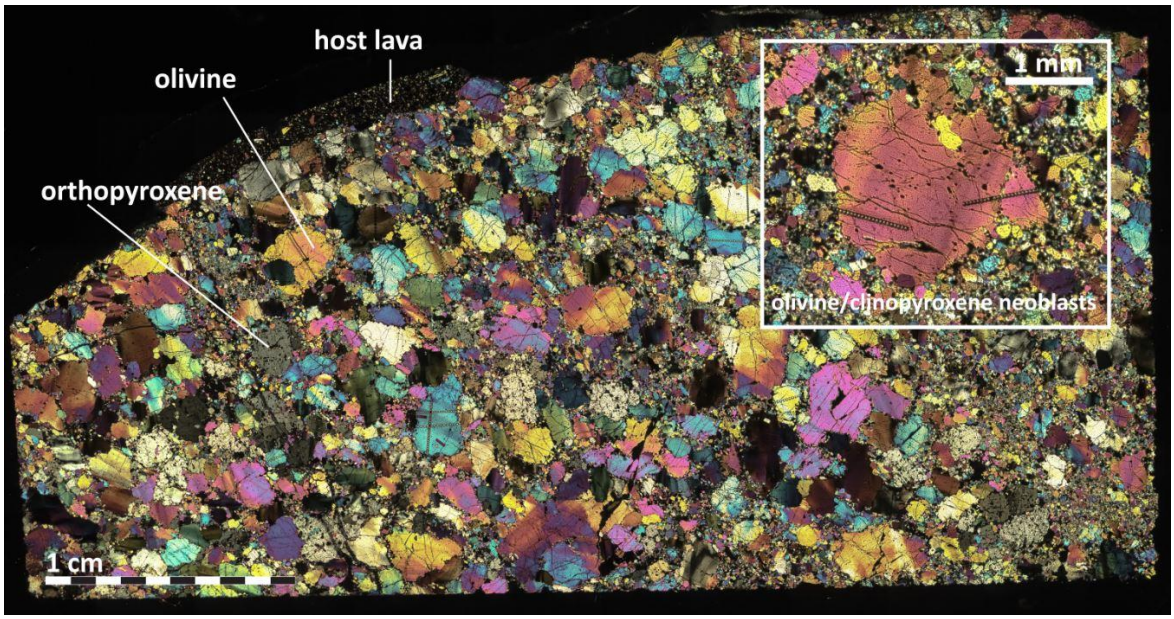

Fig. 5.1 Whole-rock photomicrograph (polarised light) of the porphyroclastic peridotite used in this study.

Since the trace element composition of olivine is sensitive to temperature, oxygen fugacity and chemical environment (Witt-Eickschen and O'Neill 2005, De Hoog et al. 2010, Foley et al. 2013, Mallmann and O'Neill 2013), olivine in rapidly exhumed, texturally deformed peridotites may retain chemical signatures which elucidate the physical conditions under which such secondary textures formed. Furthermore, chemical diffusion in olivine is fast for most elements (Spandler and O'Neill 2010), occurring over geologically short timescales and thus provides a valuable tool for determining the chronology of magmatic events (Demouchy et al. 2006, Costa and Dungan 2005, Ruprecht and Plank 2013). Yet despite this potential wealth of information that geochemical studies of olivine may yield pertinent to our understanding of dynamic mantle and magmatic processes, little attention has been paid to it in most studies of olivine-bearing samples (Foley et al. 2013).

Here we document the timescale of the development of the porphyroclastic texture in a peridotite xenolith calculated on the basis of major and trace element zoning patterns in olivine. The measured chemical zoning is cryptic in nature, with crystals appearing chemically homogeneous during petrographic inspection. Through detailed study of the composition of different olivine populations in both the peridotite and host lava, we show that the texture is associated with heating from an unusually low ambient mantle temperature of ~600 °C to the magmatic temperature of ~ 1230 °C in response to the local passage of primary hydrous mantle melts approximately one year before exhumation.

The porphyroclastic texture of the sample (67-02A(3)) detailed here (Fig. 5.1) consists of coarse (>0.5 mm), relic porphyroclasts of 'residual' olivine and orthopyroxene crystals surrounded by a recrystallized matrix consisting dominantly of olivine and clinopyroxene neoblasts. Olivine and orthopyroxene porphyroclasts are generally equant with sutured grain boundaries. They show no obvious systematic strain-induced elongation and no petrographic evidence for chemical zoning. Orthopyroxene porphyroclasts are highly reacted, often with numerous inclusions of fluid and olivine. Porphyroclastic peridotites are one of the major sub-groups of peridotite textures defined by Harte (1977) and are common occurrences in peridotite xenolith and ophiolite suites. Similar textures are widely reported in the few other examples of arc peridotites,

particularly those from Pacific subduction zones (Grégoire et al. 2001, Arai et al. 2004, Bryant et al. 2007, Ishimaru et al. 2007, Ionov 2010, Soustelle et al. 2010) but also from Grenada in the Lesser Antilles (Parkinson et al. 2003, Vanucci et al. 2007). By modelling the trace element diffusion profiles measured in olivine, our study provides a quantitative assessment of the timescales involved in the generation of these textures, allowing us to clearly link both the temporal and tectonic relationships between primary magmas in the upper mantle and the petrogenesis of arc volcanics.

5.2 Analytical methods

Analyses were performed on either a 30 µm thick polished thin section or 500 µm thick double-polished thick section, both prepared from the same sample billet. Large (> 1 mm) crystals with well-defined grain boundaries adjacent to fine-grained matrix were chosen to investigate diffusion. This allowed measurement of long profiles extending as close to crystal rims as possible from crystal cores that preserved initial mantle compositions. Cracks and other visible defects were avoided as much as possible. Major element compositions were measured on a Cameca SX100 electron probe micro-analyser (EPMA) at the Research School of Earth Sciences (RSES), Australian National University (ANU). Analyses were performed with a 15 kV operating voltage and 20 nA current, using a 1 µm spot size. The concentrations of minor and trace elements were determined at RSES using a 193 nm ArF excimer (Lambda Physik LPX120i) laser ablation system, feeding into an Agilent 7700 series quadrupole ICP-MS with dual-mode discrete dynode electron multiplier detector. Ablation was conducted in a custom-built 'HelEx' two-volume vortex sampling cell (Eggins et al. 1998) in an atmosphere of He and Ar, with ablated material extracted using H_2 as the carrier gas. The laser was run at a frequency of 5 Hz, and operating voltages varied between 26-30 kV in order to maintain energies of 30-50 mJ. Initial profiles were conducted using a 62 µm spot size on a wide range of elements (^{7}Li, ^{23}Na, ^{27}Al, ^{29}Si, ^{31}P, ^{43}Ca, ^{45}Sc, ^{47}Ti, ^{51}V, ^{53}Cr, ^{55}Mn, ^{57}Fe, ^{59}Co, ^{60}Ni, ^{63}Cu, ^{66}Zn, ^{69}Ga, and ^{89}Y).

After inspection of the concentration profiles, sub-sets of elements were chosen and measured as part of separate routines in order to extend the counting times, ensuring the highest quality data. In each profile, Ca and Cr were included as reference elements so that relative diffusion coefficients could be calculated. Additional profiles

were measured using a smaller 22 µm spot size in order to constrain the concentrations at the rims of the crystals more tightly, as these concentrations are used for the calculation of the temperature of the heating event, and therefore for extracting time information from the diffusion profiles. Trace element concentrations were also measured in porphyroclastic orthopyroxene and neoblastic olivine and clinopyroxene in order to ascertain the extent of chemical equilibrium. Finally, we also measured the fine-grained basaltic groundmass (corresponding to magmatic liquid) and its phenocrysts directly adjacent to the peridotite. Ten groundmass analyses were taken with a large (137 µm) spot size, and the results averaged. Phenocryst measurements were conducted with a 28 µm spot size. All data were inspected to identify and delete rogue data points and then reduced using SRM NIST 610 silicate glass as the external standard, and previously-determined concentration of ^{29}Si as the internal standard. Measurements of ^{45}Sc are affected by a polyatomic interference from $^{29}Si + {}^{16}O$, and the data were corrected accordingly applying the method described in Mallmann and O'Neill (2013). The corrections were small, approximately 0.5 ppm. Detection limits were typically at least two orders of magnitude lower than the lowest measured concentrations, except for Li, Na, P, Ca, Ti and Ga, which were approximately an order of magnitude lower, whilst Y concentrations in the crystal core were close to the detection limit. The natural standard glass BCR-2G was measured routinely in order to monitor accuracy and reproducibility of the data. With the exception of one measurement, all BCR-2G concentrations agreed within 10 % of each other (Table 2.5).

Water contents were determined using Fourier-transform infrared (FTIR) spectroscopy at RSES. Twenty four randomly orientated olivine porphyroclasts were measured, close to the crystal cores. In addition, a profile across a crystal adjacent to a laser ablation profile was performed to investigate variation within an individual crystal. The analyses were performed using a Bruker TENSOR 27 spectrometer equipped with a KBr beamsplitter, and attached to a Bruker Hyperion 1000 microscope with automated stage. The microscope was mounted with a nitrogen-cooled MCT-detector and the sample chamber purged with dry air to minimise atmospheric contamination. All analyses were processed using the OPUS 7 software package. Spectra were acquired in the wavenumber range 4000-600 cm^{-1} using 64 scans at a resolution of 2 cm^{-1} and a spot size

of 100x100 µm. Background spectra were recorded regularly and subtracted from the sample spectra before further processing. All analyses were performed using unpolarised light. Spectra were corrected for atmospheric contamination using the 'atmospheric compensation' software algorithm, before being baseline corrected using the 'concave rubberband correction' method, with 10 iterations and 4 baseline points. To convert the spectra to a water content, we integrated beneath peaks in the wavelength region 3600-3000 cm^{-1}. The total integration was converted to the total water content for each crystal using equation (10) from Kovacs et al. (2008):

$$C_{OH} = \frac{\sum_{n=0}^{i} A_i}{n} \cdot k \cdot 3$$

where: C_{OH} is the concentration of hydroxyl ("water") in parts per million; n is the number of crystals measured; A_i is the unpolarised absorbance of a randomly orientated crystal, normalised to 1 cm; k is the site-specific calibration factor to convert total absorbance into water concentration and its value is dependent on the substitution mechanism of water in olivine, determined by comparison of peak position with experimental studies (Kovacs et al. 2010). The factor 3 is used to convert the unpolarised partial absorbance measured in a single crystal orientation into a total absorbance. Given the anisotropic distribution of water in olivine and potential for water-loss on ascent, we estimate an uncertainty of up to ~40 % on the water content estimate of each crystal.

Crystal orientation was determined using a Zeiss UltraPlus analytical field emission scanning electron microscope with attached Oxford HKL EBSD system at the Centre for Advanced Microscopy, ANU. An accelerating voltage of 20 kV and working distance of 25.8 mm were used, with the stage tilted at 70 °. Multiple spots were acquired on each grain around the diffusion profiles. Data was acquired and processed using the Oxford HKL Channel 5 software package. The orientations of diffusion profiles relative to the principle crystallographic axes were subsequently calculated using the average Euler angles from each crystal.

	Peridotite				Basalt			
	Porphyroclast rim	Porphyroclast core	Neoblast	1 s.d.	Phenocryst	1 s.d.	Groundmass	1 s.d.
SiO_2	40.33	40.91	40.85	0.31	40.93	0.51		
TiO_2	b.d.l.	b.d.l.	b.d.l.		b.d.l.			
Al_2O_3	b.d.l.	b.d.l.	b.d.l.		0.02	0.01		
Cr_2O_3	0.08	b.d.l.	0.06	0.02	0.10	0.04		
FeO	8.39	8.02	8.63	0.11	9.64	0.80		
MnO	0.12	0.13	0.13	0.02	0.17	0.02		
MgO	49.72	50.54	50.55	0.13	49.59	0.76		
CaO	0.15	b.d.l.	0.17	0.02	0.19	0.05		
Na_2O	b.d.l.	b.d.l.	b.d.l.		b.d.l.			
NiO	0.42	0.46	0.39	0.02	0.19	0.03		
Total	99.20	100.05	100.79	0.34	100.83	1.30		
Fo	91.36	91.82	91.26	0.11	90.16	0.79		
Li (ppm)	1.75	0.93						
Na (ppm)	31.1	1.4	26.9	7.7	31.8	18.4	10081	1664
Al (ppm)	50.7	21.6	64.6	20.5	88.2	26.3	59894	10415
P (ppm)	19-24	19-23						
Ca (ppm)	1099	59	1109	47	1157	137	77880	15487
Sc (ppm)	5.46	1.96	3.96	0.21	5.29	0.86	43.3	11.2
Ti (ppm)	10.7	0.75	8.7	2.2	15.9	2.3	2248	290
V (ppm)	3.53	0.68	2.65	0.34	2.78	0.43	230	26.0
Cr (ppm)	423	7.8	332	30.2	338	83.9	625	283
Mn (ppm)	1217	899	1120	46	1181	78	1230	102
Co (ppm)	129	135	136	1	140	3	46	21
Ni (ppm)	2844	3397	2878	19	2215	277	249	279
Cu (ppm)	3.53	0.36	3.29	0.0	3.34	0.4	68.5	26.5
Zn (ppm)	52	44						
Ga (ppb)	66	25						
Y (ppb)	29.7	1.0	30.0	4.1	42.4	5.4	10371	1456

Table 5.1 Major and trace element composition of different olivine populations and glass in host magma. Porphyroclast rim and core represent maximum and minimum measured values, whereas neoblast, phenocryst and glass data are averages from multiple points

5.3 Results

The major, minor and trace element chemistry of different olivine populations are reported in Table 5.1. The trace element composition of other phases is reported in Table 5.2 and major element compositions are reported in Table 2.2. Porphyroclast cores are characterised by high *Fo* contents (~91.8 %) which decrease systematically to around 91.3 % *Fo* at the crystal rims. Orthopyroxene porphyroclasts have high Mg# (0.921), low Al_2O_3 (0.5-1.3 wt. %) and low CaO (0.7-1.8 wt. %). Olivine neoblasts have identical *Fo* contents to the porphyroclast rims (91.3 %). Clinopyroxene neoblasts have high Mg# (0.927), very low Al_2O_3 (0.4-0.8 wt. %) and CaO (19.7-21.1 wt. %) and moderately elevated Na_2O (0.19-0.25 wt. %) given the very low Al_2O_3 and CaO. Spinel has very high Cr# (0.77-0.80) and high TiO_2 (0.09-0.19 wt. %). Olivine 'phenocrysts' in the host magma have a range of compositions indicating populations of true phenocrysts as well as xenocrysts and antecrysts. The majority of measured crystals (interpreted to be phenocrysts) have high *Fo* (90.2 %) and NiO (0.27 wt. %).

	Cpx neoblast	1. s.d.	Opx 1	Opx 2	Opx 3	Opx 4	Opx 5	Opx 6	Opx 7	Opx 8	Opx 9	Opx 10
Sc (ppm)	29.0	0.74	18.5	14.2	13.7	16.5	11.6	11.7	11.2	20.1	9.72	21.3
Ti (ppm)	172	5.4	108	85.0	86.1	162	97.8	95.6	101	6.8	98.8	8.5
V (ppm)	49.3	0.50	43.2	29.0	23.5	37.1	22.3	23.3	21.7	44.6	18.9	
Cr (ppm)	5453	214	2675		2437	2886	2449	2547	2449	2983	2291	3407
Mn (ppm)	812	73	945	1038	1032	1000	1057	1069	1040	1043	1096	981
Ni (ppm)	452	24	728	712	639	1350	720	760	726	662	808	670
Cu (ppm)	2.45	0.50	2.22	3.27	2.04	2.01	2.12	2.15	3.38	1.92	2.39	
Y (ppb)	878	115	183	109	100	188	102	114	108	53.1	113	74.7

Table 5.2 Average trace element concentrations of clinopyroxene neoblasts and multiple orthopyroxene analyses.

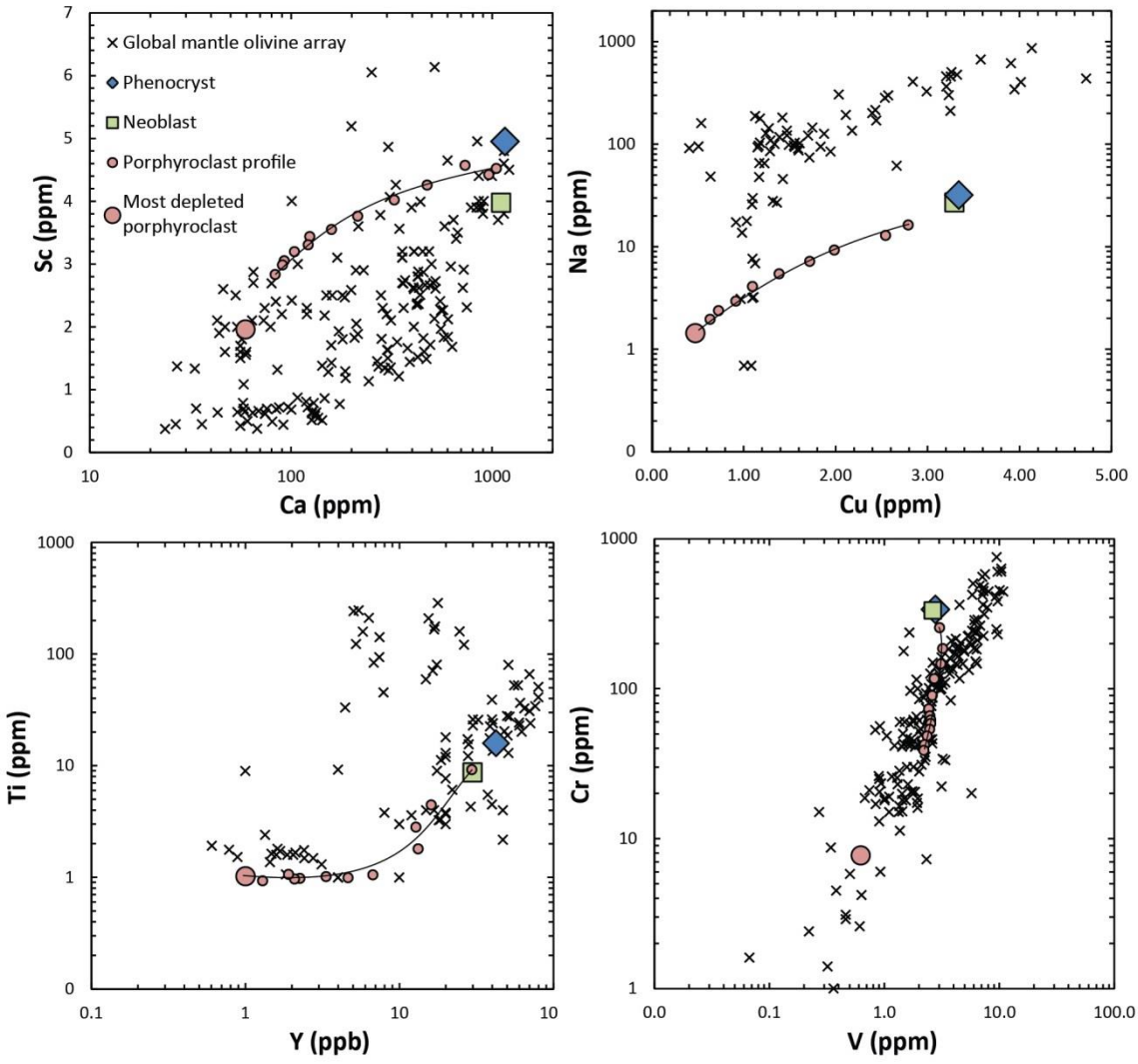

Fig. 5.2 Multi-element diagrams comparing the composition of different olivine populations with each other and the global mantle olivine array (data from Grégoire et al. 2001, Neumann et al. 2004, Witt-Eickschen and O'Neill 2005, Zheng et al. 2005, Kaeser et al. 2006, Zheng et al. 2007, De Hoog et al. 2010, Batanova et al. 2011, Ionov 2010, Pirard et al. 2013, Smith 2013). Representative porphyroclast profile is from olivine 'a3_ol3'

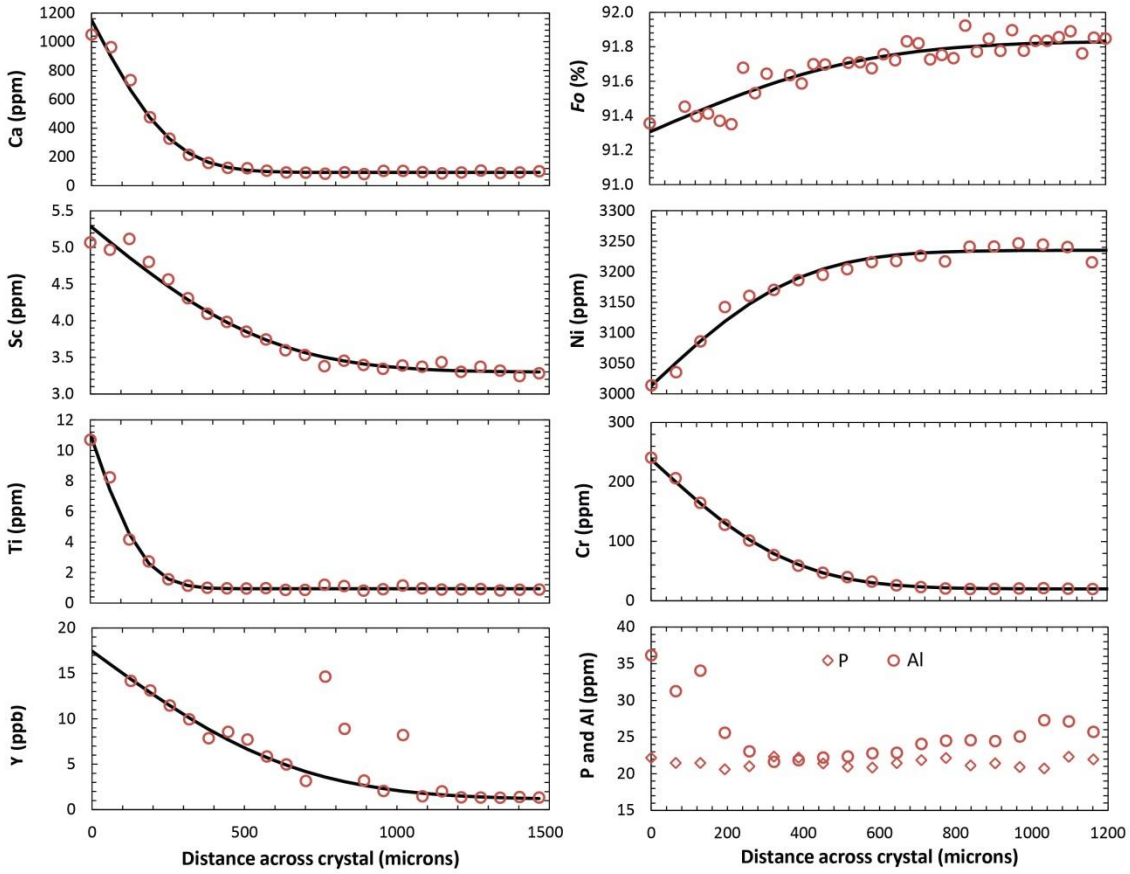

Fig. 5.3 Rim-core profiles on olivine porphyroclasts. The left and right hand columns are data for two different traverses on opposite sides of the same crystal. Black lines are models fit to the data based on the methodology described in text. Al and P were not modelled since they do not satisfy the boundary conditions of the model

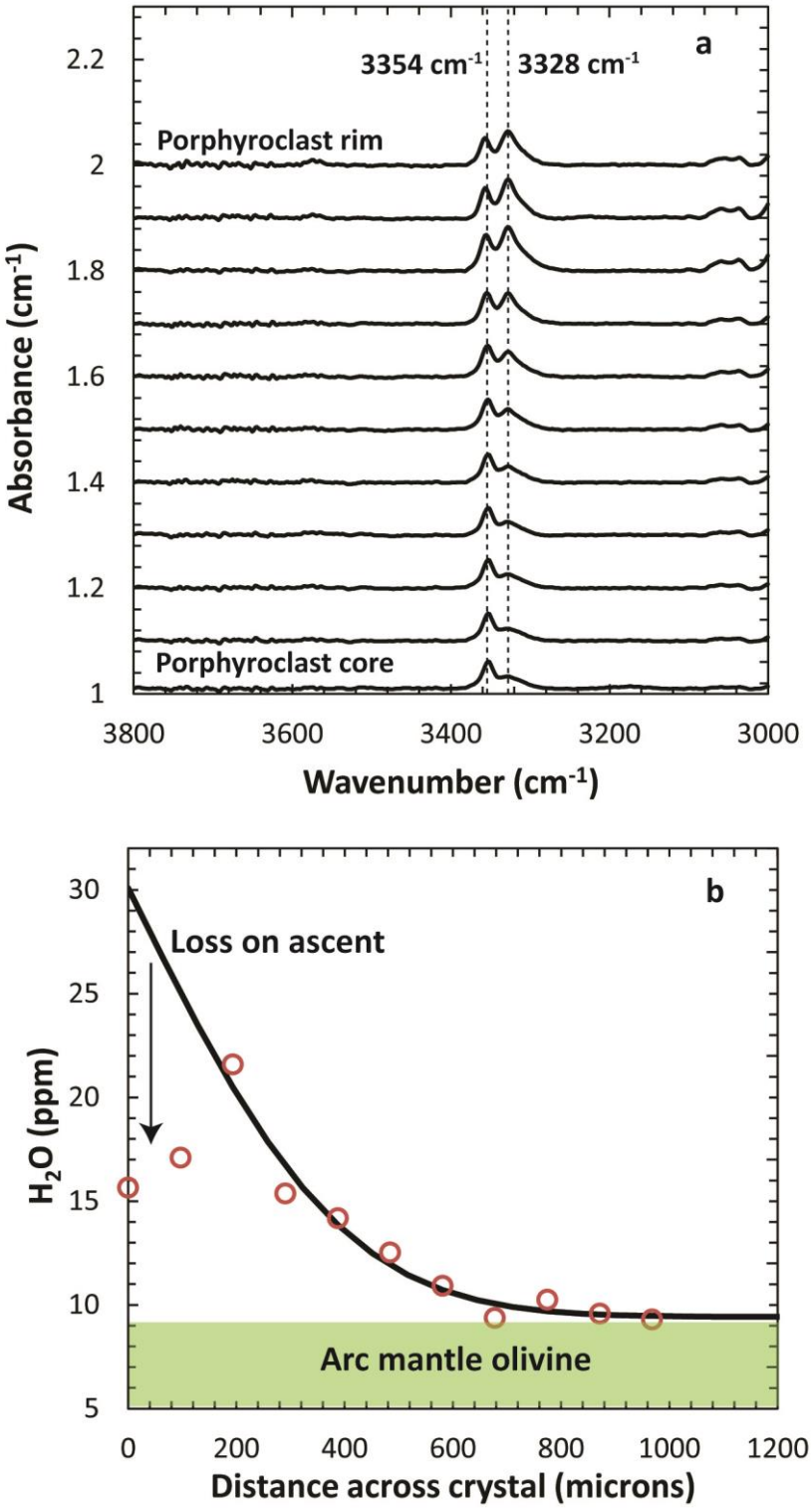

Fig. 5.4 a) Systematic change in the total infrared absorption and relative intensity of the two infrared peaks from from porphyroclast core to rim. All spectra are normalised to 1 cm and offset for clarity. b) Increase in water content from core values similar to other arc mantle olivines (Soustelle et al. 2010, Soustelle et al. 2013) to elevated rim values. Values closest to the rim record late stage water loss during magmatic ascent. Black line is a model fit to the data prior to water loss.

A total of 17 trace element profiles were measured on 11 olivine crystals. Core concentrations of all incompatible elements are very low when compared to global datasets for olivine (Fig. 5.2, De Hoog et al. 2010), particularly Na (1.5-2 ppm), Ca (80-100 ppm), Ti (0.8-1.0 ppm), Cr (as low as 8 ppm), Cu (0.4-0.5 ppm) and Y (1-2 ppb). Ni is relatively high in the crystal cores, with up to 3400 ppm. Given the low concentrations of other incompatible trace elements, Sc has relatively high core concentrations of ~2.8 ppm. Concentrations of Li, Na, Ca, Sc, Ti, Cr, Mn, Cu and Y increase systematically towards the crystal rims consistent with diffusion, with rim concentrations approximately an order of magnitude or more higher for Na, Ca, Ti, Cr, Cu and Y (Fig. 5.2, Fig. 5.3). Rim concentrations of Li, Sc and Mn are higher than in the crystal cores by a smaller amount (20-50 %). Ni decrease towards the rims by up to 14 %, but typically ~7 %. Vanadium concentration profiles are more varied. Typically V concentrations change sympathetically with other incompatible elements, but occasionally profiles have sinusoidal shapes reflecting a more complicated process or combination of processes. Likewise, Al typically displays more complex zoning rather than just simple rim enrichment. In a number of profiles there is a minor peak in the crystal centre for a number of elements (most commonly Na, Al and Cu, but occasionally Cr and Y). None of the other elements measured show quantifiable, systematic variation in concentration along crystal profiles, most notably the most slowly diffusing trace element, P. Neoblastic olivine is almost identical in composition to the highest values measured in the rims of olivine porphyroclasts, and also to phenocrysts in the host magma, with the exception of Ni which is always lower in the phenocrysts. The melt in the host magma has high MgO (15 wt. %), Cr (625 ppm) and Ni (250 ppm), and low TiO_2 (0.38 wt. %) and Na_2O (1.36 wt. %).

The infrared absorption spectra of olivine porphyroclasts (Fig. 5.4, Fig. 3.3) are characterized by double peaks at intermediate wavenumbers (3354 cm^{-1} and 3328 cm^{-1}). Converting this total absorption to water content reveals significant variation from 7 to 28 ppm, beyond what could be anticipated from simple anisotropy (see Chapter 3 of this thesis). This is confirmed by the IR profile, which reveals reverse zoning of H_2O from ~9 ppm in the core up to ~22 ppm, 200 µm from the rim. The two spots closest to the crystal rim however have lower water contents. The core water contents and associated infrared spectra are typical of olivine from other arc peridotites (Fig. 5.3.) which contain up to ~9

ppm water (Soustelle et al. 2010, Soustelle et al. 2013), whereas the elevated values near the crystal rim are amongst highest measured for olivine from non-cratonic spinel peridotites (Fig. 3.11., Peslier et al. 2010). Spectral changes are observed across the crystal accompanying the increase in water content, with the peak at 3328 cm^{-1} increasing in intensity relative to the peak at 3354 cm^{-1} towards the crystal rim.

5.4 Discussion

5.4.1 Evidence for involvement of a melt

Establishing whether a melt phase was involved in the generation of the observed texture is a prerequisite for understanding its origin. The first line of evidence for melt involvement is the high modal proportion of neoblastic clinopyroxene intermixed with olivine, which contrasts with the absence of primary clinopyroxene elsewhere in the xenolith. We interpret this neoblastic clinopyroxene to be a secondary phase formed as a product of reaction between the residual peridotite and a percolating melt during recrystallization of the porphyroclasts. The second line of evidence is the elevated water content of olivine porphyroclasts relative to similarly depleted arc peridotites (Soustelle et al. 2010, Soustelle et al. 2013) and the increase in water towards the crystal rim which indicates interaction with a hydrous fluid phase under conditions of high fH_2O (Fig. 5.4). A final line of evidence is the similar trace element composition of olivine neoblasts, olivine porphyroclast rims, and olivine phenocrysts in the host magma (Fig. 5.2), coupled with the inference that these compositions are those expected for equilibrium with the host magma, as follows. The host magma melt composition was calculated by averaging the 10 individual groundmass LA-ICP-MS measurements, which minimised the effect of modal inhomogeneity of the groundmass. Using this composition, we then calculated olivine/melt partition coefficients for phenocrysts (ignoring a few compositionally anomalous grains that may be antecrystal in provenance), the average neoblastic olivine and the maximum rim concentrations of olivine porphyroclasts. The results are in good agreement with each other and with literature values for equilibrium crystallisation experiments over a range of appropriate conditions (Fig. 5.5). This is a strong indication that the peridotite was reacting with a melt of similar composition and petrogenesis to the magma in which the xenolith was entrained during transport to the surface. The

slightly lower Ni and *Fo* contents of the phenocrysts compared to neoblasts and high sensitivity of these components to fractionation of olivine during the earliest stages of differentiation suggest that the interacting melt was probably slightly more primitive than the host magma.

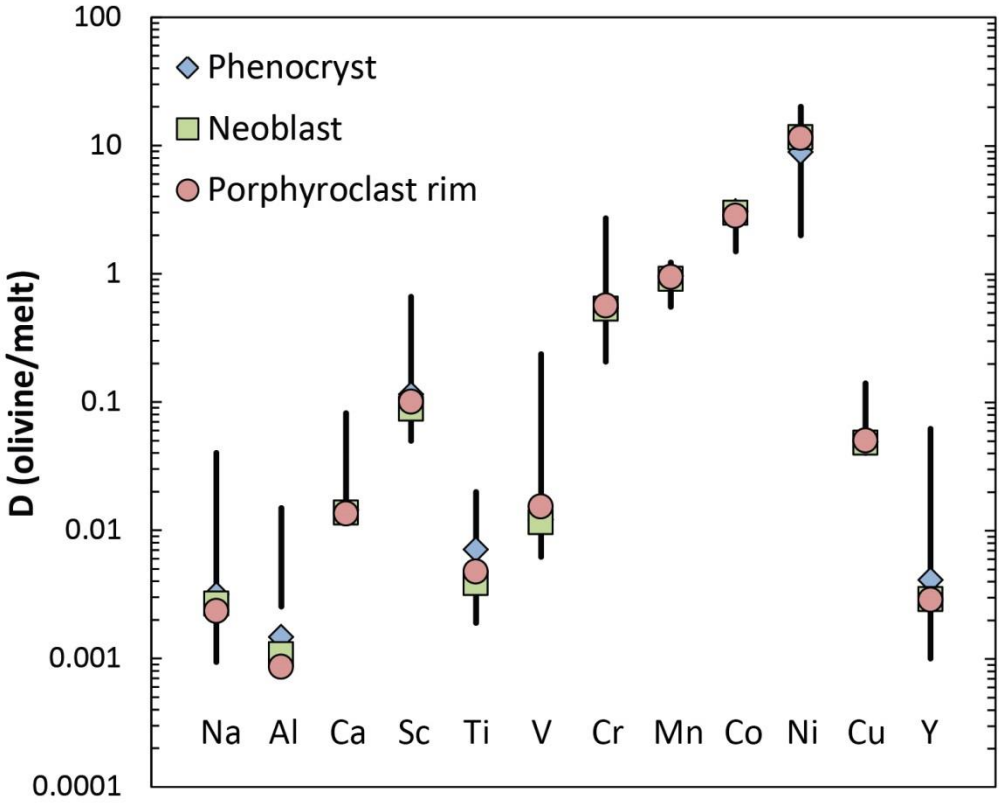

Fig. 5.5 Olivine-melt trace element partition coefficients for the average composition of neoblasts and phenocrysts and the maximum porphyroclast rim composition. The melt composition is an average of 10 individual laser spot measurements covering the extent of the host groundmass in the attached lava (Fig. 5.1). Black lines are literature data from equilibrium crystallisation experiments (Spandler and O'Neill 2010 and references within Roux et al. 2011, Mallmann et al. 2013 and Liu et al. 2014)

5.4.2 T-fO_2-H_2O of xenolith and host magma

Incompatible element partition coefficients between olivine and orthopyroxene generally vary strongly with temperature, with the olivine becoming progressively depleted in these elements with decreasing temperature (Witt-Eickschen and O'Neill 2005, De Hoog et al. 2010). The highly depleted trace element concentrations measured in the cores of porphyroclastic olivine imply very low ambient mantle temperatures. This is supported by studies on other xenoliths in the Ritter suite, whose trace and major element composition reveal unusually low equilibration temperatures of ~600 °C. The elevated olivine rim concentrations of such temperature-sensitive trace elements in olivine may thus reflect higher temperature during the formation of the porphyroclastic texture, as well as possible influx of these elements from the magma. To extract timescales from the diffusion profiles, this reaction temperature must be precisely known, as well as oxygen fugacity and water content, both of which also control the rate of element diffusion in olivine. Initially we attempted to use the composition of neoblastic olivine and clinopyroxene to constrain temperature, since they are interpreted to form synchronously by reaction with the melt. However the lack of agreement and unrealistic temperatures obtained with different trace element and major element thermometers show that even this fine-grained secondary material is not in chemical equilibrium. Instead, we turned to the host magma to provide the necessary constraints, since the demonstration that a similar melt composition reacted with the peridotite implies that the temperature and oxygen fugacity were also equivalent to that of the host magma. The occurrence of olivine phenocrysts in chemical equilibrium with the surrounding basaltic groundmass (Fig. 5.2, Fig. 5.5) allowed us to utilise the olivine-melt trace element exchange thermometer and oxybarometer of Mallmann and O'Neill (2013). We took the average Sc/Y ratio of the olivine phenocrysts and the Sc/Y ratio of the average groundmass and applied the Sc/Y olivine-melt thermometer of Mallmann and O'Neill (2013), assuming a crystallisation pressure of 0.8 GPa. This produced a magmatic temperature of 1226 °C. Combined uncertainties in both the thermometry calibration and compositional variation in phenocrysts and groundmass is approximately 50 °C. The water content of the melt is then estimated from the difference between this temperature and the anhydrous liquidus temperature of the groundmass, which was estimated using the

melt thermometer (equation 15) from Putirka (2008), again assuming a crystallisation pressure of 0.8 GPa. This parameterization is very sensitive to the MgO content of the melt, which is ~15 wt. % (McAlpine and Arculus 2011). Using these values, we calculated a temperature of 1340 °C, and hence ΔT of 114 °C. We converted this ΔT to a water content by applying the method of Médard and Grove (2008), which gave a value of ~4 wt. %, which is in the upper range of estimates for the water content of primary arc magmas (Plank et al. 2013). The oxygen fugacity of the host magma was also calculated using olivine-melt equilibria, this time utilising the partitioning of heterovalent V (Mallmann and O'Neill 2013). At 1226 °C the oxygen fugacity is 2.1 log units above the fayalite-magnetite-quartz buffer, which is typical of barometric estimates for the oxygen fugacity for primitive arc basalts (Evans et al. 2012). Combined uncertainties from both the calibration and variation in the measured data is approximately 0.4 log units.

The increase in water content towards the olivine porphyroclast rim (Fig. 5.4) could be interpreted as a diffusion profile, however the much faster rate of hydrogen diffusion compared to other trace elements precludes this possibility (Demouchy et al. 2006, Spandler and O'Neill 2010, Padrón-Navarta et al. 2014). Instead we interpret the water profile to reflect hydrogen saturating ('decorating') a similar gradient in octahedral site vacancies formed in response to the diffusive flux of trivalent elements to form the stoichiometry ($M^{3+}H^{+}$)SiO_4. Since the partitioning of hydrogen into olivine is limited by this dependence on one or more trivalent species (Berry et al. 2007), the gradient in water concentration may still reflect water saturation. The positions of the infrared peaks at intermediate wavenumbers of 3354 cm^{-1} and 3328 cm^{-1} are consistent with water associated with a trivalent cation (Berry et al. 2007), however the systematic change in the relative intensities of the two peaks indicates a change in the element(s) involved in water incorporation. The low concentrations of all measured trivalent elements in the crystal core and elevated oxygen fugacity makes Fe^{3+} a plausible candidate, with small contributions from water associated with the other trivalent elements (see chapter 3 for an in depth discussion). Towards the crystal rim, Cr shows the most significant increase in concentration, hence we propose that it is vacancies associated with this element that are dominantly responsible for olivine hydration during melt-rock reaction, in agreement with chapter 3 of this thesis. This is supported by the similar peak positions and relative

intensities compared to the Cr-doped hydrous olivine crystallisation experiments of Berry et al. (2007). The two spots closest to the crystal rim show a drop in water content. We attribute this principally to dehydration during magmatic ascent which would disturb the original H_2O profile due to rapid hydrogen diffusion (Demouchy et al. 2006, Peslier et al. 2008, Denis et al. 2013, Padrón-Navarta et al. 2014) and the sensitivity of water solubility in olivine to decompression and associated drop in water fugacity (Gaetani et al. 2014). We estimated the rim concentration prior to the water-loss episode by regressing the concentration gradient (ignoring the two points closet to the crystal rim), which produced a value of 30 ppm (Fig. 5.4). Combined with our estimate for the water content of the host magma, we calculated a water partition coefficient, $D_{H_2O}^{olivine/melt}$, of 0.0008, intermediate between the experimentally determined values of Grant et al. 2007 and Hauri et al. 2006. Although carrying significant uncertainty due to the anisotropic distribution of water in olivine, our estimate may be more representative of water partitioning in highly depleted systems, such as the mantle wedge.

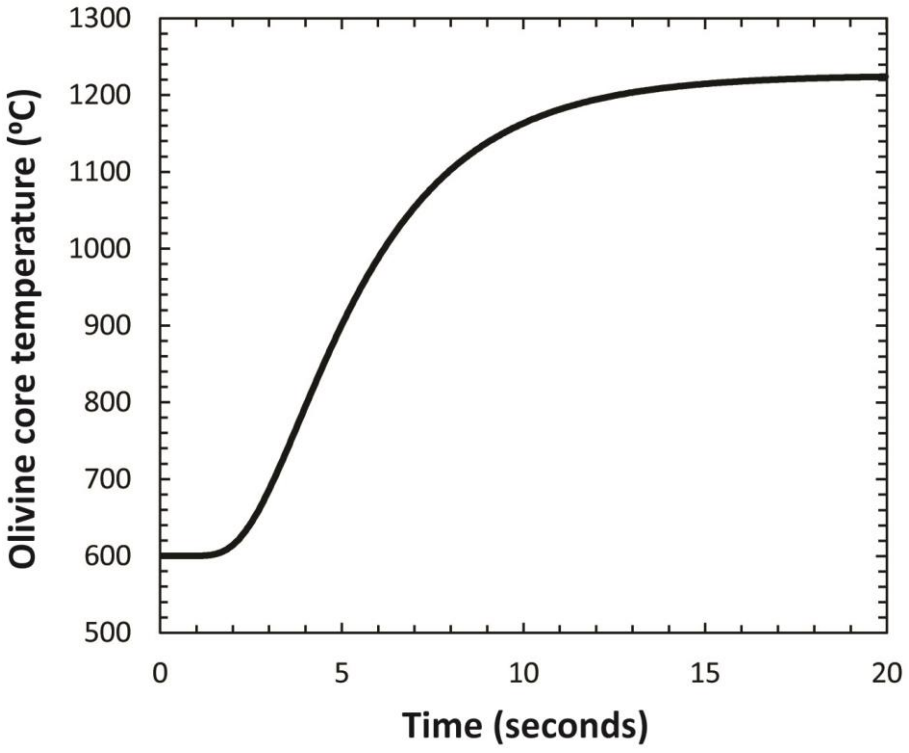

Fig. 5.6 Solution to a 1D heat conduction equation to simulate the timescale of thermal equilibration during melt-rock reaction. The core of a 2 mm radius olivine porphyroclast would equilibrate in ~20 seconds, much faster than the timescales for chemical diffusion.

5.4.3 Diffusion modelling

With these estimates for reaction temperature, oxygen fugacity and water content, we calculated a timescale for the reaction process. We assumed in our modelling that the reheating of the peridotite was essentially instantaneous compared to the time over which diffusion occurred. To test this we modelled heat flow into an olivine grain using the 1D heat conduction equation in spherical coordinates:

$$\frac{\partial T}{\partial t} = \frac{2k}{\rho c_p r}\frac{\partial T}{\partial r} + \frac{k}{\rho c}\frac{\partial^2 T}{\partial r^2}$$

where T is temperature in K, t is time in s, ρ is density of olivine (3.28 kg m^{-3}), r is radial distance from centre of the grain in m, $c_p$is specific heat capacity of olivine (1300.7 J kg^{-1} K^{-1} for Fo_{92} at 1226 °C, Kroll et al. 2012) and k is thermal conductivity of olivine (3 W m^{-1} K^{-1}, Xu et al. 2004). This equation was solved using the explicit finite difference method. The model assumed a 2 mm radius spherical olivine (Fo_{92}) crystal at an initial ambient mantle temperature of 600 °C, with the exterior of the grain held at a constant temperature of 1226 °C. The centre of the grain was assumed to be perfectly insulated. Under these conditions, the core of the olivine crystal would equilibrate with the matrix temperature in approximately 20 seconds, much faster than the timescales of diffusion calculated below (Fig. 5.6). Our diffusion modelling procedure was similar to the methodology of Qian et al. (2010). First we carefully inspected each diffusion profile and rejected any which were inconsistent with diffusion obeying Fick's law, either due to irregular crystal shape, fractures or inclusions. Unfortunately for some elements, particularly Na, Al, V and Y, this meant the majority of profiles were not usable. We then fitted the remaining profiles for each element to the solution to Fick's 2nd law for 1D diffusion into a semi-infinite body with constant melt-solid boundary position and element concentration:

$$C\ (x)\ =\ C_0 - (C_0 - C_i)erf\left(\frac{x}{2\sqrt{Dt}}\right)$$

where $C\ (x)$ is the concentration of an element in olivine at distance from the melt-olivine interface x (in meters), C_0 is the equilibrium rim concentration in the olivine, C_i is the initial concentration in the olivine, D is element diffusivity in olivine in m^2 s^{-1} and t is

the time over which diffusion occurs in seconds. By performing multiple non-linear least squares regressions of the data we simultaneously obtained values for C_0, C_i and $2\sqrt{Dt}$. As a visual confirmation that the fits and assumed model are accurate, we plotted the measured data with the diffusion models in Fig. 5.3 which are generally in excellent agreement (reduced chi-squared = 0.0-4.4). In the case of Y, the fits are poorer, with a number of anomalously high measured values in the crystal cores or right at the crystal rims. These anomalous data points were discarded during the regression procedure. The good fit of the models to the measured profiles confirms that the diffusion occurred at an approximately fixed temperature since fluctuations in temperature during the diffusion process would create stepped or multiple overlapping diffusion profiles.

To calculate timescales from these models we used the concentration profiles for Ca (Fig. 5.7), because the large difference between core and rim concentrations constrains the shape of the profiles, hence diffusivity and the diffusivity of Ca has been well constrained experimentally as a function of temperature, oxygen fugacity and crystallographic orientation (Coogan et al. 2005). The orientation of each traverse relative to the principle crystallographic axes was calculated using Euler angles obtained by EBSD and this information was then used to calculate the appropriate bulk diffusion coefficient. Using our calculation of reaction temperature and fO_2 produced values between 0.5 and 2.0 years (average of 1.2 years, Table 5.2). Since a significant source of error in the timescale calculation is in the precise position and concentration of the crystal rim, we estimated uncertainty by moving the rim spot away from the actual position by 30 µm (approximately half the spot size used) and repeating the regression procedures. This revealed uncertainties of generally < 15 % in each individual timescale (Table 5.2). Additional uncertainty is in the shape of the crystal in three dimensions and location of the measured plane relative to the core the crystal, however these cannot be assessed from our thick sections. Our calculated timescales are probably overestimates since the olivines have elevated concentrations of water, which is known to increase the rate of diffusion (Wang et al. 2004). The influence of water has only been studied for the inter-diffusion rate of Fe-Mg, but since most elements diffuse in olivine by a similar vacancy mechanism, the effect is likely to be similar. Accordingly, it is likely that the timescales we calculated and present here are ~1 order of magnitude too long. We interpret these

calculated timescales to represent the time between the initiation of melt intrusion and formation of the xenolith itself through magmatic entrainment. We cannot however discount a period of slow reheating to intermediate temperatures, perhaps in response to a nearby melt channel or magma chamber which is then overprinted by rapid diffusion during physical interaction with the melt. Therefore, the overall period of local magmatism may be longer than the timescale calculated here.

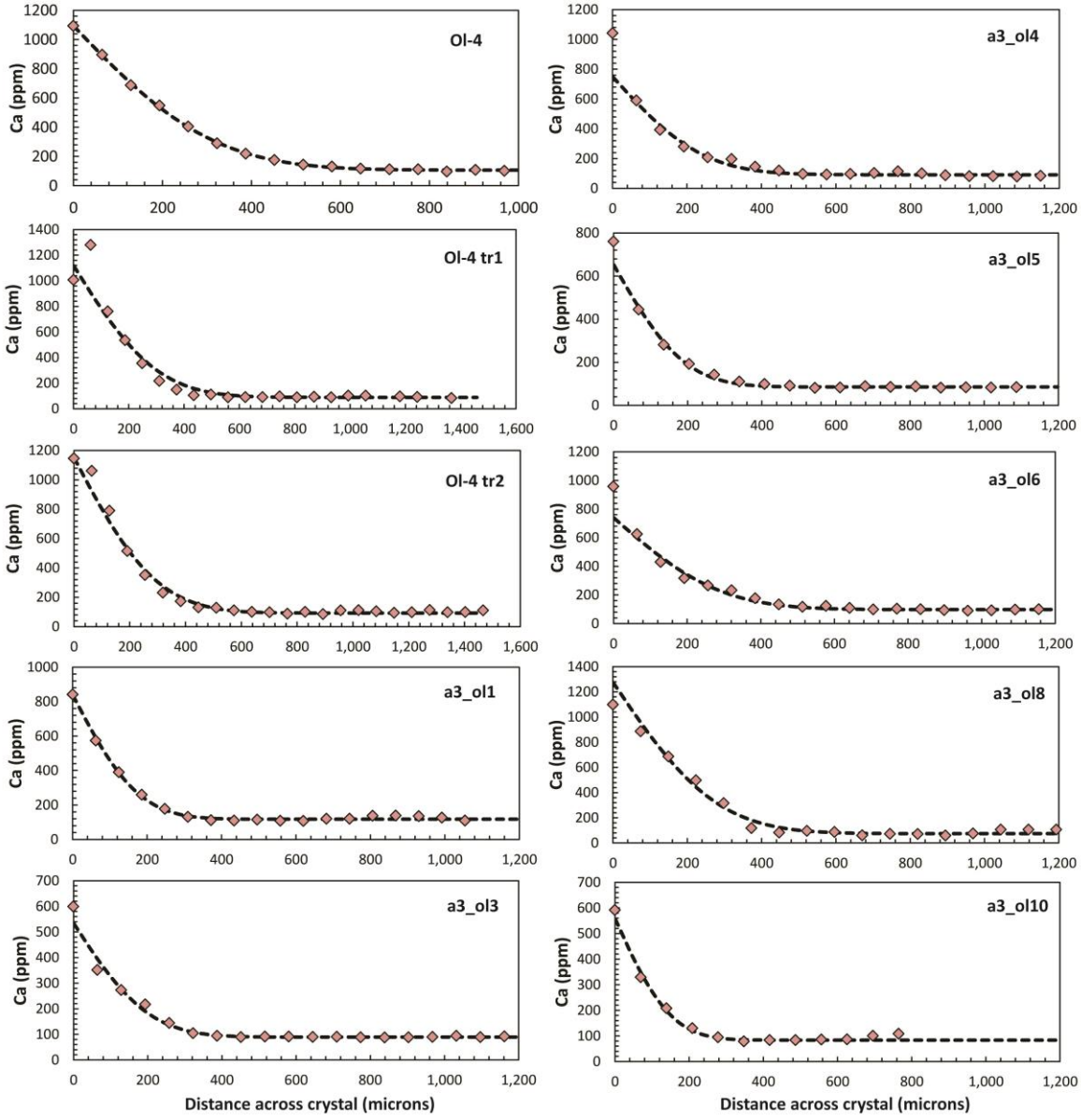

Fig. 5.7 Ca diffusion profiles (rim to core) used in the calculations of timescale. Dashed line represents a non-linear least squares regression of the data from which timescale was subsequently obtained.

We also tried to calculate the rate of ascent by measuring across the magma-peridotite contact and looking for inflections in the trace element concentration of olivine close to the boundary. Whilst Ni and Mn showed shifts in concentration which could potentially be ascent-induced, these were not reflected in similar changes in Cr and Sc concentration. Any attempts to model the profiles of Mn and Ni were hampered by uncertainty in the precise position of the contact, which at such short and relatively poorly constrained diffusion profiles introduces significant uncertainty in calculated timescales. It is also unclear whether the measured profiles were formed due to the prior episode of melt-rock reaction and have subsequently been incised during xenolith formation. We therefore conclude that the rate of ascent was probably too quick to produce any significant, quantifiable changes in the trace element concentration of olivine neighbouring the host magma, consistent with independent estimates of typical mantle xenolith ascent rates of 0.1-10 m s^{-1} (Denis et al. 2013).

Crystal	Ol-4	Ol-4 tr1	Ol-4 tr2	a3 ol1	a3 ol3	a3 ol4	a3 ol5	a3 ol6	a3 ol8	a3 ol10a	a3 ol12a
Time (years)	1.2	1.4	1.5	1.3	0.5	1.7	2.0	1.0	0.9	0.7	1.1
Uncertainty (%)	10	9	9	13	14	18	19	14	4	10	5
D Li	7.45E-16	—	—	—	—	—	—	—	—	—	—
D Na	—	—	—	—	1.70E-15	—	—	—	—	—	—
D Ca	6.4E-16	4.5E-16	5.1E-16	6.4E-16	6.7E-16	7.2E-16	7.2E-16	7.0E-16	5.1E-16	3.2E-16	6.2E-16
D Sc	1.7E-15	1.2E-15	2.6E-15	—	—	—	—	—	—	—	2.0E-15
D Ti	2.2E-16	3.1E-16	2.6E-15	—	—	—	—	—	—	—	2.3E-16
D V	—	—	—	2.7E-15	2.7E-15	—	—	—	—	—	—
D Cr	—	1.1E-15	2.2E-16	1.8E-15	2.1E-15	—	—	—	—	—	—
D Mn	—	8.7E-16	1.8E-15	—	—	—	—	—	—	—	—
D Ni	—	—	—	2.1E-15	2.3E-15	—	—	—	—	—	—
D Cu	—	—	—	2.2E-15	2.7E-15	—	—	3.0E-15	—	—	—
D Y	—	1.1E-15	0.0E+00	—	—	—	—	—	—	—	—
D Fe-Mg	—	—	3.3E-15	8.1E-15	1.7E-15	—	—	—	—	—	—

Table 5.2 Summary of the results of orientation-corrected diffusion modelling for each crystal. All diffusivities (*D*) are calculated using timescales from Ca diffusion modelling and are in units of m^2 s^{-1}. Uncertainties are calculated assuming 30 µm error in the placement of the laser spot closest to the crystal rim. Source of additional uncertainty highlighted in the discussion. Gaps in the data are due either to a particular element not being measured or the measured data being unsuitable for modelling

5.4.4 Relative rates of element diffusion in olivine

There is debate regarding the diffusion rates of a number of trace elements in olivine, particularly the rare earth elements (REE), Cr and Ti. For example, diffusion experiments conducted by Spandler and O'Neill (2010) and Cherniak (2010) differ in their measurements of REE diffusion by nearly four orders of magnitude. Similarly, Spandler and O'Neill (2010) measured Cr diffusion nearly two orders of magnitude faster than an equivalent study by Ito and Ganguly (2006). This has major implications for the calculation of minimum timescales required to preserve chemical and isotopic heterogeneities in olivine-bearing rocks and olivine-hosted melt inclusions. Studies on natural samples offer a test of experimental results and a means to extrapolate to time-temperature conditions beyond the reach of experimentation. The study of Qian et al. (2010) on diffusion profiles in olivine xenocrysts in a dioritic magma used this approach. Our study offers another opportunity to compare the rates of diffusion of different major, minor and trace elements in olivine. Fig. 5.8 shows the diffusion rates of different elements in olivine relative to Ca, with diffusion rate calculated by converting values of $2\sqrt{Dt}$ using the estimated timescale for each crystal. Plotted for comparison are the results of experimental studies by Ito and Ganguly (2006), Spandler and O'Neill (2010), Qian et al. (2010) and Cherniak (2010). Our results clearly demonstrate that the diffusion rates of Li, Na, Sc, Ti, V, Cr, Mn, Ni, Cu, Y and Fe-Mg are very similar, falling within an order of magnitude of each other in spite of large differences in ionic radius and valence state. We can extrapolate our diffusion rate estimate for Y to the REE suite since it shows almost indistinguishable chemical affinity to that of Ho. Hence diffusivities of REE are similar to or slightly faster than Fe-Mg, in agreement with Spandler and O'Neill (2010) and Qian et al. (2010). The diffusivity of most other elements in our study are also in good agreement with Spandler and O'Neill (2010) and Qian et al. (2010), even considering the different temperatures and oxygen fugacities of diffusion in those studies. Finally our profiles show no quantifiable changes in the concentration of P (Fig. 5.3), consistent with the very slow diffusion rates for this element. Zoning of P has been observed in both magmatic and mantle olivines and is thought to reflect crystal growth or metasomatism under a range of conditions, with the very slow P diffusion preventing subsequent chemical homogenisation (Milman-Barris et al. 2008, Mallmann and O'Neil 2009, Ruprecht and

Plank 2013). Therefore the absence of P zoning in these olivines is confirmation that the observed profiles are indeed related to diffusion and not to crystal growth or some other cryptic geochemical process.

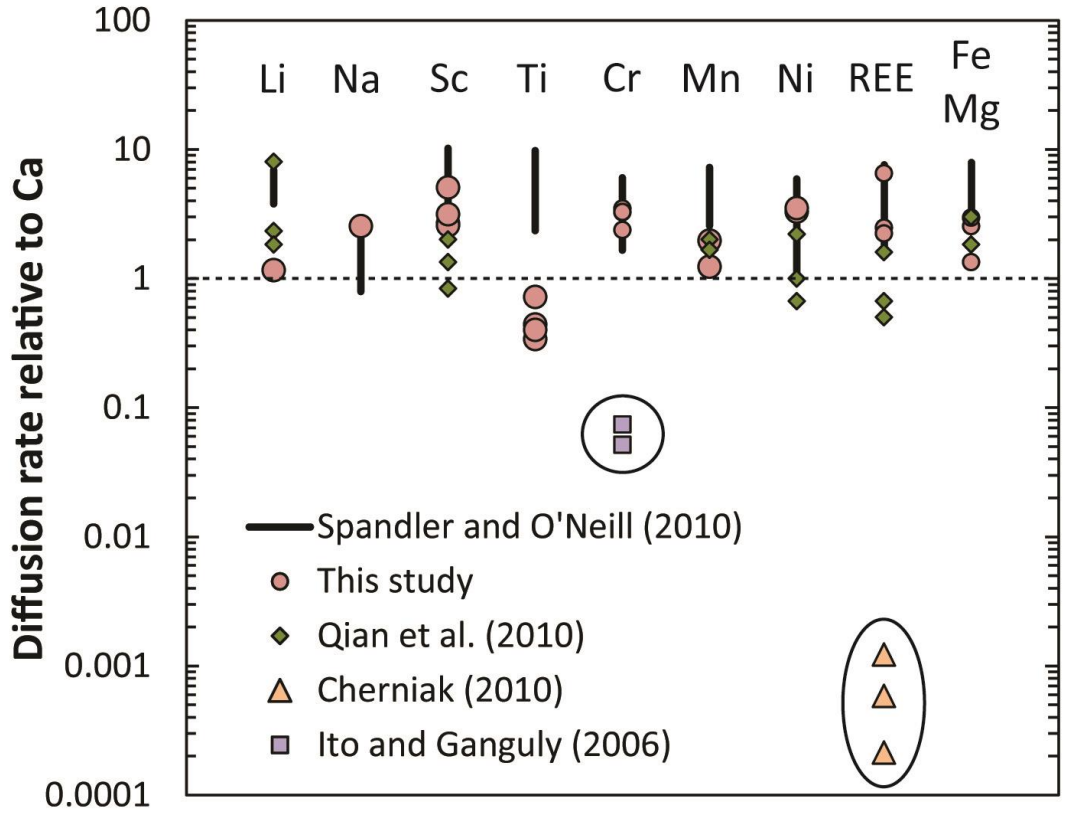

Fig. 5.8 Diffusivities of different trace elements and Fe-Mg expressed relative to Ca. Plotted are the results from this study (where each spot represents an estimate from an individual laser profile), experimental data from Ito and Ganguly (2006), Spandler and O'Neill (2010) and Cherniak 2010 and the study on an olivine xenocryst by Qian et al. (2010). All available crystal orientations are plotted. Data from Ito and Ganguly (2006) and Cherniak (2010) are calculated at 1250 °C and an oxygen fugacity relative to FMQ. Ca diffusion coefficients from Coogan et al. (2005) were used for comparison.

5.4.5 Implications for interpretation of porphyroclastic textures and magmatic systems

Porphyroclastic textures are widely observed in peridotites from a range of tectonic environments (Pearson et al. 2003). Highly deformed peridotites (mylonites or ultramylonites) represent dynamic recrystallization in shear zones due to strain localisation (Drury et al. 1991), although debate exists as to whether this is facilitated by the presence of melt (Dijkstra et al. 2002, Kaczmarek and Müntener 2008). Less deformed porphyroclastic textures are more ambiguous in their interpretation. They may represent less deformed regions of shear zones (Linckens et al. 2011) or the products of melt-rock reaction and reheating (Franz et al. 1996, Soustelle et al. 2010). Similar textures to that described here are observed in most other suites of arc peridotites (Grégoire et al. 2001, Parkinson et al. 2003, Arai et al. 2004, Bryant et al. 2007, Vanucci et al. 2007, Ishimaru et al. 2007, Ionov 2010, Soustelle et al. 2010), which suggests that they are representative of conditions in the shallow mantle wedge. The short timescales calculated here are similar to timescales calculated for the ascent and mixing of mantle-derived melts in crustal storage regions (Ruprecht and Plank 2013), but are much longer than typical timescales of xenolith exhumation from mantle depths (O'Reilly and Griffin, 2010). Our results demonstrate that these weakly deformed porphyroclastic peridotites are formed rapidly under high temperature conditions in the presence of hydrous melts as part of a dynamically evolving magmatic system shortly before the xenoliths are exhumed. The infiltration of melt and associated hydration of olivine probably acted as a weakening mechanism, allowing the concentration of deformation and observed recrystallisation and formation of the fine-grained, trace element-enriched matrix (Mei et al. 2002). The chemistry of similarly textured peridotites in other arc suites may hold important insights into the nature of primary melts within the mantle wedge. We speculate that diffusion profiles measured here, whilst amplified by the unusually strong temperature contrast between ambient mantle and magmatic conditions, may be common in other peridotite suites. Similar exercises to this in combination with estimates of ascent rate from rapidly diffusing species such as hydroxyl in olivine (Demouchy et al. 2006, Peslier et al. 2008, Denis et al. 2013), and magmatic storage from other diffusion-based and isotopic geospeedometers on host lavas (Ruprecht and Plank 2013, Cooper and Kent 2014) will

allow a full record of magmatic timescales, from interaction between peridotite and primary melts in the mantle wedge through to eruption.

5. 5 References

Arai, S., Takada, S., Michibayashi, K., Kida, M., 2004. Petrology of Peridotite Xenoliths from Iraya Volcano, Philippines, and its Implication for Dynamic Mantle-Wedge Processes. J. Petrol. 45, 369-389

Batanova, V.G., Belousov, I.A., Savelieva, G.N., Sobolev, A.V., 2011. Consequences of Channelized and Diffuse Melt Transport in Supra-subduction Zone Mantle: Evidence from the Voykar Ophiolite (Polar Urals). 52, 2483-2521

Bénard, A., Ionov, D.A., 2013. Melt- and Fluid-Rock Interaction in Supra-Subduction Lithospheric Mantle: Evidence from Andesite-hosted Veined Peridotite Xenoliths. J. Petrol. 54, 2339-2378

Berry, A.J., O'Neill, H.St.C., Hermann, J., Scott, D.R., 2007. The infrared signature of water associated with trivalent cations in olivine. Earth Planet. Sci. Lett. 261, 134-142

Bryant, J.A., Yogodzinski, G.M., Churikova, T.G., 2007. Melt-mantle interactions beneath the Kamchatka arc: Evidence from ultramafic xenoliths from Shiveluch volcano. Geochem. Geophys. Geosys. 8, doi:10.1029/2006GC001443

Cherniak, D.J., 2010. REE diffusion in olivine. Am. Mineral. 95, 2-3

Cherniak, D.J., Watson, E.B., Liang, Y., 2012. Diffusion of highly charged cations in olivine. Abstract MR22A-07, 2012 Fall Meeting, AGU

Coogan, L.A., Hain, A., Stahl, S., Chakraborty, S., 2005. Experimental determination of the diffusion coefficient for calcium in olivine between 900 °C and 1500 °C. Geochim. Cosmochim. Acta 69, 3683-3694

Cooper, K.M., Kent, A.J.R., 2014. Rapid remobilization of magmatic crystals kept in cold storage. Nature 506, 480-483

De Hoog, J.C.M., Gall, L., Cornell, D.H., 2010. Trace-element geochemistry of mantle olivine and application to mantle petrogenesis and geothermobarometry. Chemical Geology 270, 196-215

Demouchy, S., Jacobsen, S.D., Gaillard, F., Stern, C.R., 2006. Rapid magma ascent recorded by water diffusion profiles in mantle olivine. Geology 34, 429-432

Denis, C.M.M., Demouchy, S., Shaw, C.S.J., 2013. Evidence of dehydration in peridotites from Eifel Volcanic Field and estimates of the rate of magma ascent. J. Volc. Geotherm. Res. 258, 85-99

Dijkstra, A.H., Drury, M.R., Vissers, R.L.M., Newmann, J., 2002. On the role of melt-rock reaction in mantle shear zone formation in the Othris Peridotite Massif (Greece). J. Struc. Geol. 24, 1431-1450

Drury, M.R., Vissers, R.L.M., Van der Wal, D., Strating, E.H.H., 1991. Shear Localisation in Upper Mantle Peridotites. Pure Appl. Geophys. 137, 439-460

Costa, F., Dungan, M., 2005. Short time scales of magmatic assimilation from diffusion modelling of multiple elements in olivine. Geology 33, 837-840

Eggins, S.M., Kinsley, L.P.J., Shelley, J.M.G., 1998. Deposition and element fractionation processes during atmospheric pressure laser sampling for analysis by ICP-MS. Appl. Surf. Sci. 129, 278-286

Evans, K.A., Elburg, M.A., Kamenetsky, V.S., 2012. Oxidation state of subarc mantle. Geology 40, 783-786

Falus, G., Tommasi, A., Soustelle, V., 2011. The effect of dynamic recrystallization on olivine crystal preferred orientations in mantle xenoliths deformed under varied stress conditions. J. Struc. Geol. 33, 1528-1540

Foley, S.F., Prelevic, D., Rehfeldt, T., Jacob, D.E., 2013. Minor and trace elements in olivines as probes into early igneous and mantle melting processes. Earth Planet. Sci. Lett. 363, 181-191

Franz, L., Breh, G.P., Okrusch, M., 1996. Steady state geotherm, thermal disturbances, and tectonic development of the lower lithosphere underneath the Gibeon Kimberlite Province, Namibia. Contrib. Mineral. Petrol. 126, 181-198

Franz, L., Becker, K-P., Kramer, W., Herzig, P.M., 2002. Metasomatic Mantle Xenoliths from the Bismarck Microplate (Papua New Guinea)- Thermal Evolution, Geochemistry and Extent of Slab-induced Metasomatism. J. Petrol. 43, 315-343

Gaetani, G.A., O'Leary, J.A., Koga, K.T., Hauri, E.H., Rose-Koga, E.F., Monteleone, B.D., 2014. Hydration of mantle olivine under variable water and oxygen fugacity conditions. Contrib. Mineral. Petrol. 167, 965-979

Gibert, B., Seipold, U., Tommasi, A., Mainprice, D., 2003. Thermal diffusivity of upper mantle rocks: Influence of temperature, pressure and the deformation of fabric. J. Gephys. Res. 108, 2359

Grant, K.J., Brooker, R.A., Kohn, S.C., Wood, B.J., 2007. The effect of oxygen fugacity on hydroxyl concentrations and speciation in olivine: Implications for water solubility in the upper mantle. Earth Planet. Sci. Lett. 261, 217-229

Grant, K.J., Kohn, S.C., Brooker, R.A., 2007. The partitioning of water between olivine, orthopyroxene and melt in the system albite-forsterite-H_2O. Earth Planet. Sci. Lett. 260, 227-241

Grégoire, M., McInnes, B.I.A., O'Reilly, S.Y., 2001. Hydrous metasomatism of oceanic sub-arc mantle, Lihir, Papua New Guinea Part 2. Trace element characteristics of slab-derived fluids. Lithos 59, 91-108

O'Reilly, S.Y., Griffin, W.L., 2010. Rates of Magma Ascent: Constraints from Mantle-Derived xenoliths. *In* Timescales of Magmatic Processes: From Core to Atmosphere. Wiley

Harte, B., 1977. Rock Nomenclature with Particular Relation to Deformation and Recrystallisation Textures in Olivine-Bearing Xenoliths. J. Geol. 85, 279-288

Hauri, E.H., Gaetani, G.A., Green, T.H., 2006. Partitioning of water during melting of the Earth's upper mantle at H_2O-undersaturated conditions. Earth Planet. Sci. Lett. 248, 715-734

Ionov, D.A., 2010. Petrology of Mantle Wedge Lithosphere: New Data on Supra-Subduction Zone Peridotite Xenoliths from the Andesitic Avacha Volcano, Kamchatka. J.Petrol. 51, 327-361

Ishimaru, S., Arai, S., Ishida, Y., Shirasaka, M., Okrugin, V.M., 2007. Melting and Multi-stage Metasomatism in the Mantle Wedge beneath a Frontal Arc Inferred from Highly Depleted Peridotite Xenoliths from the Avacha Volcano, Southern Kamchatka. J. Petrol. 48, 395-433

Ito, M., Ganguly, J., 2006. Diffusion kinetics of Cr in olivine and ^{53}Mn-^{53}Cr thermochronology of early solar system objects. Geochim. Cosmochim. Acta 70, 799-809

Kaczmarek, M-A., Müntener, O., 2008. Juxtaposition of Melt Impregnation and High-Temperature Shear Zones in the Upper Mantle; Field and Petrological Constraints from the Lanzo Peridotite (Northern Italy). J. Petrol. 49, 49, 2187-2220

Kaeser, B., Kalt, A., Pettke, T., 2006. Evolution of the Lithospheric Mantle beneath the Marsabit Volcanic Field (Northern Kenya): Constraints from the Textural, *P-T* and Geochemical Studies on Xenoliths. J. Petrol. 47, 2149-2184

Kelemen, P.B., Dick, H.J.B., Quick, J.E., 1992. Formation of harzburgite by pervasive melt/rock reaction in the upper mantle. Nature 358, 635-641

Kovács, I., Hermann, J., O'Neill, H.St.C., Fitz Gerland, J., Sambridge, M., Horváth, G., 2008. Quantitative absorbance spectroscopy with unpolarized light: Part II. Experimental evaluation and development of a protocol for quantitative analysis of mineral IR spectra. Am. Mineral. 93, 765-778

Kovács, I., O'Neill, H.St.C., Hermann, J., Hauri, E.H., 2010. Site-specific infrared O-H absorption coefficients for water substitution into olivine. Am. Mineral. 95, 292-299

Kroll, H., Kirfel, A., Heinemann, R., Barbier, B., 2012. Volume thermal expansion and related thermophysical parameters in the Mg,Fe olivine solid-solution series. Eur. J. Mineral. 24, 935-956

Le Roux, V., Dasgupta, R., Lee, C-T.A., 2011. Mineralogical heterogeneities in the Earth's mantle: Constraints from Mn, Co, Ni and Zn partitioning during partial melting. Earth Planet. Sci. Lett. 307, 395-408

Linckens, J., Herwegh, M., Müntener, O., 2011. Linking temperature estimates and microstructures in deformed polymineralic mantle rocks. Geochem. Geophys. Geosys. 12 doi:10.1029/2011GC003536

Liu, X., Xiong, X., Audétat, A., Li., Y., Song, M., Li, L., Sun, W., Ding, X., 2014. Partitioning of copper between olivine, orthopyroxene, clinopyroxene, spinel, garnet and silicate melts at upper mantle conditions. Geochim. Cosmochim. Acta 125, 1-22

Mallmann, G., O'Neill, H.St.C., Klemme, S., 2009. Heterogeneous distribution of phosphorus in olivine from otherwise well-equilibrated spinel peridotite xenoliths and its implications for the mantle geochemistry of lithium. Contrib. Mineral. Petrol. 158, 485-504

Mallmann, G., O'Neill, H.St.C., 2013. Calibration of an Empirical Thermometer and Oxybarometer based on the Partitioning of Sc, Y and V between Olivine and Silicate Melt. J. Petrol. 54, 933-949

Mather, K.A., Pearson, D.G., McKenzie, D., Kjarsgaard, B.A., Priestly, K., 2011. Constraints on the depth and thermal history of cratonic lithosphere from peridotite xenoliths, xenocrysts and seismology. Lithos 125, 729-742

McAlpine, S.R.B., Arculus, R.J., 2011. Pristine mantle xenoliths from the active Bismarck Arc. Min. Mag. 75, 1261-1373

Médard, E., Grove, T.L., 2008. The effect of H_2O on the olivine liquidus of basaltic melts: experiments and thermodynamic models. Contrib. Mineral. Petrol. 155, 417-432

Mei, S., Bai, W., Hiraga, T., Kohlstedt, D.L., 2002. Influence of melt on the creep behaviour of olivine-basalt aggregates under hydrous conditions. Earth Planet. Sci. Lett. 201, 491-507

Milman-Barris, M.S., Beckett, J.R., Baker, M.B., Hofmann, A.E., Morgan, Z., Crowley, M.R., Vielzeuf, D., Stolper, E., 2008. Zoning of phosphorus in igneous olivine. Contrib. Mineral. Petrol. 155, 739-765

Neumann, E-R., Griffin, W.L., Pearson, N.J., O'Reilly, S.Y., 2004. The Evolution of the Upper Mantle beneath the Canary Islands: Information from Trace Elements and Sr isotope Ratios in Minerals in Mantle Xenoliths. J. Petrol. 45, 2573-2612

Padrón-Navarta, J.A., Hermann, J., O'Neill, H.St.C., 2014. Site-specific hydrogen diffusion rates in forsterite. Earth Planet. Sci. Lett. 392, 100-112

Parkinson, I.J., Pearce, J.A., 1998. Peridotites from the Izu-Bonin-Mariana Forearc (ODP Leg 125): Evidence for Mantle Melting and Melt-Mantle Interaction in a Supra-Subduction Zone Setting. J. Petrol. 39, 1577-1618

Parkinson, I.J., Arculus, R.J., 1999. The redox state of subduction zones: insights from arc-peridotites. Chemical Geology 160, 409-423

Parkinson, I.J., Arculus, R.J., Eggins, S.M., 2003. Peridotite xenoliths from Grenada, Lesser Antilles Island Arc. Contrib. Mineral. Petrol. 146, 241-262

Pearson, D.G., Canil, D., Shirey, S.B., 2003. Mantle Samples Included in Volcanic Rocks: Xenoliths and Diamonds. Treatise on Geochemistry

Peslier, A.H., Woodland, A.B, Wolff, J.A., 2008. Fast kimberlite ascent rates estimated from hydrogen diffusion profiles in xenolithic mantle olivines from southern Africa. Geochim. Cosmochim. Acta 72, 2711-2722

Peslier, A.H., 2010. A review of water contents of nominally anhydrous natural minerals in the mantles of Earth, Mars and the Moon. J. Volc. Geotherm. Res. 197, 239-258

Pirard, C., Hermann, J., O'Neill, H.St.C., 2013. Petrology and Geochemistry of the Crust-Mantle Boundary in a Nascent Arc, Massif du Sud Ophiolite, New Caledonia, SW Pacific. J. Petrol. 54, 1759-1792

Plank, T., Kelley, K.A., Zimmer, M.M., Hauri, E.H., Wallace, P.J., 2013. Why do mafic arc magmas contain ~4 wt% water on average? Earth Planet. Sci. Lett. 364, 168-179

Putirka, K.D., 2008. Thermometers and barometers for volcanic systems. Rev. Mineral. Geochem. 69, 61-120

Qian, Q., O'Neill, H.St.C., Hermann, J., 2010. Comparative diffusion coefficients of major and trace elements in olivine at ~950 °C from a xenocryst included in dioritic magma. Geology 38, 331-334

Ruprecht, P., Plank, T., 2013. Feeding andesitic eruptions with a high-speed connection from the mantle. Nature 500, 68-72

Smith, D., 2013. Olivine thermometry and source constraints for mantle fragments in the Navajo Volcanic Field, Colorado Plateau, southwest United States: Implications for the Mantle Wedge. 14 doi:10.1002/ggge.20065

Soustelle, V., Tommasi, A., Demouchy, S., Ionov, D.A., 2010. Deformation and Fluid-Rock Interaction in the Supra-subduction Mantle: Microstructures and Water Contents in Peridotite Xenoliths from the Avacha Volcano, Kamchatka. J. Petrol. 51, 363-394

Soustelle, V., Tommasi, A., Demouchy, S., Franz, L., 2013. Melt-rock interactions, deformation, hydration and seismic properties in the sub-arc lithospheric mantle inferred from xenoliths from seamounts near Lihir, Papua New Guinea. Tectonophysics 608, 330-345

Spandler, C., O'Neill, H.St.C., 2010. Diffusion and partition coefficients of minor and trace elements in San Carlos olivine at 1,300 °C with some geochemical implications. Contrib. Mineral. Petrol. 159, 791-818

Vannucci, R., Tiepolo, M., Defant, M.J., Kepezhinskas, P., 2007. The metasomatic record in the shallow peridotite mantle beneath Grenada (Lesser Antilles arc). Lithos 99, 25-44

Wang, Z.Y., Hiraga, T., Kohlstedt, D.L., 2004. Effect of H^+ on Fe-Mg interdiffusion in olivine, $(Fe,Mg)_2SiO_4$. App. Phys. Lett. 85, 209-211

Witt-Eickschen, G., O'Neill, H.St.C., 2005. The effect of temperature on the equilibrium distribution of trace elements between clinopyroxene, orthopyroxene, olivine and spinel in upper mantle peridotite. Chem. Geol. 221, 65-101

Woodhead, J., Hergt, J., Sandiford, M., Johnson, W., 2010. The big crunch: Physical and chemical expressions of arc/continent collision in the Western Bismarck arc. J. Volc. Geotherm. Res. 190, 11-24

Xu, Y., Shankland, T.J., Linhardt, S., Rubie, D.C., Langenhorst, F., Klasinski, K., 2004. Thermal diffusivity and conductivity of olivine, wadsleyite and ringwoodite to 20 GPa and 1373 K. Phys. Earth Planet. Int. 143-144, 321-336

Zheng, J.P., Zhang, R.Y., Griffin, W.L., Liou, J.G., O'Reilly, S.Y., 2005. Heterogeneous and metasomatized mantle recorded by trace elements in minerals of the Donghai garnet peridotites, Sulu UHP terrane, China. Chem. Geol. 221, 243-259

Zheng, J.P., Griffin, W.L., O'Reilly, S.Y., Yu, C.M., Zhang, H.F., Pearson, N., Zhang, M., 2007. Mechanism and timing of lithospheric modification and replacement beneath the eastern North China Craton: Peridotitic xenoliths from the 100 Ma Fuxin basalts and a regional synthesis. Geochim. Cosmochim. Acta 71, 5203-5225

Chapter 6

Conclusions and future work

6.1 Conclusions

6.1.1 Petrogenesis of the upper mantle wedge beneath Ritter Island

The mantle beneath Ritter, sampled as peridotite xenoliths, records a complex history of melting, metasomatism, cooling and melt-rock reaction.

1. The earliest stage of petrogenesis that can be reliably constrained is hydrous partial melting as part of a previous subduction zone system which resulted in highly depleted concentrations of moderately incompatible elements in orthopyroxene, corresponding to ~29-33 % partial melting. Secondary clinopyroxene was also added concurrent with or subsequent to this period of melting and records the involvement of both silicate and carbonatite metasomatic fluids likely originating from different depths of the subducted slab. Strontium isotope evidence supports a contribution from subducted material during this stage, with the samples least affected by recent melt-rock reaction displaying radiogenic compositions similar to regionally subducted sediment. This melting and metasomatism was most likely related to subduction at the now extinct Vitiaz West-Melanesian trench system, which produced lavas and peridotite xenoliths with similarly radiogenic isotopic compositions (Woodhead et al. 1998, Kamenov et al. 2008).
2. This hydrous melting episode was followed by a period of cooling to unusually low equilibration temperatures approaching 600 °C. This cooling episode can be clearly tracked through trace element equilibria, particularly between olivine and orthopyroxene. Modelling this process shows that olivine compositions were strongly affected, with greatly decreased trace element contents upon cooling, and are thus a useful record of the thermal history of the mantle. Orthopyroxene compositions, meanwhile, were less substantially affected and can be used to reliably estimate partial melting histories.
3. Enriched whole-rock and olivine trace element compositions, oxidised iron oxidation state in spinels and elevated equilibration temperatures of ‘reacted’ harzburgites reflect melt-rock reaction in the modern mantle wedge system beneath Ritter Island. This is clearly seen petrographically as veins and patches of

secondary orthopyroxene, with un-equilibrated textures, formed at the expense of olivine through reaction with silicate melts. The strontium isotope composition of these samples is less radiogenic than those with ancient metasomatism and is identical to the average composition of lavas erupted along the West Bismarck island arc, indicating that the melt involved may be related to magmas erupted at the surface.

4. Timescales and conditions for the melt-rock reaction process can be constrained from trace element zoning and partitioning in olivine from a porphyroclastic peridotite xenolith and its host lava. Trace element partitioning between olivine phenocrysts and groundmass in the basaltic host lava is consistent with a temperature of ~1230 °C and oxygen fugacity ~2 log units above FMQ. Modelling of the trace element diffusion profiles under these conditions reveals a timescale of approximately 1 year, which reflects the time between intrusion of primary melt into the ambient mantle and exhumation of the xenolith.
5. Ascent of the xenolith to the surface resulted in loss of water from olivine porphyroclasts due to a decrease in water fugacity in the host magma and resultant drop in water solubility in olivine. Correlation between water content and olivine crystal size in 'residual' harzburgites is consistent with a timescale of ~0.5 hours. This short timescale is best explained by water-loss triggered by degassing of the host magma at shallow pressures prior to eruption.

6.1.2 The water content of the upper mantle wedge and longevity of arc mantle

1. Both orthopyroxene and coarse olivine crystal cores preserve equilibrium mantle water contents. The low equilibrium water contents of olivine and orthopyroxene are related to the depleted chemistry of these phases, limiting the incorporation of hydrogen through coupled substitutions with key elements such as Ti^{4+}, Cr^{3+} and Al^{3+}.
2. The measured water content of olivine in peridotites which have cooled below their solidus is unlikely to reflect water contents at elevated temperatures, due to substantial redistribution of trivalent cations from olivine in pyroxene during cooling.

3. The water content of olivine increases during interaction with hydrous melts, facilitated by incorporation of Cr^{3+} and Fe^{3+} from the melt which create new octahedral site vacancies for hydrogen to populate. Hydrous melt-rock reaction therefore acts as a means of locally hydrating the upper mantle wedge.
4. The Ti content of olivine is relatively unaffected by sub-solidus cooling and can be used to estimate the water content associated with Ti-clinohumite point defects at conditions of melting in olivines which have subsequently suffered water loss. In highly depleted systems with low Ti concentrations, such as subduction zones, this acts as a 'chemical barrier' to hydration. Since the formation of hydrous Ti-clinohumite point defects alters the strength of olivine, nominally anhydrous arc mantle may remain relatively dry and stiff following hydrous metasomatism, increasing the preservation potential for chemically and isotopically distinct arc mantle.

6.1.3 Mobility of Os and other highly siderophile elements in subduction zones

1. An absence of correlations between Sr isotopes or HSE concentrations and Os isotopes indicates a minimal flux of these elements from the subducted slab into the mantle wedge.
2. HSE and lithophile element systematics are decoupled, indicating a dominant control by trace sulphide and alloy phases on the concentration and distribution of HSE in the Ritter samples, consistent with sulphide inclusions in olivine and orthopyroxene. Anomalous concentrations of Os and Pt in olivine separates compared to whole-rock samples requires separate, heterogeneously distributed Os- and Pt-rich alloy phases.
3. Low Pd/Ir ratios in 'residual' whole-rock samples and a subset of three 'reacted' samples correlate with moderately incompatible element concentrations in orthopyroxene, consistent with a dominant control by partial melting. Fractionated IPGE and high Pd/Ir in the remaining three 'reacted' samples is related to reaction between melt and the ambient upper mantle wedge.
4. Highly enriched Pt and Pd concentrations in a pyroxenite are complementary to depletions of these elements in the dunite. This reflects mobilisation and subsequent deposition of these elements as sulphide phases during melt-rock

reaction. Such elevated concentrations of Pt and Pd can thus be achieved through melt-rock reaction alone and do not require a flux from the subducted slab. The degree of Pt/Os and Pt/Re enrichment may also be relevant to the formation of suprachondritic $^{186}Os/^{188}Os$, if such lithologies can be preserved in the upper mantle over long timescales, negating the need for contribution from the core (e.g. Brandon et al. 1998),

5. Despite minimal control from slab-derived material and an absence of correlation with indicators of the degree of partial melting, Os isotope compositions and calculated model ages vary from 0.2 to 1.1 Ga. A negative correlation with phosphorous contents of olivine and orthopyroxene indicates that Os isotopes and P systematics may be related to ancient high-temperature processes not preserved in the other datasets presented in this thesis.

6.1.4 Origin of porphyroclastic texture and chemical diffusion in olivine

1. Olivine porphyroclasts within a xenolith displaying porphyroclastic texture contain substantial cryptic zoning of trace elements and water. Similarity between the compositions of olivine porphyroclast rims, fine-grained olivine neoblasts in the surrounding matrix and olivine phenocrysts in the host magma indicate that the texture formed in response to hydrous primitive basaltic melts percolating the upper mantle wedge.
2. Modelling of the diffusion profiles for Ca reveals timescales of approximately one year, which reflects the time between the flux of melt into the ambient mantle and exhumation of the xenolith.
3. Because of the cryptic nature of the chemical diffusion, such concentration profiles may have been overlooked in global occurrences of porphyroclastic mantle xenoliths. Similar exercises to this on similar samples may elucidate greater detail on the nature of primary melts, their interaction with ambient mantle and the timescales of xenolith formation
4. Trace and major elements, with the notable exception of phosphorous, diffuse in olivine at similar, rapid rates irrespective of the ionic charge or radius of the element.

6.2 Recommendations for future work

There are many avenues that could be explored further as a result of the research presented here. The samples studied here only represent a fraction of the total sample suite available. I would recommend performing a select number of analyses on these other samples, combined with more detailed analyses on the samples used in this study, to develop some of the key findings of my thesis:

1. *Redox state of arc mantle*. This topic is highly debated at present. The samples here clearly record trends in redox state, predominantly as a function of melt-rock reaction. However, problems with the oxybarometer calibrations when applied to high-Cr spinels and challenges in calculating precise values of oxygen fugacity based on probe data limited the extent to which the data could be interpreted. I would highly recommend a detailed study of spinel chemistry in these peridotites, combined with experimental petrology to test the veracity of different, widely applied oxybarometer calibrations. The experiments would synthesise a primitive basaltic melt, multiply-saturated with Cr-spinel, olivine and orthopyroxene over a range of oxygen fugacities constrained through both gas equilibria and solid buffers, at both 1 atm. and elevated pressure. Calculation of oxygen fugacity from the experimental assemblage using different published calibrations would be a simple test to see which one is appropriate for high-Cr spinels. This would then be combined with detailed probe and Mossbauer analyses of spinels to determine Fe^{3+}/Fe^{2+} ratios and oxygen fugacity. In particular, I would like to investigate the composition of spinel rims in 'residual' samples which may record a different oxidation state to the cores, based on their different colour and texture. Other redox-sensitive elements such as vanadium, chromium and sulphur could be measured to ascertain their partitioning behaviour between residual and secondary phases as a function of oxidation during melt-rock reaction.
2. *Cooling history of the mantle*. The partitioning of trace and major elements in 'residual' peridotites indicates that these samples cooled to unusually low equilibration temperatures, approaching 600 °C. If the cooling rate could be constrained then it would be possible to estimate the age of partial melting, represented by peak temperatures. This could be achieved in a variety of ways

and may not even necessarily require additional data from the Ritter suite. Liang (2014) recently presented a theoretical analysis of diffusive re-equilibration in bi-mineralic systems involving pyroxenes and plagioclase, with formulations for calculating timescale. I would like to extend this to olivine-bearing systems, which is perfectly feasible given reasonable constraints on the diffusion rate of a number of elements such as Ca and Ni. To accompany this, I would also like to better constrain the diffusion rates of Al and P in olivine, which are thought to diffuse slower (much slower in the case of P) than other elements. P in particular shows partitioning behaviour in this sample suite consistent with high-temperatures. If the diffusion rate of P could be determined it would be possible to place an upper limit on the cooling rate from P systematics alone. If the age of melting can be constrained from such a study, this could be combined with age estimates for tectonic events in the Bismarck Archipelago and therefore would potentially allow the ancient subduction zone setting postulated in this thesis to be identified.

3. *Hydroxylation spectroscopy.* The hydroxylation experiments described in this thesis provide a powerful tool for investigating the point defect structure of mantle and magmatic crystals. This in turn can be related to the chemistry of the crystal, the redox state of the system and other parameters such as water activity and pressure. This will allow identification of the water storage capacity and mechanisms and rates of water incorporation and loss in a range of systems, even those that have experienced complete dehydration. This experimental methodology will be developed by me as part of a postdoctoral fellowship at the Australian National University, working with Professor Hugh O'Neill with planned application to magmatic phenocrysts, cumulates and mantle samples.
4. *Mechanisms of HSE mobilisation.* The study of HSE and Os isotopes in chapter 4 reported a significant control by trace sulphide and alloy phases on how these elements behave during partial melting, cooling and melt-rock reaction, consistent with previous studies. In order to better constrain these processes I would highly recommend SEM mapping of thin sections combined with *in-situ* analyses of sulphides for HSE. This would be particularly interesting to do with the full set of dunites and pyroxenites available in the Ritter suite, since the HSE systematics of these samples may be crucial in understanding how elements such as Pt and Pd

become concentrated during melt-rock reaction, which in turn has implications for generating anomalous $^{186}Os/^{188}Os$ signatures in the mantle, otherwise attributed to core formation (Brandon et al. 1998).

6.3 References

Brandon, A.D., Walker, R.J., Morgan, J.W., Norman, M.D., Prichard, H.M., 1998. Coupled ^{186}Os and ^{187}Os Evidence for Core-Mantle Interaction. Science, 280, 1570-1573

Kamenov, G.D., Perfit, M.R., Mueller, P.A., Jonasson, I.R., 2008. Controls on magmatism in an island arc environment: study of lavas and sub-arc xenoliths from the Tabar-Lihir-Tanga-Feni island chain, Papua New Guinea. Contrib. Mineral. Petrol. 155, 635-656

Woodhead, J.D., Eggins, S.M., Johnson, R.W., 1998. Magma Genesis in the New Britain Island Arc: Further Insights into Melting and Mass Transfer Processes. J. Petrol. 39, 1641-1668

Appendix

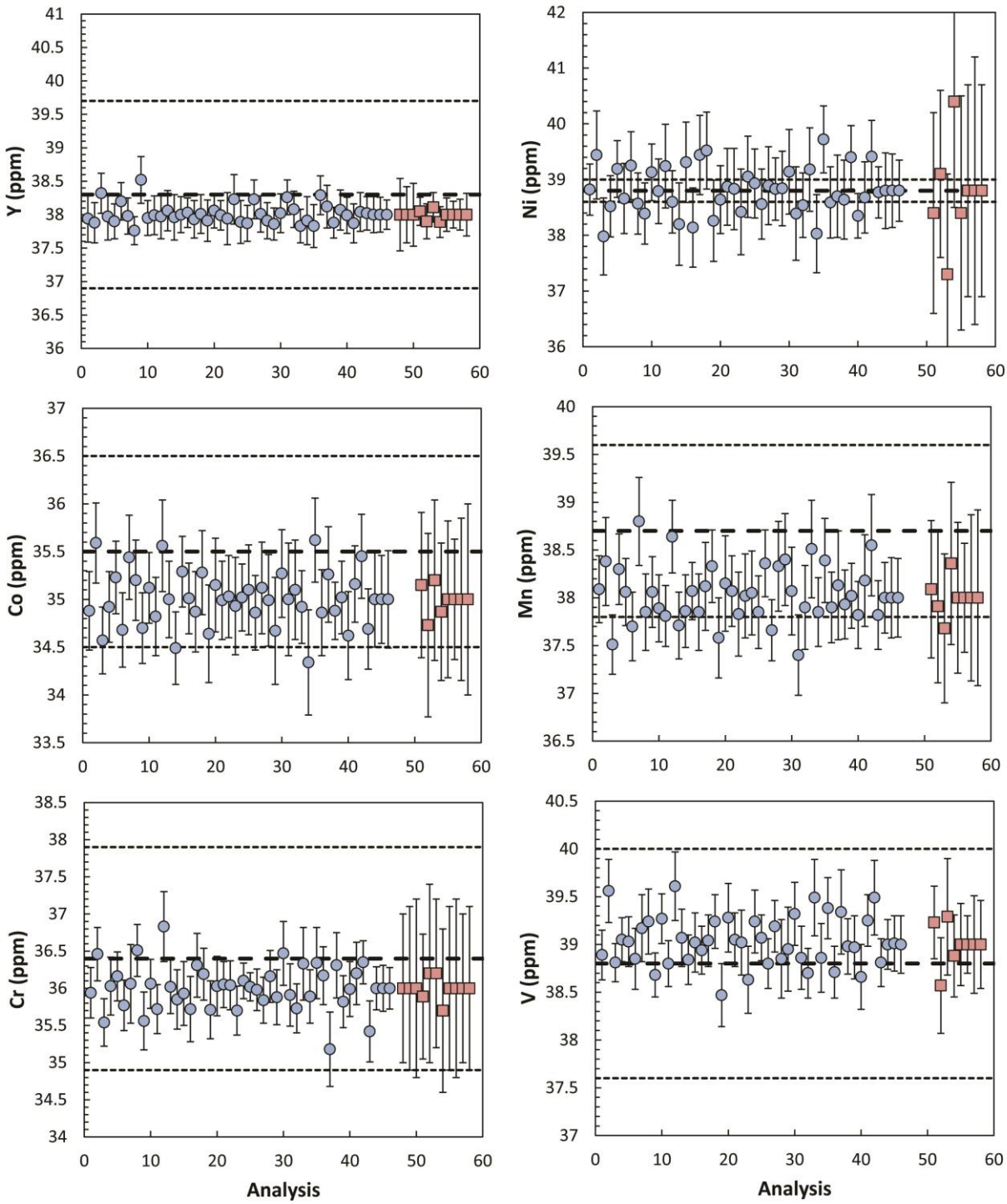

Fig. A1 Values of NIST 612 measured by LA-ICP-MS at ANU (blue circles) and Royal Holloway (pink squares). Uncertainties are ± 2 s.e. Bold dashed line is the accepted value from the GeoReM database, and the thin dashed lines are ± 1 s.d.

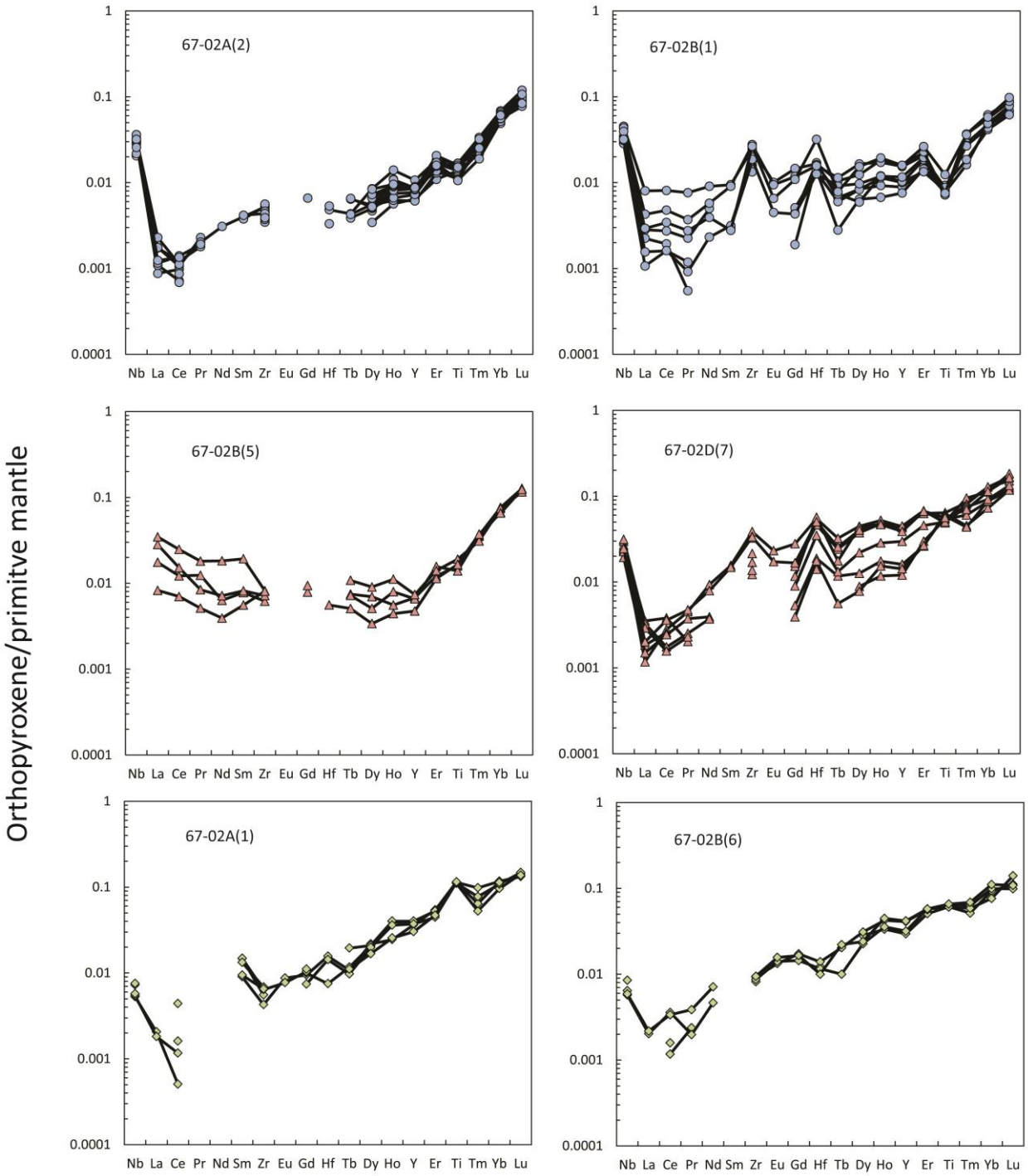

Fig. A2 Primitive-mantle normalised (Palme and O'Neill 2003) concentrations for multiple orthopyroxene crystals in individual samples

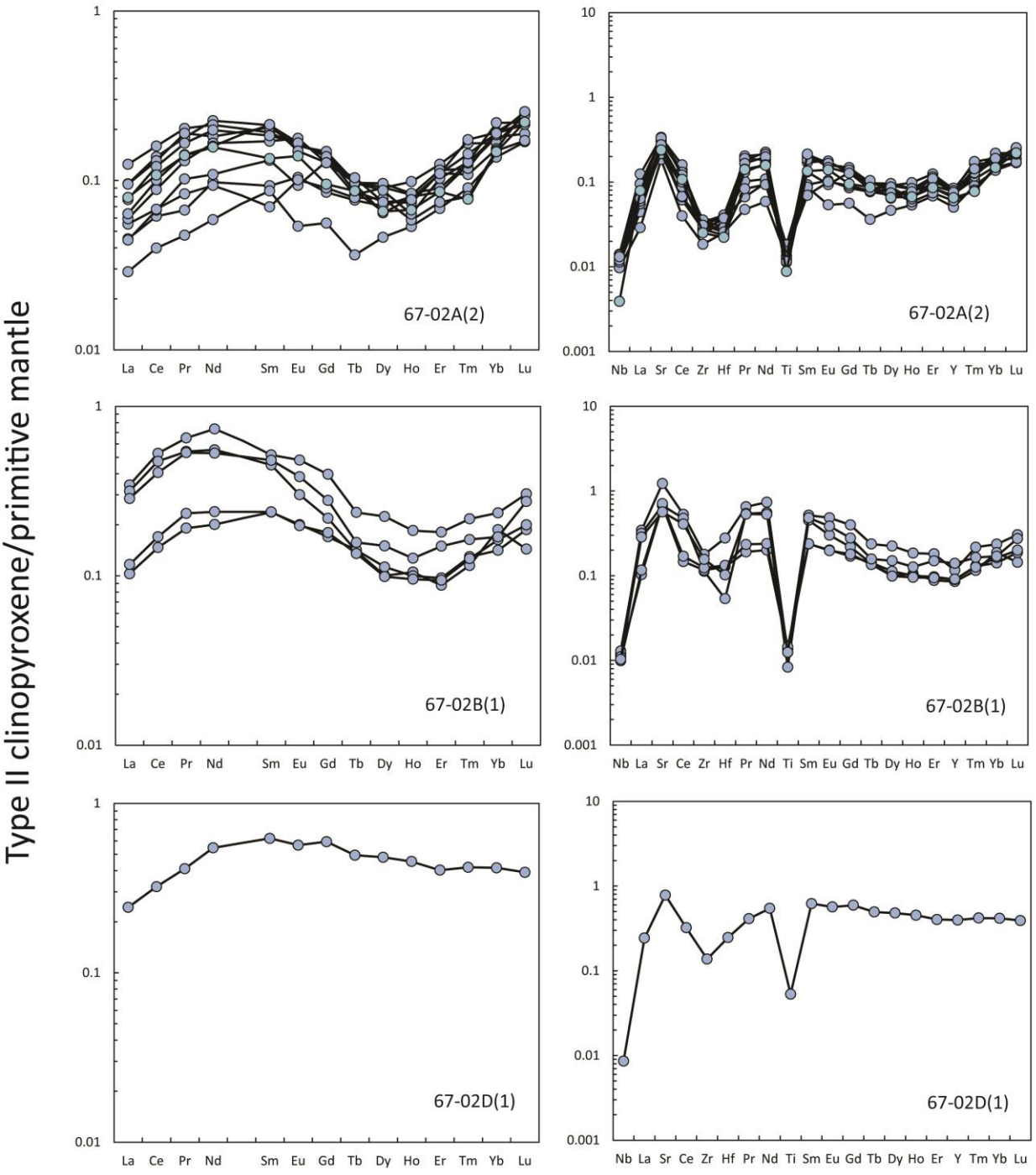
Type II clinopyroxene/primitive mantle
67-02A(2)
67-02B(1)
67-02D(1)
La Ce Pr Nd Sm Eu Gd Tb Dy Ho Er Tm Yb Lu
Nb La Sr Ce Zr Hf Pr Nd Ti Sm Eu Gd Tb Dy Ho Er Y Tm Yb Lu

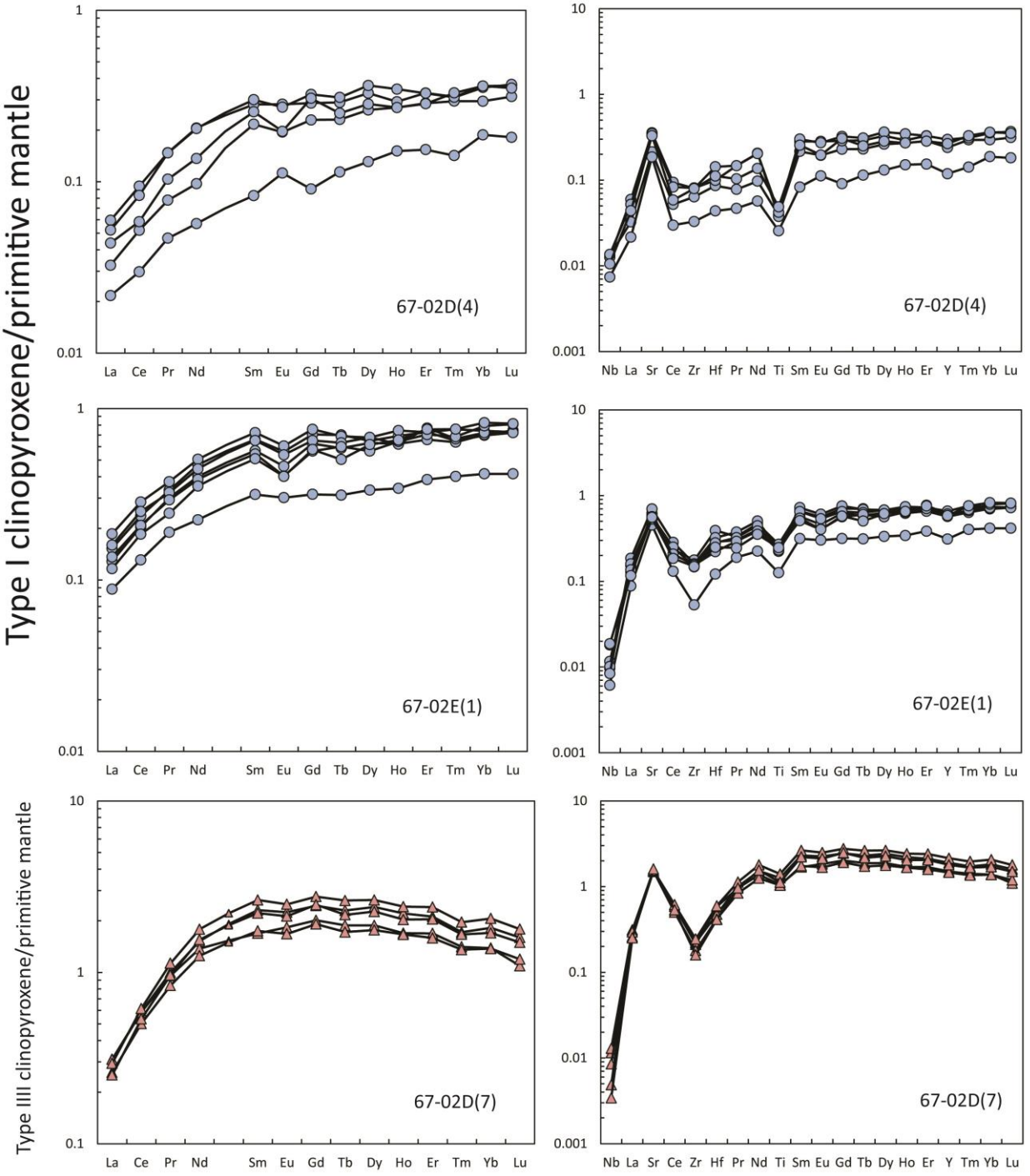

Fig. A3 Primitive-mantle normalised (Palme and O'Neill 2003) concentrations for multiple clinopyroxene crystals in individual samples. See text of chapter 2 for discussion of the different pattern types

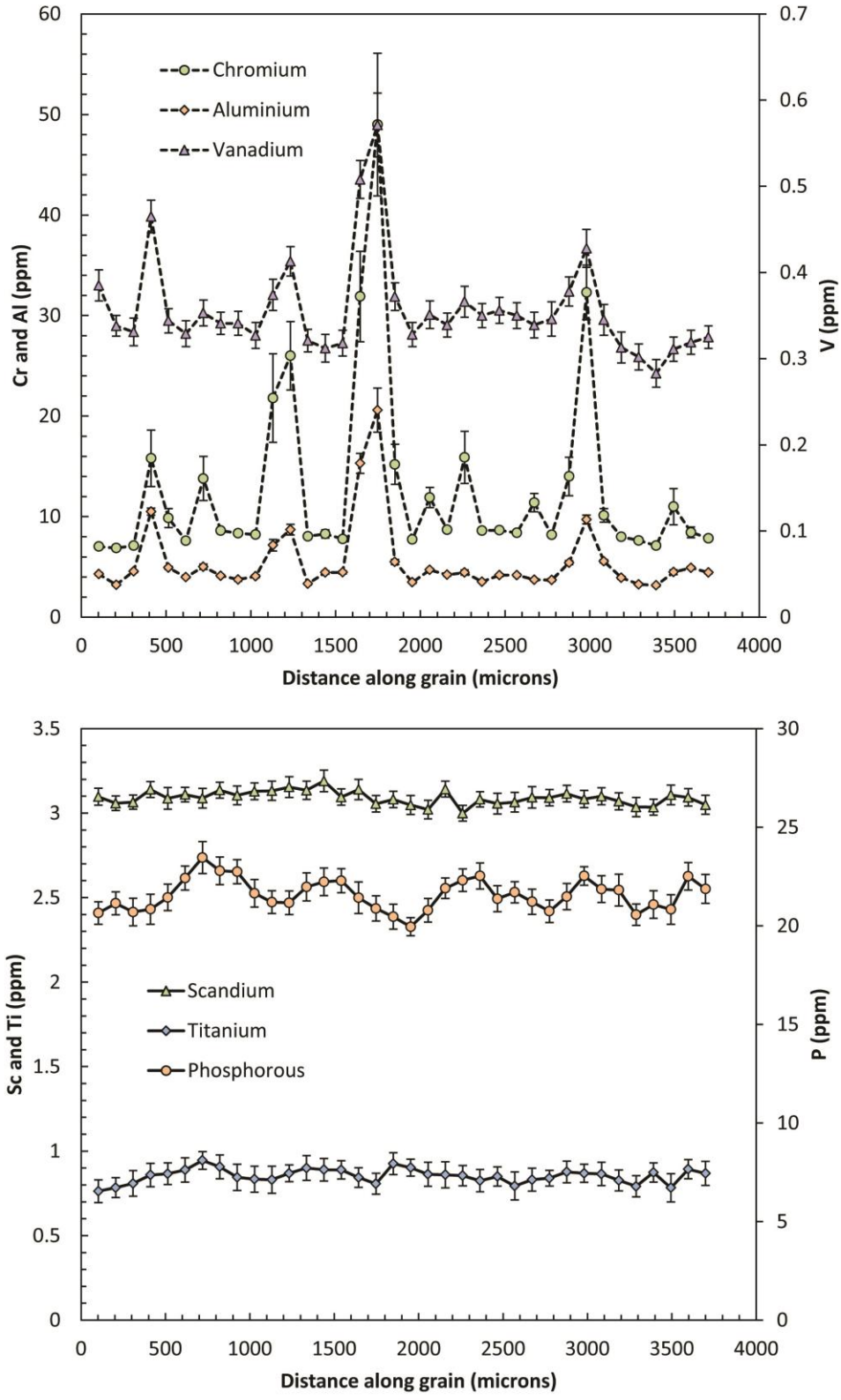

Fig. A4 Variation in trace element concentration across a large olivine in 'residual' sample 67-02A(2). Spikes in Cr, Al and V in the top panel are due to ablation of exsolved spinels formed due to very low equilibration temperatures and hence reduced solubilities

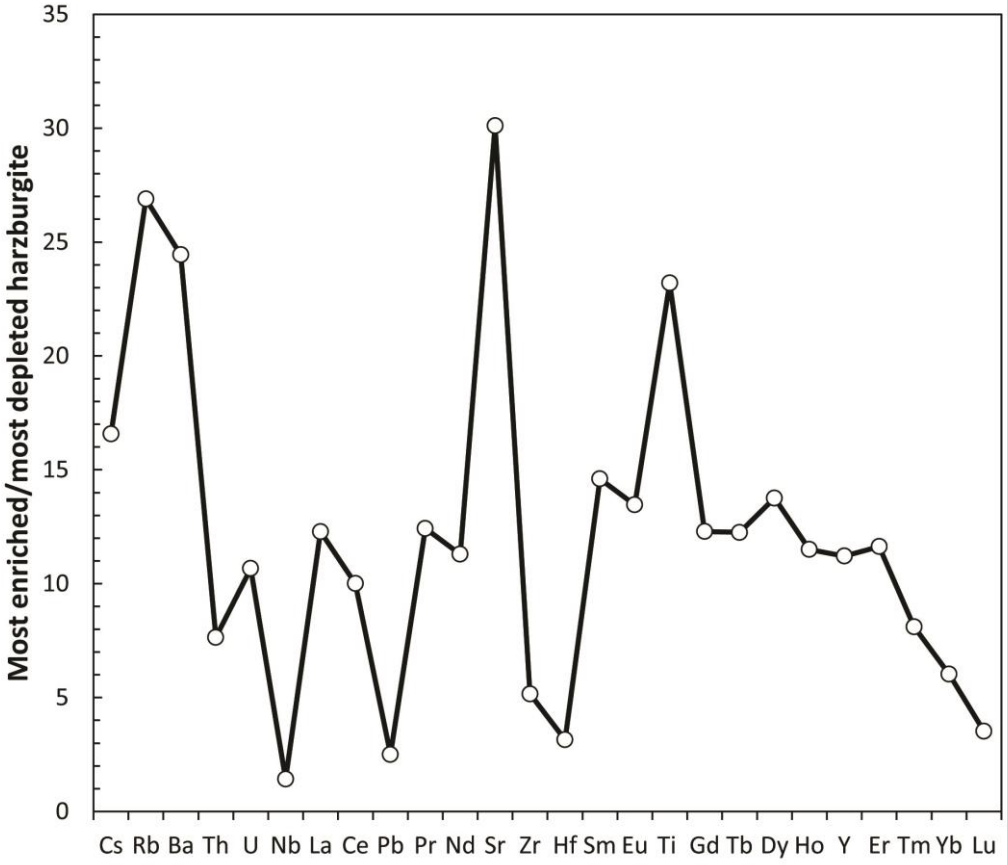

Fig. A5 The concentrations of trace elements in the most chemically enriched harzburgite divided by those of the most chemicalliy depleted peridotite. This figure therefore represents the relative enrichment of different trace elements during melt-rock reaction. Note in particular the very small increases in Nb, Zr and Hf, consistent with negative anomalies observed in West Bismarck lavas. Ti on the other hand is anomalously enriched